

**A TWO MOBILIZED-PLANE MODEL AND ITS APPLICATION  
FOR SOIL LIQUEFACTION ANALYSIS**

by

**SUNG-SIK PARK**

M.Eng., Tokyo Institute of Technology, Japan, 2000  
B.Eng., Kyungpook National University, South Korea, 1997

A THESIS SUBMITTED IN PARTIAL FULFILLMENT OF  
THE REQUIREMENTS FOR THE DEGREE OF  
DOCTOR OF PHILOSOPHY

in

THE FACULTY OF GRADUATE STUDIES

(CIVIL ENGINEERING)

THE UNIVERSITY OF BRITISH COLUMBIA

October 2005

© SUNG-SIK PARK, 2005

## ABSTRACT

Liquefaction-induced displacements have caused severe damage to buildings, bridges, and dams during past earthquakes. A reliable procedure for prediction of liquefaction and resulting displacements is necessary for rational design of earth structures resting on liquefiable soils. State-of-the-art procedures for evaluating liquefaction involve dynamic finite element or finite difference analyses using various constitutive models coupled with fluid flow effects. A constitutive model representing skeleton behaviour of soils is most important for analyses because the tendency of the soil skeleton to contract and dilate controls its liquefaction response.

Most conventional constitutive models can capture the response of conventional triaxial test specimens under hydrostatically consolidated conditions where no gradual rotation of principal axes occurs. However, field stress conditions are significantly different from such laboratory conditions, especially during earthquake loading, where conditions involve rotation of principal axes, and are more similar to simple shear loading. Conventional plasticity models cannot model rotation of principal axis, and in addition consider unloading as elastic, which is not generally consistent with observed soil behaviour.

A new constitutive model called UBCSAND2, formulated in the framework of classical plasticity, is proposed to address these concerns. The model is aimed at soil liquefaction problems that involve a reduction in mean effective stress and consider only shear-induced plastic behaviour. It is capable of handling plastic unloading and principal stress rotation associated with anisotropic consolidation during simple shear. It is referred to

as a Two Mobilized-plane model since shear-induced yielding is considered on two specific planes: a plane of maximum shear stress, which swings, and a horizontal plane which is spatially fixed. The plastic strain increments computed on the two planes are added to calculate plastic response.

Models based on the plane of maximum shear stress alone are particularly sensitive to lateral effective stress ratio  $K (= \sigma'_h/\sigma'_v)$ , whereas the proposed model gives a similar skeleton behaviour for soils at the same density and mean stress, regardless of the value of  $K$ , as observed in laboratory tests. The soil skeleton behaviour observed in cyclic drained simple shear tests, including compaction during unloading and dilation at large strain, is well captured by the new model. Undrained monotonic and cyclic response is predicted by imposing the volumetric constraint of the water on the drained or skeleton behaviour.

The proposed model is calibrated/validated using data from monotonic, cyclic drained, and constant volume (equivalent to undrained condition) simple shear tests on sands with and without initial static shear stress on a horizontal plane. The model has seven model parameters and is validated for plane strain condition. It is further validated by predicting the response observed in dynamic centrifuge tests modeling sloping ground conditions.

Several other considerations such as stress-induced densification, effect of saturation, effect of static shear, and stress reversal have been explored that significantly influence physical modeling using centrifuge tests. The proposed model becomes especially valuable when predicting soil behaviour in slopes where initial  $K$  conditions vary.

# TABLE OF CONTENTS

	<u>Page</u>
Abstract	ii
Table of Contents	iv
List of Tables	vii
List of Figures	viii
List of Symbols and Abbreviations	xv
Acknowledgements	xx
Chapter 1. Introduction.....	1
1.1 Numerical Procedures for Soil Liquefaction.....	4
1.1.1 Total Stress Analysis.....	4
1.1.2 Effective Stress Analysis.....	7
1.2 Research Motivation and Scope of Work.....	9
1.3 Outline of the Thesis.....	11
Chapter 2. Overview of Sand Behaviour and its Modeling.....	13
2.1 Direct Simple Shear Devices.....	14
2.2 Sand Behaviour under Simple Shear.....	16
2.2.1 Principal Stress Rotation and its Consequences.....	20
2.3 Modeling of Shear-induced Volume Change.....	24
2.3.1 Monotonic Loading.....	25
2.3.2 Cyclic Loading.....	27
2.4 Plasticity Models for Soil.....	31
2.4.1 Classical Plasticity Models.....	31
2.4.2 Advanced Plasticity Models.....	35
2.4.3 Micromechanical and/or Multimechanism Models.....	38
2.4.4 Summary of Plasticity Models.....	42
Chapter 3. Development of a Two Mobilized-plane Model: UBCSAND2.....	45
3.1 UBCSAND Model and its Capability.....	46
3.2 Concept of a Two Mobilized-plane Model.....	49
3.3 Elastic Behaviour.....	52
3.4 Plastic Behaviour.....	53
3.4.1 Failure and Yield Functions.....	56

3.4.2 Hardening Rule.....	60
3.4.3 Flow Rule .....	66
3.4.4 Hardening of Stress-Dilatancy.....	74
3.5 Predicted Characteristic Response.....	79
3.5.1 Simulation of Simple Shear .....	79
3.5.2 Lateral Stress Change .....	80
3.5.3 Behaviour under $K = 1$ and 0.5 Initial Stress states.....	82
3.6 Implementation of UBCSAND2 in FLAC .....	84
3.6.1 Calculation Procedure of Two Mobilized Planes .....	85
3.7 Summary.....	86
Chapter 4. Calibration of UBCSAND2 .....	88
4.1 Calibration Procedure and Input Parameters .....	88
4.2 Specific Calibration .....	93
4.2.1 Calibration of Drained Behaviour .....	95
4.2.2 Prediction of Constant Volume Tests without Initial Static Shear Stress .	103
4.2.3 Prediction of Constant Volume Tests with Initial Static Shear Stress.....	112
4.3 Comparison between UBCSAND and UBCSAND2 for Simple Shear .....	118
4.4 General Calibration.....	121
4.4.1 Volume Change during Cyclic Loading .....	122
4.4.2 Calibration of Field Performance .....	125
4.5 Summary.....	127
Chapter 5. Validation of UBCSAND2 using C-CORE Centrifuge Tests .....	129
5.1 Modeling of Sloping Ground.....	130
5.2 C-CORE Centrifuge Tests for UBC Liquefaction Research Project.....	131
5.2.1 Soil and Boundary Conditions.....	133
5.2.2 Instrumentation Layout.....	135
5.2.3 Earthquake Input Motions .....	138
5.2.4 Dynamic Centrifuge Testing .....	140
5.3 Centrifuge Testing Considerations and Inputs .....	141
5.3.1 Stress-induced Densification .....	141
5.3.2 Effect of Saturation.....	145
5.3.3 Permeability and Viscous Fluid.....	148
5.3.4 Input Parameters .....	150
5.3.5 Criteria for Comparison between Measurement and Prediction.....	151
5.4 Prediction of CT2 and its Comparison .....	152
5.4.1 Measured and Predicted Excess Pore Pressures of CT2.....	154
5.4.2 Measured and Predicted Accelerations of CT2 .....	158
5.4.3 Measured and Predicted Displacements of CT2.....	161
5.4.4 Summary of CT2 Comparison.....	164

5.5 Prediction of CT6 and its Comparison .....	165
5.5.1 Measured and Predicted Excess Pore Pressures of CT6.....	167
5.5.2 Measured and Predicted Accelerations of CT6 .....	169
5.5.3 Measured and Predicted Displacements of CT6.....	172
5.5.4 Summary of CT6 Comparison.....	174
5.6 Comparison between UBCSAND and UBCSAND2 for Centrifuge Test.....	174
5.7 Summary of C-CORE Centrifuge Tests Prediction.....	176
Chapter 6. Summary and Conclusions .....	178
6.1 Summary and Findings.....	178
6.2 Limitations of UBCSAND2 .....	181
6.3 Further Research.....	182
References .....	184
Appendix A: Derivation of Plastic Deformation on the Horizontal Plane .....	200
Appendix B: Derivation of Stress Densification Equation.....	203
Appendix C: Pore Pressure Change under Undrained Condition.....	210
Appendix D: FLAC Simulation and Boundary Conditions of C-CORE Centrifuge Tests .....	213

## LIST OF TABLES

Table 2.1	Comparison of typical plasticity models for sand under cyclic loading and their capabilities.....	44
Table 3.1	Suggested cyclic hardening parameter $C_h$ for different densities.....	77
Table 4.1	Specific calibration procedure of UBCSAND2 (test data from Sriskandakumar, 2004).....	93
Table 4.2	Summary of selected drained DSS tests on loose Fraser River sand (test data from Sriskandakumar, 2004) .....	96
Table 4.3	Input parameters for monotonic and cyclic drained DSS tests on Fraser River sand at $D_{rc} = 40\%$ .....	96
Table 4.4	Summary of selected constant volume DSS tests on loose Fraser River sand without initial static shear stress (test data from Sriskandakumar, 2004) ....	103
Table 4.5	Summary of selected constant volume DSS tests on loose Fraser River sand with initial static shear stress (test data from Sriskandakumar, 2004) .....	113
Table 4.6	General calibration procedure of UBCSAND2 .....	121
Table 4.7	Input parameters for $D_r = 45\%$ .....	122
Table 4.8	Input parameters for NCEER chart calibration .....	126
Table 4.9	UBCSAND2 calibration at 15 cycles .....	126
Table 5.1	Proposed centrifuge models at C-CORE .....	132
Table 5.2	Soil Conditions .....	135
Table 5.3(a)	Transducers' coordinates of CT2 in Category I (unit: m in prototype).....	138
Table 5.3(b)	Transducers' coordinates of CT6 in Category II (unit: m in prototype).....	138
Table 5.4	Input parameters for C-CORE centrifuge tests, CT2 and CT6.....	151
Table 5.5	Evaluation items for the comparison between the measured and predicted C-CORE centrifuge tests .....	152

## LIST OF FIGURES

Figure 1.1	Damage during the 1964 Niigata Earthquake: (a) Kawagishi-cho apartment building, and (b) the Showa bridge.....	2
Figure 1.2	Damage during the 1995 Kobe Earthquake: (a) Kobe Port cranes, and (b) the Nishinomiya Bridge.....	2
Figure 1.3	Correlation between CRR and $(N_1)_{60}$ modified from Seed et al. (1985) (after Youd et al., 2001) .....	5
Figure 1.4	Liquefaction analysis: Total and Effective stress analyses.....	7
Figure 2.1	Simple shear: (a) NGI-type simple shear apparatus at UBC (after Sivathayalan, 2000), and (b) simple shear deformation .....	15
Figure 2.2	Critical void ratio: (a) & (b) hypothesis of critical void ratio derived from direct shear tests (after Casagrande, 1976), and (c) simple shear tests on 1 mm diameter steel balls with normal stress 138 kPa: specific volume $v$ and shear displacement $x$ (after Wroth, 1958) .....	17
Figure 2.3	Results of monotonic drained simple shear tests on Ottawa sand at various densities (modified from Vaid et al., 1981).....	18
Figure 2.4	Results of cyclic drained simple shear test on loose and dense Fraser River sand (after Sriskandakumar, 2004).....	19
Figure 2.5	Dependence of dilation angle on relative density and stress level (after Vaid et al., 1981) .....	19
Figure 2.6	Principal stress rotation during simple shear .....	20
Figure 2.7	Variation of the direction of major principal stress $\alpha_\sigma$ during simple shear test on dense Leighton Buzzard sand (after Wood et al., 1979).....	21
Figure 2.8	Results of continuous rotation tests: (a) variation of principal stress directions and stress ratio, and (b) cumulative major principal strain on dense sand (after Arthur et al., 1980).....	23
Figure 2.9	Result of a pure principal stress rotation test on loose Toyoura sand (after Ishihara & Towhata, 1983).....	23
Figure 2.10	Sliding mechanism assumed for Rowe's stress-dilatancy theory (after Yang & Li, 2004) .....	25
Figure 2.11	Relationship between the stress ratio and the strain increment ratio in drained simple shear tests on Ottawa sand (after Puebla, 1999) .....	27

Figure 2.12	Idealized cross section of particulate group showing packing changes that occur during cyclic loading (after Youd, 1977).....	28
Figure 2.13	Shear stress ratio vs. dilatancy rate during loading, unloading and reloading: (a) after Lee (1991), and (b) simplified dilatancy.....	29
Figure 2.14	Concept of associated Mohr-Coulomb type of models with cap and cone yield surfaces .....	33
Figure 2.15	Concept of bounding surface (uniaxial) model (after Dafalias & Popov, 1975) .....	35
Figure 2.16	Nested surface model: (a) before straining, (b) after straining, and (c) upon unloading (after Mroz, 1967).....	37
Figure 2.17	Three mobilized planes on which $(\tau/\sigma')$ is maximum under three different principal stresses (modified from Matsuoka, 1974) .....	39
Figure 2.18	General shear and normal stresses (after Matsuoka & Sakakibara, 1987) .....	40
Figure 2.19	Schematic description of multi-laminate framework (after Cudny & Vermeer, 2004).....	41
Figure 3.1	Simple shear test under $K_0$ consolidated condition .....	47
Figure 3.2	Numerical and experimental results of monotonic drained behaviour of loose Fraser River sand (test data from Sriskandakumar, 2004) .....	48
Figure 3.3	Stress conditions on two mobilized planes after applying shear: (a) small strain level, and (b) large strain level.....	50
Figure 3.4	Stress-strain curves for one mobilized plane and two mobilized planes.....	51
Figure 3.5	Flow chart of UBCSAND2 calculation .....	56
Figure 3.6	Initial stress condition imposed on $K_0$ -consolidated simple shear test specimen and two mobilized planes .....	57
Figure 3.7	Yield locus and failure state .....	59
Figure 3.8	Hyperbolic stress-strain hardening relationship .....	61
Figure 3.9	Stress-strain cycle: (a) definition of loading, unloading and reloading, and (b) modified shear stresses .....	64
Figure 3.10	One-sided loading stress-strain curve.....	65
Figure 3.11	Non-associated flow rule and dilation angle .....	66
Figure 3.12	Plastic potential function and direction of plastic strain increments .....	67
Figure 3.13	Two extreme cases of principal stress rotation.....	69

Figure 3.14	Effect of a parameter $\chi$ on phasing-out pattern .....	70
Figure 3.15	Principal stress rotation angle $\alpha_\sigma$ : (a) small strain, and (b) large strain level.	70
Figure 3.16	Stress-dilatancy equation during one cycle of stress-strain curve (modified from Lee, 1991) .....	71
Figure 3.17	Measured stress-dilatancy relationship and proposed flow rule with a contraction limit (basic data obtained from Sriskandakumar, 2004).....	73
Figure 3.18	Volumetric strains from constant amplitude cyclic simple shear tests (after Martin et al., 1975) .....	75
Figure 3.19	Determination of a modified shear strain ( $\gamma^*$ ) used in plastic volume hardener: (a) two-sided loading, and (b) one-sided loading .....	78
Figure 3.20	Simulation of the hardening function $H_c$ during cyclic loading: (a) variation pattern of $H_c$ , and (b) shear stress cycles .....	78
Figure 3.21	A single element of unit dimensions: (a) drained test, and (b) constant volume test.....	79
Figure 3.22	Measured lateral stress from drained simple shear test (after Finn, 1985).....	80
Figure 3.23	Predicted lateral stress ( $\sigma'_x$ ) of UBCSAND2 during monotonic DSS test.....	81
Figure 3.24	Initial stress conditions for numerical simulation with $K = 0.5$ and $1.0$ with the same initial mean stress .....	83
Figure 3.25	Comparison of test result and numerical simulation of $K = 0.5$ and $1.0$ with the same initial mean stress (test data from Sriskandakumar, 2004).....	83
Figure 3.26	Numerical simulation for different $K$ states, $0.5$ , $0.7$ and $1.0$ : (a) Initial stress conditions, and (b) UBCSAND2 results.....	84
Figure 3.27	Initial stress state and first time loading .....	86
Figure 4.1	Model calibration and validation procedures of UBCSAND2 .....	89
Figure 4.2	Grain size distribution of Fraser River sand .....	95
Figure 4.3	Monotonic drained simple shear response of loose Fraser River sand: (a) shear stress vs. shear strain, and (b) volumetric strain vs. shear strain (test data from Sriskandakumar, 2004) .....	98
Figure 4.4	Predicted lateral stress and vertical effective stress (100 kPa constant) during monotonic drained simple shear test on loose Fraser River sand .....	99
Figure 4.5	Measured (left side) and calibrated (right side) cyclic drained test on loose Fraser River sand with $\gamma_{cyc} = 0.5\%$ : (a) shear stress vs. shear strain, and (b) volumetric strain vs. shear strain (test data from Sriskandakumar, 2004)....	100

Figure 4.6	Measured (left side) and calibrated (right side) cyclic drained test on loose Fraser River sand with $\gamma_{cyc} = 1.0\%$ : (a) shear stress vs. shear strain, and (b) volumetric strain vs. shear strain (test data from Sriskandakumar, 2004)....	101
Figure 4.7	Computed lateral stress from cyclic drained test on loose Fraser River sand with $\gamma_{cyc} = 0.5\%$ .....	102
Figure 4.8	Computed lateral stress from cyclic drained test on loose Fraser River sand with $\gamma_{cyc} = 1.0\%$ .....	102
Figure 4.9	Measured and predicted monotonic constant volume test on loose Fraser River sand: (a) shear stress vs. shear strain, and (b) shear stress vs. vertical effective stress (test data from Sriskandakumar, 2004).....	105
Figure 4.10	Comparison of numerical predictions based on constant volume and undrained conditions of loose Fraser River sand: (a) shear stress vs. shear strain, and (b) shear stress vs. vertical effective stress .....	106
Figure 4.11	Measured (left side) and predicted (right side) cyclic constant volume test on loose Fraser River sand under $CSR = 0.08$ : (a) stress path, and (b) shear stress vs. shear strain (test data from Sriskandakumar, 2004).....	108
Figure 4.12	Measured (left side) and predicted (right side) cyclic constant volume test on loose Fraser River sand under $CSR = 0.1$ : (a) stress path, and (b) shear stress vs. shear strain (test data from Sriskandakumar, 2004).....	109
Figure 4.13	Measured (left side) and predicted (right side) cyclic constant volume test on loose Fraser River sand under $CSR = 0.15$ : (a) stress path, and (b) shear stress vs. shear strain (test data from Sriskandakumar, 2004).....	110
Figure 4.14	Predicted liquefaction resistance and test result in terms of $\tau_{cyc}/\sigma'_{y0}$ (test data from Sriskandakumar, 2004) .....	111
Figure 4.15	Predicted liquefaction resistance in terms of $\tau_{cyc}/\sigma'_{m0}$ under $K = 0.5$ and $1.0$ and test result (test data from Sriskandakumar, 2004) .....	112
Figure 4.16	Measured (left side) and predicted (right side) cyclic constant volume test on loose Fraser River sand with initial static shear stress ( $\alpha = 0.1$ ) under $CSR = 0.065$ : (a) stress path, and (b) stress-strain curve (test data from Sriskandakumar, 2004).....	114
Figure 4.17	Measured (left side) and predicted (right side) cyclic constant volume test on loose Fraser River sand with initial static shear stress ( $\alpha = 0.1$ ) under $CSR = 0.1$ : (a) stress path, and (b) stress-strain curve (test data from Sriskandakumar, 2004).....	115
Figure 4.18	Measured (left side) and predicted (right side) cyclic constant volume test on loose Fraser River sand with initial static shear stress ( $\alpha = 0.05$ ) under $CSR =$	

	0.15: (a) stress path, and (b) stress-strain curve (test data from Sriskandakumar, 2004).....	116
Figure 4.19	Predicted liquefaction resistance under $K = 0.5$ and test result with and without initial static shear stress in terms of $\tau_{cyc}/\sigma'_{y0}$ (test data from Sriskandakumar, 2004).....	117
Figure 4.20	Comparison of UBCSAND (left) and UBCSAND2 (right) using cyclic drained test on loose Fraser River sand with $\gamma_{cyc} = 0.5\%$ : (a) shear stress vs. shear strain, and (b) shear stress vs. volumetric strain .....	118
Figure 4.21	Comparison of UBCSAND (left) and UBCSAND2 (right) using cyclic constant volume test on loose Fraser River sand under CSR = 0.1: (a) stress path, and (b) shear stress vs. shear strain.....	119
Figure 4.22	Comparison of UBCSAND (left) and UBCSAND2 (right) using cyclic constant volume test on loose Fraser River sand with initial static shear stress ( $\alpha = 0.1$ ) under CSR = 0.1: (a) stress path, and (b) shear stress vs. shear strain .....	120
Figure 4.23	Volumetric strains from constant amplitude cyclic simple shear and calibration (test data from Marin et al., 1975).....	123
Figure 4.24	Relationship between a volumetric strain and a shear strain for a uniform crystal silica sand (test data from Silver & Seed, 1971) and its UBCSAND2 calibration .....	124
Figure 4.25	Relationship between volumetric strain ratio and number of cycles for a uniform crystal silica sand (Tokimatsu & Seed, 1987) .....	125
Figure 4.26	Comparison of calibrated (UBCSAND2) and field-observed liquefaction resistance (NCEER chart from Youd & Idriss, 1997).....	127
Figure 5.1	Patterns of shear stress reversal (after Hyodo et al., 1991) .....	131
Figure 5.2	Centrifuge model configurations: (a) Category I used for CT1 to CT4, and (b) Category II used for CT5 to CT8 (unit: m in prototype).....	134
Figure 5.3	Particle size distribution curves for Fraser Rive sand and Coarse sand .....	136
Figure 5.4	General instrumentations: (a) CT2 in Category I, and (b) CT6 in Category II (unit: m in prototype).....	137
Figure 5.5	Target earthquake input motions: (a) A475 event with 10%/50yr, and (b) A2475 event with 2%/50yr.....	139
Figure 5.6	Measured excess pore pressures (EPP) of RPI centrifuge test and predicted EPP with (right side) and without (left side) stress densification after Park et al. (2004) (measurements from Gonzalez et al., 2002).....	142

Figure 5.7	Relative density change predicted and measured for Fraser River sand .....	144
Figure 5.8	As-placed density and increased density of C-CORE centrifuge model .....	145
Figure 5.9	Variation of fluid stiffness on different initial saturations.....	148
Figure 5.10	Measured hydraulic conductivity $k$ of Fraser River sand using water as a pore fluid (after Sriskandakumar, 2003).....	149
Figure 5.11	Liquefaction resistance of loose Fraser River sand and UBCSAND2 prediction (test data from Sriskandakumar, 2004) .....	150
Figure 5.12	Comparison of target A2475 motion and actual input motions applied into CT2: (a) target A2475 motion, and (b) actual A2475 input .....	153
Figure 5.13	Comparison of Excess Pore Pressures (EPP): (a) measured, and (b) predicted EPP at free field of CT2 (test data from C-CORE, 2004) .....	155
Figure 5.14	Comparison of Excess Pore Pressures (EPP): (a) measured, and (b) predicted EPP at Near-crest zone of CT2 (test data from C-CORE, 2004).....	156
Figure 5.15	Comparison of Excess Pore Pressures (EPP): (a) measured, and (b) predicted EPP at Near-slope zone of CT2 (test data from C-CORE, 2004).....	157
Figure 5.16	Comparison of Accelerations (ACC): (a) measured, and (b) predicted ACC at free field of CT2 (test data from C-CORE, 2004) .....	158
Figure 5.17	Comparison of Accelerations (ACC): (a) measured, and (b) predicted ACC at Near-crest zone of CT2 (test data from C-CORE, 2004) .....	159
Figure 5.18	Comparison of Accelerations (ACC): (a) measured, and (b) predicted ACC at Near-slope zone of CT2 (test data from C-CORE, 2004) .....	160
Figure 5.19	Comparison of Displacements (Disp): (a) measured, and (b) predicted Disp of CT2 (test data from C-CORE, 2004).....	162
Figure 5.20	CT2 Deformations before and after tests: (a) Measured deformation (after C-CORE, 2004), and (b) predicted deformation .....	163
Figure 5.21	Comparison of target $2 \times A2475$ motion and actual input motions applied into CT6: (a) target $2 \times A2475$ motion, and (b) actual $2 \times A2475$ input.....	166
Figure 5.22	Comparison of Excess Pore Pressures (EPP): (a) measured, and (b) predicted EPP at deep area of CT6 (test data from C-CORE, 2005a).....	167
Figure 5.23	Comparison of Excess Pore Pressures (EPP): (a) measured, and (b) predicted EPP at shallow area near slope of CT6 (test data from C-CORE, 2005a)....	168
Figure 5.24	Comparison of Accelerations (ACC): (a) measured, and (b) predicted ACC at deep area of CT6 (test data from C-CORE, 2005a).....	170

Figure 5.25	Comparison of Accelerations (ACC): (a) measured, and (b) predicted ACC at shallow area near slope of CT6 (test data from C-CORE, 2005a) .....	171
Figure 5.26	CT6 Deformations before and after tests: (a) Measured deformation (modified from C-CORE, 2005a), and (b) predicted deformation.....	173
Figure 5.27	Comparison of CT2 excess pore pressures predicted by UBCSAND and UBCSAND2 and measurement .....	175
Figure 5.28	Comparison of CT2 accelerations predicted by UBCSAND and UBCSAND2 and measurement (ACC5 was malfunction, C-CORE 2004) .....	176

## LIST OF SYMBOLS AND ABBREVIATIONS

The sign convention used in this thesis is that positive values of stress and strain indicate compression and contraction, respectively. All analyses in this thesis assume plane strain and hence stress and strain measures are defined to ignore the out of plane component. Anticlockwise shear stresses are taken as positive.

### Greek Letter Symbols

$\alpha$	Initial static shear stress ratio, $\tau_{sta}/\sigma'_{y0}$
$\alpha_B$	Bulk modulus factor
$\alpha_D$	Coefficient of stress densification
$\alpha_\sigma$	Angle between a major principal stress increment and the vertical
$\beta$	Angle between the horizontal and maximum shear stress planes
$\chi$	Adjustment parameter of horizontal plane phasing out
$\varepsilon^e$	Elastic strain
$\varepsilon^p$	Plastic strain
$\varepsilon_v$	Volumetric strain, $\varepsilon_1 + \varepsilon_3$
$\varepsilon_v^e$	Elastic volumetric strain
$\varepsilon_v^p$	Plastic volumetric strain, $\varepsilon_1^p + \varepsilon_3^p$
$\phi$	Friction angle
$\phi_{cv}$	Friction angle at constant volume
$\phi_f$	Friction angle at failure
$\phi_m$	Mobilized friction angle
$\phi_{m1}$	Mobilized friction angle on the plane of maximum shear
$\phi_{m2}$	Mobilized friction angle on a horizontal plane

$\gamma$	Total shear strain, $\varepsilon_1 - \varepsilon_3$
$\gamma^*$	Modified shear strain
$\gamma_{cyc}$	Cyclic shear strain
$\gamma_r$	Shear strain at stress reversal
$\gamma^p$	Plastic shear strain, $\varepsilon_1^p - \varepsilon_3^p$
$\gamma_{11}^p$	Plastic shear strain occurring on the plane of maximum shear stress
$\gamma_{22}^p$	Plastic shear strain occurring on the horizontal plane
$\gamma_{xy}^{ac}$	Shear strain due to anisotropic consolidation
$\gamma_{xy}^r$	Shear strain due to principal stress rotation
$\gamma_{xy}^s$	Shear strain due to shear
$\eta$	Stress ratio, $\tau/\sigma'$
$\eta^*$	Modified stress ratio
$\eta_f$	Stress ratio at failure
$\eta_f^*$	Modified stress ratio at failure
$\eta_{ult}$	Stress ratio at ultimate condition
$\eta_1$	Stress ratio on maximum shear stress plane, $(\sigma'_1 - \sigma'_3)/(\sigma'_1 + \sigma'_3)$
$\eta_2$	Stress ratio on horizontal plane, $2\tau_{xy}/(\sigma'_x + \sigma'_y)$
$\eta_2^*$	Modified stress ratio on horizontal plane
$\lambda$	Scalar number
$\lambda_2$	Scalar number related to the horizontal plane
$\lambda_2^*$	Adjusted scalar number $\lambda_2$
$\nu$	Poisson's ratio
$\sigma'$	Normal effective stress
$\sigma'_h$	Horizontal effective stress
$\sigma'_m$	Mean normal effective stress in the plane of loading $(= (\sigma'_x + \sigma'_y)/2)$
$\sigma'_{m0}$	Initial mean normal effective stress
$\sigma'_v$	Vertical effective stress
$\sigma'_{v0}$	Initial vertical effective stress
$\sigma'_x$	Lateral normal effective stress

$\sigma'_{x0}$	Initial lateral normal effective stress
$\sigma'_y$	Vertical normal effective stress
$\sigma'_{y0}$	Initial vertical normal effective stress
$\sigma'_1$	Major principal effective stress
$\sigma'_2$	Intermediate principal effective stress
$\sigma'_3$	Minor principal effective stress
$\tau$	Shear stress
$\tau^*$	Modified shear stress
$\tau_{cyc}$	Cyclic shear stress
$\tau_f$	Shear stress at failure
$\tau_f^*$	Modified shear stress at failure
$\tau_r$	Shear stress at stress reversal
$\tau_{sta}$	Static shear stress
$\tau_{xy}$	Shear stress on horizontal plane
$\tau_0$	Initial shear stress or shear stress at the beginning
$\tau_1$	Shear stress on the plane of maximum shear
$\tau_2$	Shear stress on a horizontal plane
$\psi$	Dilation angle
$\psi_m$	Mobilized dilation angle
$\psi_{m1}$	Mobilized dilation angle on the plane of maximum shear
$\psi_{m2}$	Mobilized dilation angle on a horizontal plane

### **Roman Letter Symbols and Abbreviations**

B	Elastic bulk modulus of soil skeleton
$B_f$	Bulk modulus of fluid
$B_{skem}$	Skempton's B value
C	Sand stiffness number
$C_h$	Cyclic hardening parameter
CRR	Cyclic resistance ratio

CSR	Cyclic stress ratio, $\tau_{cyc}/\sigma'_{y0}$
D	Dilatancy
$D_r$	Relative density
$D_{rc}$	Relative density at the end of consolidation
$D_{r0}$	Relative density at zero pressure
e	Void ratio
$e_c$	Void ratio at eh critical state
f	Yield function
$f_1$	Yield function on the plane of maximum shear stress
$f_2$	Yield function on the horizontal plane
g	Acceleration due to gravity
$g_1$	Plastic potential on the plane of maximum shear stress
$g_2$	Plastic potential on the horizontal plane
G	Elastic shear modulus
$G^p$	Plastic shear modulus
$G^p_1$	Plastic shear modulus on the plane of maximum shear stress
$G^p_2$	Plastic shear modulus on the horizontal plane
$G^p_{max}$	Maximum plastic shear modulus
$H_c$	Cyclic hardener
k	Hydraulic conductivity
$k^*$	Effective hydraulic conductivity in the centrifuge
$k^e_G$	Elastic shear modulus number
$k^p_G$	Plastic shear modulus number
K	Lateral stress ratio, $\sigma'_h/\sigma'_v$ (coefficient of lateral stress)
$K_0$	Lateral stress ratio at rest (coefficient of lateral stress at rest)
$K_{2max}$	Modulus coefficient for estimating $G_{max}$
$N_{Liq}$	Number of cycles to liquefaction
n	Porosity
ne	Elastic exponent for shear modulus
np	Plastic exponent for shear modulus

$(N_1)_{60}$	Blow count from SPT corrected to $\sigma'_{v0} = 96$ kPa and 60% efficiency
$p$	Current absolute pressure of the fluid
$p'$	Effective mean stress at triaxial conditions
$P_a$	Atmospheric pressure
$q$	Shear stress at triaxial conditions
$R_f$	Failure ratio
$R_u$	Pore pressure ratio, $\Delta u / \sigma'_{y0} = (u - u_0) / \sigma'_{y0}$
$s'$	Stress parameter for plane strain, $(\sigma'_1 + \sigma'_3) / 2$ or $(\sigma'_x + \sigma'_y) / 2$
$S_r$	Degree of saturation
$S_{r0}$	Initial saturation
SPT	Standard penetration test
$t$	Stress parameter for plane strain, $(\sigma'_1 - \sigma'_3) / 2$
$t_1$	Shear stress on the plane of maximum shear stress, $(\sigma'_1 - \sigma'_3) / 2$
$t_2$	Shear stress on the horizontal plane, $\tau_{xy}$
$u$	Pore (water) pressure
$u_0$	Initial pore (water) pressure

## ACKNOWLEDGEMENTS

I would like to express my deepest gratitude to my research supervisor, Dr. P.M. Byrne, who has guided and supported me for the past five years of my graduate study. His teaching and passion and emphasis on understanding fundamental soil mechanics made me a better engineer. His encouragement and support in various ways enabled me to complete this thesis throughout many challenges. I would also like to thank the following individuals:

- My official supervisor Dr. D. Wijewickreme for his guidance and valuable comments, which have better shaped my thesis, and committee members, Drs. J. Howie and D. Shuttle, and Mr. A. Wightman, for their generous and valuable comments.
- Emeritus professors, Drs. D. Anderson and Y.P. Vaid, for their kindness and advice. Dr. M. Beaty for reviewing the manuscript and his help during early stage of the numerical study. My former supervisors, Dr. J. Takemura at Tokyo Institute of Technology and Dr. Y.S. Kim at the Kyungpook National University, for their encouragements.
- E. Naesgaard and M.G. Jefferies for reviewing the manuscript, sharing their knowledge and their valuable comments, Dr. T. White for reviewing the manuscript, Kumar for providing simple shear tests data, Dr. R. Phillips and Mr. M. Tu at C-CORE and the Memorial University of Newfoundland for providing valuable centrifuge tests data. My senior Mr. S.H. Chung for his help and encouragement. Mahmood and all colleagues at UBC geotechnical group.

This research was funded by the Natural Sciences and Engineering Research Council (NSERC) of Canada.

I appreciate my family: my late grandmother, parents, older sister and younger brothers for their prayers, support, and patience. Especially I deeply thank my wife, Yoon-Jung, for her belief, encouragement, endless love and understanding during my seven years of graduate study in both Canada and Japan. I wish to express my special thanks to my daughters, Ji-Won, who watched my studies from Japan to Canada and always brings us happy smiles, songs and many talents, and Jung-Won (Joy), who brings joy and also many challenges to our family.

I would like to express my thanks to all members of Galilee Korean Presbyterian Church for their friendship, sharing, and prayers for my study and family. Finally, I would like to thank our Lord Jesus Christ who led me from South Korea to Japan and Canada, so I could learn and experience many things.

---

# Chapter 1

## Introduction

When granular soils (e.g., gravel, sand, and silt) are subject to cyclic shear loading, they tend to compact. If the pores in a soil are filled with water, this tendency transfers load from grain contacts to the water. This causes pore pressure rise and can lead to a large drop in effective stress, the stress carried by the grains. If the effective stress drops to zero the soil temporarily loses all its strength and stiffness, and can be said to have liquefied. Liquefaction can be induced under laboratory conditions by constraining its volume, regardless of saturated conditions. In the field, liquefaction can occur in granular soil below the water table under both static and dynamic loading conditions. Large displacements or instability can result from liquefaction.

For example, during the 1964 Niigata Earthquake, severe damage to buildings and bridges due to soil liquefaction (see Figure 1.1) was reported in broad areas of the city because it was underlain by a deep deposit of saturated sand (Seed & Idriss, 1967). Following the earthquake an extensive investigation of the distribution of damages was made. Many structures underlain by liquefied soils settled more than 0.9 m, and such settlement often caused severe tilting of buildings as shown in Figure 1.1(a). Buried sewer pipes, tanks and manholes floated. Bridges and port facilities were severely damaged by large lateral movements of foundation soils. Sand boils were often observed near liquefaction sites. During the 1995 Kobe Earthquake, as another

example, bridges and quay walls in a port were heavily damaged due to liquefaction-induced lateral movements as shown in Figure 1.2.

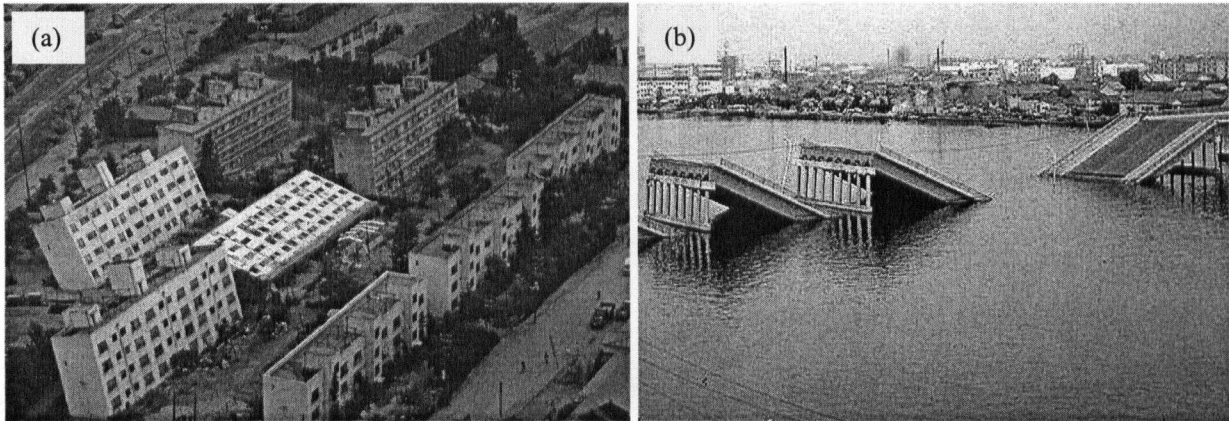


**Figure 1.1** Damage during the 1964 Niigata Earthquake: (a) Kawagishi-cho apartment building, and (b) the Showa bridge (after <http://www.ce.washington.edu/~liquefaction/>).

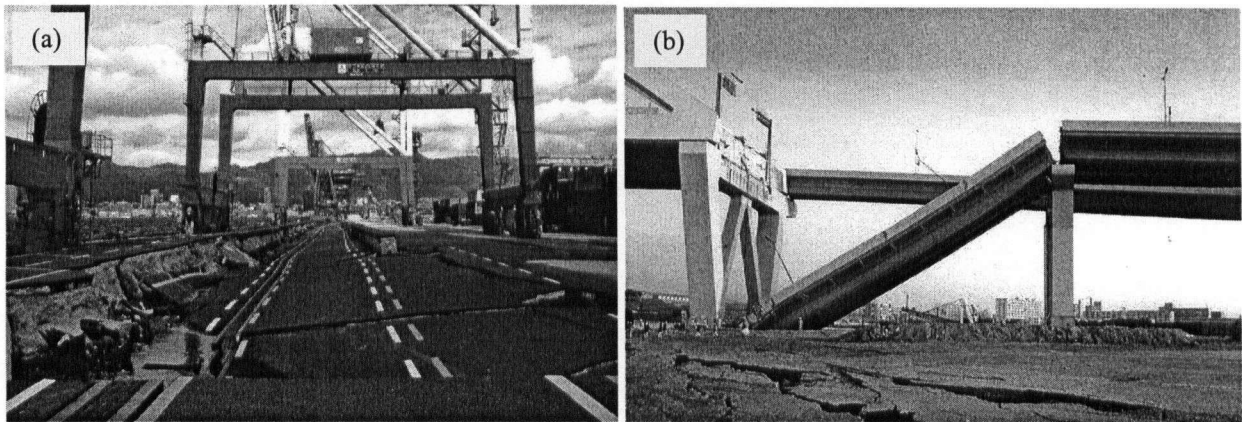


**Figure 1.2** Damage during the 1995 Kobe Earthquake: (a) Kobe Port cranes, and (b) the Nishinomiya Bridge (after <http://www.ce.washington.edu/~liquefaction/>).

Past earthquakes indicate that liquefaction can involve various types of soil displacements including ground settlement, lateral movement, land slides and flow slides resulting in various damage to soil-structures.

---

Ground improvement methods to mitigate liquefaction-induced displacements have been widely used over the past four decades. Hausler and Sitar (2001) compiled over 90 case histories on the performance of improved sites, and found that improved sites generally performed well. During the 1964 Niigata and 1995 Kobe, Japan and 1999 Kocaeli, Turkey Earthquakes, improved areas subsided less than adjacent unimproved areas (Hausler & Sitar, 2001). From those case histories, the effectiveness of ground improvement was validated by reducing displacement during earthquakes. Tens of millions of dollars are spent annually on retrofit of soil-structure systems to curtail damage in the event of a major earthquake in Greater Vancouver alone (Byrne, 2001). Much of the expected damage is due to soil liquefaction (Byrne, 2001). The recent trend in both geotechnical and structural earthquake engineering has emphasized displacements, and moved toward performance-based design. This requires a reliable procedure for predicting liquefaction and associated displacements during earthquakes. Geotechnical engineers can then rationally design remediation, and this may lead to substantial savings or safer structures.

Over the past 30 years, many researchers have developed sophisticated numerical procedures to predict earthquake-induced displacements. These have been validated on the basis of laboratory element test data, back-analyses of field case histories and dynamic centrifuge tests. The numerical procedures can be mainly categorized under total stress or effective stress analyses. The current state-of-practice for predicting displacements is mostly based on total stress analysis.

## 1.1 Numerical Procedures for Soil Liquefaction

### 1.1.1 Total Stress Analysis

When designing soil-structures against liquefaction, three questions arise:

- (a) Will liquefaction be triggered in significant zones by the design earthquake? If so,
- (b) Could a flow slide occur? If not,
- (c) What displacements will occur?

State-of-practice procedure is to use a three-stage total stress analysis approach to answer each of the above questions:

- (a) Triggering analysis;
- (b) Flow slide analysis; and
- (c) Displacement analysis.

In a triggering analysis, the Cyclic Stress Ratio (CSR) caused by the design earthquake is compared with the Cyclic Resistance Ratio (CRR) from penetration tests and field experience during past earthquakes to identify zones that will liquefy. Liquefaction is evaluated by:

$$FS_{\text{trig}} = \frac{\text{CRR}}{\text{CSR}} \quad [1-1]$$

where  $FS_{\text{trig}}$  is a factor of safety against triggering of liquefaction. When the CSR is greater than the CRR, it is considered that liquefaction would trigger (i.e.,  $FS_{\text{trig}} < 1.0$ ).

The CSR is estimated by dynamic ground response analysis such as SHAKE91 (Idriss & Sun 1992) and FLUSH (Lysmer et al., 1975), or using a simple formula (Seed & Idriss, 1971). While the CRR can be obtained directly from laboratory tests (e.g., cyclic triaxial tests), it is mainly obtained by empirical correlation with in situ tests. An empirical approach proposed by Seed (Seed & Idriss, 1971; Seed et al., 1985) and based on Standard Penetration Test (SPT) is commonly used to determine the CRR. The CRR for coarse-grained soils is usually determined

using an empirical correlation between CRR for a magnitude 7.5 earthquake and corrected SPT blowcount ( $(N_1)_{60}$ ) given by the National Center for Earthquake Engineering Research (NCEER) (Youd et al., 2001) and shown in Figure 1.3. In order to account for site specific conditions, the CRR is corrected for initial horizontal shear stress ( $K_\alpha$ ), effective overburden pressure ( $K_\sigma$ ), and different earthquake magnitudes ( $K_m$ ) as prescribed by Youd et al. (2001) and given below:

$$\text{CRR} = \text{CRR}_{\text{chart}} \cdot K_\alpha \cdot K_\sigma \cdot K_m \quad [1-2]$$

where  $\text{CRR}_{\text{chart}}$  is the value of CRR obtained from Figure 1.3. Values of  $K_\alpha$ ,  $K_\sigma$ , and  $K_m$  are given in the Youd et al. (2001).

The CRR can also be determined from laboratory testing on undisturbed samples.

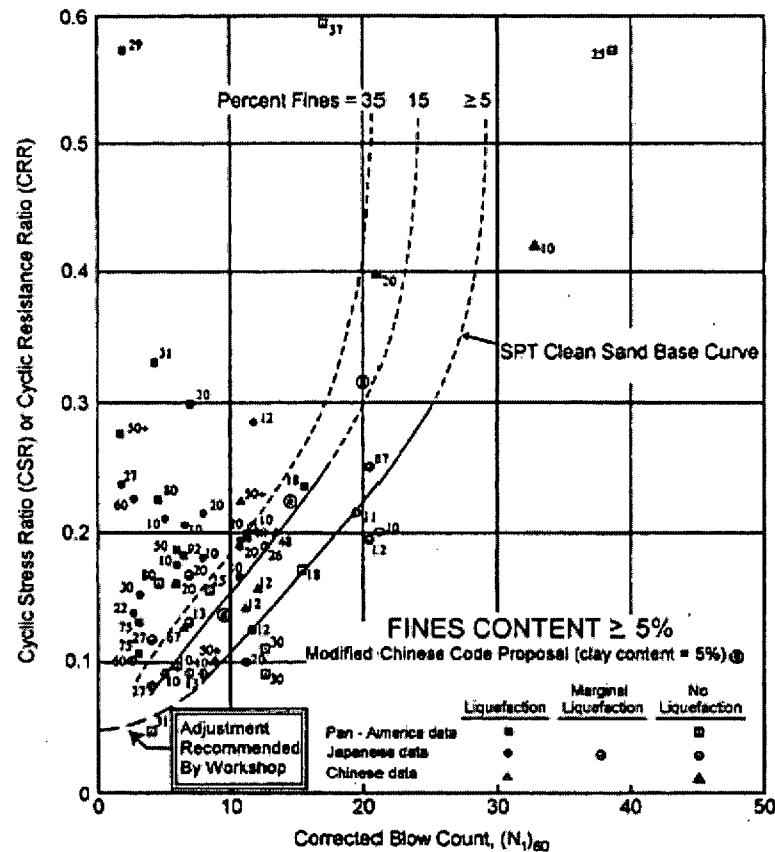


Figure 1.3 Correlation between CRR and  $(N_1)_{60}$  modified from Seed et al. (1985) (after Youd et al., 2001).

Once the zones of liquefaction are identified, post-liquefaction stability is analyzed to assess the possibility of a flow slide. In this regard, residual strengths are specified in zones predicted to liquefy, and a limit equilibrium analysis used to compute a factor of safety against sliding.

If the residual strength is sufficient for static stability, a further analysis is carried out to check that the displacements due to shaking are tolerable. Generally, a simple Newmark sliding block analysis (Newmark, 1965) is used with residual strength in the zones predicted to liquefy. The Newmark (1965) method does not give the pattern of displacements. If there is no liquefaction, estimated seismic displacements will generally be small unless the acceleration levels are very high. If liquefaction is predicted to be widespread, very large displacements may occur and treatment will be necessary.

Flow slide and displacements analyses can be combined into one, i.e., deformation analysis. The synthesized total stress approach developed by Beaty (2001) and Byrne at the University of British Columbia (UBC) advances the current state-of-practice approach by combining the pre- and post-liquefaction response into a single analysis. The method has been calibrated with field experience, and it has been currently used by the engineering profession in the design and retrofit works related to a number of major bridge, pipeline, and dam projects.

The use of an effective stress approach to analyze soil liquefaction problems is fundamentally sound in comparison to the aforementioned total stress approaches where pore pressure effects are not directly accounted for. The effective stress approach is discussed in the next section, and Figure 1.4 schematically compares the two analysis methods. Effective stress analysis can be split into loose-coupled and fully-coupled analyses depending on the manner in which the real time pore pressure change is accounted for.

### 1.1.2 Effective Stress Analysis

Martin et al. (1975) provided a method to model rising pore pressures due to cyclic loading. This may have been the first effective stress model for liquefaction analysis. The method fundamentally captures skeleton behaviour under cyclic loading, and imposes a volumetric constraint to consider pore pressure rise. Finn et al. (1986) have developed and refined this model, called TARA-3, and it has been used to predict liquefaction-induced displacements on many projects (Finn, 1998; Finn et al., 1999). This is a loose-coupled analysis that considers shear-induced pore pressure at each cycle or half cycle. Basically, the method combines a nonlinear hysteretic stress-strain relationship, and a pore pressure model by Martin-Finn-Seed (Martin et al., 1975). Wu (2001) applied a similar model to simulate the liquefaction-induced deformations of the Upper San Fernando Dam of California, USA, during the 1971 San Fernando Earthquake.

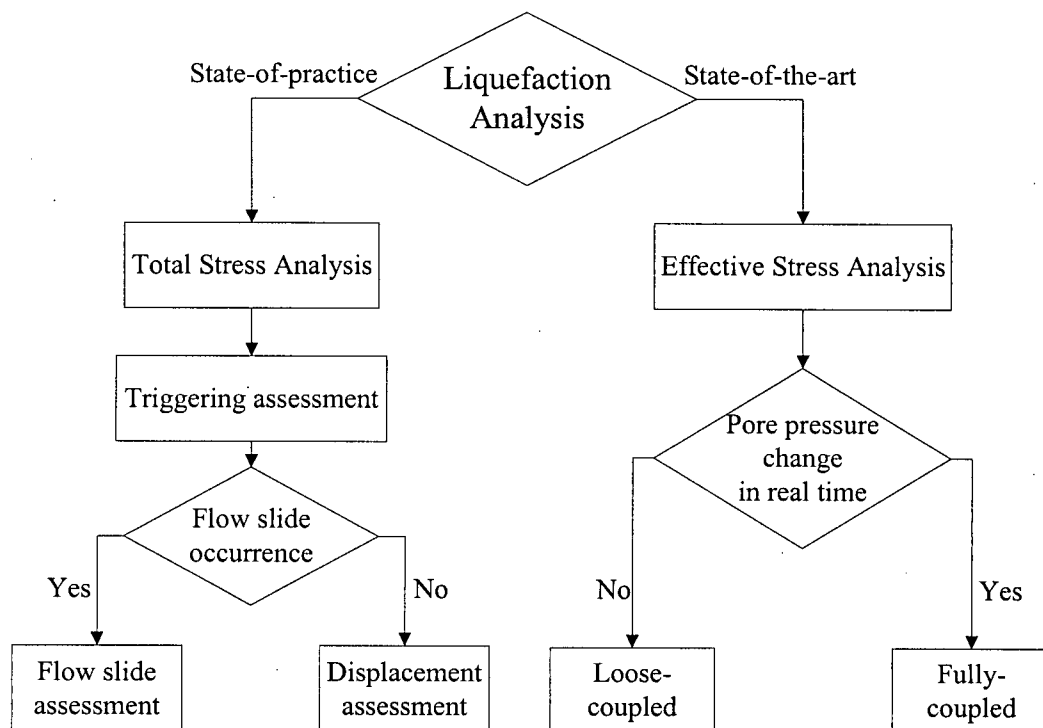


**Figure 1.4** Liquefaction analysis: Total and Effective stress analyses.

State-of-the-art procedures involve dynamic finite element or finite difference analyses using effective stress constitutive models coupled with fluid flow effects. These analyses can estimate the displacements, accelerations and porewater pressures caused by a specified input motion. Triggering of liquefaction, displacements and flow slide potential are addressed in an all encompassing single analysis. Fully-coupled effective stress approaches which consider shear induced pore pressures at each time step, rather than at each cycle or half cycle, have been developed by several researchers. Advanced constitutive models implemented in the fully-coupled analysis can consider shear-induced plastic volumetric strain that can lead to pore pressure development under undrained conditions. A substantial advancement in this approach has resulted from the development of bounding surface models (Dafalias & Popov, 1976) and multi-yield surfaces models (Prevost, 1977). Popescu and Prevost (1995) chose three types of plasticity models (i.e., bounding surface plasticity, multi-yield surfaces plasticity, and generalized plasticity) involved in the Verification of Liquefaction Analysis by Centrifuge Studies (VELACS) (Arulanandan & Scott, 1993) Class 'A' predictions, and then carried out a comparative assessment of the performance of these models in predicting dynamically induced excess pore water pressure. It was noted that for various centrifuge models, generally good agreement was provided by all three plasticity models. Detailed review of advanced constitutive models is given in Chapter 2.

Computer codes such as DIANA-SWANDYNE II (Chan 1993), DYNAFLOW<sup>TM</sup> (Prevost, 1998), DYSAC2 (Muraleetharan et al., 1988), SUMDES2D (Ming & Li, 2001), and SWANDYNE (Zienkiewicz et al., 1990) are some of the typical numerical procedures with advanced constitutive models used in engineering practice.

## 1.2 Research Motivation and Scope of Work

The purpose of this thesis was to develop and verify a relatively simple and practical plasticity model to account for plastic unloading and principal stress rotation. As noted earlier, many different types of effective stress models are available for soil liquefaction analysis and prediction of ground movements. While significant progress has been made in these models, the practical application of the models has been limited due to their complexity. As indicated by Kolymbas (2000), the practicality of utilizing numerical models depends on their simplicity and robustness. First of all, their practicality is directly related to the number of required model parameters. Many geotechnical structures are simplified and analyzed with plane strain conditions. For earthquake loadings, conditions most closely resemble simple shear. Therefore, the practicality can also be related to the capability to replicate field loading mechanisms under monotonic and especially earthquake loadings (e.g., plane strain condition, simple shear).

Conventional plasticity with isotropic hardening considers unloading as elastic. From a practical point of view, elastic unloading may be adequate for preliminary analysis. However, laboratory data indicate that for loose sands, significant plastic deformations always occur during the unloading cycles. For example, if liquefaction is expected, it is important to include plastic unloading because elastic unloading cannot capture the collapse of soil fabric that occurs during stress reversal following a large stress cycle that induces dilation.

Classical plasticity formulation in terms of stress invariants has a deficiency in the handling of principal stress rotation that commonly occurs under field loading conditions and can significantly influence soil behaviour (Matsuoka, 1974; Lee & Pande, 2004). As pointed out by Iai et al. (1992), conventional plasticity models cannot simulate  $K_0$ -consolidated simple shear because it involves rotation of principal stress axes. However, they can simulate hydrostatically

consolidated conditions very well because there is no rotation effect. In field problems, where the value of lateral effective stress ratio  $K (= \sigma'_h/\sigma'_v)$  (Lambe & Whitman, 1986a) varies, accompanying rotation of principal stresses cannot be ignored. If different  $K$  conditions are not appropriately accounted for in a constitutive model, especially when analyzing dams, slopes and embankments, it can lead to erroneous conclusions. As such, a numerical model capable of handling different  $K$  conditions is preferable for predicting displacements under monotonic and cyclic loading.

If the UBCSAND model by Byrne et al. (1995) is considered, for example, the model is simple and robust, and it is also capable of representing loading under plane strain conditions as it captures simple shear loading. However, it does not consider unloading as plastic nor the effect of principal stress rotation associated with simple shear on different  $K$  conditions. In consideration of this, substantial improvements to the UBCSAND model were undertaken to account for principal stress rotation and plastic unloading, and this work forms a major part of this thesis.

Motivation for the refined model called UBCSAND2 stems from a multi-laminate model proposed by Pande and Sharma (1983) that uses many mobilized planes. UBCSAND2 combines a conventional plasticity model with one stress plane and a multi-laminate model based on many mobilized or contact planes. The mechanical behaviour is captured by considering the stress state on two mobilized planes, a plane of maximum shear stress, which rotates or swings as the direction of the principal stress rotates, and a horizontal plane which is spatially fixed. This concept proposed in this study is new and called a Two Mobilized-plane model. It captures the complex skeleton behaviour during cyclic loading including principal stress rotation and plastic unloading effects. It is validated for plane strain conditions and is relatively simple to use for

practical design problems as it involves only a few parameters that can be obtained from in situ penetration tests or laboratory tests.

### 1.3 Outline of the Thesis

This thesis deals with the development and calibration of a new constitutive model and its application for soil liquefaction analysis. The thesis is comprised of six chapters:

- Chapter 1 introduces the liquefaction-induced damage during earthquakes and briefly reviews existing numerical procedures for predicting liquefaction triggering and post-liquefaction displacements. The scope and objectives of research are also addressed.
- Typical results of simple shear tests including simple shear devices, and associated principal stress rotation tests are addressed in Chapter 2. Various plasticity models used for soil liquefaction analysis are briefly reviewed, and their capabilities are evaluated for practical purposes. Some relevant models capable of modeling principal stress rotation are also introduced.
- Chapter 3 presents the concept, formulation and characteristics of the proposed model called UBCSAND2.
- The detailed calibration procedures of UBCSAND2 are described in Chapter 4. A comparison between predicted and measured simple shear test results is also given. The two models, UBCSAND and UBCSAND2, are compared considering the mode of simple shear loading.
- Chapter 5 describes a series of centrifuge tests conducted at the Centre for Cold Ocean Research (C-CORE) and the observations are compared with the predictions made using

UBCSAND2. Important considerations for centrifuge modeling, stress densification and initial saturation, are also discussed.

- Chapter 6 summarizes the research work and findings from this study. It also addresses the limitations of UBCSAND2 model, and includes suggestions for further research.

## Chapter 2

# Overview of Sand Behaviour and its Modeling

Many geotechnical problems (e.g., retaining walls, continuous footings, and earth dams) can be approximated as plane strain and their stress-strain relations derived for the plane strain condition. In such field problems the rotation of principal stress occurs even under applied static vertical load (e.g., Leroueil & Hight, 2003). A simple shear device is one of most common soil testing devices that incorporate both plane strain and principal stress rotation. It is worthwhile to review the typical drained behaviour of sand under simple shear loading and its modeling.

This chapter reviews simple shear devices, typical results of simple shear tests, and associated principal stress rotation tests. The stress-dilatancy of sand is interpreted in a simple way by considering its dependence on stress ratio only.

Plasticity has been invoked to capture the irrecoverable volume change of sand. Since Drucker et al. (1957) proposed the concept of work-hardening plasticity in soil, advanced constitutive models have been developed in the area of soil statics as well as soil dynamics. Representative plasticity models, which have been applied to the modeling of sand under earthquake loading, are reviewed. Their capabilities are evaluated in terms of modeling principal stress rotation, validation under plane strain conditions, and number of model parameters.

## 2.1 Direct Simple Shear Devices

Two types of direct simple shear (DSS) apparatus have been used in soil testing: one developed at Cambridge (Roscoe, 1953) and the other developed at the Norwegian Geotechnical Institute (NGI) (Bjerrum & Landva, 1966). Budhu (1984) compared the results of monotonic and cyclic drained tests in two elaborately instrumented DSS devices. He pointed out that the Cambridge DSS apparatus gives reliable data on the stress-strain behaviour in monotonic loading, but both apparatus give similar performance on the strain characteristics under cyclic loading particularly at strain levels below 5%. The NGI-type DSS apparatus is simple and common today, and a schematic diagram of an NGI-type apparatus at the University of British Columbia (UBC) is given in Figure 2.1(a). This type of apparatus uses a cylindrical reinforced rubber membrane to constrain lateral deformation (i.e.,  $\varepsilon_x = 0$ ), and only total vertical and horizontal loads on a horizontal plane (boundary) are measured (i.e.,  $\sigma'_y$  and  $\tau_{xy}$  in Figure 2.1(b)).

The soil sample in direct simple shear will be deformed in a plane strain condition, and is considered suitable to simulate the anticipated cyclic stress conditions in the field. In addition, a simple shear device simulates a gradual rotation of principal stresses as occurs in the field and is therefore appropriate for developing a constitutive model that can account for the effect of principal stress rotation. The conventional triaxial device cannot be used for this purpose since it does not allow any continuous rotation of principal stresses. Several researchers (Peacock & Seed, 1968; Silver & Seed, 1971) pointed out that cyclic direct simple shear tests can better simulate the wave-induced loading to offshore structures and the earthquake loading caused by shear waves propagating vertically. Ishihara and Li (1972) described the difference between triaxial and simple shear tests in terms of direction of principal stress, initial stress condition, and stress distribution within the sample.

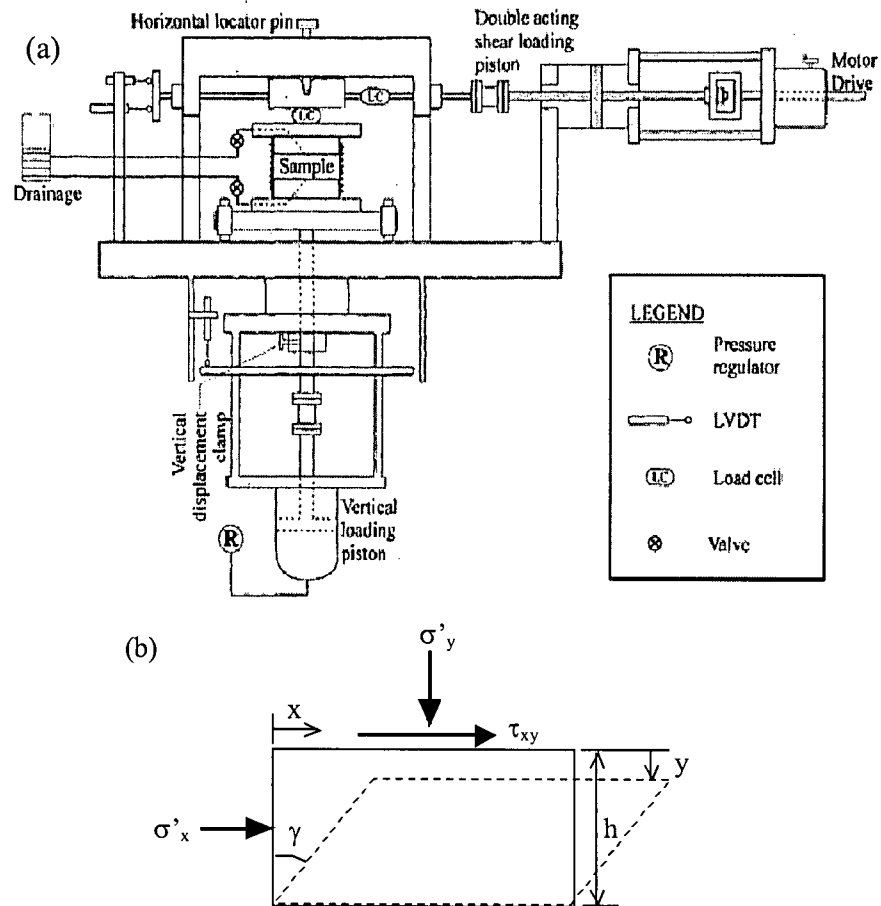


**Figure 2.1** Simple shear: (a) NGI-type simple shear apparatus at UBC (after Sivathayalan, 2000), and (b) simple shear deformation.

In conventional simple shear testing the lateral stress is not measured, however, lateral or radial stresses can and have been measured in both the Cambridge simple shear apparatus and the NGI-type apparatus (Budhu, 1984). The complementary shear stresses on vertical boundaries in the simple shear apparatus do not exist, which leads to nonuniform stress conditions. Roscoe (1953) showed from elastic analysis of the specimen in the Cambridge DSS apparatus that the shear stress on a horizontal plane is essentially uniform in the middle third of the sample. Lucks et al. (1972) pointed out using linear elastic finite element analyses that approximately 70% of the cylindrical sample tested in the NGI apparatus would be under a

remarkably uniform stress condition. De Alba et al. (1976) compared results from large-scale shaking table tests, which can minimize the lack of complementary shear stresses, and small-scale simple shear tests. They reported that the liquefaction resistance of sand ( $D_r = 50\%$ ) was in very good agreement from these results having a different scale.

The hollow cylinder torsional (HCT) shear device allows continuous rotation of principal stresses with better definition of complementary shear (Hight et al., 1983; Miura, 1985; Vaid et al., 1990). However, as Wijewickreme and Vaid (1991) pointed out, HCT device is also not exempted from generating non-uniform stress under certain stress path loading condition.

With this background, the use of a DSS device is acceptable for understanding the performance of soil under earthquake loading for engineering purposes.

## 2.2 Sand Behaviour under Simple Shear

Casagrande (1936) carried out shear box tests using loose and dense samples of sand, and he postulated that loose and dense samples reached the same void ratio if shearing could be carried out far enough as shown in Figure 2.2(b). Based on his findings, Casagrande (1936) proposed the term “critical density” or “critical void ratio” (the horizontal line M' in Figure 2.2(b)) as a state that can allow any amount of shear deformation without volume change. Wroth (1958) carried out simple shear tests at various initial void ratios with 1 mm diameter steel balls, and showed the supporting results to Casagrande's (1936) “critical void ratio” concept as illustrated in Figure 2.2(c). Based on Casagrande's idea, Roscoe et al. (1958) defined the critical state as one in which a soil “*continues to deform at constant stress and constant void ratio*”. Schofield and Wroth (1968) formulated this critical state concept within the framework of plasticity

theory. It has been called critical state soil mechanics, and it could be the earliest soil model to consider volume change during shearing.

While the critical state is usually related to drained conditions, the similar term called “steady state” is mainly used for undrained conditions (Poulos, 1981). Regarding these terms and the determination of critical state line or steady state line, different researchers have different theories regarding its uniqueness. For example, Been et al. (1991) believe, based on data from drained triaxial tests on Erksak sand, that a unique critical state line exists which is independent of stress paths and sample preparation methods. Such issues on a critical state of sand are beyond the scope of this chapter, and they are mainly based on data from drained triaxial tests (axisymmetric conditions). Attention is focused here on the simple shear test.

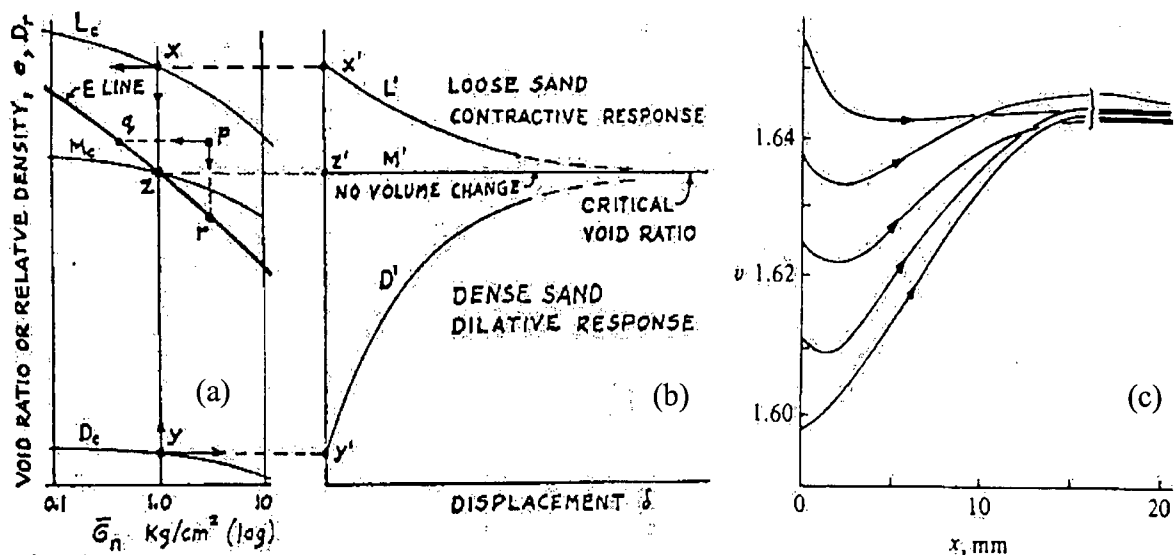


**Figure 2.2** Critical void ratio: (a) & (b) hypothesis of critical void ratio derived from direct shear tests (after Casagrande, 1976), and (c) simple shear tests on 1 mm diameter steel balls with normal stress 138 kPa: specific volume  $v$  and shear displacement  $x$  (after Wroth, 1958).

As an example, Vaid et al. (1981) carried out monotonic drained simple shear tests on Ottawa sand at various relative densities after consolidation ( $D_{rc}$ ) under an initial vertical effective stress ( $\sigma'_{v0}$ ) of 200 kPa. These tests in Figure 2.3 show the characteristic shear stress-

strain and volume change response of sand, with contraction below a certain stress ratio (e.g., a sine of the friction angle at constant volume,  $\sin \phi_{cv}$ ) and expansion above. Note also that only the very dense sand with  $D_r = 93\%$  shows a drop in stress ratio or strength at large strain.

Sriskandakumar (2004) carried out a series of simple shear tests on Fraser River sand. Results of his cyclic drained simple shear tests on loose and dense samples are shown in Figure 2.4. It may be seen that both loose and dense sand contract for stress ratio below  $\sin \phi_{cv}$  and dilate above. For both loose and dense sand, there is an accumulation of contractive strain with number of cycles. The increment of shear-induced volume change can be expressed in terms of a dilation angle  $\psi$  defined as  $\sin \psi = d\varepsilon_v/d\gamma$  (Hansen, 1958).

The variation of dilation angle with relative density and vertical effective stress based on a series of simple shear tests on Leighton Buzzard sand by Cole (1967) is shown in Figure 2.5. It is clearly shown that this sand dilates more as the initial vertical effective stress decreases, and as relative density increases.

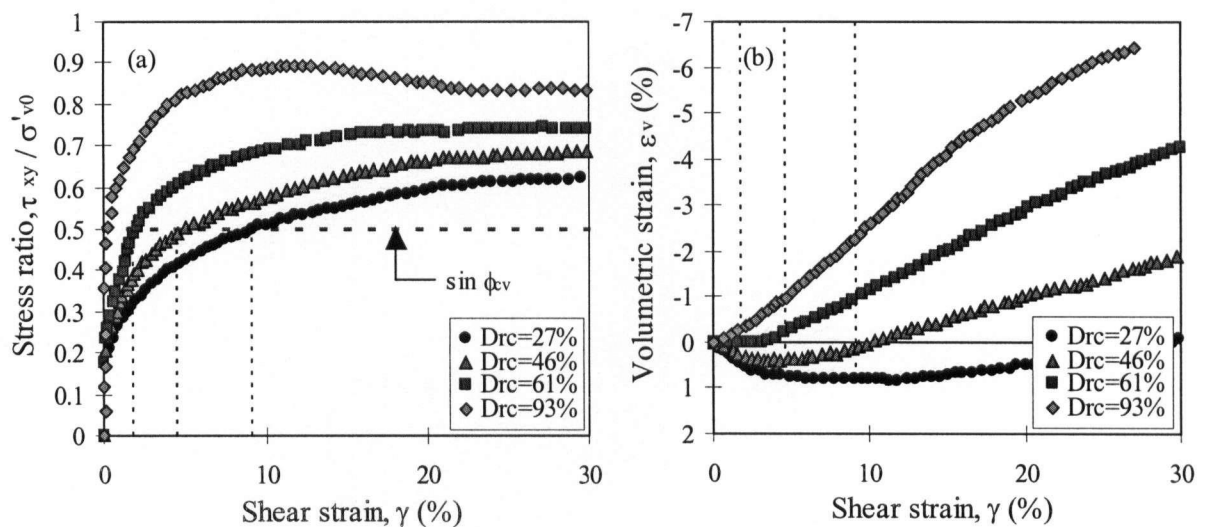


**Figure 2.3** Results of monotonic drained simple shear tests on Ottawa sand at various densities (modified from Vaid et al., 1981).

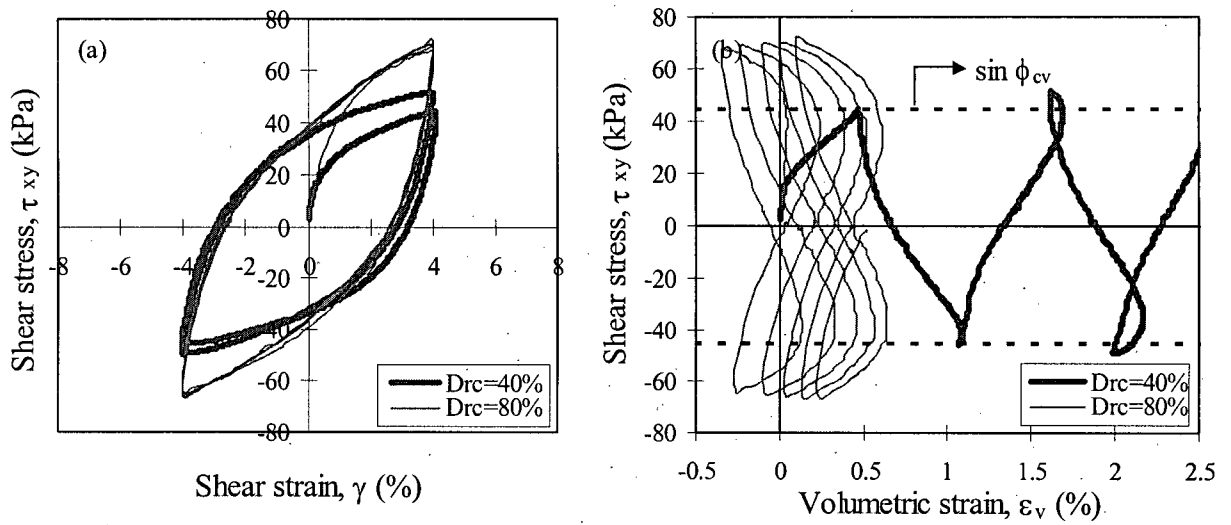


Figure 2.4 Results of cyclic drained simple shear test on loose and dense Fraser River sand (after Sriskandakumar, 2004).

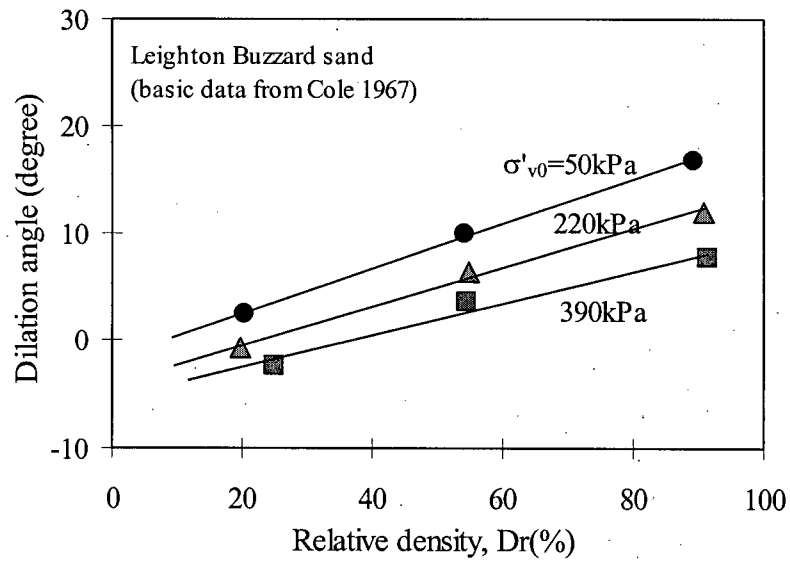


Figure 2.5 Dependence of dilation angle on relative density and stress level (after Vaid et al., 1981).

Principal stress rotation induces plastic shear strain that induces volume change, and this is discussed in the section to follow.

### 2.2.1 Principal Stress Rotation and its Consequences

Principal stress rotation significantly influences soil behaviour, and has received substantial attention since Arthur et al. (1980) who called it “a missing parameter”. As a shear stress on a horizontal plane ( $\tau_{xy}$ ) is applied to a test sample under simple shear with  $K_0 (< 1.0)$ , the plane of maximum shear stress gradually rotates from its initial  $45^\circ$  location and becomes approximately horizontal at failure (Roscoe, 1970). Thus, there is a gradual rotation of principal stresses during loading.

The direction of a major principal stress to the vertical,  $\alpha_\sigma$ , is determined by

$$\tan 2\alpha_\sigma = 2\tau_{xy} / (\sigma'_y - \sigma'_x) \quad [2-1]$$

as illustrated in Figure 2.6(b). When a positive  $\tau_{xy}$  approaches its maximum value (i.e.,  $\tau_{xy} \approx 0.5 \cdot (\sigma'_1 - \sigma'_3)$ ),  $\alpha_\sigma$  becomes nearly  $+45$  degrees to the vertical (counterclockwise is positive angle). Therefore, a major principal stress during cyclic simple shear tests rotates between approximately  $\pm 45$  degrees while a horizontal shear stress applies to both directions.

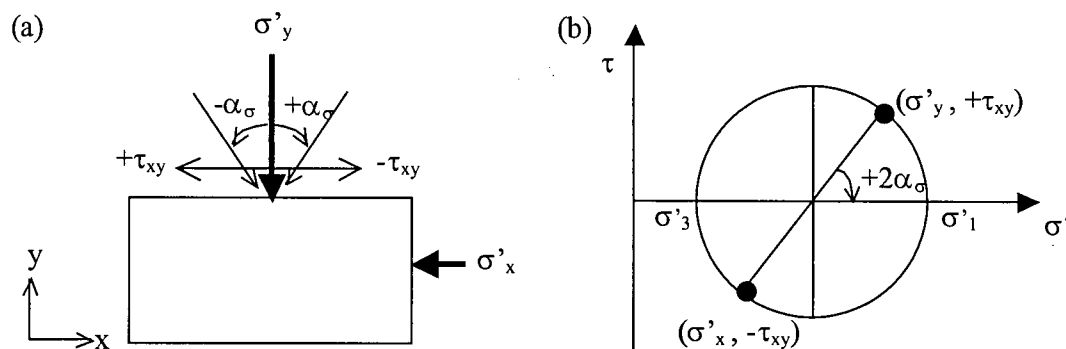


**Figure 2.6** Principal stress rotation during simple shear.

As mentioned in Section 2.1, the Cambridge simple shear device (Roscoe, 1953) with an array of load cells (contact stress transducers) measured the complete distribution of boundary

stresses during testing. Wood et al. (1979) corrected the measured forces and eccentricities from the Cambridge simple shear device, and then showed the variation of the angle  $\alpha_\sigma$  under cyclic loading on dense sand in Figure 2.7. Their data confirmed that the angle  $\alpha_\sigma$  rotates approximately between  $\pm 45$  degrees, where the maximum  $\tau_{xy}$  is applied. The angle  $\alpha_\sigma$  can be 45 degrees only when  $\sigma'_x$  is equal to  $\sigma'_y$ . This indicates that the lateral stress  $\sigma'_x$  rises from its initial state to reach the vertical stress values  $\sigma'_y$  as the sample is loaded to failure.

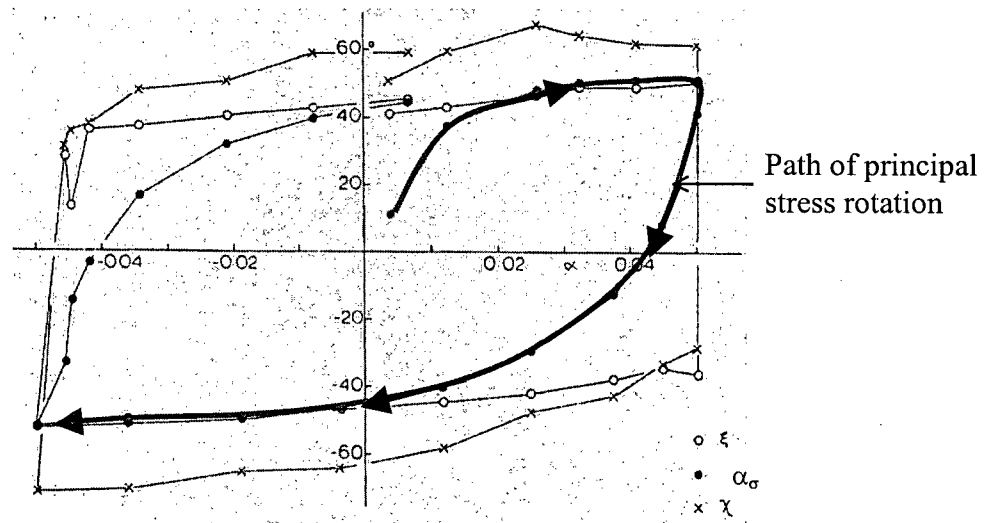


**Figure 2.7** Variation of the direction of major principal stress  $\alpha_\sigma$  during simple shear test on dense Leighton Buzzard sand (after Wood et al., 1979).

Arthur and co-workers (1977, 1980) and Sture et al. (1987) developed a Directional Shear Cell (DSC) where all principal stresses are measured. Using the DSC, Arthur et al. (1980) carried out “pure principal stress rotation tests” under plane strain by varying the direction of principal stress in a sine-wave at constant stress ratio (see Figure 2.8(a)). When dense Leighton Buzzard sand ( $D_r = 90\%$ ) was subjected to principal stress rotation at a near constant stress ratio ( $\sigma'_1/\sigma'_3 = 4.0$ ), Figure 2.8(a), strains accumulated with each loading cycle as shown in Figure

2.8(b). As noted from two cyclic rotation angles  $\theta = 40^\circ$  and  $70^\circ$  in the same figure, the greater the principal stress rotation the greater the plastic straining induced.

Several researchers (e.g., Ishihara & Towhata, 1983; Symes et al., 1982, 1988; Miura, 1985; Sayao, 1989; Wijewickreme & Vaid, 1993) have carried out torsional shear tests on a hollow cylindrical sample solely to investigate the effect of principal stress rotation. Granular materials show more contractive behaviour under higher confining stresses and looser states (Lee & Seed, 1967). Sayao (1989) observed such typical behaviour even from stress paths involving principal stress rotation from drained torsional tests on a hollow cylindrical sample.

Ishihara and Towhata (1983) showed the effect of a pure rotation of principal stresses using drained cyclic tests on loose Toyoura sand. The direction of the principal stresses was rotated continuously from 0 degree to  $\pm 45$  degrees following a semi-circular stress path as shown in Figure 2.9. It can be seen that a pure principal stress rotation caused an irrecoverable volumetric strain but its increment gradually decreased as the number of cycles increased. At the end of three cycles, the volumetric strain increment due to principal stress rotation drops to nearly zero (see Figure 2.9(b)).

The DSC and the hollow cylinder torsional device can impose continuous rotation of principal stresses on a soil specimen at constant stress ratio (e.g.,  $\sigma'_1/\sigma'_3$ ) and do not have the disadvantage of having an unknown stress. However, data from those tests are not common due to the rarity of testing devices, the considerable expense of testing, and the relatively complex testing procedure.

As noted from this section, simple shear loading caused volume change, which was partially attributed to principal stress rotation. This volume change can be related to the applied stress ratio through the stress-dilatancy equation.

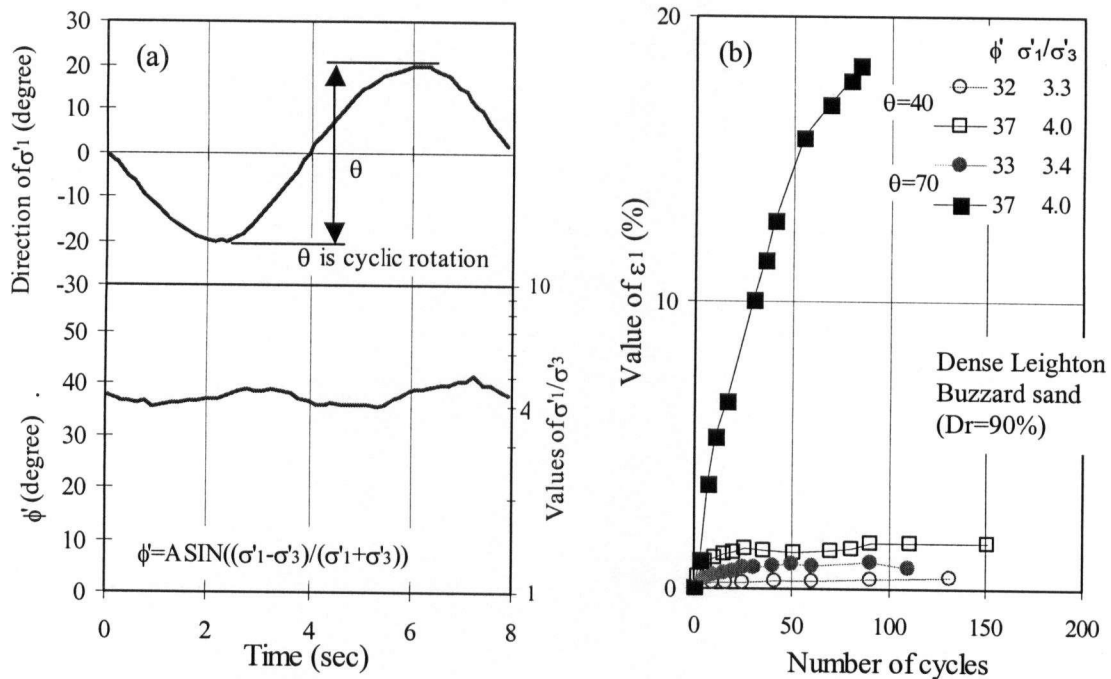


Figure 2.8 Results of continuous rotation tests: (a) variation of principal stress directions and stress ratio, and (b) cumulative major principal strain on dense sand (after Arthur et al., 1980).

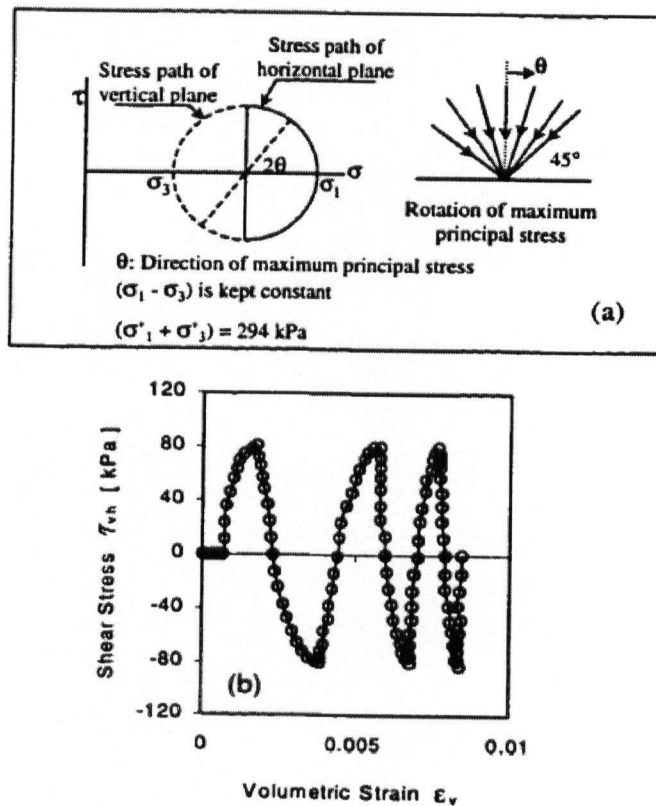


Figure 2.9 Result of a pure principal stress rotation test on loose Toyoura sand (after Ishihara & Towhata, 1983).

### 2.3 Modeling of Shear-induced Volume Change

The term dilatancy is usually defined as the ratio of volumetric strain increment to shear strain increment. The dilatancy, or the plastic strain rate, is generally related to stress ratio or a mobilized friction angle, and this is called a stress-dilatancy relationship. There are many stress-dilatancy relationships in the literature, many of which can be related to Rowe's (1962) original work. Rowe examined the stress-strain-volume change relations for ideal assemblies of rods and spheres by means of the theory of least rate of internal work (principle of minimum energy), and related the mobilized stress ratio to strain increments (or rates) as follows

$$\frac{\sigma'_1}{\sigma'_3} = K_D \left( 1 - \frac{d\varepsilon_v}{d\varepsilon_1} \right) \quad [2-2]$$

where the constant  $K_D$  is defined as  $K_D = \frac{1 + \sin \phi}{1 - \sin \phi}$  where  $\phi$  is a friction angle having a value between the interparticle friction angle  $\phi_\mu$  and the critical state friction angle  $\phi_{cs}$ ;  $\sigma'_1$  and  $\sigma'_3$  are the major and minor principal effective stresses as shown in Figure 2.10, respectively;  $d\varepsilon_v$  is the volumetric strain increment;  $d\varepsilon_1$  is the major principal strain increment.

The early work on shear-induced volume change or dilation related total volumetric strain to total shear strain. For plasticity based modeling, it is more appropriate to model dilation in terms of plastic strains, whereas Eq. [2-2] includes an elastic component of strain increment. This elastic component should be removed when reducing test data (Been & Jefferies, 2004). However, due to the difficulty of removing the elastic strain component from data in the published literature, total and plastic strains in stress-dilatancy relations are considered the same unless otherwise noted.

Stress-dilatancy relations were initially developed from drained monotonic loading. As such, monotonic behaviour of sand is first interpreted to derive a simple relationship.

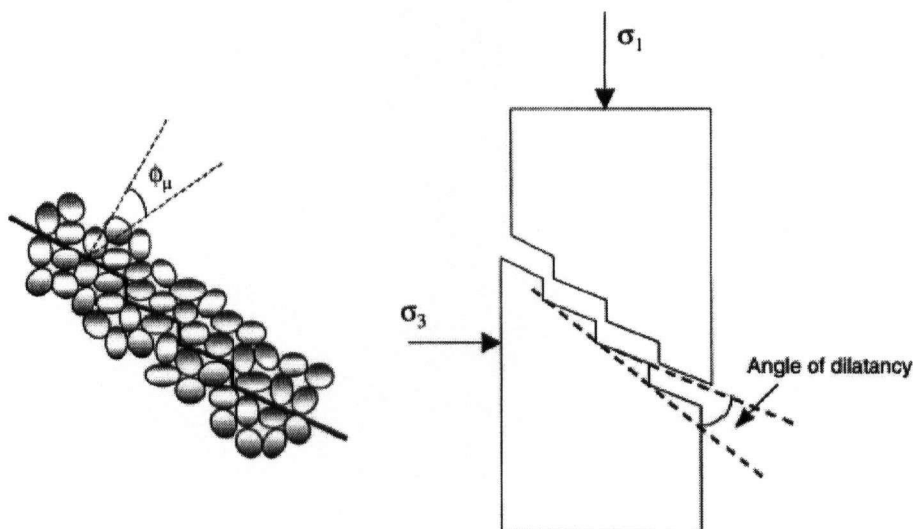


**Figure 2.10** Sliding mechanism assumed for Rowe's stress–dilatancy theory (after Yang & Li, 2004).

### 2.3.1 Monotonic Loading

Dilatancy  $D$  under plane strain conditions can be defined as the ratio of plastic volumetric strain increment,  $d\varepsilon_v^p (= d\varepsilon_1^p + d\varepsilon_3^p)$ , to plastic shear strain increment,  $d\gamma^p (= d\varepsilon_1^p - d\varepsilon_3^p)$ . Dilatancy  $D$  is also expressed in terms of a dilation angle  $\psi$ , and defined as  $\sin \psi = d\varepsilon_v^p / |d\gamma^p|$ .

As pointed out earlier in Section 2.2, data from monotonic drained simple shear tests at the same initial stress condition (see Figure 2.3) show that dilatancy is a function of the stress ratio  $\eta = t/s'$ , where  $t = (\sigma'_1 - \sigma'_3)/2$  and  $s' = (\sigma'_1 + \sigma'_3)/2$ , as originally proposed by Rowe (1962). Dilatancy  $D$  is equal to zero at  $\eta = \sin \phi_{cv}$ . Therefore, the simplest expression for dilatancy  $D$  is  $D = \sin \phi_{cv} - \eta$  for both loose and dense samples.

Puebla (1999) examined Vaid et al.'s (1981) drained simple shear tests at various relative densities (Figure 2.3), and expressed the data in terms of the stress ratio ( $\tau_{xy}/\sigma'_y$ ) and total strain increment ratio ( $-d\varepsilon_v/d\gamma$ ) as shown in Figure 2.11 for three relative densities. These data at high stress ratio can be approximated by the thick line in Figure 2.11, which was defined as  $\tau_{xy}/\sigma'_y = (-d\varepsilon_v/d\gamma) + 0.5$ . This approximation at high stress ratio is equivalent to  $\eta = -D + \sin\phi_{cv}$  if we assume  $\phi_{cv} = 30^\circ$  and the total strain increment as the plastic strain increment as mentioned earlier. However, at low stress ratio (inside circle in Figure 2.11), the elastic strain increment is not negligible, so it is inaccurate to assume that plastic and total strain increments are approximately equal. Therefore, direct comparison is not possible without separating elastic strain increment from measured total strain increment.

As mentioned earlier (see Figure 2.5), the tendency of sand to contract or dilate depends on its density and applied pressure. Based on the results of simple shear tests, Wroth and Bassett (1965) proposed the parameter ' $\chi_c$ ' as the distance between the current state of the soil in  $e$ - $\log\sigma'$  space and the image point with different stress state at the critical state. To define the image point it requires the particular value describing the test under consideration.

Been and Jefferies (1985) proposed a similar, yet simple concept, called the state parameter ( $\psi$ ), which describes the difference between the current void ratio of the soil,  $e$ , and the void ratio at the critical state at the same mean effective stress,  $e_c$ . Recently, Li and Dafalias (2000) argued that based on undrained triaxial tests, sand under the same confining stress may either contract or dilate at the same stress ratio depending on its density. Then, they proposed a unified formulation of dilatancy for sand called "state-dependent dilatancy". As a result, the dilatancy can be a function of both stress ratio in triaxial tests  $\eta_t = q/p'$ , where  $p' = (\sigma'_1 + 2\sigma'_3)/3$  and  $q = \sigma'_1 - \sigma'_3$ , and  $\psi = e - e_c$  (Li & Dafalias, 2000). Consequently, the state-dependent dilatancy

can directly consider volume change during loading, and simulate sand at different densities using a single set of parameters. As pointed out by several researchers (Gudehus, 1996; Manzari & Dafalias, 1997; Gajo & Wood, 1999, Wan & Guo, 1998; Li & Dafalias, 2000; Li 2002), a stress-dilatancy equation with a material state (e.g., current void ratio) dependence is desirable to treat a single sand with different initial densities in the same way.

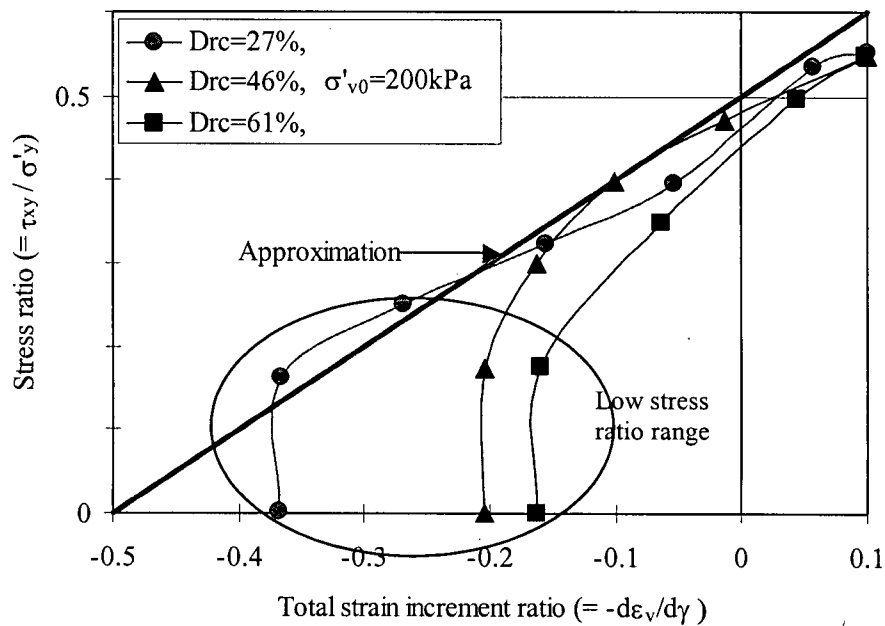


**Figure 2.11** Relationship between the stress ratio and the strain increment ratio in drained simple shear tests on Ottawa sand (after Puebla, 1999).

### 2.3.2 Cyclic Loading

The aforementioned volume change is primarily related to monotonic loading. Soil elements under wave loading or earthquake loading will experience unloading and reloading (i.e., cyclic or repeated loading). Youd (1977) explained packing change during cyclic loading and the resulting pore pressure change using Figure 2.12, which schematically illustrates how sand dilates and compacts during cyclic shear loading.

When the shear stress is reversed, a large volume contraction occurs for both loose and dense samples as shown in Figure 2.4(b). This was also illustrated conceptually in Figure 2.12(d) due to the collapse of small holes. From Sriskandakumar's (2004) tests, all unloading was contractive, and particularly so if the previous loading had been above  $\phi_{cv}$ . The plastic deformation of loose and dense Fraser River sand during unloading is inferred from those volume changes. However, at the very beginning of the shear stress reversal volume change would be small enough to ignore, which implies elastic response as mentioned by Jefferies (1997) using data from triaxial tests on dense sand.

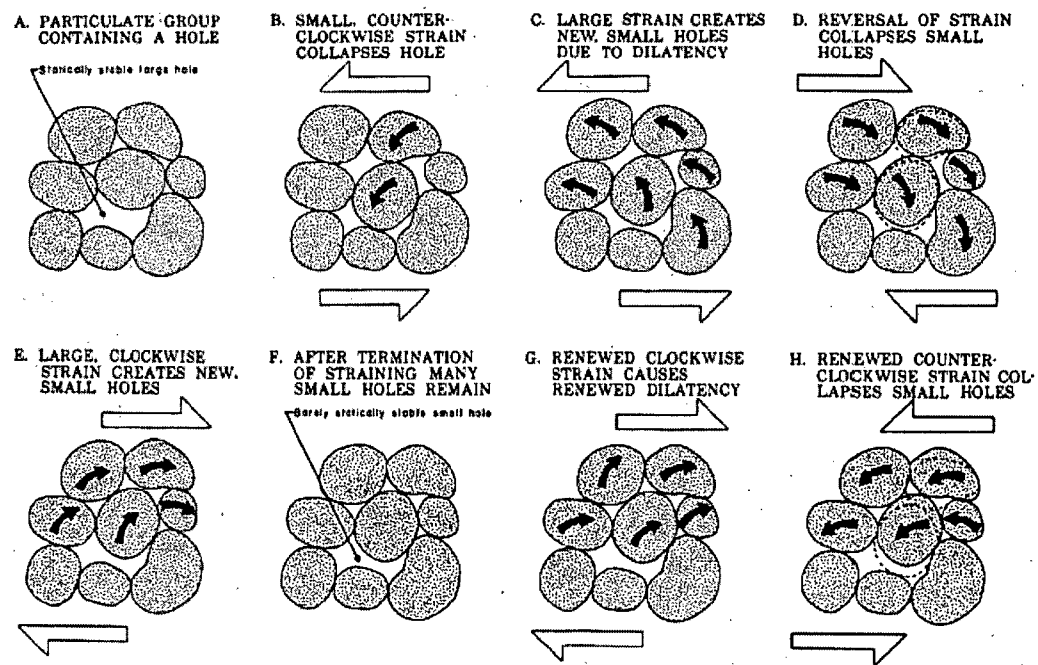


**Figure 2.12** Idealized cross section of particulate group showing packing changes that occur during cyclic loading (after Youd, 1977).

Lee (1991) carried out constant load cyclic drained simple shear tests on Ottawa sand at various densities, and presented the results in Figure 2.13(a) in terms of stress ratio  $\tau_{xy}/\sigma'_y$  (i.e.,  $\tau_{xy}/\sigma'_{v0}$ ) and dilatancy rate  $(dV/V_0)/d\gamma$  (i.e.,  $d\varepsilon_v/d\gamma$ ), where  $\sigma'_y$  is a vertical effective stress

(constant in Lee's tests),  $dV$  is a volume change,  $V_0$  is an initial volume, and  $d\gamma$  is a shear strain increment and always positive. Based on these results, Lee (1991) proposed two equations: one for increasing shear stress and one for decreasing shear stress, which are given by

$$\tau_{xy} / \sigma'_y = 0.42 - 1.68 \cdot (dV / V_0) / |d\gamma| \quad \text{when the shear stress increased} \quad [2-3a]$$

$$\tau_{xy} / \sigma'_y = -0.42 + 1.68 \cdot (dV / V_0) / |d\gamma| \quad \text{when the shear stress decreased} \quad [2-3b]$$

The equation corresponding to the positive shear stress in Eq. [2-3] has a similar form to the one above,  $\eta = -D + \sin \phi_{cv}$ . It is schematically illustrated in Figure 2.13(b).

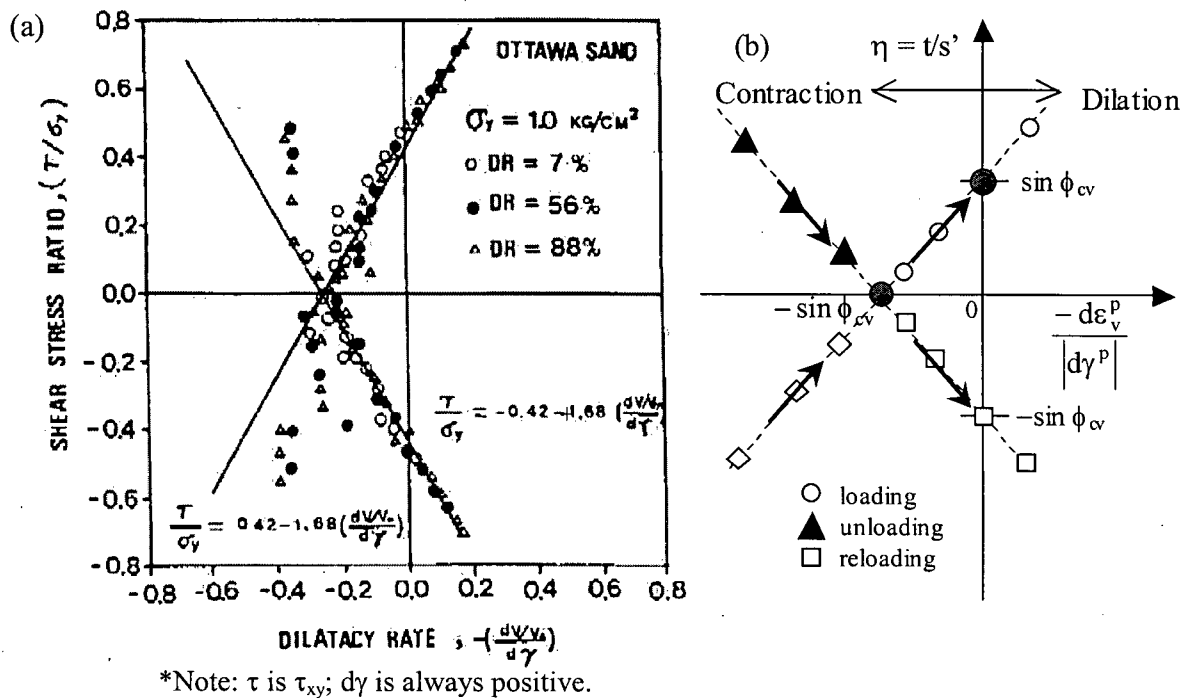


Figure 2.13 Shear stress ratio vs. dilatancy rate during loading, unloading and reloading: (a) after Lee (1991), and (b) simplified dilatancy.

As mentioned earlier, it was seen that Lee's (1991) equation [2-3] reasonably represents the test results, regardless of density. The equation [2-3b] infers that the unloading phase always causes contraction. On the other hand, it seems to overpredict the observed volume change at the beginning of the shear stress reversal. Lee (1991) suggested that the measurement difficulty

in precise volume change during unloading might cause such discrepancy between the measurement and the equation [2-3]. The stress-dilatancy equation [2-3b] during unloading/reloading is similar to the simplified equation corresponding to unloading/reloading,  $\eta = D - \sin \phi_{cv}$  in Figure 2.13(b). The slope of both equations could be different but the pattern of dilatancy is in good agreement as shown in Figure 2.13. This simplified stress-dilatancy equation in Figure 2.13(b) will be discussed more in Chapter 3. Plastic unloading is quite important when it causes soil fabric collapse that occurs during stress reversal following a large stress cycle that induces dilation.

Data from large cyclic shear strain level (e.g.,  $\gamma_{cyc} = 4\%$ ) in Figure 2.4(b) shows that loose Fraser River sand ( $D_{rc} = 40\%$ ) contracts less and less due to the hardening nature of soil skeletons as the number of cycles increases. Such cyclic hardening on shear-induced volume change seems to be independent of applied shear strain, vertical effective stress, and density as observed from cyclic drained simple shear tests (Silver & Seed, 1971; Martin et al., 1975; Sriskandakumar, 2004). Therefore, it is important to capture the decreasing pattern of volumetric strain, which in turn influences the pattern of pore pressure generation if drainage is prevented in saturated soils. Lee (1991) pointed out, based on cyclic drained simple shear tests, that the stress-dilatancy equation derived from the first cycle seems to mislead as the number of cycles increases. Such a hardening effect on loose sand may be simulated by including the current void ratio into the dilatancy as the state-dependent dilatancy proposed.

It is noted in this section that deformations imposed on soil are largely irrecoverable. A most fundamental aspect of geotechnics is how this behaviour may be represented within a single constitutive model.

## 2.4 Plasticity Models for Soil

Nearly all advanced models for soil are based on plasticity, which is natural since even the simplest of tests on soil show that irrecoverable strains are a key aspect of soil behaviour. Plasticity models are formulated along the lines of classical continuum mechanics, and a stress increment is specified by a strain increment (Dafalias, 1994). Therefore, the stress-strain relationship is incremental in form, and the total strain increment is separated into elastic and plastic strain increments (Hill, 1950). In addition, zones of elastic and plastic behaviour are assumed to be separated by a boundary called a yield surface.

Plasticity models have developed over the past fifty years, and there are numerous models today. However, models tend to fall into groups with similar idealizations and only small differences in implementation or detail. Lade (2005) reviewed numerous constitutive models ranging from simple elastic models to advanced and complex plasticity models, and compared their capabilities in terms of cyclic loading applicability, number of parameters, and experiments required for parameter determination. Here, the present constitutive models for soil liquefaction analysis are reviewed in terms of their characteristics and capabilities.

### 2.4.1 Classical Plasticity Models

A classical plasticity model consists of three distinct components: a yield criterion, a flow rule, and a hardening rule. Yield criteria are defined exclusively in stress space, and define the size of the elastic domain. Any stress probe pushing outwards of the yield surface will cause plastic strains. The flow rule determines the directions of plastic shear and volumetric strain increments. It could be associated (yield locus = plastic potential) or non-associated (yield locus  $\neq$  plastic potential). The hardening rule specifies the manner in which the elastic region evolves

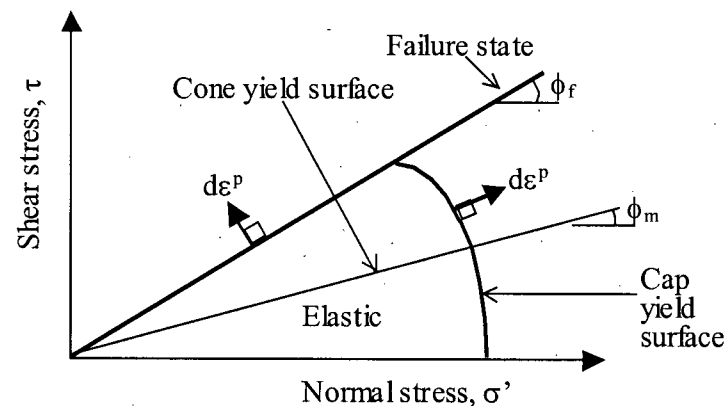
as yielding takes place. Prager (1956) proposed two possible hardening mechanisms: isotropic and kinematic hardening. The majority of classical plasticity models can be separated into two types: extended Mohr-Coulomb models (or Mohr-Coulomb type of models) and critical state type of models (Puebla, 1999).

### **(i) Extended Mohr-Coulomb models**

Extended Mohr-Coulomb models are based on the classic associated (or non-associated) Mohr-Coulomb elasto-perfect plastic model (hereafter called Mohr-Coulomb model). This model has only a cone yield surface as shown in Figure 2.14. As pointed out by Vermeer (1978, 1998), a Mohr-Coulomb model with associated flow rule gives unrealistic dilation, whereas a Mohr-Coulomb model with non-associated flow rule captures many aspects of drained soil behaviour well. The Mohr-Coulomb model with a non-associated flow rule has been routinely implemented in commercial finite element/difference codes (e.g., PLAXIS, FLAC) and it requires only four parameters,  $E$  (Young's modulus),  $\nu$  (Poisson's ratio),  $\phi$  (friction angle),  $\psi$  (dilation angle). However, the model cannot calculate realistic pore pressure and is also too simple for soils since plastic strains also occur for stress states below the strength envelope and during unloading.

It is known that sands yield or harden continuously below the failure line. This kind of continuous shear-induced yielding can be modeled by continuously changing the mobilized friction angle,  $\phi_m$ , as load is applied (e.g., Roscoe, 1970). To simulate such continuous yielding, the Mohr-Coulomb model with non-associated flow rule can be modified by using a variable friction and dilation angle to capture the plastic strains that occur at all stages of loading. The increase in friction angle can be related to an isotropic hardening rule, which is based on a

hardening parameter such as a plastic shear strain. Vermeer (1984) was one of the earliest to consider the mobilization of friction and dilation angles within plasticity, which allowed the continuous yielding of sands in a simple way. He proposed a model called a double hardening model (Vermeer, 1978), which can consider both cone and cap yield surfaces as shown in Figure 2.14. Others including Molenkamp (1981) and Wan and Guo (1998) have used double hardening models for monotonic loading. Such a simple modification was also incorporated into the constitutive model UBCSAND (Byrne et al., 1995; Beaty & Byrne, 1998). UBCSAND used a cone yield surface which hardens as plastic shear strain increases and a non-associated flow rule based on Rowe's stress-dilatancy. It is calibrated based on simple shear tests and requires only six model parameters. Puebla (1999) proposed an extended Mohr-Coulomb model with cone and cap yield surfaces and mixed hardening (isotropic and kinematic hardening) to apply for soil liquefaction analysis.



Note:  $\phi_f$  is a friction angle at failure;  $d\epsilon^p$  is a plastic strain increment.

**Figure 2.14** Concept of associated Mohr-Coulomb type of models with cap and cone yield surfaces.

## (ii) Critical state type of models

There are two key features with regard to critical state models. (a) Critical state models are idealized and based on postulated work dissipation. There is no curve fitting. This makes them extremely powerful in terms of predictions for general stress paths and states, but is also a limitation if the idealizations become too extreme. (b) Critical state models couple void ratio to mechanical behaviour. As such, a critical state concept with associated flow rule and isotropic hardening rule has successfully captured normally consolidated clays under monotonic loading (Roscoe et al., 1963). It is noted that the Modified Cam-Clay model (Roscoe & Burland, 1968) is by far the most widely available advanced soil model in commercial software (e.g., PLAXIS, FLAC).

However, some researchers (e.g., Poorooshasb et al., 1966; Lade & Duncan, 1975; Lade, 2005) argued that an associated flow rule was not consistent with observed sand behaviour. It is generally noted that isotropic hardening is not enough to simulate unloading and reloading (i.e., cyclic loading). On the other hand, the concept of a critical state has been often adopted in other concepts (e.g., bounding surface concept, state parameter, state-dependent dilatancy) to model sand behaviour (Manzari & Dafalias, 1997; Li et al., 1999). All models which predict the effect of void ratio change on soil behaviour have been variants or developments of the critical state ideas. For example, the NorSand model proposed by Jefferies (1993) can capture the behaviour of sand by postulating an infinity of isotropic normal consolidation loci and using the state parameter (Been & Jefferies, 1985) rather than void ratio. He also emphasized the usage of a single set of parameters for the same sand at different densities. Jefferies (1997) proposed an internal cap that changes or shrinks its size, and this modification enables cyclic loading to be represented.

## 2.4.2 Advanced Plasticity Models

### (i) Bounding Surface Models

The concept of a bounding surface was originally introduced for metals by Dafalias and Popov (1975), and Krieg (1975), independently. It was motivated by the observation that any stress-strain curve for monotonic loading, or for monotonic loading followed by reverse loading, eventually converges to certain “Bounds” in the stress-strain space as shown in Figure 2.15. Bounding surface models allow the smooth stress-strain curve using plastic modulus, which is a function of distance from actual stress point to an image point at the bounding surface.

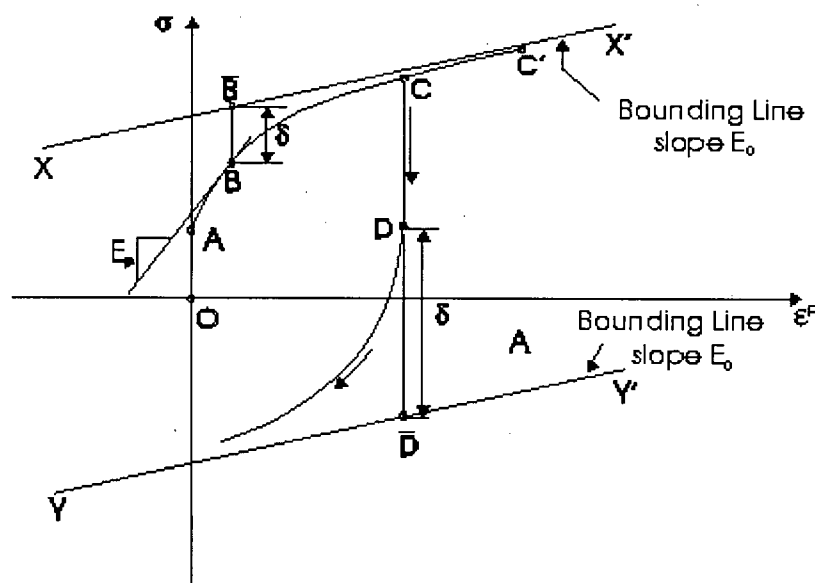


**Figure 2.15** Concept of bounding surface (uniaxial) model (after Dafalias & Popov, 1975).

The bounding surface concept has been adopted in various forms of formulations for soil liquefaction analysis by Bardet (1985, 1986, 1995), Muraleetharan (1990), and Wang and Makdisi (1999). HOPDYNE proposed by Anandarajah (1990) is a standard associative bounding surface model for soil liquefaction analysis. The bounding surface plasticity based code DYSAC2 (Muraleetharan et al., 1988, 1997) is a result of comprehensive research on soil

liquefaction at the University of California, Davis. This model has been extensively involved in predicting soil liquefaction problems by Arulanandan (1996), Muraleetharan and Arulanandan (1991), and Yogachandran (1991). Recently, Muraleetharan et al. (2004) reported successful use of DYSAC2 to predict the dynamic response of embankments in centrifuge tests.

## (ii) Multi-yield or Nested-surfaces Models

Nested-surface model was originally proposed by Mroz (1967) and Iwan (1967). It involves isotropic and kinematic hardening, and is similar to a bounding surface model. This model defines a series of surfaces  $f_0, f_1, f_2 \dots f_n$ , whereas a bounding surface model defines two surfaces, a bounding surface (e.g.,  $f_n$  in Figure 2.16) and a loading surface (e.g.  $f_0$  in Figure 2.16). The initial yield surface  $f_0$  defines the minimum elastic zone or initial state that moves along as loading proceeds. Under a loading phase (see Figure 2.16(b)), the elastic zone moves with the stress point until the next yield surface is reached. Upon unloading (see Figure 2.16(c)), the stress point moves with the elastic zone until its yield surface is reached again. However, continuous tracking of the position of every yield surface could be complex when applied for cyclic loading.

Prevost (1985) formalized the concept of multi-yield surfaces for soil behaviour and incorporated it in DYNAFLOW<sup>TM</sup> (Prevost, 1998). This model has successfully predicted some of the dynamic centrifuge tests in the Verification of Liquefaction Analysis by Centrifuge Studies (VELACS) project (Arulanandan & Scott, 1993). Arulanandan (1996) reported that it adequately predicted the dynamic response of a submerged embankment in a centrifuge test. Multi-yield surfaces may remain the same size and translate in principal stress space (purely deviatoric-kinematic hardening) (e.g., Prevost, 1985) or they may expand and translate at the

same time (isotropic and deviatoric-kinematic hardening) (e.g., ALTERNAT proposed by Molenkamp, 1982 and Woodward & Molenkamp, 1999).

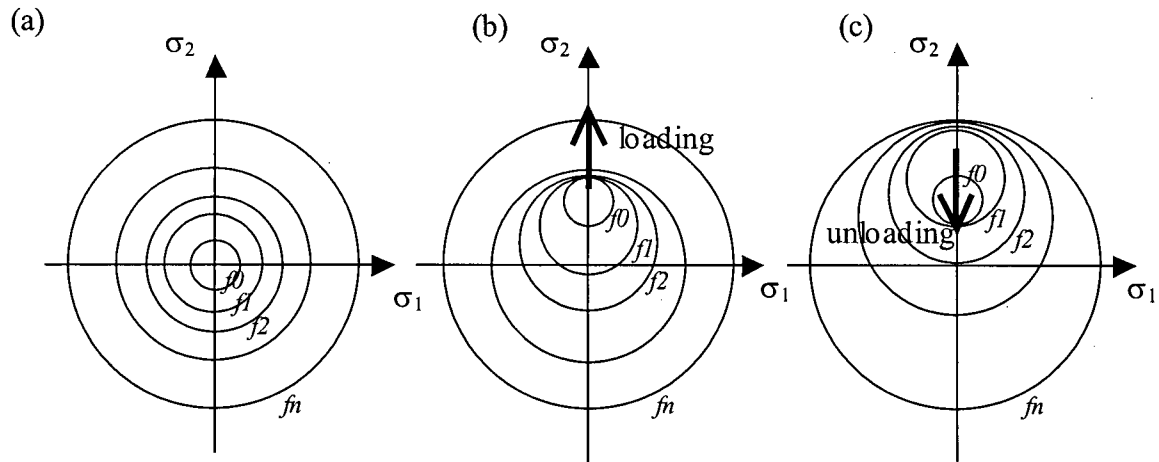


**Figure 2.16** Nested surface model: (a) before straining, (b) after straining, and (c) upon unloading (after Mroz, 1967).

### (iii) Generalized Plasticity Models

A generalized plasticity model was proposed by Zienkiewicz and Mroz (1984). A generalized plasticity model has several merits. The unloading can be freely determined not being based on a strict plasticity formulation (Dafalias, 1994). Iai et al. (1992) successfully simulated different  $K_0$  states using a generalized plasticity. They mentioned that conventional plasticity models cannot simulate initial  $K_0 = 0.5$  consolidated simple shear because it involves effects of principal stress rotation. Computer codes such as SWANDYNE (Zienkiewicz et al., 1990) and DIANA-SWANDYNE II (Chan, 1993; Zienkiewicz et al., 1990, 1999) with Pastor-Zienkiewicz Mark III constitutive model (Pastor et al., 1985, 1990) and Nova's (1982) dilatancy are some of typical numerical procedures based on a generalized plasticity. Madabhushi and Zeng (1998) successfully predicted the response of a gravity quay wall against soil liquefaction in a centrifuge test using SWANDYNE. Recently, Aydingun and Adalier (2003) verified DIANA-

SWANDYNE II by capturing the seismic response of various embankments with and without remedial measures in centrifuge tests.

### 2.4.3 Micromechanical and/or Multimechanism Models

Most of the aforementioned plasticity models are formulated in terms of stress invariants, and therefore they have a deficiency in handling of principal stress rotation (Matsuoka, 1974; Lee & Pande, 2004). Matsuoka et al. (1988) state that classical plasticity cannot explain the volumetric strains caused by “rotation tests” which keep a constant size of Mohr’s stress circle while rotating the principal stress direction. Iai et al. (1992) also state that conventional plasticity models cannot simulate  $K_0$ -consolidated simple shear because it involves rotation of principal stress axis.

The effect of principal stress rotation presents a number of challenges to numerical modeling. As an example, micromechanical and/or multimechanism models capable of simulating principal stress rotation are reviewed in this section. They calculate the overall response by superposing or adding-up the response of smaller units or mechanisms of deformation (Dafalias, 1994).

#### (i) Multimechanism Models

In order to simulate “rotation tests”, Matsuoka (1974) studied an approach called multimechanism that used only a maximum obliquity plane,  $45^\circ + \phi/2$  for three different shearing mechanisms as illustrated in Figure 2.17. Matsuoka (1976) developed the concept called “spatially mobilized plane (SMP)” for three-dimensional analyses. Kabilamany and Ishihara (1991) also proposed a similar concept in three dimensional stress space. In their

models plastic strains from three mechanisms are independently produced and superimposed. In fact, those models consider one mobilized plane from each combination of principal stresses.

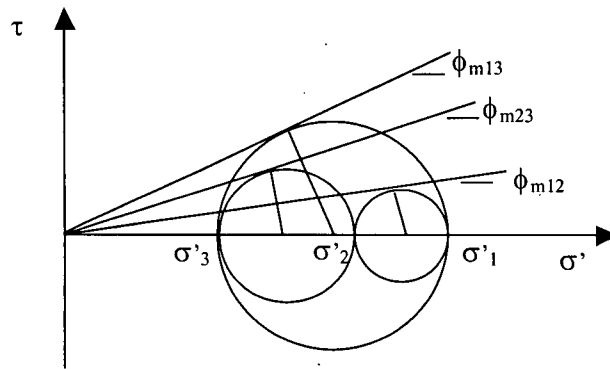


**Figure 2.17** Three mobilized planes on which  $(\tau/\sigma')$  is maximum under three different principal stresses (modified from Matsuoka, 1974).

Matsuoka and Sakakibara (1987) proposed a similar model based on stress ratio on the horizontal plane rather than on the plane of maximum obliquity as before. General shear and normal stresses in Cartesian coordinate,  $\sigma'_x$ ,  $\sigma'_y$ ,  $\tau_{xy}$ , are illustrated in Figure 2.18, where  $\phi_m$  is the mobilized friction angle and  $\alpha_\sigma$  is the angle between an arbitrary plane (e.g., horizontal plane) and the principal stress plane. The model handles the effect of principal stress rotation by defining general shear strain increment,  $d\gamma_{xy}$ , as follows:

$$d\gamma_{xy} = d\gamma_{xy}^s + d\gamma_{xy}^r + d\gamma_{xy}^{ac} \quad [2-4]$$

where  $d\gamma_{xy}^s$  = shear strain increment due to shear;  $d\gamma_{xy}^r$  = shear strain increment due to principal stress rotation;  $d\gamma_{xy}^{ac}$  = shear strain increment due to anisotropic consolidation. This is an explicit way to deal with principal stress rotation problems, but it has only been applied to monotonic loading. Therefore, it is doubtful whether such a model can handle cyclic loading including unloading and reloading due to its complexity.

Beyond stress invariants-based formulations, any plane with general normal and tangential stresses can be used to define yielding in two-dimensional analyses. Murayama (1964) termed such a plane as a mobilized plane. A single mobilized plane may not be adequate to model such behaviour. Pande and Sharma (1983) proposed a multi-laminate model that is capable of capturing the monotonic shear response of clays via accounting for the stresses mobilized on multiple planes.

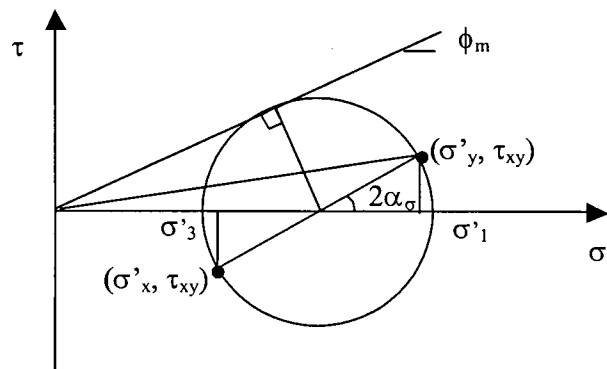


**Figure 2.18** General shear and normal stresses (after Matsuoka & Sakakibara, 1987).

## (ii) Multi-laminate Model

Calladine (1971) proposed a micro-structural model of clays based on the slip theory of plasticity for metals proposed by Batdorf and Budiansky (1949). The micro-structural model assumes that a solid block of perfectly plastic material consists of an assemblage of a large number of fitting polyhedral blocks. A similar block intersected by many sampling or contact planes is shown in Figure 2.19 (Cudny & Vermeer, 2004).

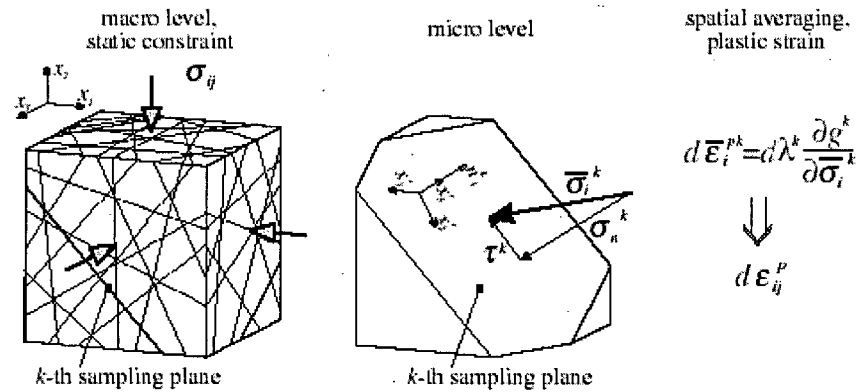


**Figure 2.19** Schematic description of multi-laminate framework (after Cudny & Vermeer, 2004).

As an extension of a micro-structural model, Pande and Sharma (1983) attempted to bridge the gap between physical and mathematical theories of plasticity. As a result, they successfully formulated the physical concept of a micro-structural model into a multi-laminate model. A multi-laminate model was originally proposed to study rock joint behaviour by considering many slip planes by Zienkiewicz and Pande (1977). It had been developed to account for the rotation of principal stress axes, which takes place in most field problems. In the context of a multi-laminate framework, a yield function may be given on more than one plane. Such a yield function is decided on any specific plane in terms of effective normal and shear stresses on that plane (Pande & Sharma, 1983). Those models use an appropriate superposition of each mechanism using an integration rule. A multi-laminate model by Pande and Sharma (1983) originally considered unloading as elastic as in classical plasticity. Later, Pande and Pietruszczak (1982) proposed a multi-laminate reflecting surface model to include plastic unloading. Consequently, their model can handle the effect of principal stress rotation as well as plastic unloading. Recently, the model has been extended to apply to cyclic loading tests including the effect of principal stress rotation (Lee & Pande, 2004).

Several key assumptions have been used in the development of multi-laminate models. For example, the deformational behaviour of soils can be obtained from sliding mechanism along the boundaries of the blocks under current normal and shear stresses. All the boundaries of contact have been assumed to have the same characteristics in sliding with no interaction between them. Another assumption is that a higher number of contact planes lead to a higher accuracy (Pande & Yamada, 1994). The assumptions adopted in multi-laminate models have been successfully applied to monotonic loading problems in rocks, clays, and sands. However, they may pose significant difficulties in relation to granular soils particularly under cyclic loading conditions.

While a multi-laminate model is capable of simulating principal stress rotation, the basic assumptions for a multi-laminate model may not be applicable for granular soils under cyclic loading conditions since soil fabric may change during stress reversal or unloading. It is also necessary to track shear stress reversal on each mobilized (sampling) plane during cyclic loading (Lee & Pande, 2004). Other problems may arise from its complexity as more planes are involved.

#### **2.4.4 Summary of Plasticity Models**

Conventional plasticity models with isotropic hardening cannot simulate cyclic loading. Furthermore, they cannot predict plastic deformation during unloading. Advanced plasticity models introduced in Section 2.4.2 were able to capture realistic cyclic behaviour of sand. They can simulate plastic unloading by varying the hardening rule, with yield surfaces and flow rules being unchanged.

The foregoing review for constitutive models indicates that advanced plasticity models have made significant progress in predicting excess pore pressure due to earthquake loading by capturing dynamic centrifuge tests. However, most constitutive models are calibrated based on data from triaxial tests, which have no rotation of principal stress, whereas principal stress rotation occurs in the field (e.g., plastic volume change induced by principal stress rotation). While some constitutive models can simulate the effect of principal stress rotation, they have not yet been applied to soil liquefaction problems in the field. Most models were calibrated based on axisymmetric condition (e.g., triaxial tests), whereas many geotechnical problems can be approximated as plane strain.

Some typical plasticity models (numerical codes or constitutive models) for soil liquefaction analysis are summarized, and their attributes, including the type of model and three plasticity components, are compared in Table 2.1. A recent representative reference for each constitutive model is used for comparison with the other plasticity models. The primary concern of this comparison is the capabilities of each model such as the number of model parameters, validation in plane strain as well as modeling of principal stress rotation. It is noted that some models require more than ten model parameters and are not validated in plane strain conditions (e.g., simple shear tests). In particular, most of these models cannot simulate the effect of principal stress rotation (e.g., plastic volume change). UBCSAND2 is able to simulate principal stress rotation.

As described in Table 2.1, a very attractive feature of the UBCSAND model is that it is validated in plane strain conditions and requires few model parameters. In consideration of this, a new constitutive model capable of modeling principal stress rotation is proposed in this study while retaining those features of UBCSAND.

**Table 2.1** Comparison of typical plasticity models for sand under cyclic loading and their capabilities.

Type of Model	Constitutive Model or Code	Recent Reference	Plasticity Components			Practicality and Capability		
			Yield Surface Type	Flow Rule (Dilatancy)	Hardening Parameter	Number of Parameters	Validated in Plane Strain <sup>(i)</sup>	Models PSR <sup>(ii)</sup>
1	2	3	4	5	6	7	8	9
Bounding surface plasticity	DYSAC2	Muraleetharan et al., 2004	Elliptical Cap	Non-associated	Plastic shear & volumetric strain	13	No	No
	MIT-S1	Pestana et al., 2000, 2002	Distorted lemniscate	Non-associated	Plastic shear & volumetric strain	13	Yes	No
Multi-yield plasticity	ALTERNAT	Woodward & Molenkamp, 1999	Cone (Lade)	Non-associated & associated, Rowe <sup>(iii)</sup>	Plastic shear & volumetric strain	22	No	No
	DYNAFLOW	Azizian & Popescu, 2001	Cone (Drucker-Prager)	Associated or Non-associated	Work-hardening moduli <sup>(iv)</sup>	8	No	No
Generalized plasticity	DIANA-SWANDYNE II	Aydingun & Adalier, 2003	Elliptical Cap	Non-associated, Nova <sup>(v)</sup>	Plastic shear & volumetric strain	11	No	No
Critical state plasticity	NorSand	Been et al., 1993	Bullet-shaped	Associated, Nova	Plastic work	9	Yes	Yes
Mohr-Coulomb type plasticity	UBCSAND	Byrne et al., 2004a	Cone (Mohr-Coulomb)	Non-associated, Rowe	Plastic shear strain	6	Yes	No
	UBCSAND2 <sup>(vi)</sup>	Park et al., 2005	Double Cone (Mohr-Coulomb)	Non-associated, Rowe	Plastic shear strain	7	Yes	Yes

Note: All statements in Table 2.1 are referred to the recent reference in column 3; (i) referred to simple shear tests; (ii) PSR stands for Principal Stress Rotation; (iii) Rowe denotes Rowe (1962) stress-dilatancy; (iv) refers to Iwan (1967), Mroz (1967), Prevost (1977); (v) Nova denotes Nova (1982) stress-dilatancy; (vi) Model proposed in this study; Col.7: parameter number was obtained from a given recent reference, and initial stress, initial density, and cohesion were excluded from counting; Col.8: This answer is based on the given reference and may be different in different versions.

## Chapter 3

# Development of a Two Mobilized-plane Model: UBCSAND2

The UBCSAND model, which was validated under plane strain conditions with six model parameters, has been enhanced to account for plastic unloading and principal stress rotation that commonly occurs and can significantly influence soil behaviour. The proposed model considers the current shear stresses along two mobilized planes to describe shear-induced yielding. The model uses a conventional plasticity formulation to describe the first plane and assumes that the same relationships hold for the second plane. It adds plastic strain increments obtained from the description of two mobilized planes, a plane of maximum shear stress, which rotates or swings as the direction of the principal stress rotates, and a horizontal plane which is spatially fixed. This is a new concept developed in this study. It is referred to as Two Mobilized-plane model from its framework and also UBCSAND2 from its extension of UBCSAND. By adding the horizontal plane (i.e., the second plane), the model can take into account the effect of principal stress rotation as well as plastic unloading.

The concept and elastic and plastic formulations of this model are described and implemented into FLAC (Fast Lagrangian Analysis of Continua) (Itasca, 2000). Pore fluid stiffness and Darcy hydraulic flow are basic to the FLAC program so that only the skeleton stress-strain relation needs to be described in this chapter. An early version of the proposed model had been presented in several conferences (Park & Byrne, 2004c, 2005; Park et al., 2005)

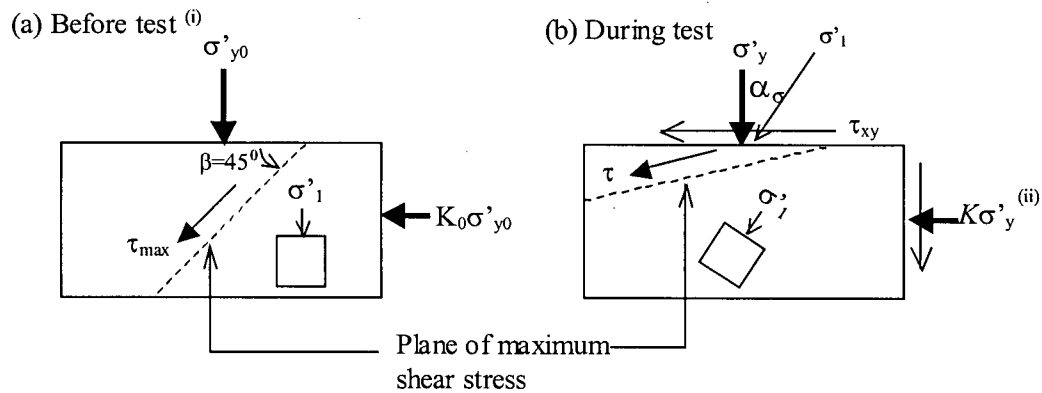
during the early development stage of UBCSAND2. Since then, substantial improvements have been achieved and these are included in this chapter.

### 3.1 UBCSAND Model and its Capability

Byrne and co-workers at UBC have developed a simple plasticity based effective stress constitutive model called UBCSAND for soil liquefaction (Byrne et al., 1995; Beaty & Byrne, 1998; Byrne et al., 2004a). The underlying feature of UBCSAND is simplicity and robustness for practical purposes. The effective stress UBCSAND procedure is a fully coupled stress-flow plasticity approach in which shear induced contraction and a dilation of the skeleton induce pre- and post-liquefaction response characteristics. The soil skeleton controls the response, and the effect of the pore fluid is purely one of controlling the skeleton volume and bulk stiffness. As mentioned earlier in Section 2.4, the UBCSAND model is validated in plane strain condition by emulating a simple shear loading condition similar to earthquake loading. The UBCSAND model has been successfully applied to modeling of observation from several centrifuge tests (Byrne et al., 2004a, 2004b; Yang et al., 2004a).

The effect of principal stress rotation in a simple shear test depends very much on the initial state of stress. If a state of stress where  $K (= \sigma'_h/\sigma'_v) = 1.0$  exists, then the horizontal plane becomes the plane of maximum shear stress as soon as any horizontal shear stress is applied. For this case, the plane of maximum shear stress is horizontal and essentially stays unchanged for the remaining part of the loading, and there is no rotation effect. Classical plasticity with a single plane simulates this condition very well. In simple shear testing, specimens are typically consolidated under  $K_0$  conditions (i.e.,  $K = \sigma'_h/\sigma'_v = K_0$ ). Note that a

horizontal stress  $\sigma'_h$  and a vertical stress  $\sigma'_v$  are equal to  $\sigma'_x$  and  $\sigma'_y$ , respectively. For example, if  $K = 0.5$ , then a large shear stress acts on the 45-degree plane (i.e.,  $\beta = 45^\circ$  plane in Figure 3.1(a)). As the horizontal shear stress is applied, the plane of maximum shear stress gradually rotates and becomes approximately horizontal at failure (Roscoe, 1970). Thus, there is a gradual rotation of principal stress during the loading process. A classical plasticity approach with a single plane cannot capture the observed response in this case.



Note: (i) represents  $K_0$ -consolidated specimen prior to cyclic loading; (ii)  $K = \sigma'_x / \sigma'_y$

**Figure 3.1** Simple shear test under  $K_0$  consolidated condition.

As an example, UBCSAND computed two  $K$  conditions (i.e., 0.5 & 1.0) with the same initial vertical stress (100 kPa), and they are compared with monotonic drained behaviour of loose Fraser River sand in Figure 3.2. It is assumed that simple shear test specimens are consolidated under  $K = K_0 = 0.5$  unless otherwise stated. The prediction based on  $K = 0.5$  gives much stiffer behaviour, which is not consistent with observed behaviour.

When only the plane of maximum shear stress is considered, the initial shear stress increment on a horizontal plane ( $\tau_{xy}$ ) does not cause any significant plastic shear strain on the plane of maximum shear stress when  $K = 0.5$  (i.e.,  $\beta = 45^\circ$  plane in Figure 3.1(a)). Therefore,

the specimen consolidated to  $K = 0.5$  would predict much stiffer response than  $K = 1.0$  state as shown in Figure 3.2.

In essence, an initially elastic material response is predicted when initial  $K$  is 0.5. It is noted that the UBCSAND model, based on the plane of maximum shear stress alone, cannot capture  $K_0$ -consolidated (e.g.,  $K = 0.5$ ) simple shear test specimens.

In addition, from laboratory tests presented in Chapter 2, significant plastic deformation always occurs during the unloading phase, whereas UBCSAND does not predict such behaviour. The UBCSAND model overpredicts the area of the loop associated with cyclic loading, and hence overpredicts damping.

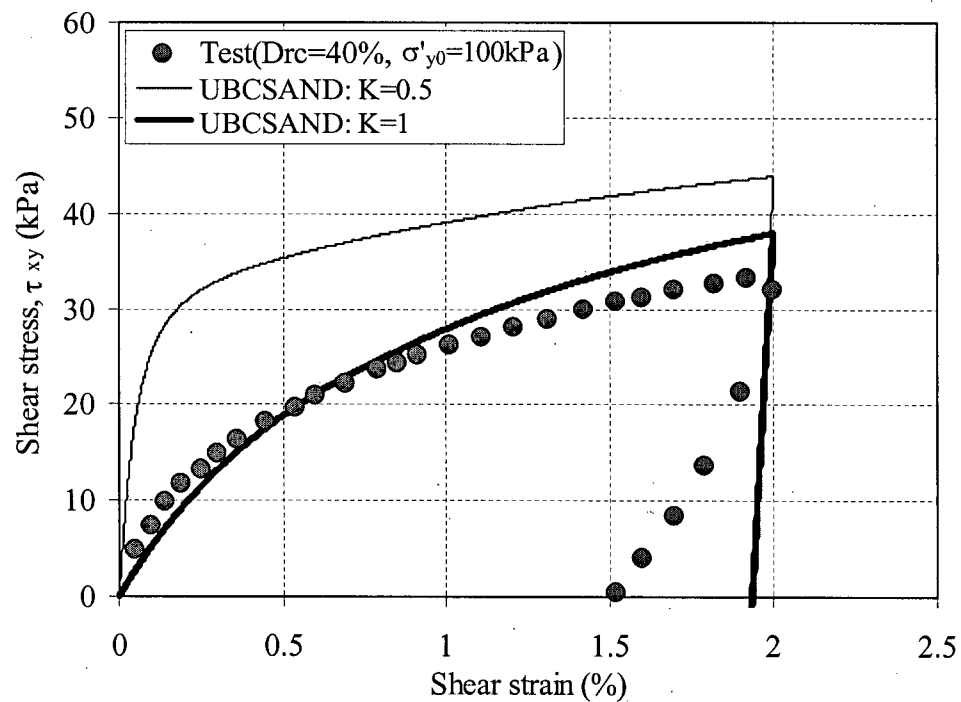


**Figure 3.2** Numerical and experimental results of monotonic drained behaviour of loose Fraser River sand (test data from Sriskandakumar, 2004).

In recognition of the above, the UBCSAND model has been improved to account for the effect of principal stress rotation or  $K$  effect and plastic unloading. A new model called

UBCSAND2 considers the horizontal plane in addition to the plane of maximum shear stress previously considered in UBCSAND. The combination of two mobilized planes in UBCSAND2 makes it possible to simulate rotation of principal stresses and plastic unloading associated with simple shear loading. This makes UBCSAND2 an appropriate model for representing earthquake loading for practical problems.

### 3.2 Concept of a Two Mobilized-plane Model

The concept of a Two Mobilized-plane model is described here. Shear stress increments on two planes (i.e., maximum shear stress, and horizontal planes) causing plastic strains are illustrated in Figure 3.3 for simple shear conditions with initial  $K = 0.5$ . Figure 3.3(a) represents conditions at the start of shearing when  $\tau_{xy} = 0$  and a small increment  $\Delta\tau_{xy}$  is applied. In this case the plane of maximum shear stress is at 45 degrees and while there is a large shear stress from the initial  $K$  condition, the increment of shear stress  $\Delta\tau$  on the plane of maximum shear stress is zero, and hence no plastic strains are predicted on the plane of maximum shear stress. This results in an initially very stiff elastic response from classical plasticity, based on a single plane as described earlier in Figure 3.2. However, the stress increment on the horizontal plane,  $\Delta\tau_{xy}$  will cause plastic strains on this plane and all other planes except for the 45-degree plane. When this second plane (i.e., the horizontal plane) is considered, a much softer response is predicted as shown by the dashed curve 2 in Figure 3.4, "Stage A". In other words, the second plane takes into consideration the plastic deformation caused by principal stress rotation.

Therefore, the appropriate plastic strains can be obtained from a combination of two plastic strain increments obtained from two mobilized planes. The total strain increment  $\Delta\varepsilon$  is then given by

$$\Delta\varepsilon = \Delta\varepsilon^e + \Delta\varepsilon^p = \Delta\varepsilon^e + (\Delta\bar{\varepsilon}^p)_1 + (\Delta\bar{\varepsilon}^p)_2 \quad [3-1]$$

where  $\Delta\varepsilon$ ,  $\Delta\varepsilon^e$ , and  $\Delta\varepsilon^p$  = total, elastic, and plastic strain increments, respectively.  $(\Delta\bar{\varepsilon}^p)_1$  and  $(\Delta\bar{\varepsilon}^p)_2$  denote the plastic shear strain increments obtained from the first and second planes.

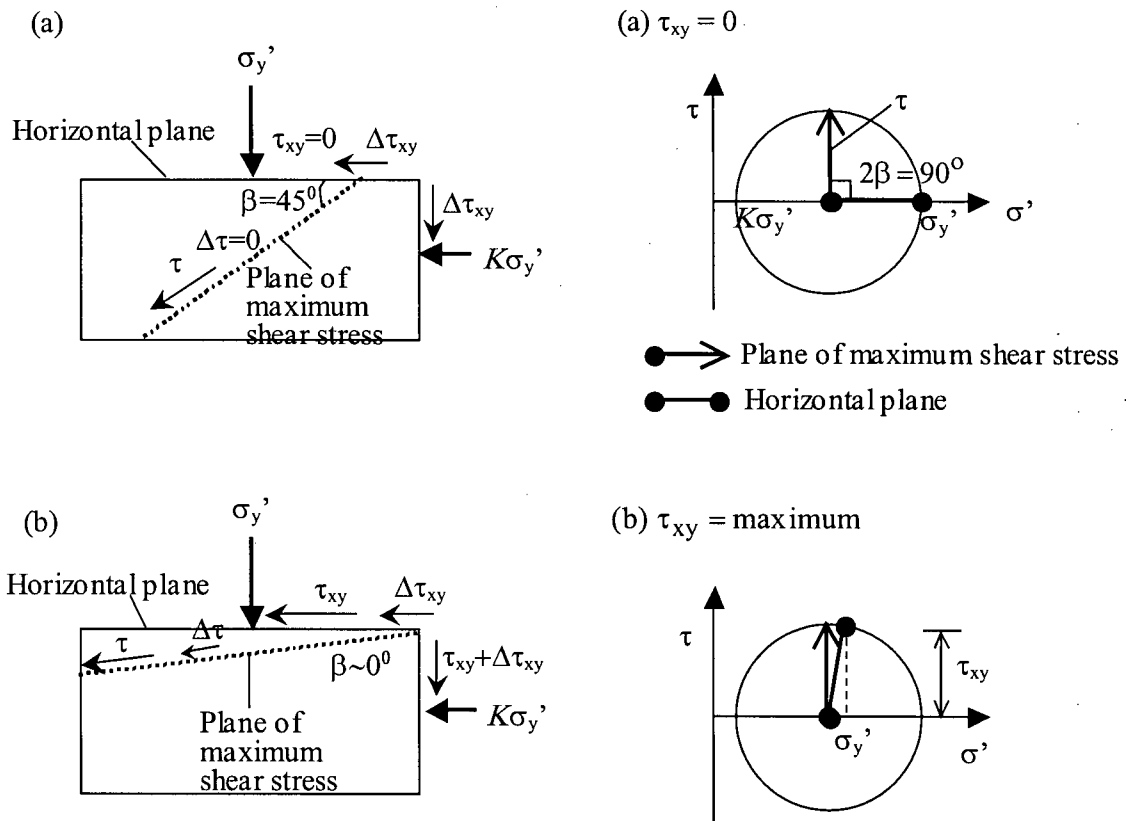


**Figure 3.3** Stress conditions on two mobilized planes after applying shear: (a) small strain level, and (b) large strain level.

A later stage of loading is depicted in Figure 3.3(b). Here  $\tau_{xy}$  is approaching its failure value and the plane of maximum shear stress has swung around to become nearly horizontal. At

this point  $\Delta\tau \approx \Delta\tau_{xy}$  and both planes essentially coincide; consideration of both planes would essentially predict double the plastic strain. This is accounted for by gradually phasing out the plastic strain increment from the horizontal plane  $(\Delta\bar{\epsilon}^P)_2$  as the plane of maximum shear stress becomes horizontal. This is the essence of this concept. The stress-strain condition at a later stage of loading is depicted as “Stage B” on Figure 3.4. Note that if the initial stress state is hydrostatic (i.e.,  $K = 1$ ) then the plane of maximum shear stress becomes horizontal as soon as the first increment of  $\Delta\tau_{xy}$  is applied and the horizontal plane contribution is not needed (i.e.,  $(\Delta\bar{\epsilon}^P)_2 = 0$ ).

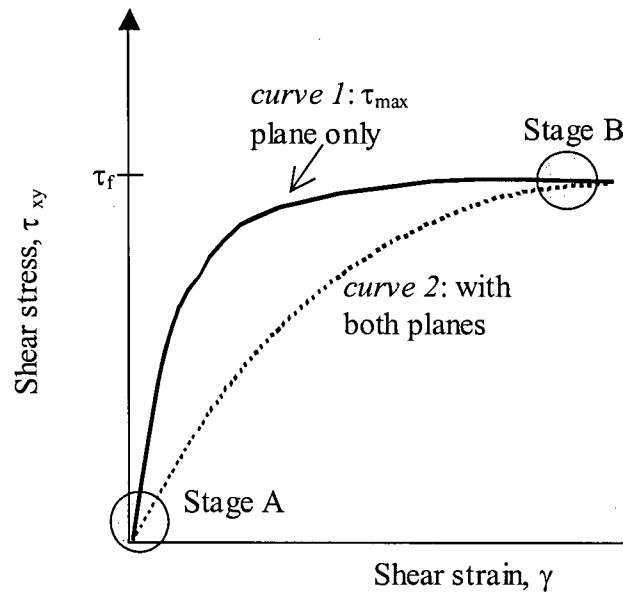


**Figure 3.4** Stress-strain curves for one mobilized plane and two mobilized planes.

For conventional cyclic triaxial tests, the direction of principal stress remains vertical or horizontal and there is no gradual rotation of principal stress and no need to consider a second plane. However, earthquake-induced loading conditions are much closer to simple shear than conventional triaxial loading, and a second plane is able to account for this seismic loading.

The response of sand is controlled by the skeleton behaviour. Provided the skeleton or drained behaviour is appropriately modeled under monotonic and cyclic loading conditions, and the stiffness of the pore fluid and drainage are accounted for, the undrained response can be predicted. This is the basic approach taken here. Elastic and plastic responses for the UBCSAND2 model are described as follows.

### 3.3 Elastic Behaviour

The elastic stress-strain relation in incremental form is expressed by Hooke's law in plane strain. Many geotechnical problems such as tunnels, dams, slopes and retaining walls are analyzed as a plane strain condition. Hooke's law was formulated in terms of Young's modulus,  $E$ , and Poisson's ratio,  $\nu$ . However, it is more fundamental to use an elastic shear modulus,  $G$ , and an elastic bulk modulus,  $B$ , which divide the elastic deformation into a shear part and a volumetric part, respectively. The elastic component of response is assumed to be isotropic, and specified by a shear modulus  $G$  and a bulk modulus  $B$  that are stress level dependent.  $G$  is often estimated from shear wave velocity or through correlations with penetration resistance. As a modified correlation from Seed et al. (1986),  $G$  can be expressed by

$$G = k_G^e \cdot P_a \cdot \left( \frac{\sigma'_m}{P_a} \right)^{nc} \quad [3-2]$$

where  $k_G^e$  = an elastic shear modulus number that depends on the density of the sand and varies from about 500 for loose sand to 2000 for dense sand;  $P_a$  is a reference pressure in the chosen units (i.e., 100 kPa);  $\sigma'_m$  is the mean normal effective stress in the plane of loading where

$\sigma'_m = (\sigma'_x + \sigma'_y)/2$  (hereafter referred to as “mean stress”);  $ne$  is an elastic exponent that varies between 0.4 and 0.6, and can be taken approximately as 0.5.

Based on Seed and Idriss (1970),  $k_G^e$  can be related to  $K_{2\max}$  as follows:

$$k_G^e = 21.7 \cdot (K_{2\max}) \quad [3-3]$$

where  $K_{2\max}$  is a function of  $(N_1)_{60}$  and Seed et al. (1986) suggested  $K_{2\max} = 20 \cdot (N_1)_{60}^{1/3}$ . For Fraser River sand a factor of 15 is recommended in preference to 20 in  $K_{2\max}$  (P.M. Byrne, personal communication, 2004). Using the correlation “ $(N_1)_{60}/D_r^2 = \text{constant}$ ” proposed by Skempton (1986),  $(N_1)_{60}$  can be converted to a relative density ( $D_r$ ).

There is little direct measurement of elastic bulk modulus,  $B$ . One direct measurement is to use high quality measurements of volumetric response during unloading. Alternatively, the elastic bulk modulus  $B$  can be obtained indirectly from the elastic shear modulus  $G$  as a function of Poisson’s ratio,  $\nu$ ,

$$B = \alpha_B \cdot G \quad [3-4]$$

where  $\alpha_B = \left( \frac{2(1+\nu)}{3(1-2\nu)} \right)$  depends on the elastic Poisson’s ratio,  $\nu$ , which is in the range 0.0 ~ 0.2

(Hardin, 1978), with the result that  $\alpha_B$  varies between 2/3 and 4/3 and can be approximated as unity.

### 3.4 Plastic Behaviour

This section describes plastic response including new features of the proposed model. In order to emulate complex soil behaviour a constitutive model always requires assumptions. The first

key assumption for the proposed model is that plastic deformations are added from two mobilized planes: a plane of maximum shear stress (swinging plane) and a horizontal plane. The horizontal plane always contributes plastic deformation when the plane of maximum shear stress is not coincident with the horizontal plane. If  $\sigma'_x = \sigma'_y$ , the two planes are essentially the same and only the plane of maximum shear stress will be activated. Initial contribution from the horizontal plane in terms of plastic shear strain is very important for the  $K_0$  state where  $\sigma'_{x0} \neq \sigma'_{y0}$ . With increasing shear stress ( $\tau_{xy}$ ), when the plane of maximum shear stress becomes a horizontal plane, the shear behaviour will be controlled by the plane of maximum shear stress only. This leads to the second key assumption; the horizontal plane phases out as principal stress rotates. This second assumption is a key item to accommodate the contribution caused by principal stress rotation, the effect of which gradually reduces and disappears, in terms of plastic strain increments.

The formulation of two mobilized planes is based on plasticity. For isotropic materials, Hill (1950, p38) postulates that based on the theory of plasticity the principal axes of the plastic strain increment coincide with the principal axes of stress. This condition is called coaxiality and is applied to the swinging plane or conventional component of plastic strain. This condition is not applied to the contribution from the horizontal plane, which means non-coaxiality, and allows the effect of principal stress rotation to be simulated.

The incremental formulation of a constitutive model can be expressed as follows (Prevost, 1985):

$$\{\Delta\sigma'\} = [D]\{\Delta\varepsilon^e\} = [D]\{\{\Delta\varepsilon\} - \{\Delta\varepsilon^p\}\} \quad [3-5]$$

where  $\{\Delta\sigma'\}$  = a vector of effective stress increments,  $[D]$  = an elastic stiffness matrix, and  $\{\Delta\varepsilon\}$ ,  $\{\Delta\varepsilon^e\}$  and  $\{\Delta\varepsilon^p\}$  = vectors of total, elastic, and plastic strain increments, respectively.

Stress increments are controlled by elastic strain increments as described in Eq. [3-5]. In numerical analysis, total strain increments in Eq. [3-5] are predicted. Consequently, these need to be separated into their elastic and plastic components. The plastic strains,  $\{\Delta\varepsilon^P\}$ , can be obtained from plasticity theory. The plastic strains occur from the two mobilized planes, and depend on stress state, and loading and unloading, and they are added as follows:

$$\{\Delta\varepsilon^P\} = \sum_{i=1}^2 (\Delta\bar{\varepsilon}^P)_i \quad i = 1, 2 \quad [3-6]$$

where,  $(\Delta\bar{\varepsilon}^P)_i = \lambda_i \cdot \frac{\partial g_i}{\partial \sigma}$

where  $i$  indicates each mobilized plane;  $\lambda$  is a scalar number, and determined by a consistency condition (i.e.,  $df = 0$ ,  $f$  is a yield function);  $g$  is a plastic potential function. These  $f$  and  $g$  are different and lead to a non-associated flow rule for each mobilized plane. Each plane can be idealized by the shearing mechanism to cause plastic deformation, and its calculation flow is illustrated in Figure 3.5 and further discussed in Section 3.6.

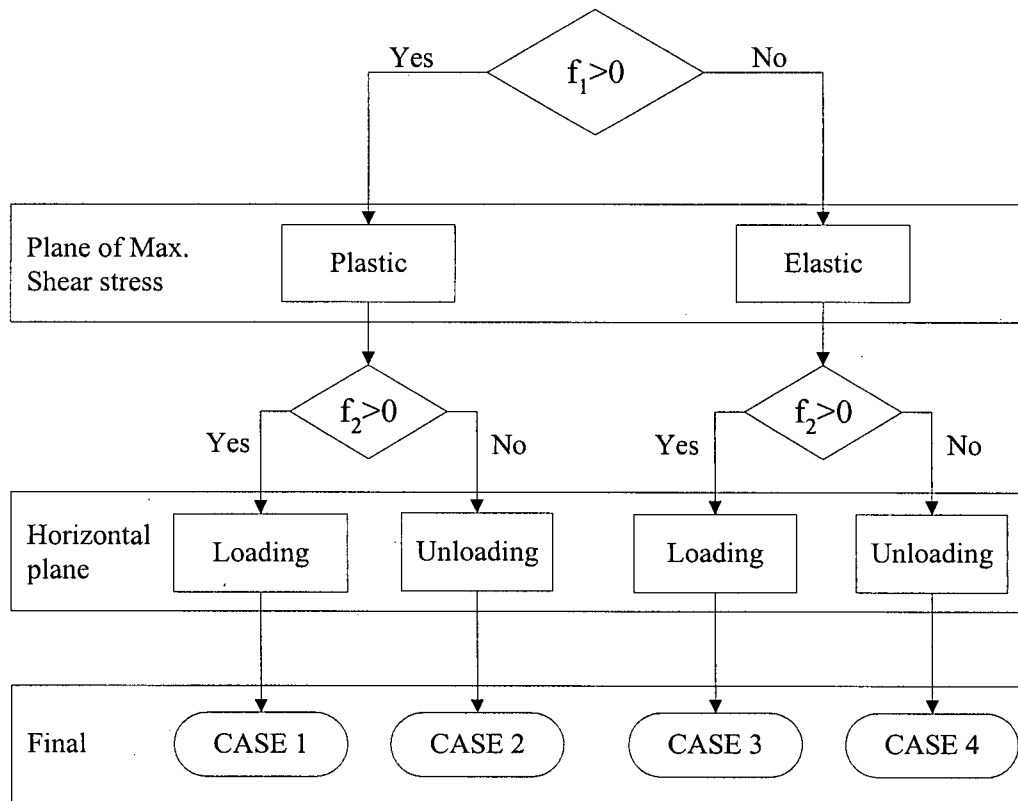
In summary, the incremental plastic response is given by superposition of two plastic components:

- $(\Delta\bar{\varepsilon}^P)_1$  is assumed to respond only to stress paths in which the stress ratio on the plane of maximum shear stress increases, and
- $(\Delta\bar{\varepsilon}^P)_2$  is assumed to respond only to stress paths in which the stress ratio on the horizontal plane increases, and this accounts for the plastic deformation due to principal stress rotation.

The plasticity approach involves three components:

- (a) Yield function; (b) Hardening rule; and (c) Flow rule.

In practice, the above three components must be considered simultaneously, but the detailed formulations of them are described separately in the following subsection. In addition, the horizontal plane phasing-out function and volumetric hardening function are also introduced.



Note:  $f_1$  is related to yielding on the plane of maximum shear  
 $f_2$  decides loading/unloading on the horizontal plane  
 $f_1 > 0$  means yielding

Figure 3.5 Flow chart of UBCSAND2 calculation.

### 3.4.1 Failure and Yield Functions

In plasticity, a yield function determines whether plastic deformation occurs or not. If yielding occurs, plastic strain increments must be known in order to calculate the stress increment as described in Eq. [3-5]. In the UBCSAND2 model, the yield loci are assumed to be radial lines of constant stress ratio. The model has the same shape of yield locus as the Mohr-Coulomb failure

criterion. The highest yield locus, or yield locus with the highest stress ratio corresponds with the Mohr-Coulomb failure envelope. A Mohr-Coulomb failure state is assumed to determine the ultimate strength of this model, and described by a friction angle at failure.

From a microstructural point of view, any plane can be mobilized to consider plastic strains in two-dimensions. Figure 3.6(a) shows an initial stress condition or  $K_0$  condition imposed on simple shear tests. Figure 3.6(b) shows two mobilized planes considered in the proposed model before applying any shear stress on a horizontal plane.

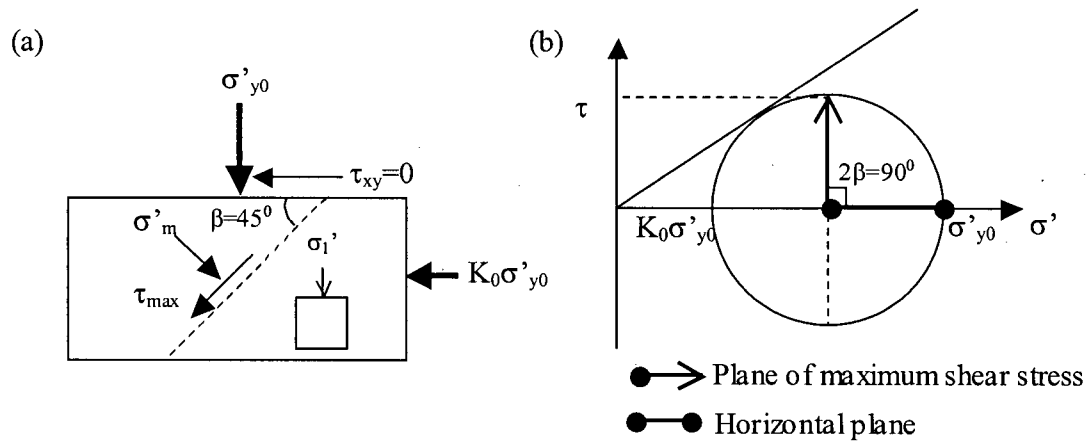


**Figure 3.6** Initial stress condition imposed on  $K_0$ -consolidated simple shear test specimen and two mobilized planes.

In the proposed model, yielding occurs if the stress ratio on either the plane of maximum shear stress or the horizontal plane increases. For unloading, yielding is assumed to be controlled by the horizontal plane only. Yield conditions for both planes,  $f_i$ , are specified in the same way in the proposed model as follows:

$$f_i = t_i - s' \sin \phi_{mi} \quad i = 1, 2 \quad [3-7]$$

where  $i$  indicates either the plane of maximum shear stress ( $i = 1$ ) or the horizontal plane ( $i = 2$ );  $t_i$  is a shear stress acting on each mobilized plane;  $s'$  is a stress parameter for plane strain

( $= (\sigma'_1 + \sigma'_3)/2$  or  $(\sigma'_x + \sigma'_y)/2$  which are the same); and  $\phi_{mi}$  is a friction angle mobilized on each plane. The stresses acting on the plane of maximum shear stress are first tested for the yielding condition.

### (i) Yield function mobilized on the plane of maximum shear stress

Initial stress states can be calculated from elastic or any stress-strain model, and they are assumed to be known. If stress conditions change due to applied loading, new principal stresses are derived and tested for yielding on the plane of maximum shear stress. If no yielding occurs, there is no stress correction, whereas if it yields, plastic strain increments must be determined.

Plastic strains are controlled by the yield loci, which are assumed to be radial lines of constant stress ratio starting at the origin of stress space as shown in Figure 3.7. From Eq. [3-7], yield loci mobilized on the plane of maximum shear stress,  $f_1$ , are expressed by

$$f_1 = t_1 - s' \sin \phi_{m1} \quad [3-8]$$

where  $t_1$  is the shear stress on the plane of maximum shear stress ( $= (\sigma'_1 - \sigma'_3)/2$ );

$s' = (\sigma'_1 + \sigma'_3)/2$ ; and  $\phi_{m1}$  is the friction angle mobilized on the plane of maximum shear stress. Yielding occurs due to the increase in stress ratio  $\eta_1$ , which is the ratio of maximum shear stress,  $t_1$ , to stress parameter,  $s'$  and equal to  $\sin \phi_{m1}$ . The stress ratio  $\eta_1$  is expressed by

$$\eta_1 = \frac{t_1}{s'} = \sin \phi_{m1} \quad [3-9]$$

From Eq. [3-9], it is indicated that yielding (i.e., stress ratio increase) could be caused not only by a shear stress increase, but also by reducing the stress parameter  $s'$  (i.e., mean stress).

### (ii) Yield function mobilized on the horizontal plane

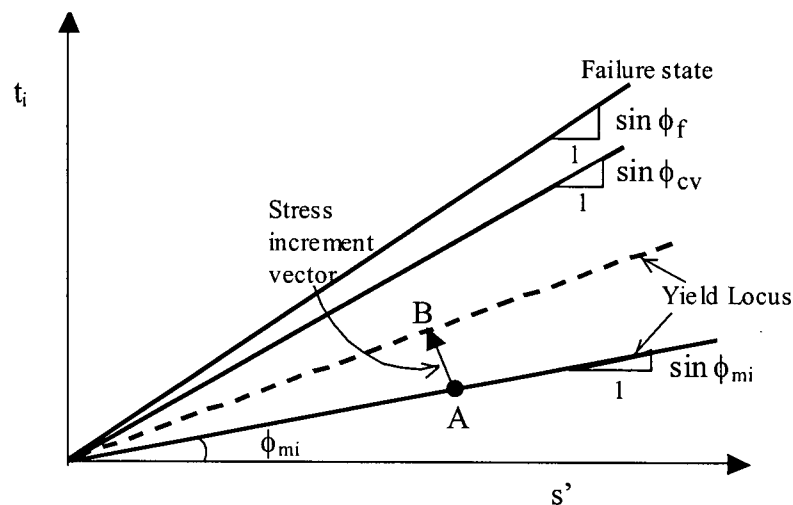
Once the plane of maximum shear stress is tested for yielding, new general  $x, y$  stresses are now used to check yielding on the second (horizontal plane). Yield loci associated with the horizontal plane,  $f_2$ , have the same shape as for the plane of maximum shear stress as shown in Figure 3.7. In this case, shear stress on the horizontal plane is  $\tau_{xy}$  rather than  $(\sigma'_1 - \sigma'_3)/2$ .

Therefore, the yield function acting on the horizontal plane,  $f_2$ , can be expressed by

$$f_2 = t_2 - s' \sin \phi_{m2} \quad [3-10]$$

where  $t_2$  is the shear stress acting on the horizontal plane ( $= \tau_{xy}$ );  $s' = (\sigma'_x + \sigma'_y)/2$ ; and  $\phi_{m2}$  is the friction angle mobilized on the horizontal plane. In this mobilized plane, a stress ratio  $\eta_2$  is defined as  $t_2/s' (= \sin \phi_{m2})$  and an increase in  $\eta_2$  causes yielding.

Yield functions on both planes have been specified. Their hardening rule is described next.



Note: subscript 'i' is 1 for the plane of maximum shear stress, and 2 for the horizontal plane.

**Figure 3.7** Yield locus and failure state.

### 3.4.2 Hardening Rule

Yield locus separates elastic and plastic zones. A hardening rule basically allows continuous plastic deformation or yielding below the failure envelope and determines the amount of the plastic strain increments. Plastic shear strain is the hardener in this model, and its increment is assumed to be caused by an increase in stress ratio  $d\eta_i$  as shown in Figure 3.8. In this study, the plastic shear modulus relates the shear stress and the plastic shear strain, and is assumed to be hyperbolic with stress ratio as shown in Figure 3.8.

Hyperbolic formulations have been widely used for non-linear elasticity by many researchers such as Kondner (1963), Duncan and Chang (1970). Puebla et al. (1997) and Puebla (1999) modified Duncan and Chang's formulation for shear-induced hardening as follows: (a) only the plastic component of shear strain is assumed to follow a hyperbolic shape, and (b) the plastic shear strain is controlled by the stress ratio rather than the shear stress only. It is shown in Figure 3.8 and expressed as Eq. [3-11a]:

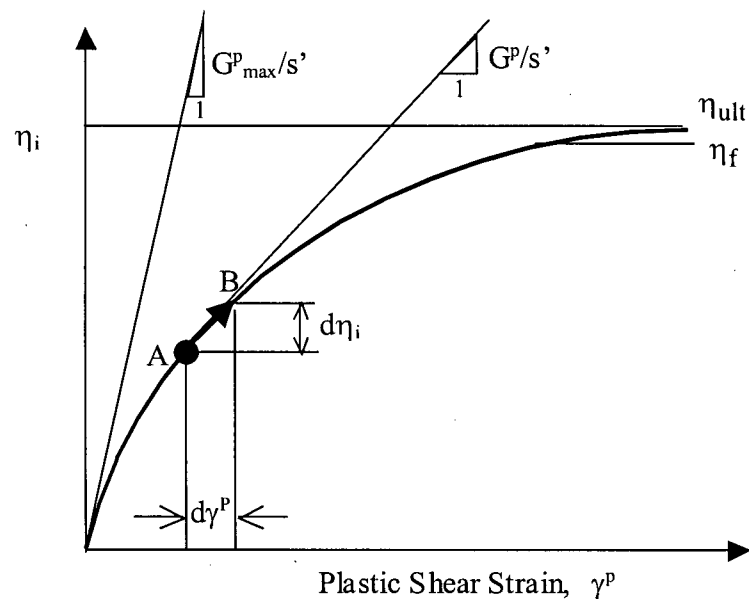
$$\eta_i = \frac{\gamma^p}{\left(\frac{s'}{G_{\max}^p}\right) + \left(\frac{\gamma^p}{\eta_{\text{ult}}}\right)} \quad [3-11a]$$

where  $\eta_i$  is a stress ratio ( $= t_1/s'$  or  $t_2/s'$ );  $\gamma^p$  is a plastic shear strain;  $G_{\max}^p$  is a maximum plastic shear modulus or plastic modulus at low stress ratio level; and  $\eta_{\text{ult}}$  is the stress ratio at the ultimate condition.

Equation [3-11a] can be written in incremental form as follows:

$$d\gamma^p = \frac{1}{G^p / s'} \cdot d\eta_i \quad [3-11b]$$

where  $d\gamma^p$  is a plastic shear strain increment;  $G^p$  is a plastic shear modulus;  $d\eta_i$  is a stress ratio increment ( $= dt_1/s'$  or  $dt_2/s'$ ). The plastic strain increments required for calculating stress increments are controlled by a normalized plastic shear modulus ( $= G^p/s'$ ) in this model.



Note: subscript 'i' is 1 for the plane of maximum shear stress, and 2 for the horizontal plane.

**Figure 3.8** Hyperbolic stress-strain hardening relationship.

### (i) Hardening rule for loading on the plane of maximum shear stress

For first time shear loading, the yield locus is controlled by the current stress state, point *A* in Figure 3.7. As the shear stress increases, the stress ratio  $\eta_1 (= t_1/s')$  imposed on the plane of maximum shear stress increases and causes the stress point to move to point *B*. The yield locus is dragged to the new location passing through point *B* and the origin. This results in plastic strain increments, both shear and volumetric. This plastic shear strain increment occurring on the plane of maximum shear stress,  $d\gamma^p_1$ , is related to the change in shear stress ratio,  $d\eta_1$ , as shown in Figure 3.8 and can be expressed as

$$d\gamma^{p_1} = 1 / (G^{p_1} / s') \cdot d\eta_1 \quad [3-12]$$

where  $G^{p_1}$  is the plastic shear modulus on the plane of maximum shear stress and given by

$$G^{p_1} = G_{\max}^p \cdot \left( 1 - \frac{\eta_1}{\eta_f} \cdot R_f \right)^2 \quad [3-13]$$

where  $\eta_f$  is the stress ratio at failure and equals  $\sin \phi_f$  where  $\phi_f$  is the peak friction angle; and

$R_f$  is the failure ratio ( $= \eta_f / \eta_{ult}$ ) used to truncate the hyperbolic relationship. A maximum

plastic shear modulus  $G_{\max}^p$  is given by the following form:

$$G_{\max}^p = k_G^p \cdot P_a \cdot \left( \frac{\sigma'_m}{P_a} \right)^{np} \quad [3-14]$$

where  $k_G^p$  is a plastic shear modulus number, which is dimensionless and depends on soil

density,  $np$  is a plastic exponent ( $= 0.4 \sim 0.5$ ). Based on modeling Nevada sand at various

densities it has been found that  $k_G^p$  is related to  $k_G^e$  by  $k_G^p \approx 4.2 \cdot (D_r)^4 \cdot k_G^e + 100$  ( $D_r$  is a

fraction) (Byrne et al., 2004a).

For loading on the plane of maximum shear stress, the position of the yield locus,  $\sin \phi_{m1}$ ,

is initially specified for each element. When yield occurs due to stress ratio increase, plastic

strain is predicted and the yield locus for that element is pushed up by an amount  $d(\sin \phi_{m1})$  as

given by Eq. [3-15]:

$$d(\sin \phi_{m1}) = \left[ \frac{G^{p_1}}{s'} \right] \cdot d\gamma^{p_1} \quad [3-15]$$

The new yield locus  $(\sin \phi_{m1})_{\text{new}}$  is specified by

$$(\sin \phi_{m1})_{\text{new}} = (\sin \phi_{m1})_{\text{old}} + d(\sin \phi_{m1}) \quad [3-16]$$

### (ii) Hardening rule for loading on the horizontal plane

The hardening rule for loading on the horizontal plane is similar to the one on the plane of maximum shear stress. The hardening rule is expressed in terms of the plastic shear strain increment occurring on the horizontal plane,  $d\gamma^{p_2}$ ,

$$d\gamma^{p_2} = 1 / (G^{p_2} / s') \cdot d\eta_2 \quad [3-17]$$

The only difference is the developed stress ratio,  $\eta_2$ , and plastic shear modulus,  $G^{p_2}$ . The plastic shear modulus on the horizontal plane,  $G^{p_2}$ , is given by

$$G^{p_2} = G_{\max}^p \cdot \left( 1 - \frac{\eta_2}{\eta_f} \cdot R_f \right)^2 \quad [3-18]$$

where  $\eta_2$  is a stress ratio on the horizontal plane ( $= \tau_{xy}/s'$ ). A plastic anisotropy indicates that plastic properties on the horizontal plane may be different to those on the plane of maximum shear stress.

### (iii) Hardening rule for unloading on the horizontal plane

Unlike the plane of maximum shear stress, the horizontal plane works for both loading and unloading. The plastic deformations during unloading are described here. Upon unloading, the plastic deformation is controlled by the stress condition imposed on the horizontal plane using an incremental formulation of a yield function (i.e., Eq. [3-10]) and expressed in Eq. [3-19]. The initial yield locus is set at the stress reversal point *C* in Figure 3.9 and unloading is predicted based on Eq. [3-19] until the shear stress changes sign, or reversal occurs. During unloading and reloading, the plastic shear modulus,  $G^{p_2}$ , is based on modified shear stress  $\tau_{xy}^*$  (i.e.,

$\tau_{xy}^* = \tau_r - \tau_{xy}$  for unloading and  $\tau_{xy}^* = \tau_r + \tau_{xy}$  for reloading, where  $\tau_r$  is a shear stress at stress reversal point C) and modified shear stress at failure  $\tau_f^*$  (i.e.,  $\tau_f^* = \tau_r + \tau_f$ , where  $\tau_f$  is the shear stress at failure). It is given by Eq. [3-20] and illustrated in Figure 3.9. Reloading then occurs with a stiffened modulus.

$$df_2 = dt_2 - ds' \cdot \sin \phi_{m2} - G^{p2} \cdot d\gamma^{p2} = 0 \quad [3-19]$$

$$G^{p2} = G_{\max}^p \cdot \left(1 - \frac{\eta_2^*}{\eta_f^*} R_f\right)^2 = G_{\max}^p \cdot \left(1 - \frac{\tau_{xy}^*}{\tau_f^*} R_f\right)^2 \quad [3-20]$$

where  $\eta_2^*$  and  $\eta_f^*$  are modified stress ratios based on modified shear stresses  $\tau_{xy}^*$  and  $\tau_f^*$  as shown in Figure 3.9, and  $\eta_2^* / \eta_f^*$  in Eq. [3-20] is equal to  $\tau_{xy}^* / \tau_f^*$ .

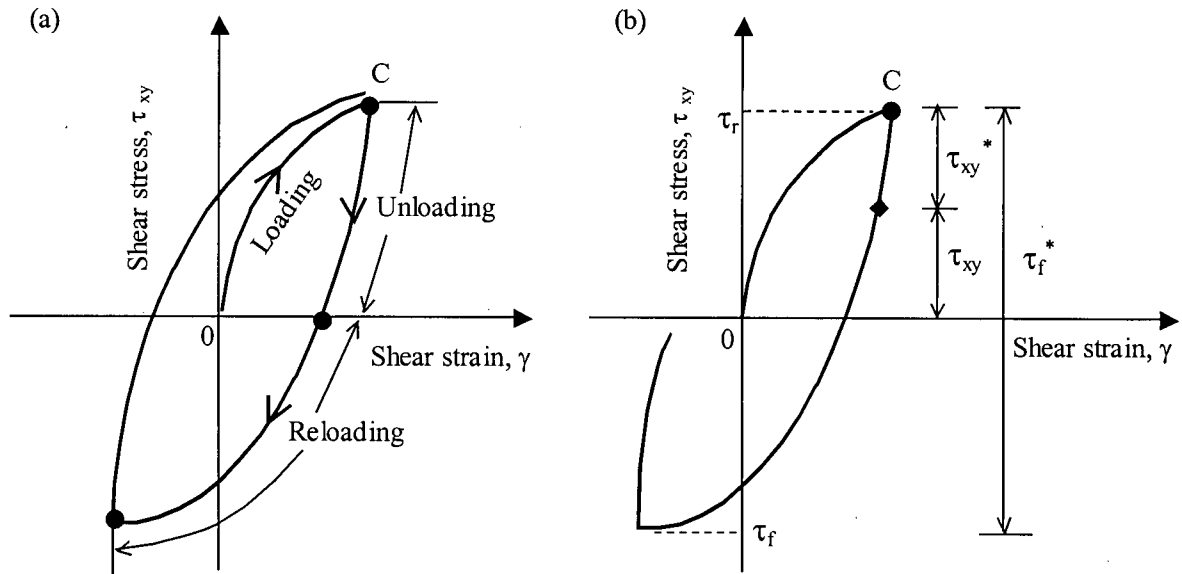


Figure 3.9 Stress-strain cycle: (a) definition of loading, unloading and reloading, and (b) modified shear stresses.

#### (iv) One-sided loading

Soil elements near a slope, under an embankment, or beneath footings may experience one-sided loading during cyclic loading or earthquakes. Consequently, a change in the sign of the shear stress may not occur. One-sided loading is here defined as a cyclic loading where the cyclic shear stress does not change its sign. For one-sided loading, the stress-strain behaviour of soils is controlled by the horizontal plane unless the stress ratio on the plane of maximum shear stress is greater than the one retained previously. This loading condition is illustrated in Figure 3.5 and corresponds to Case 3 and Case 4.

The schematic behaviour of one-sided loading is shown in Figure 3.10. For sloping ground conditions under dynamic loading, this kind of stress-strain response may be expected and is important to simulate. To do so requires that  $\tau_{xy}^*$  and  $\tau_f^*$  be differently defined as  $\tau_{xy}^* = \tau_{xy} - \tau_0$  and  $\tau_f^* = \tau_f - \tau_0$ , where  $\tau_0$  is a shear stress at the beginning of the one-sided loading as depicted in Figure 3.10.  $G^p_2$  for the horizontal plane is then determined from Eq. [3-20] where  $\eta_2^* / \eta_f^*$  is equal to  $\tau_{xy}^* / \tau_f^*$ .

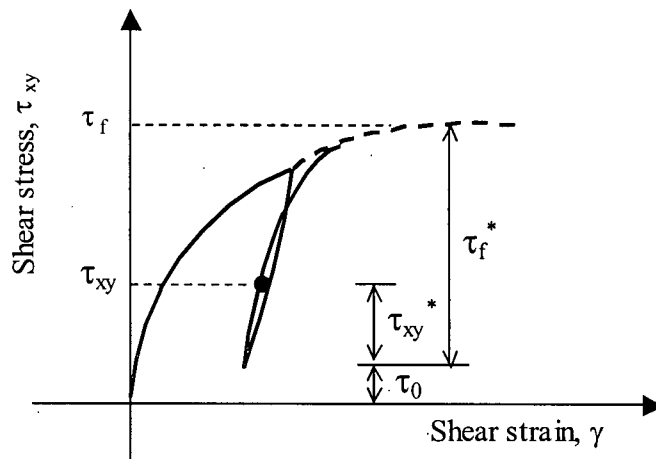
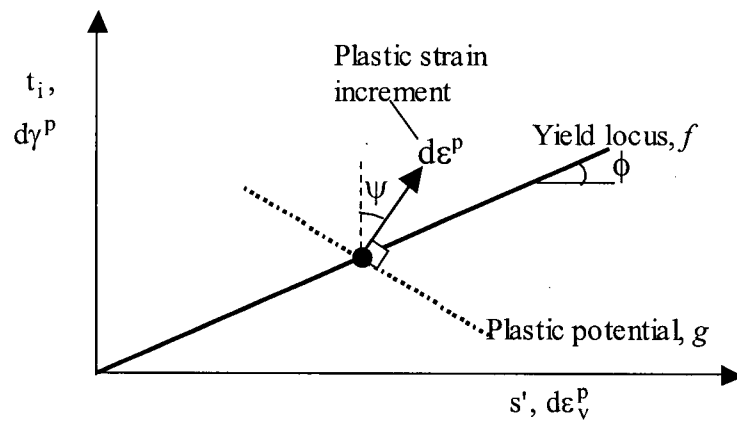


Figure 3.10 One-sided loading stress-strain curve.

### 3.4.3 Flow Rule

The flow rule gives the direction or relative magnitude of a plastic shear strain increment,  $d\gamma^p$ , and a plastic volumetric strain increment,  $d\varepsilon_v^p$ . It is referred to as “dilatancy” and related through the dilation angle  $\psi$  in Eq. [3-21] and illustrated in Figure 3.11.

$$\sin \psi = \frac{d\varepsilon_v^p}{|d\gamma^p|} \quad [3-21]$$



Note: subscript 'i' is 1 for the plane of maximum shear stress, and 2 for the horizontal plane.

**Figure 3.11** Non-associated flow rule and dilation angle.

#### (i) Flow rule on the plane of maximum shear stress

The flow rule for granular soils in plasticity can be expressed by the dilatancy. Similarly, in this study the associated increment of plastic volumetric strain,  $d\varepsilon_v^p$ , is related to the increment of plastic shear strain,  $d\gamma^p$ , through the flow rule as follows:

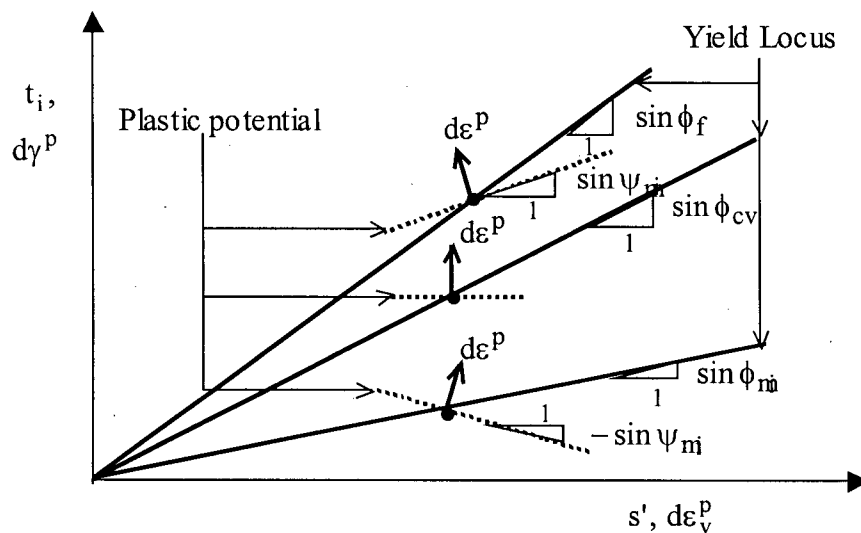
$$\frac{d\varepsilon_v^p}{|d\gamma^p|} = \frac{\sin \phi_{cv} - t_1 / s'}{1 - \sin \phi_{cv} \cdot (t_1 / s')} = \sin \psi_{m1} \quad [3-22]$$

where  $\phi_{cv}$  is the friction angle at constant volume. This is the flow rule for the plane of maximum shear stress, and works for loading and reloading, not for unloading. It can be derived from energy considerations and corresponds to the stress-dilatancy theory for the plane strain condition proposed by Rowe (1972).

The plastic potential for the plane of maximum shear stress,  $g_1$ , is given by

$$g_1 = t_1 - s' \cdot \sin \psi_{m1} \quad [3-23]$$

This conforms to a non-associated flow rule. The yield loci and direction of the plastic strains resulting from the flow rule are shown in Figure 3.12. It may be seen that at low stress ratios, significant shear induced plastic compaction is occurring, while no compaction is predicted at stress ratios corresponding to  $\phi_{cv}$ . For stress ratios greater than  $\phi_{cv}$ , shear induced plastic expansion or dilation is predicted. This simple flow rule is in close agreement with the characteristic behaviour of sand observed in laboratory element testing.



Note: subscript 'i' is 1 for the plane of maximum shear stress, and 2 for the horizontal plane.

**Figure 3.12** Plastic potential function and direction of plastic strain increments.

**(ii) Flow rule on the horizontal plane and phasing-out function**

The plastic potential acting on the horizontal plane,  $g_2$ , can be expressed as

$$g_2 = t_2 - s' \cdot \sin \psi_{m2} \quad [3-24]$$

$$\text{where } \sin \psi_{m2} = \frac{\sin \phi_{cv} - t_2 / s'}{1 - \sin \phi_{cv} \cdot (t_2 / s')} = D_{t2}.$$

Plastic strain increments on the horizontal plane are obtained as follows:

$$\left( d\bar{\epsilon}^p \right)_2 = \lambda_2^* \cdot \frac{\partial g_2}{\partial \sigma} \quad [3-25]$$

Since  $\frac{\partial g_2}{\partial \sigma_x} = -0.5D_{t2}$ ,  $\frac{\partial g_2}{\partial \sigma_y} = -0.5D_{t2}$ , and  $\frac{\partial g_2}{\partial \tau_{xy}} = 1$ ; Eq. [3-25] becomes

$$\left( d\bar{\epsilon}_x^p \right)_2 = \lambda_2^* \cdot \frac{\partial g_2}{\partial \sigma_x} = -0.5D_{t2} \cdot \lambda_2^* \quad [3-26a]$$

$$\left( d\bar{\epsilon}_y^p \right)_2 = \lambda_2^* \cdot \frac{\partial g_2}{\partial \sigma_y} = -0.5D_{t2} \cdot \lambda_2^* \quad [3-26b]$$

$$\left( d\bar{\gamma}^p \right)_2 = \lambda_2^* \cdot \frac{\partial g_2}{\partial \tau_{xy}} = \lambda_2^* \quad [3-26c]$$

where  $\lambda_2^*$  is an adjusted  $\lambda_2$ .  $\lambda_2$  is a plastic multiplier on the horizontal plane and is obtained from the consistency condition ( $df_2 = 0$ ). The detailed derivation for  $\lambda_2$  is presented in

Appendix A.

The plastic strain increments generated from the horizontal plane are phased-out as the principal stresses rotate. Therefore,  $\lambda_2$  is adjusted to  $\lambda_2^*$  as a function of  $\cos 2\alpha_\sigma$  by Eq. [3-27], where  $\alpha_\sigma$  is the angle between the direction of major principal stress and the vertical as illustrated in Figure 3.1.

$$\lambda_2^* = \lambda_2 \cdot (\cos 2\alpha_\sigma)^\chi, \text{ where } 0 \leq (\cos 2\alpha_\sigma)^\chi \leq 1.0 \quad [3-27]$$

where  $\chi$  is an adjustment parameter which controls the phasing out pattern. When  $\alpha_\sigma$  is  $0^\circ$  (e.g.,  $K = K_0$ ),  $\lambda_2^* = \lambda_2$  which corresponds to Figure 3.13(a). When  $\alpha_\sigma$  is  $45^\circ$ ,  $\lambda_2^* = 0$  which corresponds to Figure 3.13(b). Therefore,  $\lambda_2^*$  is generally between 0 and  $\lambda_2$ .

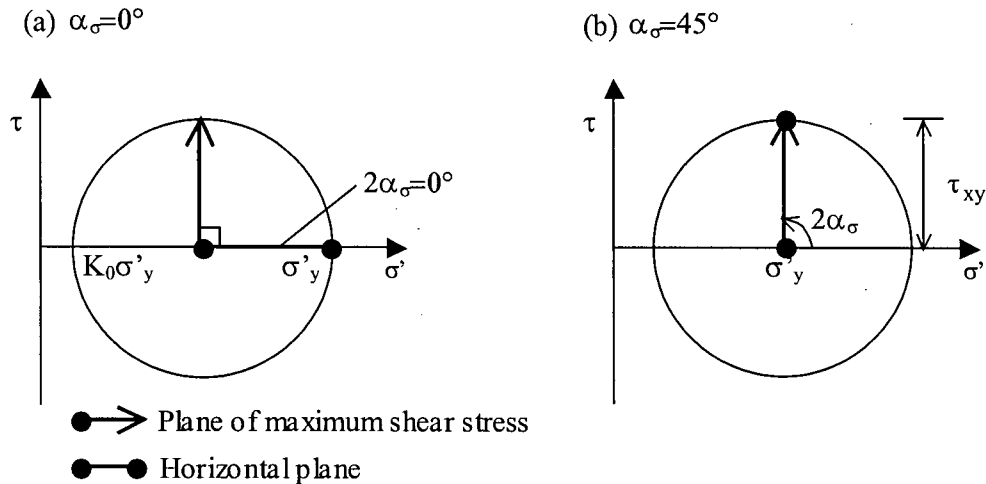


**Figure 3.13** Two extreme cases of principal stress rotation.

The effect of  $\chi$  on phasing-out pattern versus angle  $2\alpha_\sigma$  is compared in Figure 3.14. The gradual phasing-out of the plastic strain increments mobilized on the horizontal plane is a key aspect of the Two Mobilized-plane model. It was found that  $\chi = 0.1$  gave the best overall agreement with experimental data. In terms of the amount of plastic strain increment (i.e.,  $(d\bar{\epsilon}^p)_2$ ), the maximum contribution is when shearing starts under a  $K_0$  state as illustrated in Figure 3.13(a). It gradually decreases as the plane of maximum shear stress rotates. After the plane of maximum shear stress becomes horizontal (no more principal stress rotation), the contribution from this horizontal plane becomes zero as illustrated in Figure 3.13(b).

For  $K_0$ -consolidated soils at small strain level,  $\cos 2\alpha_\sigma$  is almost 1.0 as shown in Figure 3.15(a) and therefore a horizontal plane contributes fully, i.e.  $\lambda_2^* = \lambda_2$ . At large strain level,  $\cos 2\alpha_\sigma$  is close to 0.0 as shown in Figure 3.15(b) and a horizontal plane phases out (i.e.  $\lambda_2^* = 0$ ).

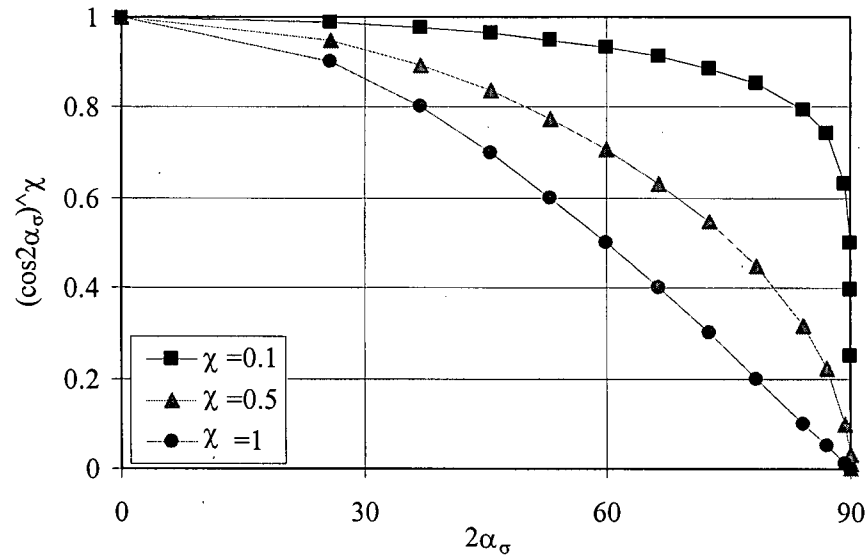


Figure 3.14 Effect of a parameter  $\chi$  on phasing-out pattern.

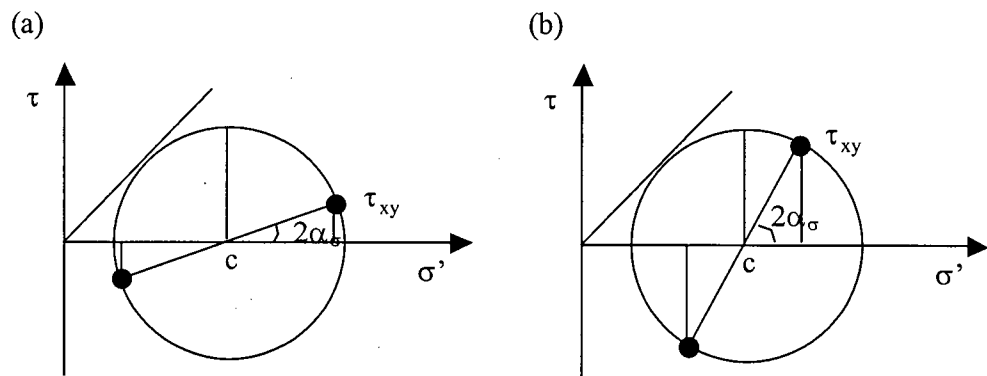


Figure 3.15 Principal stress rotation angle  $\alpha_\sigma$ : (a) small strain, and (b) large strain level.

The plastic volumetric strain increment is obtained from Eqs. [3-28] and [3-29] through dilation angle,  $\sin \psi_{m2}$ . Eq. [3-28] is for loading and Eq. [3-29] is for unloading as illustrated in

Figure 3.16. These equations are based on stress-dilatancy theory as well as the results of drained cyclic simple shear tests as shown in Figure 2.16(a), Lee (1991). Lee's results showed that the dilation angle depended on the stress ratio,  $\eta_i$ , and whether loading or unloading occurred, but was not influenced by the initial density, or normal stress. Lee found less agreement in the stress-dilatancy equation based on the first cycle from cycle to cycle. This topic will be further discussed in next Section 3.4.4.

$$\frac{d\varepsilon_v^p}{|d\gamma^p|} = \frac{\sin \phi_{cv} - t_2 / s'}{1 - \sin \phi_{cv} \cdot (t_2 / s')} = (\sin \psi_{m2})_{L \text{ (Loading)}} \quad [3-28]$$

$$\frac{d\varepsilon_v^p}{|d\gamma^p|} = \frac{\sin \phi_{cv} + t_2 / s'}{1 - \sin \phi_{cv} \cdot (t_2 / s')} = (\sin \psi_{m2})_{U \text{ (Unloading)}} \quad [3-29]$$

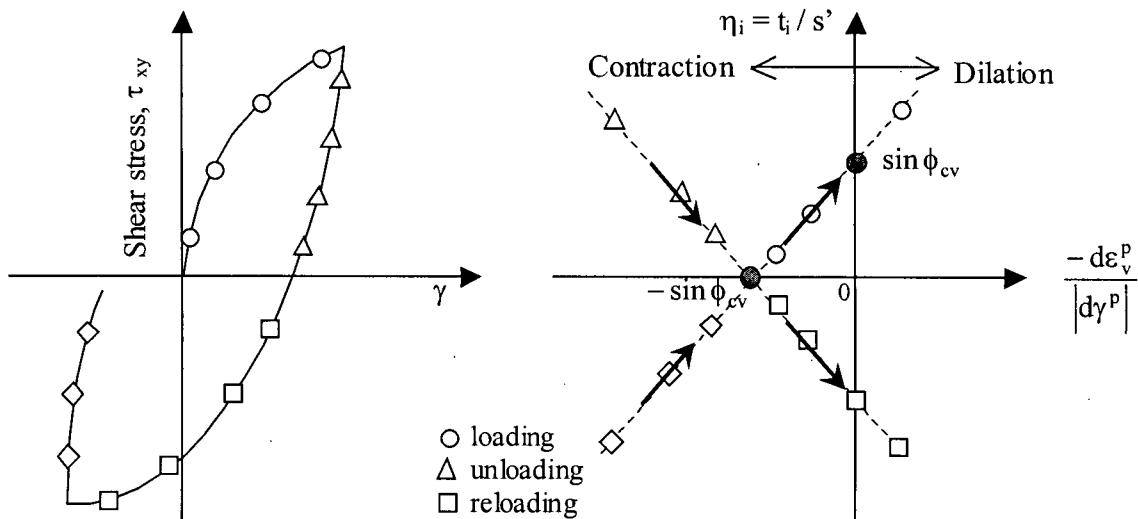


**Figure 3.16** Stress-dilatancy equation during one cycle of stress-strain curve (modified from Lee, 1991).

Plastic shear and volumetric strain increments are computed for both the plane of maximum shear stress and the horizontal plane. Upon loading both planes are considered to calculate plastic strain increments, but upon unloading the horizontal plane only is considered.

Plastic strain increments resulting from principal stress rotation are essentially accounted for by the contribution from the horizontal plane.

### (iii) Contraction limit on flow rule

Upon loading it is noted that at a low stress ratio ( $t_i/s'$ ), the relationships in Eqs. [3-22] and [3-28] seem to give too much volume compaction for loose sand, when compared with observed sand behaviour (e.g., Fraser River sand under simple shear loading). Been and Jefferies (2004) used a central-difference approach to define the ratio of strain increments at a stress, and then eliminated elastic strain components to describe a stress-dilatancy in terms of plastic strain increments. Similarly, from the drained simple shear test on Fraser River sand, the plastic strain increment ratio ( $-d\varepsilon_v^p/d\gamma^p$ ) at scan  $j$  has been derived as follows:

$$\left( \frac{d\varepsilon_v^p}{d\gamma^p} \right)_j = \frac{(\varepsilon_{v,j+1} - \varepsilon_{v,j-1}) - (\sigma'_{m,j+1} - \sigma'_{m,j-1})/B}{(\gamma_{j+1} - \gamma_{j-1}) - (\tau_{xy,j+1} - \tau_{xy,j-1})/G} \quad [3-30]$$

The elastic shear modulus ( $G$ ) and bulk modulus ( $B$ ) in Eq. [3-30] were assumed constant for simplicity although they change.  $G$  and  $B$  were assumed  $G = 59100$  kPa and  $B = 0.7 \cdot G = 41370$  kPa, respectively, where  $G$  is calculated from Eq. [3-2] with  $k_G^c = 591$  and  $\sigma'_m = 100$  kPa. The stress parameter  $s'$  in the definition of stress ratio ( $\tau_{xy}/s'$ ) is obtained from measured  $\sigma'_y$  and assumed  $\sigma'_x$  (calculated from UBCSAND2). Therefore, the measured stress-dilatancy in terms of stress ratio ( $\tau_{xy}/s'$ ) and plastic strain increment ratio ( $-d\varepsilon_v^p/d\gamma^p$ ) is presented in Figure 3.17, which shows some scatter at low stress ratio (e.g.,  $\tau_{xy}/s' < 0.3$ ). The trend line may be drawn with a certain contraction limit rather than the dashed line at the low stress ratio in Figure 3.17. This has been taken into account in the previous UBCSAND model.

Such a contraction limit in simple shear tests may be seen from other simple shear data on Ottawa sand (Figure 2.11). Based on triaxial data, Been and Jefferies (2004) also pointed out that the stress-dilatancy relationship deviated from its linear trend at low stress ratio (e.g., dashed line in Figure 3.17) owing to no initial plastic strains. They mentioned that the initial nonlinear part or deviation from the trend line can be attributed to initial fabric effects and overconsolidation.

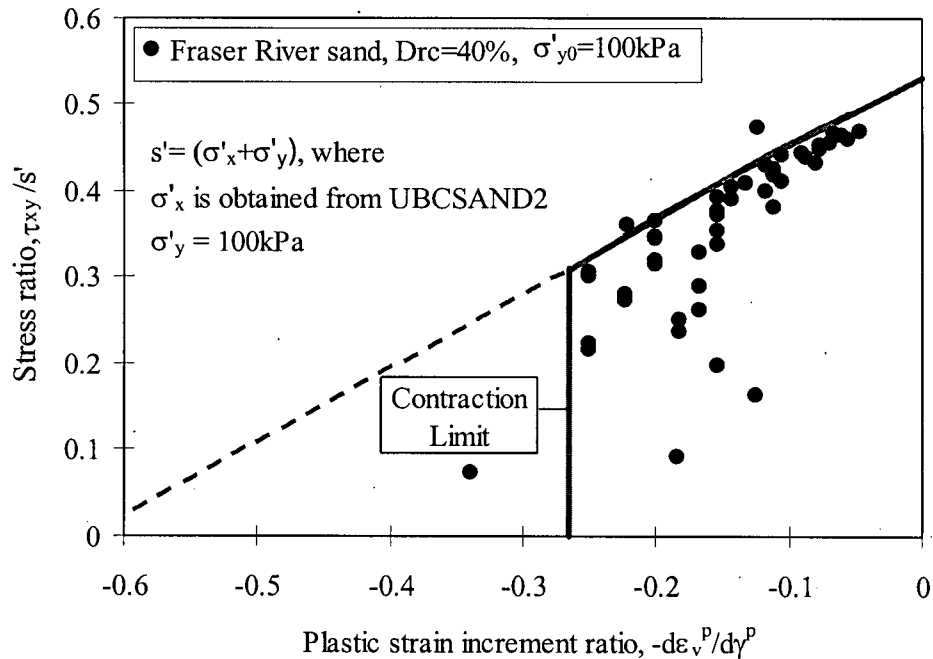


**Figure 3.17** Measured stress-dilatancy relationship and proposed flow rule with a contraction limit (basic data obtained from Sriskandakumar, 2004).

In order to match the observed volume change from drained simple shear tests, this model sets the contraction limit as a  $0.5(\sin \phi_{cv})$  based on previous UBCSAND calibration, i.e.,

$$\begin{aligned} \sin \psi_{m1} &\leq 0.5 \sin \phi_{cv} \\ (\sin \psi_{m2})_L &\leq 0.5 \sin \phi_{cv} \end{aligned} \quad [3-31]$$

This proposed flow rule with a contraction limit,  $0.5 \sin \phi_{cv}$ , where  $\phi_{cv} = 33^\circ$  as indicated by a vertical solid line in Figure 3.17, is shown in Figure 3.17. This limit applies for loading phase on both the planes.

Upon unloading, the relationship of Eq. [3-29] seems to overpredict the observed volume change. In order to match the measured volume change the flow rule during unloading has been modified from  $(\sin \psi_{m2})_U$  to  $(\sin \psi_{m2})_U^* = 0.5 \cdot (\sin \psi_{m2})_U$ . This is consistent with Lee's findings (1991) based on cyclic drained simple shear tests (see Section 2.3.2).

#### 3.4.4 Hardening of Stress-Dilatancy

Martin et al. (1975) carried out constant amplitude cyclic simple shear tests using crystal silica sand at relatively small cyclic shear strains (e.g.,  $\gamma_{cyc} = 0.1\%$ ,  $0.2\%$  and  $0.3\%$ ). Initial conditions were  $D_{rc} = 45\%$  and  $\sigma'_{y0} = 200$  kPa. As shown in Figure 3.18, the increment of shear-induced volume change decreases as the number of cycles increases. The decrease of volumetric strain increment from cycle to cycle observed from cyclic simple shear test is hereafter termed "volumetric hardening". Martin et al. (1975) proposed the incremental shear-volume coupling equation with four material constants for pore pressure calculation. As a simplified version, Byrne (1991) proposed a following relation with two constants:

$$d\varepsilon_v = C_1(\gamma) \text{EXP} \left( -C_2 \frac{\varepsilon_v}{\gamma} \right) \quad [3-32]$$

where  $d\varepsilon_v$  = the increment of volumetric strain in percent per cycle of shear strain;  $\varepsilon_v$  = the accumulated volumetric strain from previous cycles in percent;  $\gamma$  = the amplitude of shear strain

in percent for the cycle in question; and  $C_1$ ,  $C_2$ , = constants for the sand in question at the relative density under consideration.

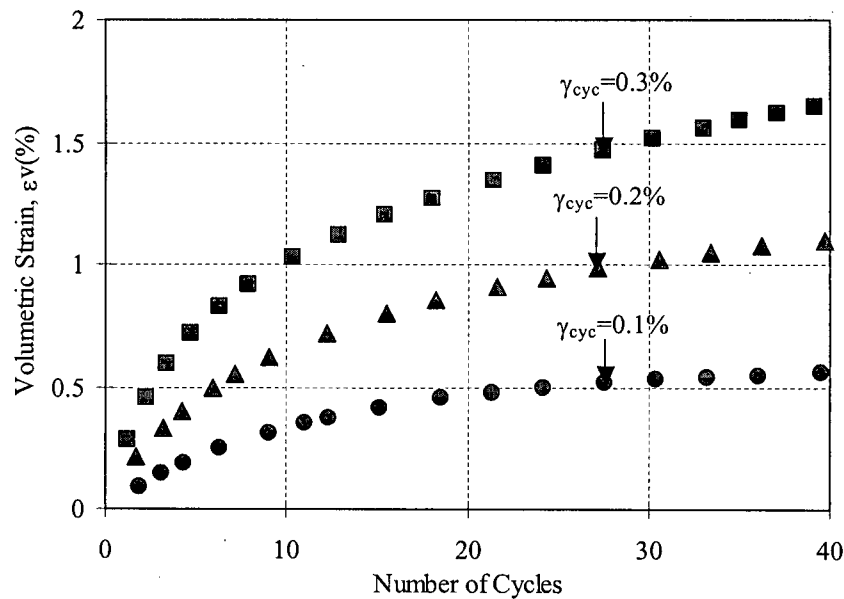


**Figure 3.18** Volumetric strains from constant amplitude cyclic simple shear tests (after Martin et al., 1975).

As observed from many cyclic drained tests of loose sands, the increment of volumetric strains decreases from cycle to cycle, regardless of shear strain levels. For cyclic loading purposes, the numerical model needs to capture the pattern of volume change (mainly volume contraction) as a function of the number of cycles. For a certain density of sand (e.g.,  $D_r = 45\%$ ) and a given shear strain (e.g.,  $\gamma_{cyc} = 0.1\%$ ), the increment of volumetric strain seems to be a function of an accumulated volumetric strain as inferred from Eq. [3-32]. Most stress-dilatancy equations are derived based on data from monotonic loading, or one full cycle of loading. Therefore, they may not consider volume change during more than one cycle. In order to account for reducing volumetric strains with number of cycles (volumetric hardening), it is

necessary to either change the stress-dilatancy equation (e.g., state-dependent dilatancy) or stiffen the plastic shear modulus.

While a sand model with state-dependent dilatancy (e.g., Li, 2002) may directly capture such observed behaviour by accounting for current void ratio, the empirical correlation derived from cyclic loading tests can be added to the stress-dilatancy equation based on a single cycle or monotonic loading.

A hardening function that emulates accumulated volume change with number of cycles is called here the cyclic hardener,  $H_c$ . Two possibilities can be considered as a hardening function: (a) a number of cycles, and (b) an accumulated volumetric strain ( $\epsilon_v$ ). The number of cycles as a hardener is much simpler to apply, but has some difficulties related to accounting for cycles from irregular or one-sided loading. This may be good enough for conventional laboratory tests with constant amplitude shear strain, but not for earthquake motions because it cannot consider the size of the shear stress cycle, and consequently gives the same hardening regardless of the size of shear stress or strain due to small or large earthquakes.

An accumulated plastic volumetric strain ( $\epsilon_v^p$ ) depending on both shear strain level and number of cycles may be more appropriate as a hardener. UBCSAND2 considers an accumulated plastic volumetric strain and shear strain as given by Eq. [3-33] that is based on Eq. [3-32].

$$\frac{d\epsilon_v^p}{|d\gamma^p|} = \sin \psi_m \cdot H_c \quad [3-33]$$

where  $H_c = \text{EXP}\left(-C_h \frac{\epsilon_v^p}{\gamma^*}\right)$ ,  $C_h$  is a cyclic hardening parameter that varies with relative density, and  $\gamma^*$  is the modified shear strain which is a difference between a current shear strain,

$\gamma$ , and a shear strain at the turning point,  $\gamma_r$ , as illustrated in Figure 3.19. It is an absolute value as  $\gamma^* = |\gamma - \gamma_r|$  and is independent of loading patterns (i.e., two-sided or one-sided loading) as shown in Figures 3.19(a) and 3.19(b). Therefore, Eq. [3-33] is more effective for actual earthquake motions. When the dilation occurs (i.e.,  $d\varepsilon_v^p < 0$ ),  $H_c$  is set to 1.0. Based on modeling sands at various densities (e.g., matching Silver & Seed's (1971) data on crystal silica sand, Sriskandakumar's (2004) data on Fraser River sand), the range of suggested cyclic hardening parameter  $C_h$  for various densities is presented in Table 3.1.

**Table 3.1** Suggested cyclic hardening parameter  $C_h$  for different densities.

State	Dr (%)	$C_h$
Loose or Medium dense	35 ~ 65	1.5-2.5
Dense	65 ~ 85	2.5-4

The variation of  $H_c$  is reproduced from UBCSAND2 output file, and illustrated in Figure 3.20 for constant shear stress amplitude tests.  $H_c = 1.0$  is the maximum value, and represents maximum plastic volume change (no hardening) and corresponds with first time loading.  $H_c \sim 0$  is a full hardening which means almost no plastic volume change. It may happen due to very small shear strain (i.e.,  $\gamma^* \sim 0.0$ ) or large accumulated volumetric strain after many loading cycles. Upon unloading,  $H_c$  is quite small due to the small modified shear strain,  $\gamma^*$ , but increases as  $\gamma^*$  increases. As volumetric strain is accumulated by cyclic loading,  $H_c$  will decrease as illustrated in Figure 3.20. The amount of hardening depends on the parameter  $C_h$  in Eq. [3-33], which varies with soil densities. As density increases (i.e.,  $C_h$  increases),  $H_c$  drops dramatically within a few cycles.

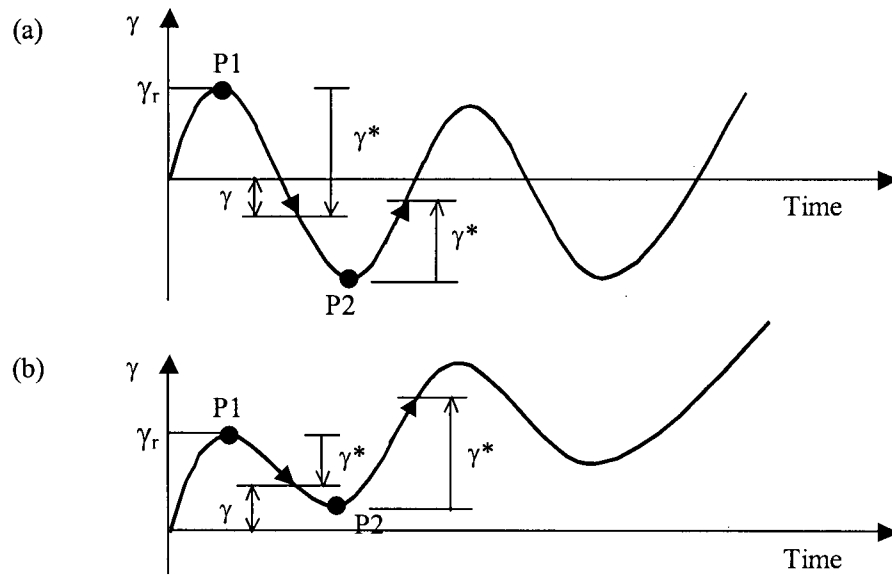


**Figure 3.19** Determination of a modified shear strain ( $\gamma^*$ ) used in plastic volume hardener: (a) two-sided loading, and (b) one-sided loading.

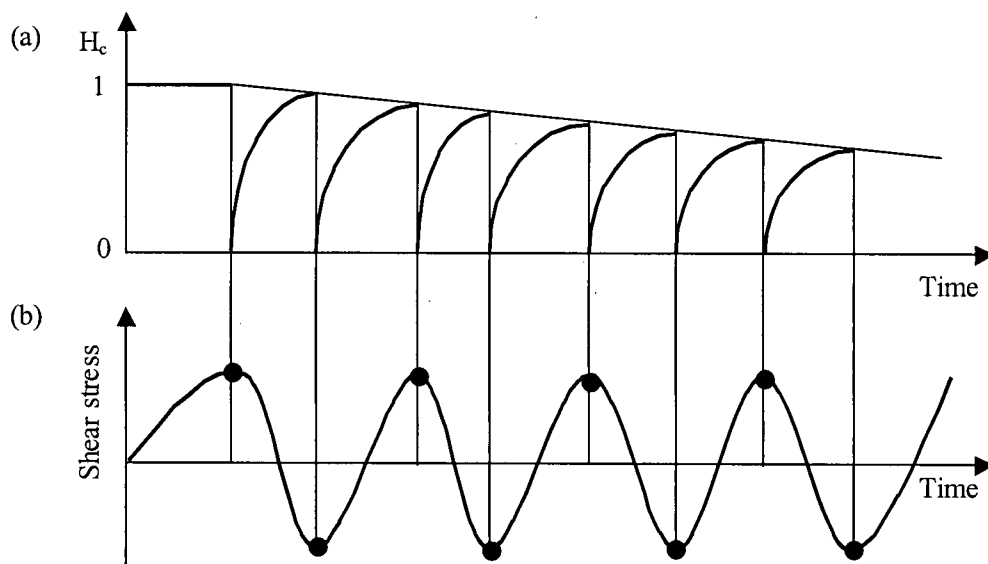


**Figure 3.20** Simulation of the hardening function  $H_c$  during cyclic loading: (a) variation pattern of  $H_c$ , and (b) shear stress cycles.

### 3.5 Predicted Characteristic Response

In this section, some characteristic performance of the proposed model is introduced and compared with measurements. All numerical simulations of a simple shear test in the following subsection are related to loose Fraser River sand with  $D_{rc} = 40\%$ , which will be discussed in the next chapter (see Table 4.3 for input parameters). Prior to this, modeling of a single element and its boundary conditions are described.

#### 3.5.1 Simulation of Simple Shear

In order to simulate simple shear tests, a single element of unit dimensions is used as shown in Figure 3.21. The bottom boundary is fixed in both  $x$  and  $y$  directions, and top boundary is fixed in  $x$  direction. The top nodes are attached to each other in order to force them to move uniformly in the horizontal direction. Numerical simulation can be achieved by applying a small nodal velocity in the  $x$  direction at the top nodes. For drained tests, the  $y$  direction of top nodes is freed to allow volume change as shown in Figure 3.21(a). For constant volume tests, the  $y$  direction of top nodes is fixed in order to prevent volume change as shown in Figure 3.21(b).

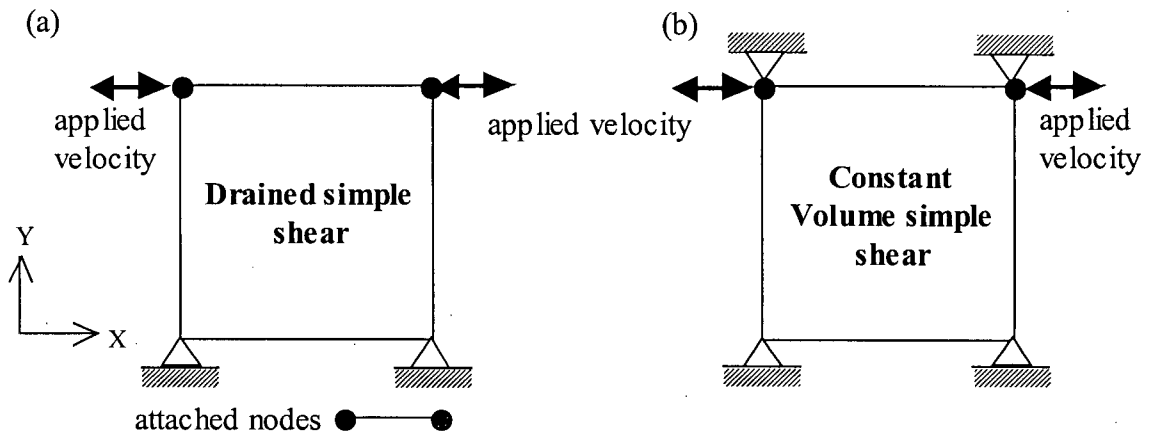


**Figure 3.21** A single element of unit dimensions: (a) drained test, and (b) constant volume test.

### 3.5.2 Lateral Stress Change

In contrast with triaxial tests, the lateral stress is generally not measured in conventional simple shear testing devices. Finn (1985) directly measured lateral stress change under cyclic loading using a Cambridge-type simple shear device. Ottawa sand with  $D_r = 45\%$  was tested under  $\sigma'_{y0} = 200$  kPa. Measured lateral stress averaged from top and bottom pressure transducers is shown in Figure 3.22. The lateral stresses measured from two attached load cells were different from each other, and might not represent the stress condition of the entire sample. Youd and Craven (1975) used an NGI-type simple shear apparatus to measure a lateral stress during cycling of shear loads. The variation of lateral stress during cycling of shear load within each cycle was not presented, but their result showed that most of the lateral stress increase occurred during the initial several cycles while  $\sigma'_y$  was held constant. Roscoe (1970) also pointed out that the lateral stress  $\sigma'_x$  reached the vertical stress values  $\sigma'_y$  at failure (i.e.,  $\sigma'_x = \sigma'_y$  at failure).

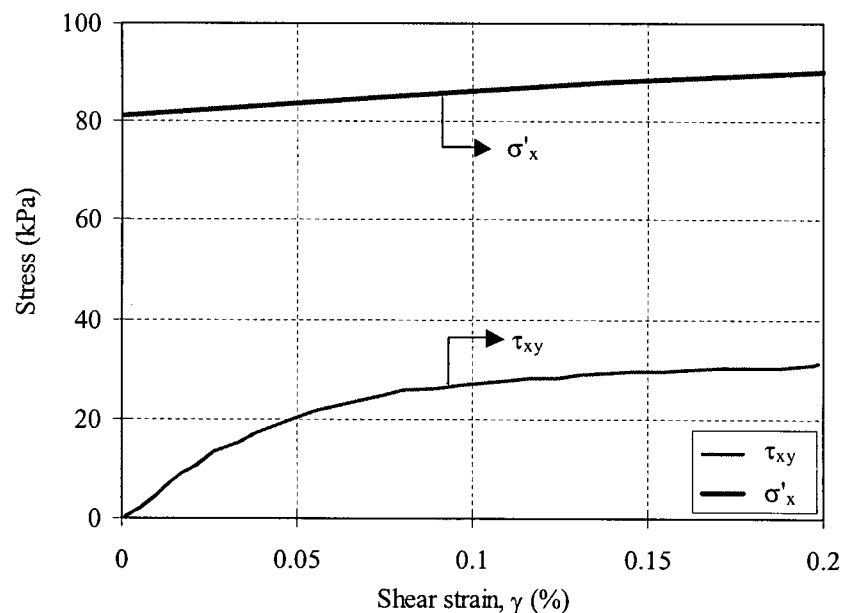


Figure 3.22 Measured lateral stress from drained simple shear test (after Finn, 1985).

The typical pattern of lateral stress is generally not measured from cyclic simple shear tests. If the material were isotropic elastic,  $\sigma'_x$  would stay constant while  $\sigma'_y$  is constant in conventional simple shear tests, and there would be no volume change.

Numerical prediction of lateral stress ( $\sigma'_x$ ) using UBCSAND2 (see Table 4.3 for input parameters) is presented in Figure 3.23. For drained simple shear tests, the vertical stress ( $\sigma'_y$ ) remains constant but the lateral stress ( $\sigma'_x$ ) is predicted to increase during shearing. This can be indirectly verified by capturing the observed volume change from monotonic loading tests. No change in lateral stress implies no volume change. This will be useful as a guideline to future work of numerical calibration using simple shear.

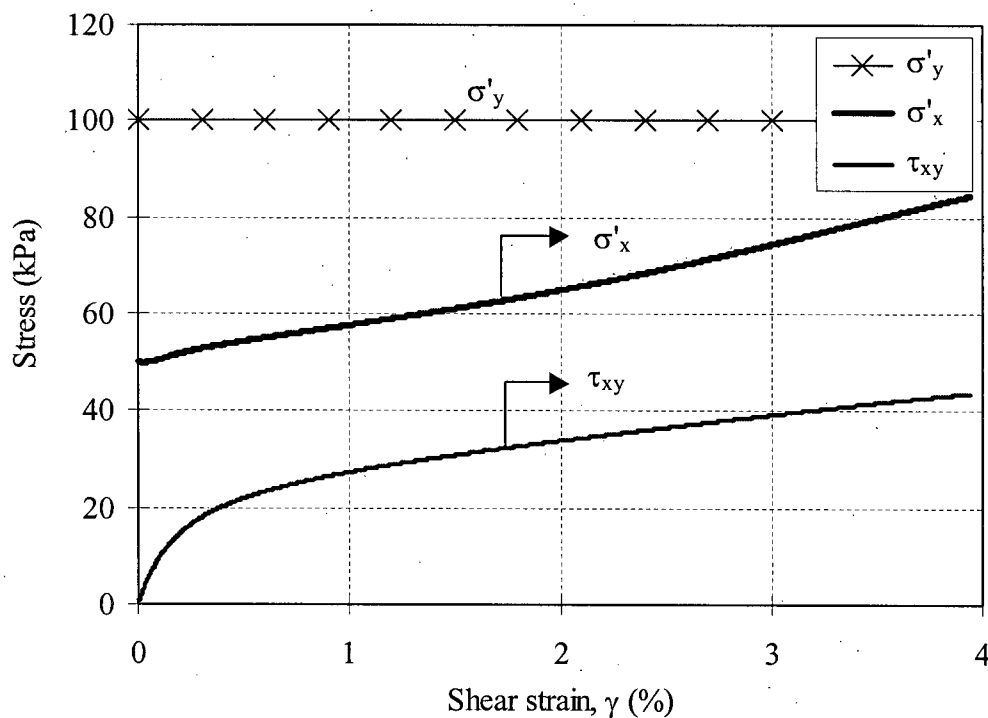
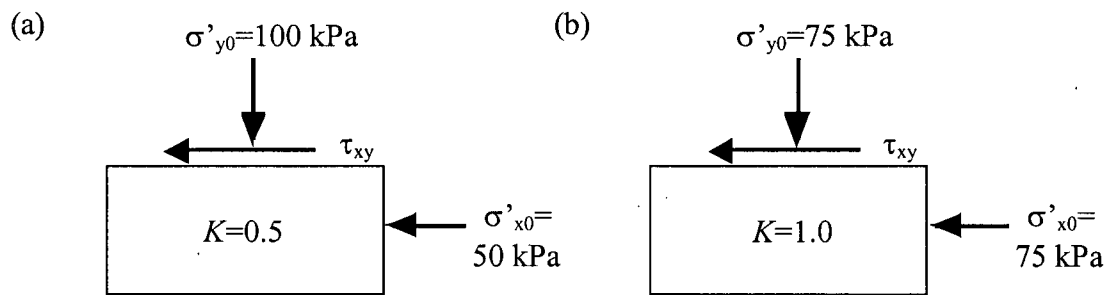


Figure 3.23 Predicted lateral stress ( $\sigma'_x$ ) of UBCSAND2 during monotonic DSS test.

### 3.5.3 Behaviour under $K = 1$ and 0.5 Initial Stress States

Experimental results showed that the skeleton behaviour of sand depends on mean stress level or confining pressure at constant relative density (Lee & Seed, 1967; Vesic & Clough, 1968; Ishihara, 1996; Wijewickreme & Vaid, 2005). For different  $K$  states having the same initial mean stress UBCSAND2 gives essentially the same stress-strain behaviour for low shear strain levels. This characteristic behaviour of the proposed model is simulated here. Two different  $K$  states, 0.5 and 1.0 are numerically simulated with the same initial mean stress 75 kPa as illustrated in Figure 3.24. For the case of  $K = 0.5$ , initial horizontal and vertical effective stresses are 50 kPa and 100 kPa, respectively. As shown in Figure 3.25, both predictions of UBCSAND2 (see Table 4.3 for input parameters) give exactly the same stress-strain relationship at small strain level, which is in agreement with test results (shown as filled circles in Figure 3.25) by Sriskandakumar (2004). Upon further shearing,  $K = 0.5$  case (thick line) gives a stiffer response because the lateral stress rises and increases the mean stress  $\sigma'_m$ . For  $K = 1$  case, the mean stress changes slightly but stays around 75 kPa for the duration of shearing.

The effect of various  $K$  states is modeled in Figure 3.26 using a single set of parameters. Three  $K$  states, 0.5, 0.7 and 1.0, are simulated (see Table 4.3 for input parameters). Initial stress conditions are shown in Figure 3.26(a). Initial vertical effective stresses are all the same at 100 kPa, but initial horizontal effective stresses vary depending on  $K$ . Numerical predictions for three  $K$  states are shown in Figure 3.26(b). UBCSAND2 predicts stiffer stress-strain behaviour as  $K$  increases, which is consistent with experimental results (Lee & Seed, 1967; Vesic & Clough, 1968; Ishihara, 1996; Wijewickreme & Vaid, 2005).



**Figure 3.24** Initial stress conditions for numerical simulation with  $K = 0.5$  and  $1.0$  with the same initial mean stress.

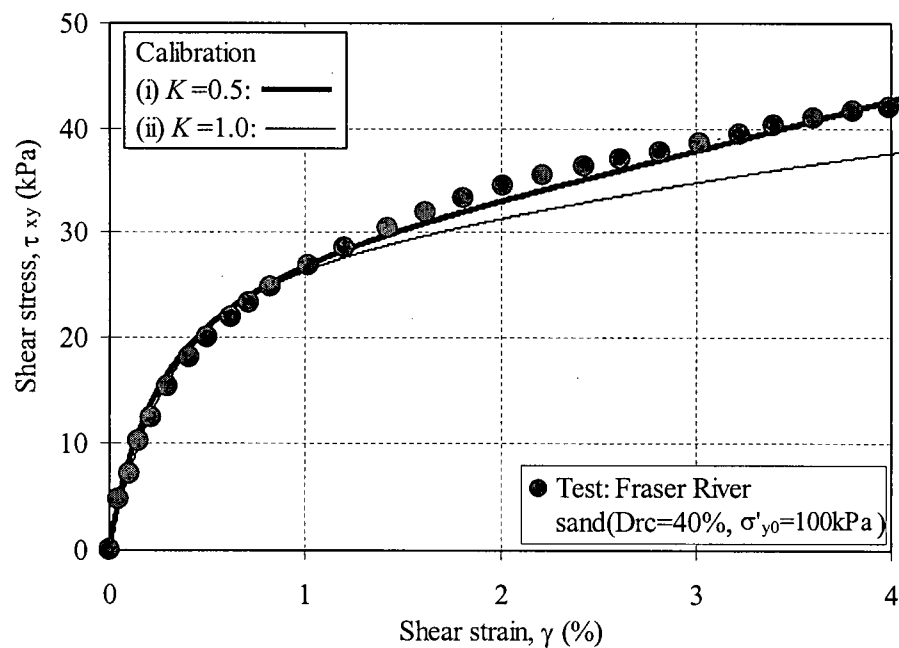


**Figure 3.25** Comparison of test result and numerical simulation of  $K = 0.5$  and  $1.0$  with the same initial mean stress (test data from Sriskandakumar, 2004).

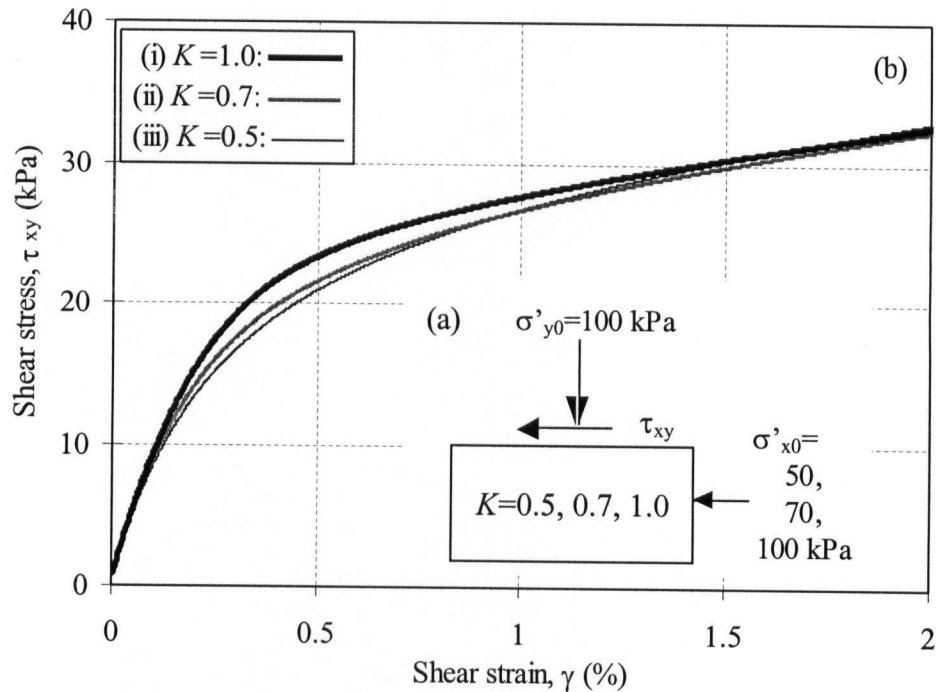


**Figure 3.26** Numerical simulation for different  $K$  states, 0.5, 0.7 and 1.0: (a) Initial stress conditions, and (b) UBCSAND2 results.

### 3.6 Implementation of UBCSAND2 in FLAC

The concepts discussed above are implemented into FLAC. The FLAC program is a well-known commercial code in geotechnical engineering and used in this study. The FLAC program models the soil mass as a collection of grid zones or elements, and solves the coupled stress flow problem using an explicit time stepping approach. Such an explicit scheme requires a very small timestep to maintain numerical stability. Pore fluid stiffness and Darcy hydraulic flow are basic to the FLAC program so that only the skeleton stress-strain relation is needed to define the model. Drained, undrained, or coupled stress flow conditions are specified by the user. The reader is referred to the FLAC manual regarding the numerical technique.

The FLAC program has a number of built-in stress-strain models including an elasto-plastic Mohr-Coulomb model. It allows a user to specify their own stress-strain relationship (i.e., user defined model). The previous UBCSAND model is a modified version of the built-in Mohr-Coulomb model, where the Mohr-Coulomb model has been adopted to continuously vary the friction and dilation angles to incorporate the yield loci and flow rule. The enhanced model UBCSAND2 was implemented as a user-defined constitutive model in FLAC using an embedded programming language FISH. The UBCSAND2 model adds each plastic strain increment based on two mobilized planes. Each plane has a corresponding yield function  $f$  and decides yielding separately. The calculation flow for the two mobilized planes is illustrated in Figure 3.5 and is explained next.

### 3.6.1 Calculation Procedure of Two Mobilized Planes

The initial stress state prior to monotonic or dynamic loading can be computed from either UBCSAND2 or Mohr-Coulomb models. The initial state is illustrated in Figure 3.27. At the initial stress state, first time loading could be either loading or unloading as shown in Figure 3.27.

Stress increments are related to elastic strain increments. Therefore, plastic strain increments are necessary to obtain elastic strain increments from given total strain increments as follows:  $\{\Delta\sigma'\} = [D]\{\Delta\varepsilon^e\} = [D]\{\{\Delta\varepsilon\} - \{\Delta\varepsilon^p\}\}$ . A plastic deformation is based on two mobilized planes and stress ratio on the respective plane. A stress-strain loop during cyclic loading can be separated into 3 phases as illustrated in Figure 3.9(a): loading, unloading, and reloading. The plane of maximum shear stress is considered first and the horizontal plane next. Among those 3 phases, one phase is determined by current stress ratio and next stress ratio increment.

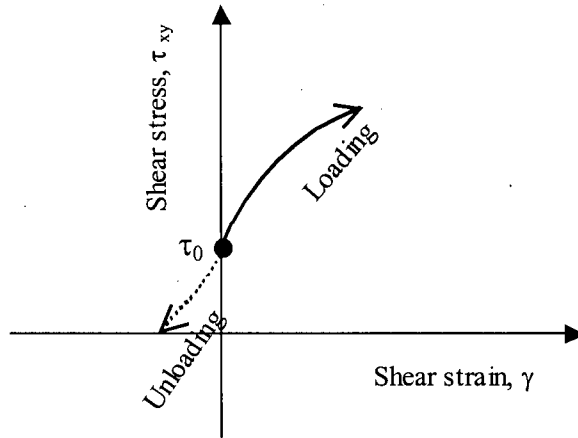


**Figure 3.27** Initial stress state and first time loading.

As illustrated in Figure 3.5, the plane of maximum shear stress is first considered for yielding conditions using  $f_1$ . If the yield function on the plane of maximum shear stress  $f_1$  is greater than zero, it indicates plastic yielding, otherwise it is elastic. Once the plane of maximum shear stress is tested, new stresses are determined regardless of yielding. The resulting stresses can be general  $x, y$  stresses. The calculation then proceeds to the horizontal plane, which determines yielding based on general  $x, y$  stresses as illustrated in Figure 3.5. Regardless of the previous  $f_1$  conditions, the horizontal plane decides either loading or unloading using  $f_2$ , independently. Therefore, the final four cases are possible as shown in Figure 3.5. A new stress increment can be calculated from one of four cases, and then added to an old stress to get a new stress.

### 3.7 Summary

A refined model called UBCSAND2 has been proposed, which better models sand behaviour by considering plastic unloading and principal stress rotation. It uses two mobilized planes:

---

maximum shear stress and horizontal planes. The way of phasing-out plastic deformations on the horizontal plane is a key issue in the Two Mobilized-plane model. The background and the detailed formulations of Two Mobilized-plane model are presented, and several predicted characteristic performances are also described and compared with measurements. The model predicts that elements having the same initial density and mean stress have similar drained response at small shear strain, in agreement with laboratory element tests. The UBCSAND2 can simulate principal stress rotation associated with different initial  $K$  conditions. In other words, under all the same conditions except initial  $K$  states, the UBCSAND2 prediction gives slightly stiffer behaviour for higher  $K$  conditions. The calculation procedure of UBCSAND2 is described, which explains how to combine plastic strain increments from two mobilized planes. In the following chapter, the systematic calibration of the proposed constitutive model UBCSAND2 is presented.

# Chapter 4

## Calibration of UBCSAND2

In this chapter, UBCSAND2 is systematically calibrated to capture measured element behaviour observed in laboratory testing. The specific behaviour observed from monotonic and cyclic direct simple shear (DSS) tests will be captured in the first stage. This stage is referred to as “specific calibration”. Secondly, the general behaviour of sand under cyclic loading conditions will be captured in terms of volumetric strain versus number of cycles, and liquefaction triggering based on the “SPT clean sand base curve” proposed by the NCEER (Youd & Idriss, 1997) and referred to hereafter as the “NCEER chart”. This is referred to as “general calibration”.

### 4.1 Calibration Procedure and Input Parameters

The validation of UBCSAND2 model consists of a calibration and a prediction with laboratory tests, as well as a validation of boundary value problems as illustrated in Figure 4.1.

The model is calibrated using data from drained DSS tests (i.e., skeleton response). The results from constant volume DSS tests (equivalent to undrained tests) are predicted to validate the applicability of the model for general coupled stress-flow conditions. From a presentation point of view, the above modeling of the drained and constant volume tests (equivalent to

undrained tests) are referred to as a calibration procedure unless otherwise stated. The calibration of laboratory tests uses a single element and is separated into two stages: specific calibration and general calibration. This chapter will focus on these two stages.

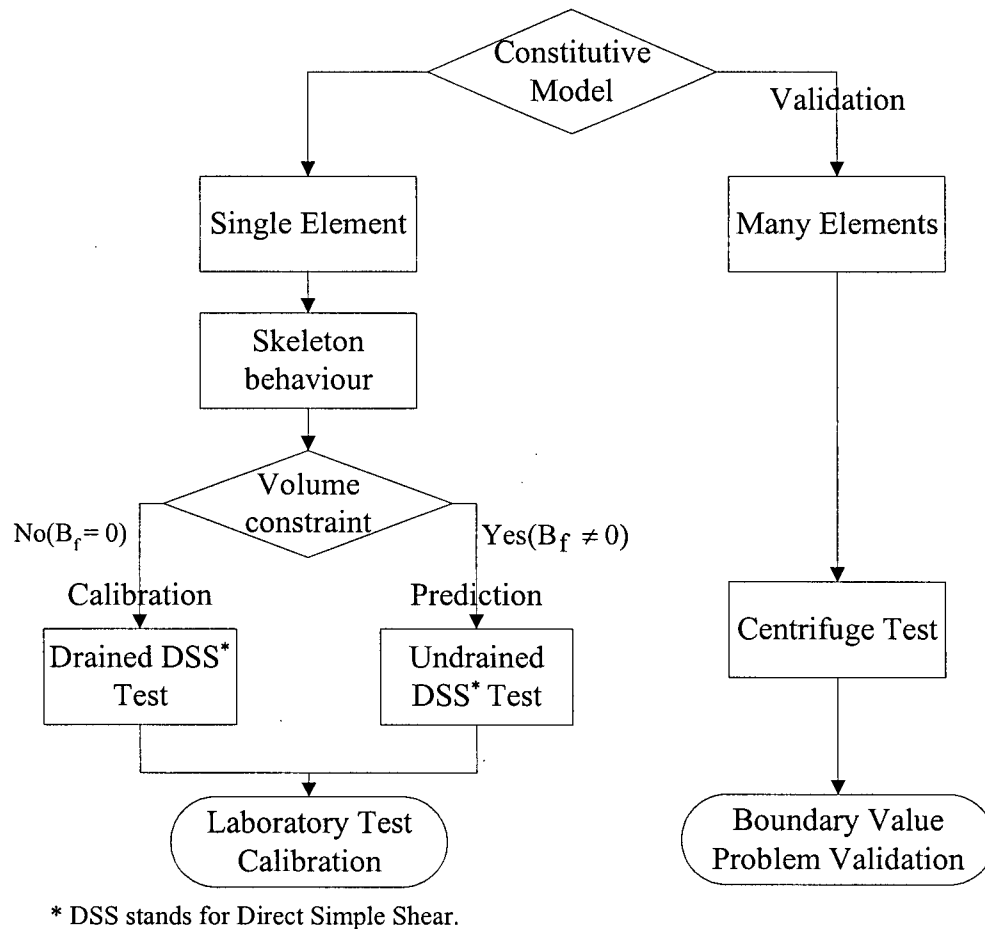


**Figure 4.1** Model calibration and validation procedures of UBCSAND2.

There are two approaches to obtain model input parameters. The direct approach is to use laboratory test data (e.g., DSS tests) to adjust parameters. The indirect approach is to use the correlations between input parameters and relative density or normalized standard penetration test values,  $(N_1)_{60}$ . Initial estimates of these parameters have been approximated from published data and calibration of the previous UBCSAND model. The response of sand elements under

monotonic and cyclic loading is predicted and compared with laboratory data. In this way, the model can be calibrated to match the observed response over the range of relative densities. Seven parameters are required for the UBCSAND2 model; two parameters for elastic response and five parameters for plastic response, respectively. Although laboratory tests are preferred, many empirical correlations are available for most parameters, especially for elastic shear and bulk moduli, and friction angle at constant volume and peak friction angle.

#### (a) Elastic shear modulus

The elastic shear modulus  $G$  is stress level dependent and was given by Eq. [3-1]. The  $ne$  in Eq. [3-2] is mostly assumed to be 0.5 (Byrne et al., 2004a). Then, the elastic shear modulus,  $G$ , is given by

$$G = k_G^e \cdot P_a \cdot \left( \frac{\sigma'_m}{P_a} \right)^{0.5} \quad [4-1]$$

The value of  $k_G^e$  is obtained indirectly from empirical relationships or directly from shear wave velocity or resonant column tests, and it is primarily a function of relative density (Byrne et al., 1987).

#### (b) Elastic bulk modulus

The elastic bulk modulus  $B$  is related to the shear modulus, and given by

$$B = \alpha_B \cdot G \quad [4-2]$$

The value of  $\alpha_B$  is a function of a Poisson's ratio,  $\nu$ , and ranges between 2/3 and 4/3 for  $0 < \nu < 0.2$ .

### (c) Plastic shear modulus

Plastic shear modulus  $G^p$  gradually decreases from its maximum value at very low strain  $G_{\max}^p$ , and can be calculated from either Eqs. [3-13] or [3-18]. In those equations,  $G_{\max}^p$  needs to be specified. Assuming that  $np$  in Eq. [3-14] is 0.5,  $G_{\max}^p$  is given by

$$G_{\max}^p = k_G^p \cdot P_a \cdot \left( \frac{\sigma'_m}{P_a} \right)^{0.5} \quad [4-3]$$

$k_G^p$ , which is related to  $k_G^e$  and the density of the soil through the approximate relationship  $k_G^p \approx 4.2 \cdot (D_r)^4 \cdot k_G^e + 100$  (Byrne et al., 2004a).

### (d) Friction angle at constant volume

The friction angle at constant volume,  $\phi_{cv}$ , has been observed to be a unique property, and it is reasonably assumed to be 32-33 degrees from laboratory data (Chern, 1985; Negussey et al., 1988; Thomas, 1992). As such,  $\phi_{cv}$  can be assumed to be the same for both drained and undrained conditions. The value of  $\phi_{cv}$  has been noted to be equal to the friction angle at the phase transformation state under undrained loading (Negussey et al., 1988). The friction angle at the phase transformation state appears unique for a given sand regardless of confining stress and relative density (Chern, 1985; Chung, 1985). Considering this available information, a value of  $\phi_{cv} = 33^\circ$  was used in the model calibration/prediction.

### (e) Peak Friction angle

Although laboratory tests are preferred, many empirical data are available for the peak friction angle. Kulhawy and Mayne (1990) had compiled commonly used relationships in the Electric Power Research Institute (EPRI) manual on foundation design. The selection of the peak friction angle  $\phi_f$  should consider the effects of relative density and stress level. However, for the

sake of model simplicity,  $\phi_f$  was considered to depend on only relative density and, based on previous UBCSAND calibration of Nevada sand and Fraser River sand (P.M. Byrne, personal communication, 2004), it is given by

$$\phi_f = \phi_{cv} + 11.4 \cdot (D_r)^2 \quad [4-4]$$

The peak friction angle,  $\phi_f$ , may not be the same in undrained loading due to the pore fluid constraint changing the stress path between drained and undrained loading. But in these analyses it has been assumed to be the same for both drained and undrained conditions.

#### (f) Failure ratio, $R_f$

$R_f$  in plastic shear strain hardening equations [3-13] and [3-18] in Chapter 3 is the failure ratio that modifies the plastic stiffness and is always less than unity. It is the ratio of the failure stress level to the ultimate strength ratio predicted from the best-fit hyperbola. The values of  $R_f = 0.99$  and  $R_f = 0.92$  were used for monotonic and cyclic DSS tests on loose and dense Fraser River sand, respectively (determined from stress-strain curve fitting).

#### (g) Cyclic hardening shape parameter, $C_h$

$H_c$  is used to harden a plastic volumetric strain increment during cyclic loading and is given by

$$H_c = \text{EXP} \left( -C_h \frac{\varepsilon_v^p}{\gamma^*} \right) \quad [4-5]$$

$C_h$ , termed a cyclic hardening shape parameter, is required in the cyclic hardening function  $H_c$ . It determines the shape of hardening and is obtained by fitting data. For monotonic loading,  $C_h$  is zero as no cycling loading occurs.  $C_h$  increases with relative density and ranges between 1.0 and 2.0 for loose to medium dense sands (e.g.,  $D_r = 40 - 50\%$ ).

## 4.2 Specific Calibration

The first stage of laboratory calibration is referred to as “specific calibration”. Model parameters are adjusted to capture the specific soil behaviour in terms of stress path, stress-strain curve, and volume change measured from monotonic and cyclic DSS tests. Laboratory tests with different drainage boundary conditions such as drained and constant volume tests are captured. The test conditions are summarized in Table 4.1. The calibration is carried out using a single element of unit dimensions. Model calibration is carried out as follows:

- (a) Monotonic and cyclic drained DSS tests,
- (b) Monotonic and cyclic constant volume DSS tests (equivalent to undrained test) without initial static shear stress, and
- (c) Cyclic constant volume DSS tests (equivalent to undrained test) with initial static shear stress.

**Table 4.1** Specific calibration procedure of UBCSAND2 (test data from Sriskandakumar, 2004).

Boundary Condition	Test Type	Case	Comparison
Drained test	Monotonic	$\gamma_{\max} = 4\%$	Shear stress-shear strain ( $\tau$ vs. $\gamma$ ), volumetric strain-shear strain ( $\epsilon_v$ vs. $\gamma$ )
	Cyclic constant strain amplitude	$\gamma_{\text{cyc}} = 0.5, 1\%$	
Constant volume test (equivalent to undrained test)	Monotonic		Shear stress-shear strain ( $\tau$ vs. $\gamma$ ), stress path
	Cyclic constant stress amplitude	$\text{CSR}^{(i)} = 0.08, 0.1, 0.15$	
	Cyclic constant stress amplitude with initial static shear stress	$\text{CSR} = 0.065$ ( $\alpha^{(ii)} = 0.1$ ), $0.1$ ( $\alpha = 0.05$ ), $0.1$ ( $\alpha = 0.1$ )	

Note: (i) CSR is Cyclic Stress Ratio and defined as  $\tau_{\text{cyc}}/\sigma'_{y0}$ , where  $\tau_{\text{cyc}}$  is a cyclic shear stress and  $\sigma'_{y0}$  is an initial vertical effective stress; (ii)  $\alpha$  is the ratio of an initial static shear stress ( $\tau_{\text{sta}}$ ) to  $\sigma'_{y0}$ .

All DSS tests data used in this calibration have been carried out at UBC using the NGI-type simple shear (Bjerrum & Landva, 1966) by Sriskandakumar (2004). For more detailed information regarding tests, the reader is referred to Sriskandakumar (2004).

#### **(i) DSS test database of Fraser River sand at UBC**

Data from a series of DSS tests performed on Fraser River sand (Sriskandakumar, 2004; Wijewickreme et al., 2005) was used to calibrate the numerical model element response. Test data are available on the web site (<http://www.civil.ubc.ca/liquefaction/>). The laboratory test specimens were prepared by the air pluviation method, which is the normally adopted specimen preparation approach in centrifuge tests. Two stress levels (i.e., 100 kPa and 200 kPa) were applied to two densities (i.e.,  $D_r = 40\%$  and  $80\%$ ) for various test conditions. All samples were placed at  $D_r = 34\%$  at zero pressure and consolidated to  $40\%$  and  $44\%$  under applied pressures of 100 kPa and 200 kPa, respectively. Dense samples were tamped to reach  $D_r = 80\%$  under an applied pressure of 100 kPa. The sample preparation and testing methods have been described in detail by Sriskandakumar (2004). Samples were then subjected to large cyclic shear strain under drained condition or cyclic shear stress under constant volume conditions as well as monotonic loading.

For the purpose of liquefaction analysis, DSS tests for loose sand under an applied pressure of 100 kPa are compared in this chapter.

#### **(ii) Material tested: Fraser River sand**

Fraser River sand dredged from the Fraser River in the Lower Mainland of British Columbia in Canada was used for laboratory element testing. Fraser River sand has a specific gravity

$G_s = 2.71$ , an average particle size  $D_{50} = 0.26$  mm and  $D_{10} = 0.17$  mm, minimum and maximum void ratios of  $e_{\min} = 0.62$  and  $e_{\max} = 0.94$ , respectively. Grain size distribution of Fraser River sand is shown in Figure 4.2.

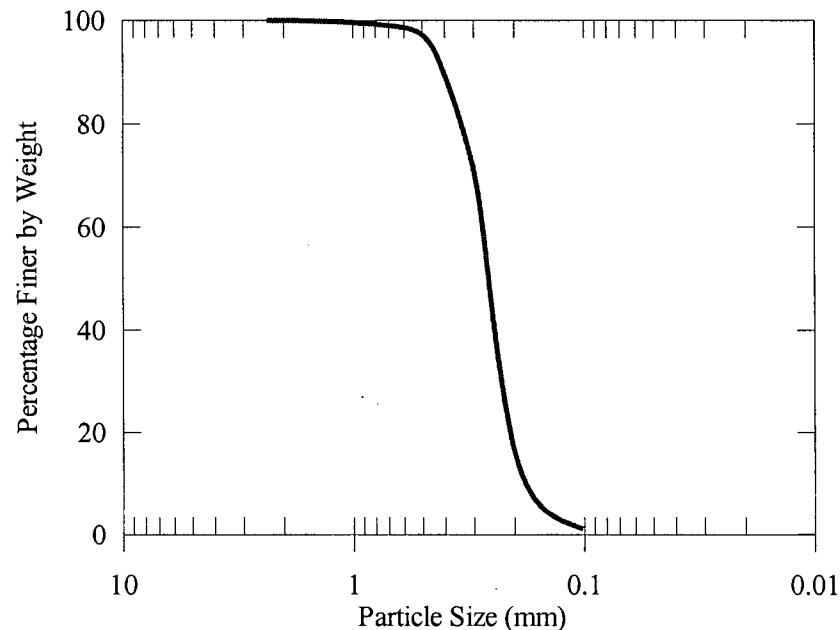


**Figure 4.2** Grain size distribution of Fraser River sand.

#### 4.2.1 Calibration of Drained Behaviour

The characteristic behaviour of air-pluviated Fraser River sand under monotonic and cyclic DSS tests is captured herein using UBCSAND2. Drained monotonic behaviour of Fraser River sand is first captured. The drained tests data on loose Fraser River sand selected for the calibration are summarized in Table 4.2. Monotonic behaviour of loose Fraser River sand is first compared, and then cyclic behaviour will follow.

The calibration was carried out in the same way as the tests, i.e., under drained condition. A single element was used. The boundary conditions were shown in Figure 3.21, Chapter 3. The elastic and plastic parameters selected for the calibration of drained tests were the same for all

cases having the same relative density at the end of consolidation ( $D_{rc}$ ) as listed in Table 4.3. These parameters are related to the previous UBCSAND model calibration except  $C_h$ , an additional parameter for UBCSAND2. It was assumed that the initial lateral stress in the test was 50 kPa, i.e.,  $K_0 = 0.5$ . The same initial stresses were assumed in the numerical simulation.

**Table 4.2** Summary of selected drained DSS tests on loose Fraser River sand (test data from Sriskandakumar, 2004).

Test Type	$\sigma'_{y0}$ (kPa)	$D_{rc}^{(i)}$ (%)	$\gamma_{max}$ or $\gamma_{cyc}$ (%)	Strain Rate (%/hr)	Duration (cycles)
Monotonic	100	40	4	10	N/A
Cyclic	100	40	0.5	20	5
			1	20	4.25

Note: (i)  $D_{rc}$  is the relative density at the end of consolidation.

**Table 4.3** Input parameters for monotonic and cyclic drained DSS tests on Fraser River sand at  $D_{rc} = 40\%$ .

Parameter	Symbol	Value
Elastic shear modulus number	$k_G^e$	591
Bulk modulus factor	$\alpha_B$	0.7
Plastic shear modulus number	$k_G^p$	164
Friction angle at constant volume	$\phi_{cv}$	33°
Peak friction angle	$\phi_f$	34.8°
Failure ratio	$R_f$	0.99 (monotonic test) 0.92 (cyclic test)
Cyclic hardening shape parameter	$C_h$	1.6

#### (i) Monotonic drained behaviour

Monotonic drained behaviour of loose Fraser River sand is calibrated in Figure 4.3. Shear stress versus shear strain and volumetric strain versus shear strain are compared up to  $\gamma_{max} = 4\%$  in

Figure 4.3. A shear strain over 10% in simple shear may not be reliable due to sample distortion. The thick line is the test result and the thin line is the calibration. The calibrations generally give a reasonable agreement with the observed response including shear stress and volumetric strain.

The predicted lateral stress  $\sigma'_x$  versus shear strain is shown as a thick line in Figure 4.4, along with a vertical stress which remains constant. As the specimen is sheared, the predicted lateral stress gradually increases as shown in Figure 4.4. The lateral stress was not measured so there is no comparison.

### **(ii) Cyclic drained behaviour**

Cyclic drained behaviour of loose Fraser River sand is calibrated for two cyclic shear strain levels, 0.5% and 1%. Shear stress versus shear strain and volumetric strain versus shear strain during several cycles are compared in Figures 4.5 and 4.6. The left side is the test result and the right side is the calibration. In both tests, the first cycle gives a significant amount of contraction, and then further contraction decreases from cycle to cycle.

The calibrated stress-strain loops are similar to those observed in the tests. The characteristic drained behaviour under cyclic loading, in which plastic volumetric strains accumulate during cycling but at a decreasing rate (volumetric hardening), is captured by UBCSAND2 as compared in Figures 4.5 and 4.6. The computed decreasing plastic volumetric strain increment derives from the cyclic hardening introduced in Section 3.4.4. The calibrations provide a good representation of the observed shear stress versus shear strain response including plastic unloading and decreasing pattern of volumetric strain for both tests with  $\gamma_{cyc} = 0.5\%$  and  $1.0\%$ . However, the difference between calibrated and measured amounts of volumetric strain at the end of tests becomes significant as a cyclic shear strain increases from 0.5% to 1%. It is also

noted that the calibration underestimates the volumetric strain for initial 1 or 2 cycles but afterward reasonably computes the volumetric strain. Based on previous experience (UBCSAND calibration), fitting a volumetric strain at higher cyclic shear strain levels (e.g.,  $\gamma_{\text{cyc}} \geq 1\%$ ) resulted in the overestimate of excess pore pressure, and therefore the current fits (i.e., focused on a volumetric strain after initial 1 or 2 cycles) were preferred.

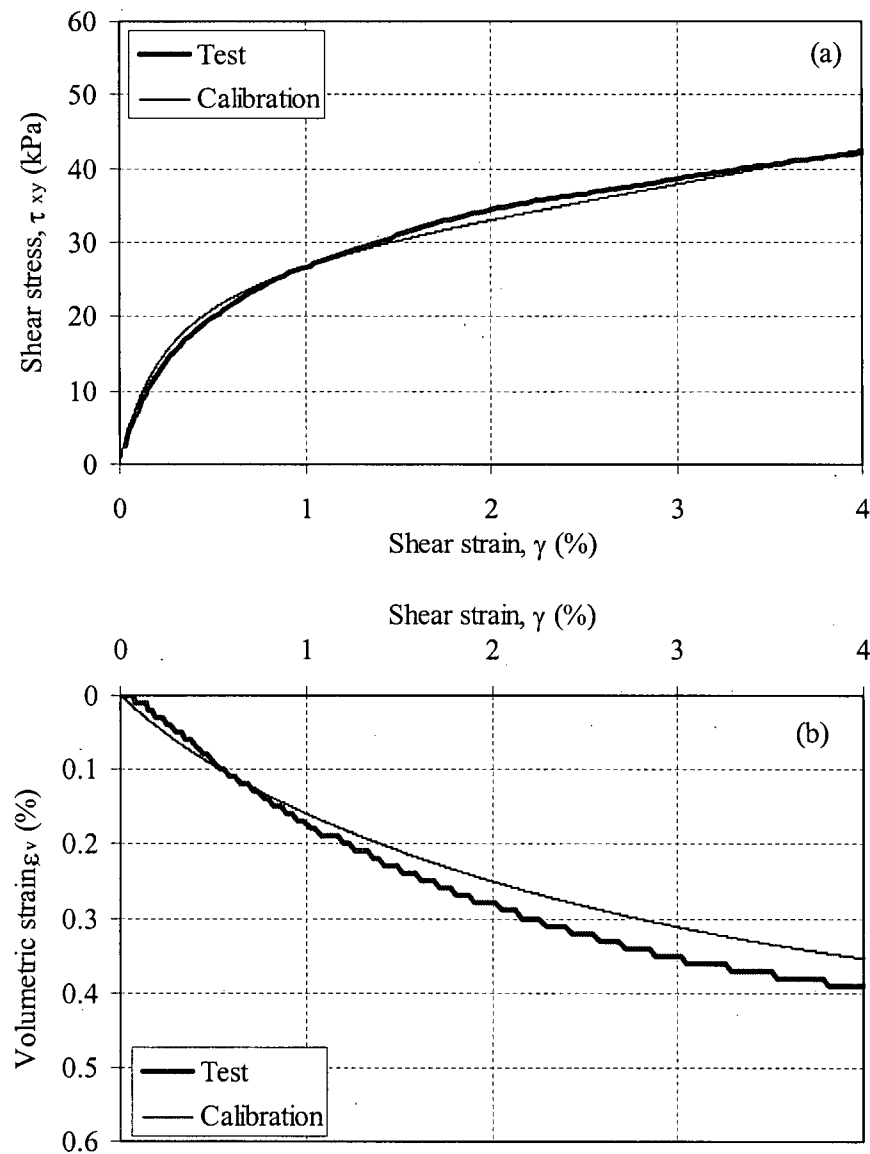


**Figure 4.3** Monotonic drained simple shear response of loose Fraser River sand: (a) shear stress vs. shear strain, and (b) volumetric strain vs. shear strain (test data from Sriskandakumar, 2004).

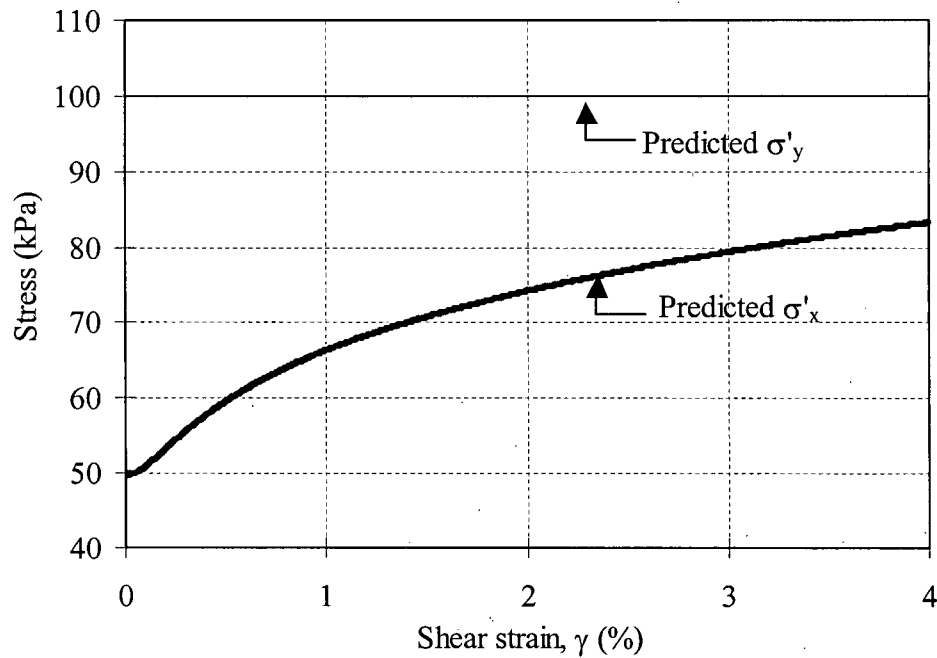


**Figure 4.4** Predicted lateral stress and vertical effective stress (100 kPa constant) during monotonic drained simple shear test on loose Fraser River sand.

The predicted lateral stress variations are shown in Figures 4.7 and 4.8 during cyclic loading. With increasing number of cycles, in an overall sense, the lateral stress increases and approaches the applied vertical stress. However, the lateral stress decreases during the unloading phase of a given cycle.

The proposed model was calibrated based on drained DSS tests, and then used to predict constant volume DSS tests.

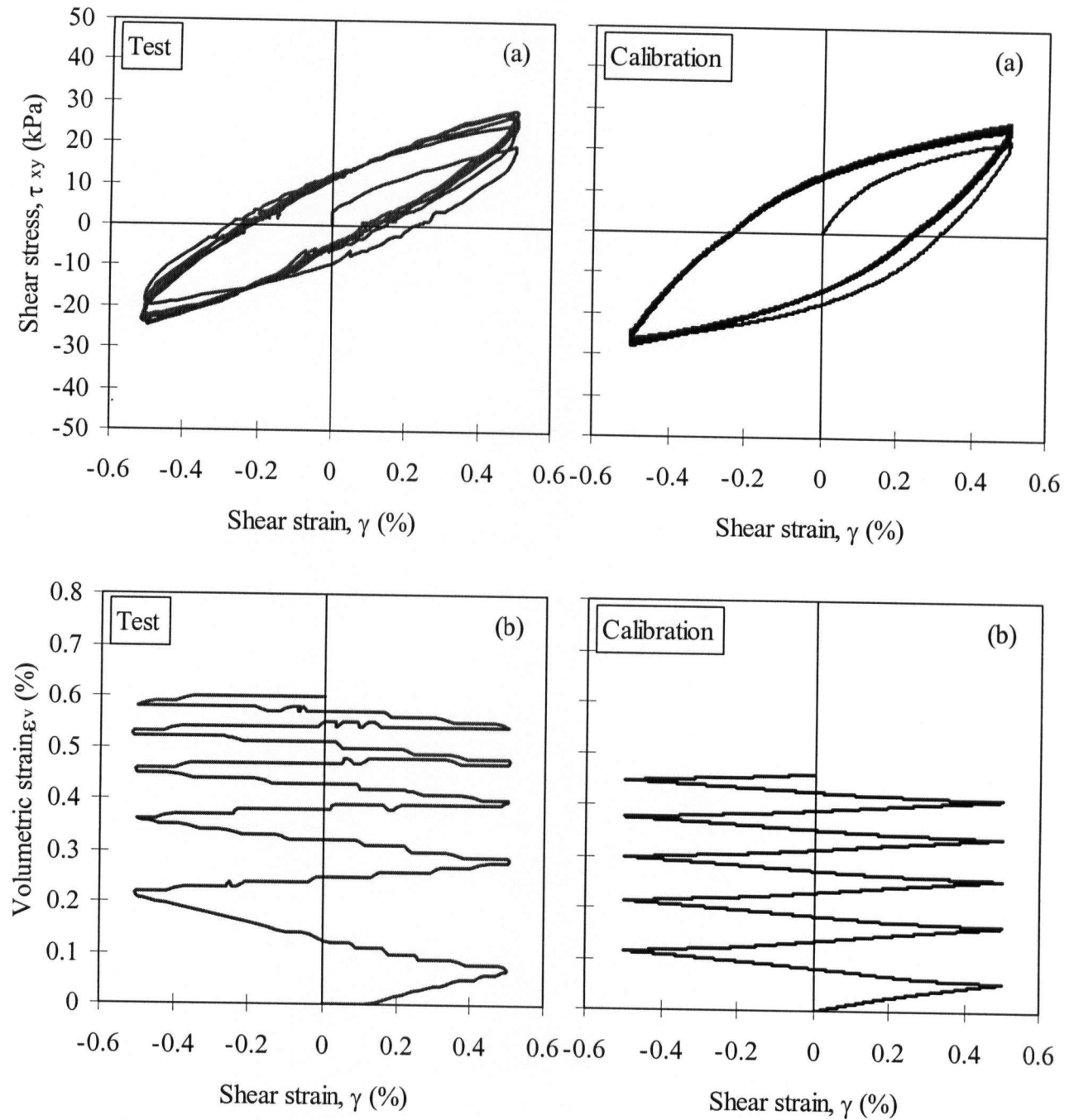


**Figure 4.5** Measured (left side) and calibrated (right side) cyclic drained test on loose Fraser River sand with  $\gamma_{cyc} = 0.5\%$ : (a) shear stress vs. shear strain, and (b) volumetric strain vs. shear strain (test data from Sriskandakumar, 2004).

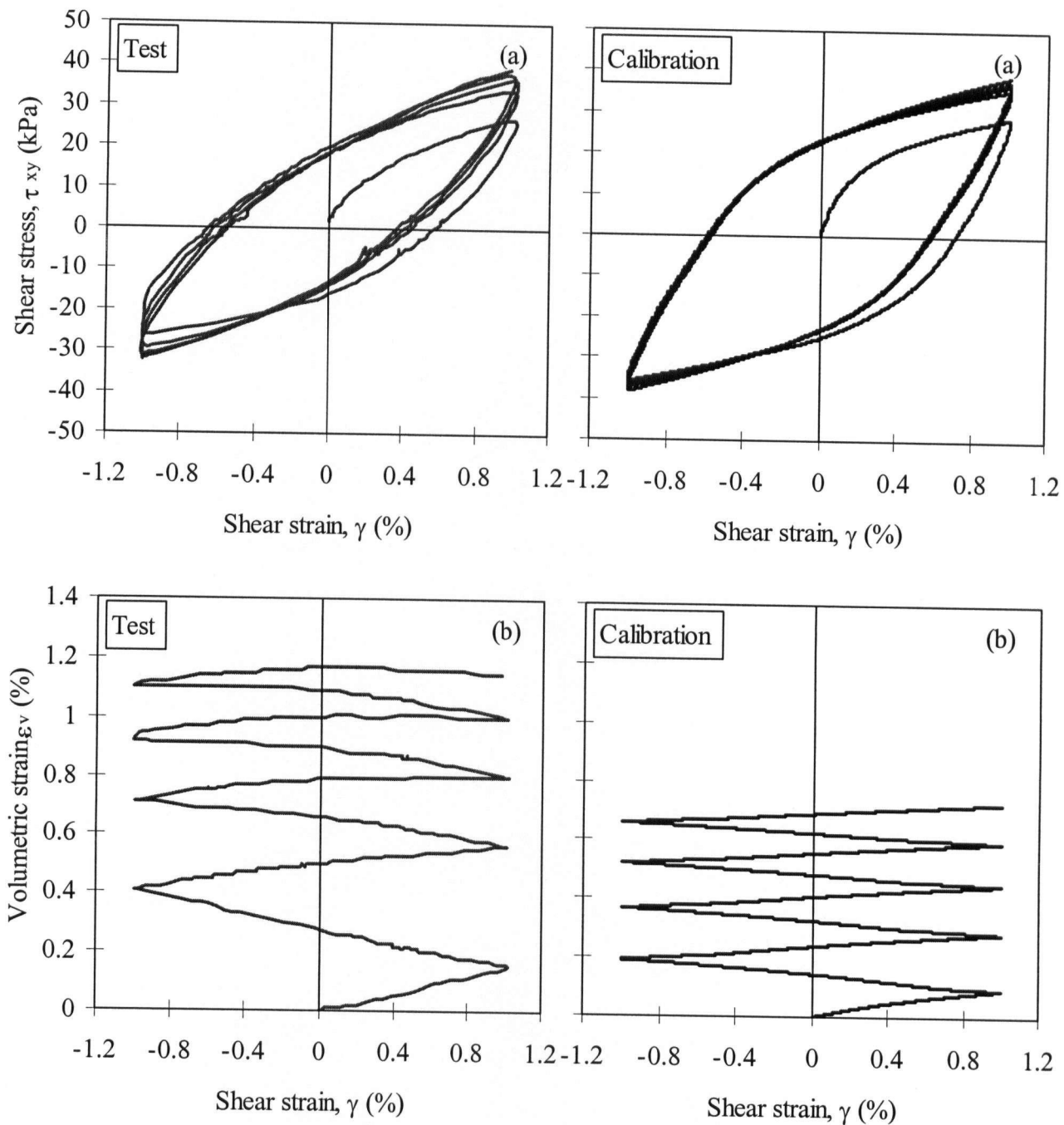


**Figure 4.6** Measured (left side) and calibrated (right side) cyclic drained test on loose Fraser River sand with  $\gamma_{cyc} = 1.0\%$ : (a) shear stress vs. shear strain, and (b) volumetric strain vs. shear strain (test data from Sriskandakumar, 2004).

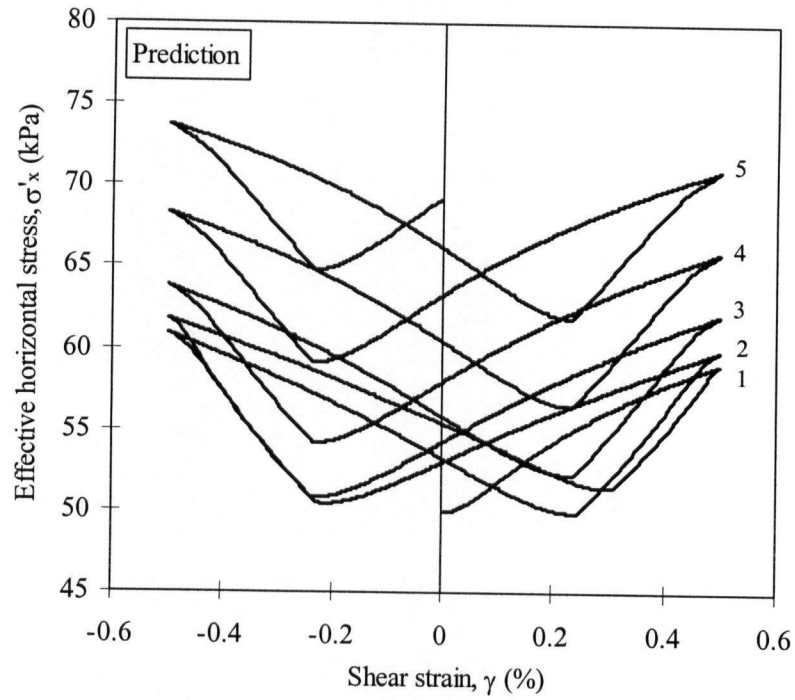


**Figure 4.7** Computed lateral stress from cyclic drained test on loose Fraser River sand with  $\gamma_{cyc} = 0.5\%$ .

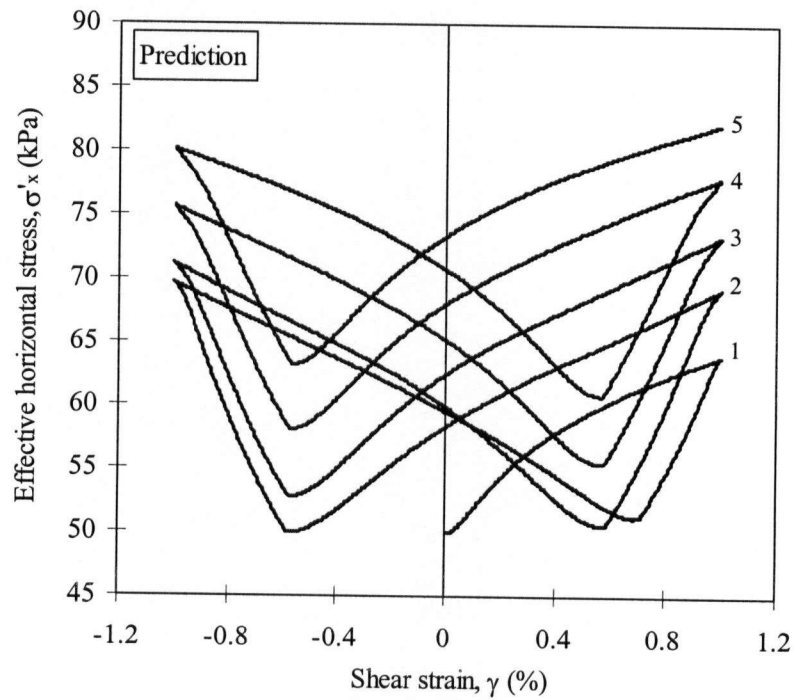


**Figure 4.8** Computed lateral stress from cyclic drained test on loose Fraser River sand with  $\gamma_{cyc} = 1.0\%$ .

#### 4.2.2 Prediction of Constant Volume Tests without Initial Static Shear Stress

The constant volume test is equivalent to an undrained test and has several advantages: (i) eliminating the error due to compliance, (ii) making the testing easier by eliminating the saturation procedure (Finn & Vaid, 1977; Finn et al., 1978). Constant volume DSS tests on Fraser River sand, carried out with and without initial static shear stress (Wijewickreme et al., 2005), were used to verify the proposed model. The constant volume DSS tests under  $\sigma'_{y0} = 100$  kPa without initial static shear stress were predicted first. Simulation of tests with initial static shear stress will be presented next. The selected constant volume test data without initial static shear stress on loose Fraser River sand for the calibration are summarized in Table 4.4.

**Table 4.4** Summary of selected constant volume DSS tests on loose Fraser River sand without initial static shear stress (test data from Sriskandakumar, 2004).

Test Type	$\sigma'_{y0}$ (kPa)	$D_{rc}$ (%)	CSR	$N_{Liq}$ (test) <sup>(i)</sup>	$N_{Liq}$ (predicted) <sup>(ii)</sup>
Monotonic	100	40	N/A	N/A	N/A
			0.08	17.5	14.5
Cyclic	100	40	0.10	6.5	7.5
			0.15	1.0	2.0

Note: (i)  $N_{Liq}$  is the number of cycles to liquefaction and round off 0.5 cycle, and  $N_{Liq}$  (test) is the  $N_{Liq}$  from test result; (ii)  $N_{Liq}$  (predicted) from model prediction.

The prediction was carried out simulating the constant volume condition of the tests using a single element. Boundary conditions were previously shown in Figure 3.21 of Chapter 3. It was again assumed that the specimen was initially subjected to  $K_0$  consolidation with  $K_0 = 0.5$ . The same initial stresses were assumed in the numerical simulation. The input parameters used herein are identical to the parameters listed in Table 4.3 that were used for the drained tests.

**(i) Monotonic behaviour**

The monotonic constant volume test on loose Fraser River sand is first predicted. The shear stress versus shear strain and shear stress versus vertical effective stress are compared in Figure 4.9. The thick line is the test result and the thin line is the prediction. The predictions give a reasonable representation of the observed response, even for a relatively large shear strain of 6%.

**(ii) Comparisons of numerical predictions based on constant volume and undrained conditions**

It is known that the constant volume tests used in this calibration are equivalent to undrained tests with an incompressible fluid (Finn et al., 1978; Dyvik et al., 1987). Water has a compressibility of  $2 \times 10^6$  kPa. However, less than 100% saturation results in greater compressibility as air is extremely compressible. Since the skeleton behaviour of loose Fraser River sand has been captured, the saturated undrained behaviour of the same soil can be predicted by imposing a volumetric constraint by using a high bulk modulus of pore fluid,  $B_f$ . Three different levels of bulk modulus,  $5 \times 10^4$  kPa,  $1 \times 10^5$  kPa and  $1 \times 10^6$  kPa, are examined. These values represent a range of saturation. Numerical predictions based on constant volume and undrained conditions are compared in Figure 4.10. Input parameters for the undrained tests are all the same as were used for the constant volume test, except  $B_f$ . It is found that the prediction based on undrained condition with  $B_f = 1 \times 10^6$  kPa gives very similar behaviour to the constant volume test.

It is indirectly confirmed that in undrained tests the saturation procedure is very important to achieve a high degree of saturation resulting in a high bulk modulus of pore fluid such as  $1 \times 10^6$  kPa.

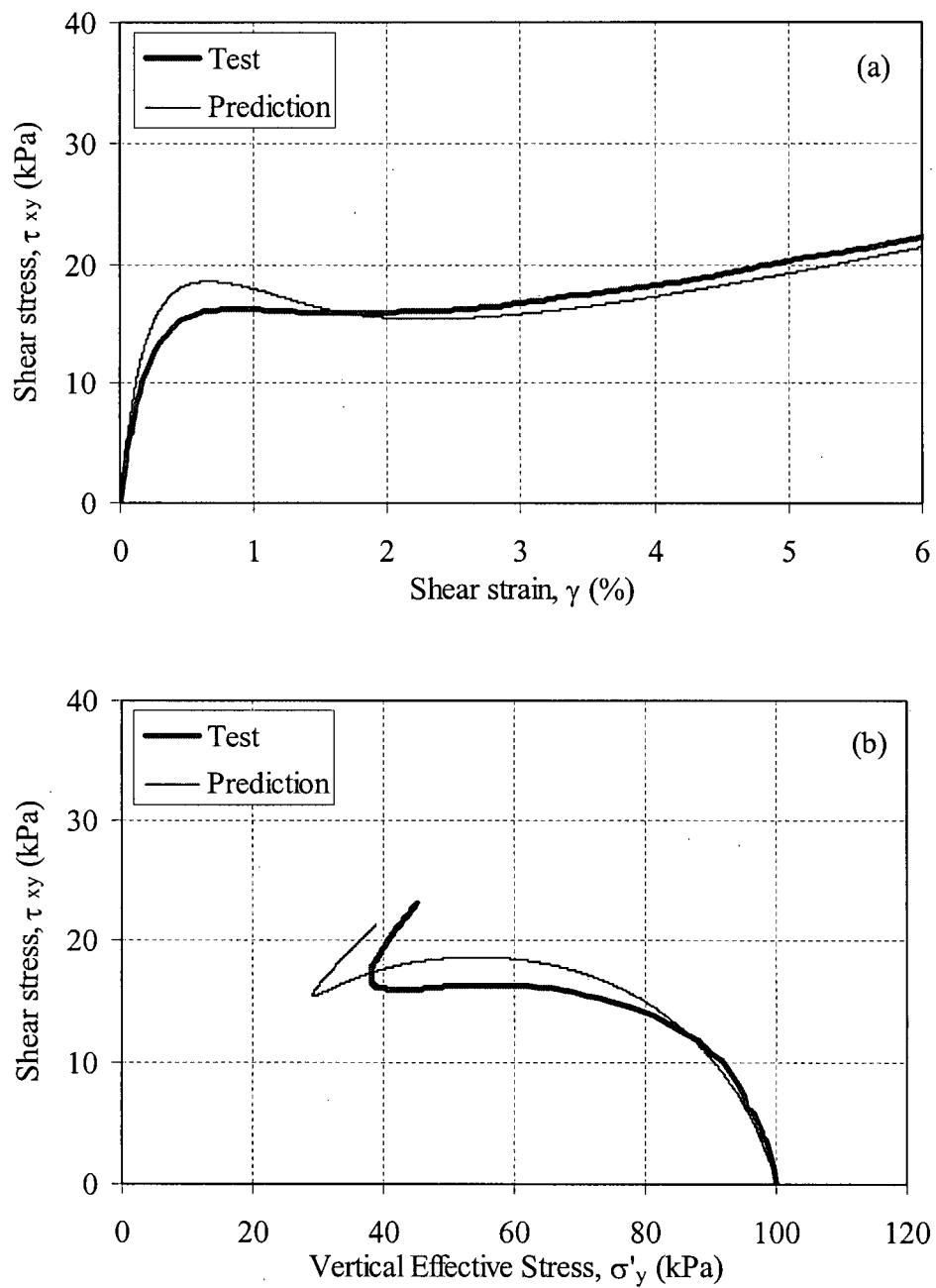


**Figure 4.9** Measured and predicted monotonic constant volume test on loose Fraser River sand: (a) shear stress vs. shear strain, and (b) shear stress vs. vertical effective stress (test data from Sriskandakumar, 2004).

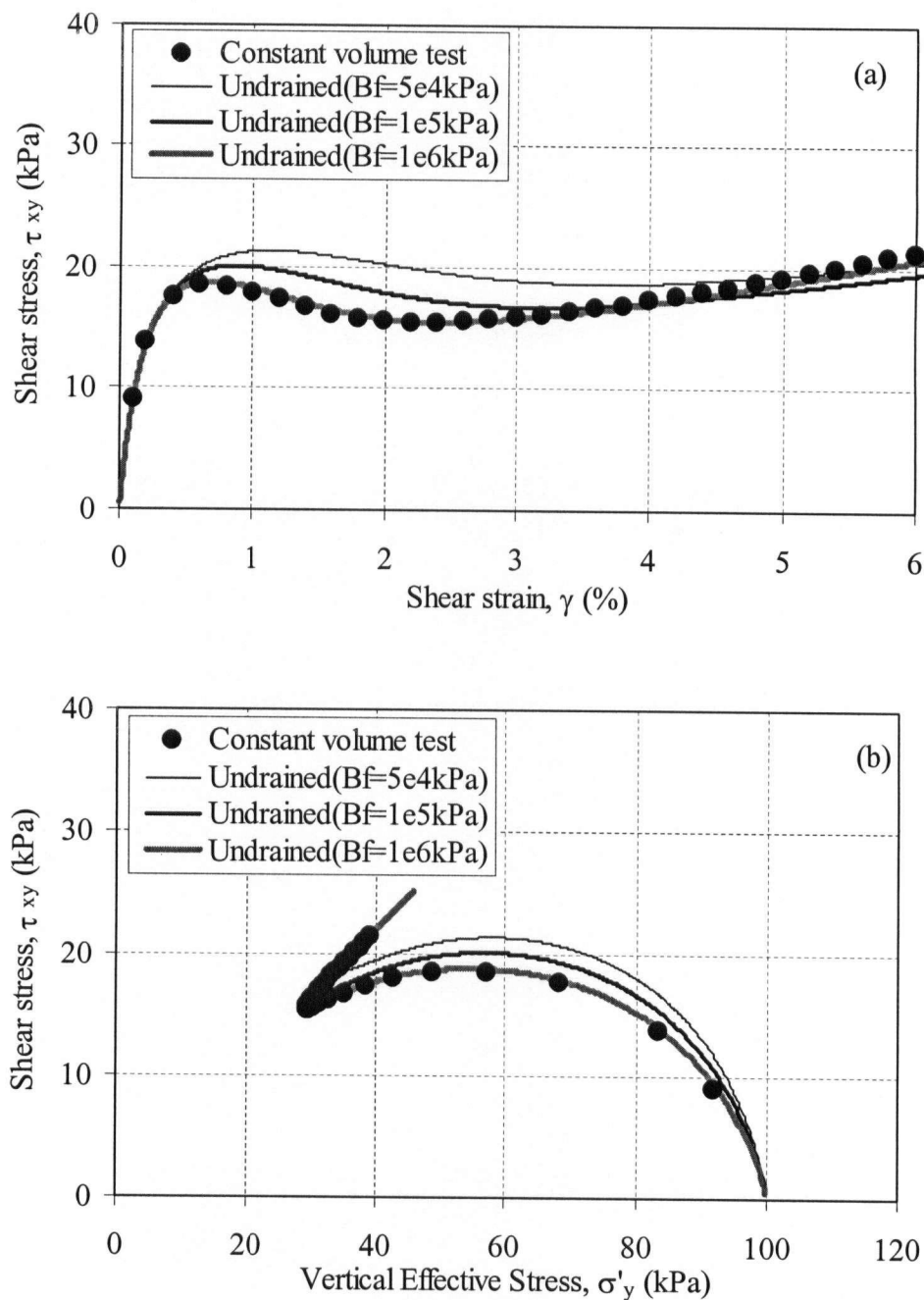


**Figure 4. 10** Comparison of numerical predictions based on constant volume and undrained conditions of loose Fraser River sand: (a) shear stress vs. shear strain, and (b) shear stress vs. vertical effective stress.

### (iii) Cyclic behaviour

The cyclic behaviour of loose Fraser River sand under constant volume condition is compared with the UBCSAND2 prediction in this section. Three different CSRs (Cyclic Stress Ratios), 0.08, 0.1, and 0.15, are compared with predictions. Figures 4.11 to 4.13 show the comparison for three CSRs applied on loose Fraser River sand with the same initial stress condition. Test data are shown in left sides of the same figures. The right side is the numerical predictions.

The prediction for CSR = 0.08 (see Figure 4.11(a), right side) indicates two distinct phases in the stress path: (i) rapid effective stress drop for the initial 7 cycles, and (ii) slow effective stress drop for the following 7 cycles. This is attributed to the manner in which the principal stress rotation is accounted for in the model (i.e., initially both the plane of maximum shear stress and the horizontal plane participate in generating plastic strains). This effect gradually reduces as the direction of the principal stress rotates, and it disappears when  $\sigma'_x = \sigma'_y$  (i.e., at 7 cycles in this prediction). In other words, during the initial 7 cycles two planes work together due to principal stress rotation, and then only one plane works for the remaining cycles because no more principal stress rotation occurs. This is consistent with the test results of Matsuoka et al. (1988) and Ishihara and Towhata (1983) who found that after several cycles the volumetric strain increment caused by pure principal stress rotation becomes nearly zero (see Figure 2.9(b)).

The test result for CSR = 0.08 (see Figure 4.11(a), left side) shows a rapid drop of effective stress for the first or second cycles followed by a slow drop. It suggests that the effect of principal stress rotation disappears much faster (within the first or second cycles) than the model prediction.

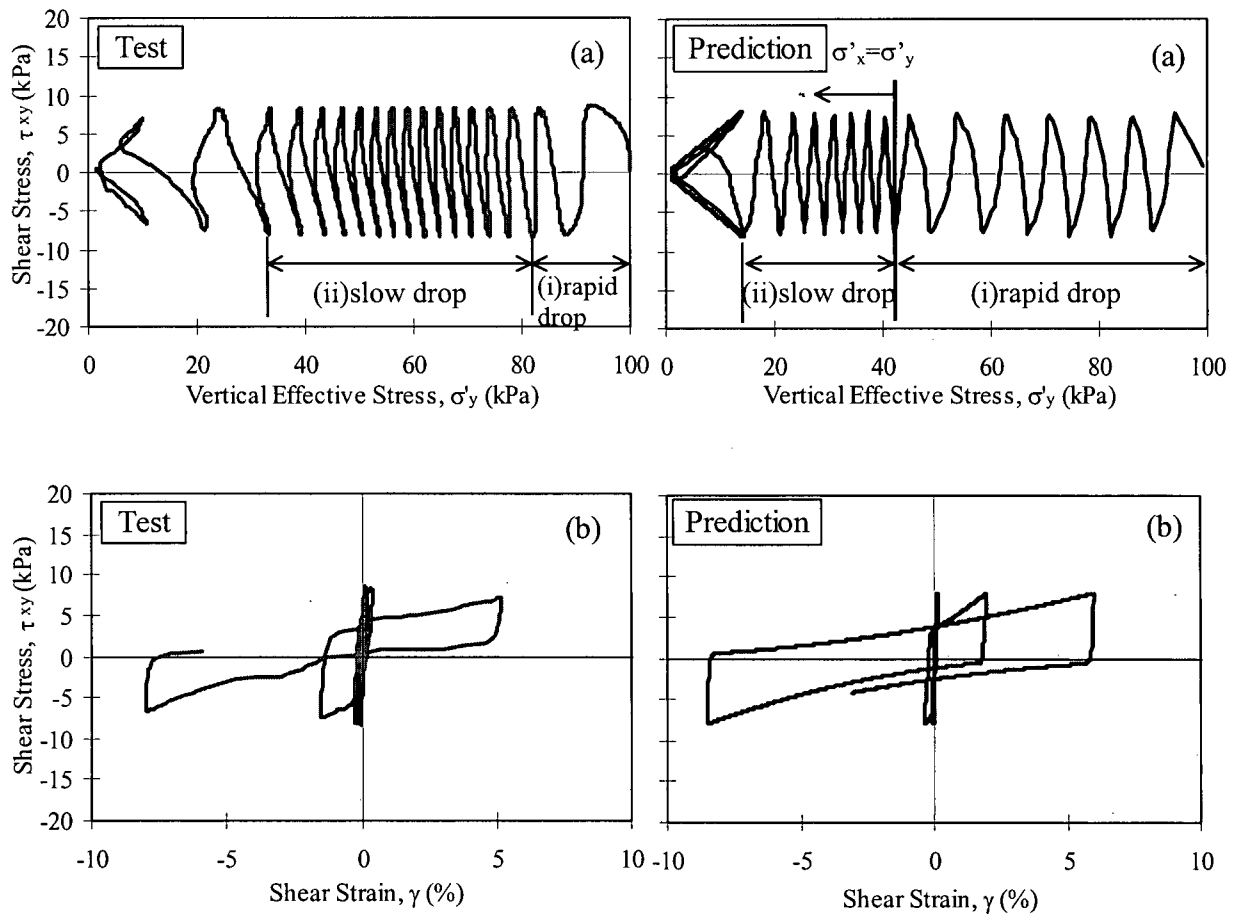


**Figure 4.11** Measured (left side) and predicted (right side) cyclic constant volume test on loose Fraser River sand under  $CSR = 0.08$ : (a) stress path, and (b) shear stress vs. shear strain (test data from Sriskandakumar, 2004).

When  $CSR = 0.1$  (see Figure 4.12(a), left side), the test specimen liquefied in 6 cycles. It is observed that the first and last (6<sup>th</sup>) cycles contributed to large excess pore pressure generation. Once the vertical effective stress became nearly zero, large strains developed. The model can capture large strains, up to even 10%, developed after liquefaction as shown in the stress-strain curves. The unloading process after dilation causes a large drop in effective stress. This is captured by the UBCSAND2, whereas the previous model UBCSAND could not consider plastic deformation upon unloading. The detailed comparison of UBCSAND and

UBCSAND2 is given in Section 4.3. Generally, the predictions of stress path and stress-strain curve are in good agreement with measurements.

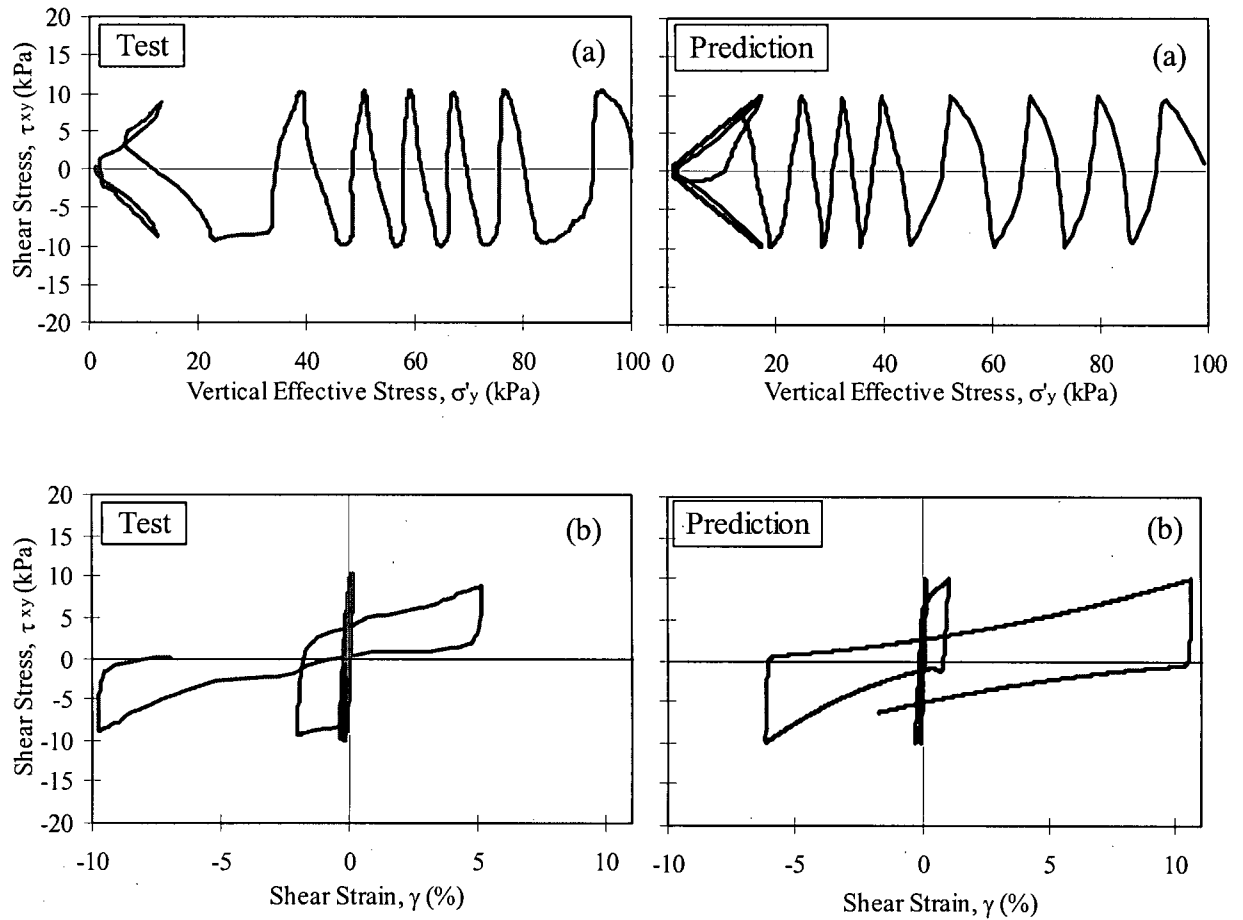


**Figure 4.12** Measured (left side) and predicted (right side) cyclic constant volume test on loose Fraser River sand under  $CSR = 0.1$ : (a) stress path, and (b) shear stress vs. shear strain (test data from Sriskandakumar, 2004).

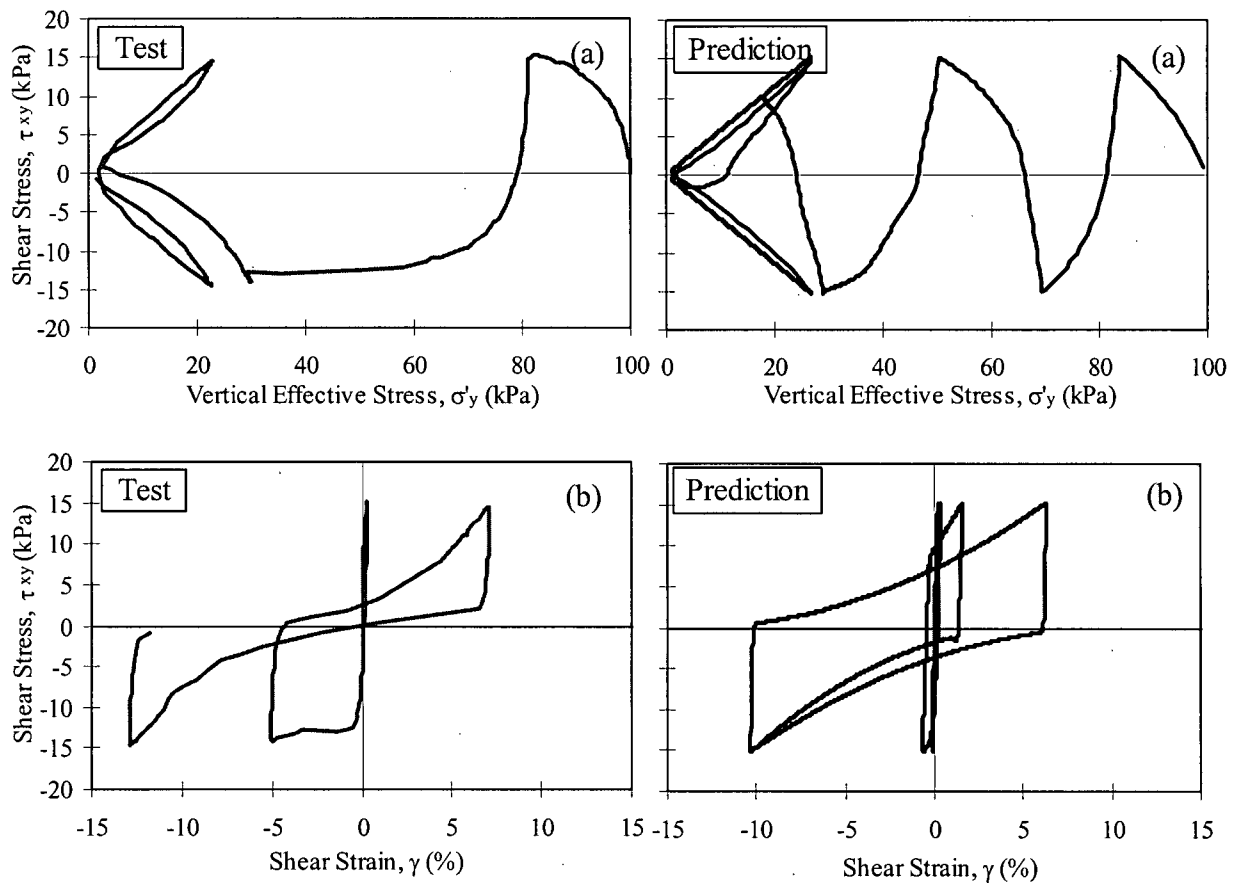


**Figure 4.13** Measured (left side) and predicted (right side) cyclic constant volume test on loose Fraser River sand under  $CSR = 0.15$ : (a) stress path, and (b) shear stress vs. shear strain (test data from Sriskandakumar, 2004).

#### (iv) Liquefaction resistance

The CSR versus number of cycles to liquefaction observed from laboratory tests is compared with the model prediction in Figure 4.14. Liquefaction triggering was defined as  $\gamma > 3.75\%$ , and at this point  $R_u (= (\sigma'_{y0} - \sigma'_y)/\sigma'_{y0}$ , pore pressure ratio) is 90 - 95%. This strain level is equivalent to reaching a 2.5% single-amplitude axial strain in a triaxial sample, which is a definition for liquefaction previously suggested by the National Research Council of United States (NRC, 1985). Both the definitions of liquefaction triggering (i.e.,  $\gamma > 3.75\%$  and  $R_u >$

90%) showed almost the same number of cycles to liquefaction. The prediction with  $K = 0.5$  (i.e.,  $\sigma'_{y0} = 100$  kPa,  $\sigma'_{x0} = 50$  kPa) is in good agreement with measurements as shown in Figure 4.14.

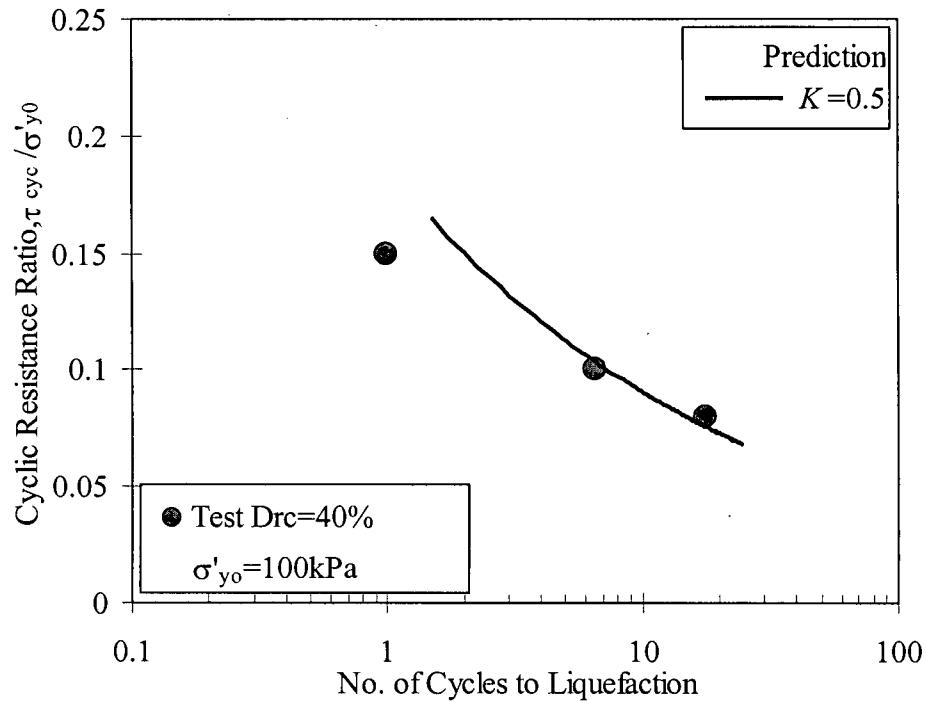


**Figure 4.14** Predicted liquefaction resistance and test result in terms of  $\tau_{cyc} / \sigma'_{y0}$  (test data from Sriskandakumar, 2004).

An examination of the effect of  $K$  on prediction of liquefaction resistance is shown in Figure 4.15. To make this comparison, the stress ratio was expressed in terms of  $\tau_{cyc} / \sigma'_{m0}$ , where an initial mean normal stress  $\sigma'_{m0}$  is defined as  $(\sigma'_{x0} + \sigma'_{y0}) / 2$ . The  $K = 0.5$  case had initial stresses of 100 kPa and 50 kPa, and thus a mean stress of 75 kPa. The  $K = 1.0$  case had stresses of 75 kPa, and thus a mean stress of 75 kPa as well. The predicted results show that both  $K = 0.5$  and  $K = 1.0$  states liquefy in about the same number of cycles when the  $\sigma'_{m0}$  is the same. Both predictions are also close to Fraser River sand test data that were assumed to have

the same initial mean stress,  $\sigma'_{m0} = 75$  kPa. They are shown as filled circles in Figure 4.15. This is in agreement with Ishihara's finding (1996) that samples at the same density and mean stress had similar liquefaction response.

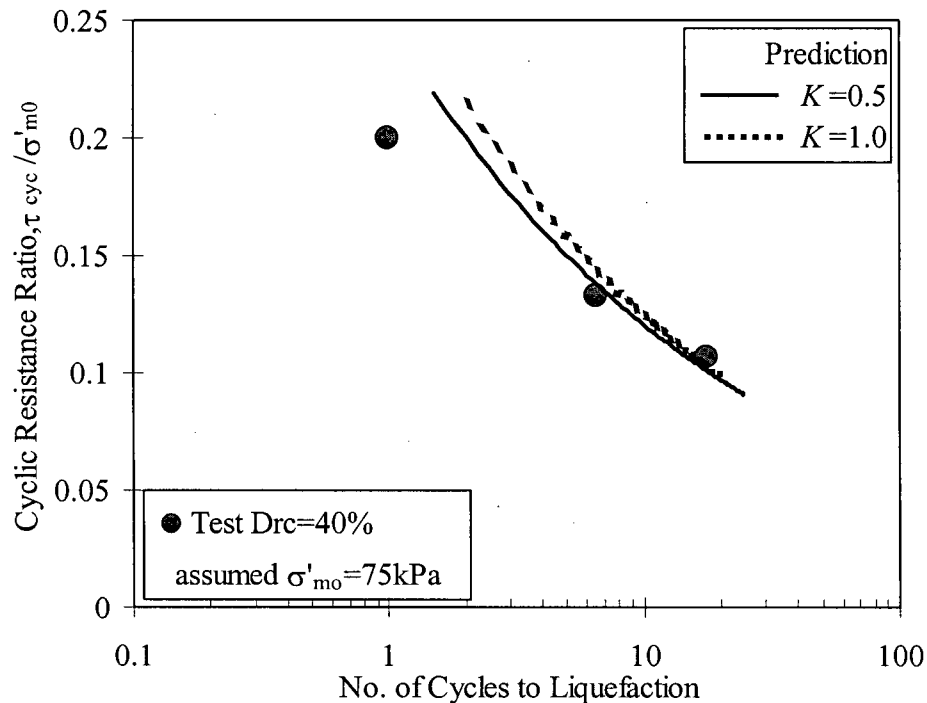


**Figure 4.15** Predicted liquefaction resistance in terms of  $\tau_{cyc}/\sigma'_{m0}$  under  $K = 0.5$  and  $1.0$  and test result (test data from Sriskandakumar, 2004).

#### 4.2.3 Prediction of Constant Volume Tests with Initial Static Shear Stress

The cyclic behaviour of loose Fraser River sand under constant volume condition with initial static shear stress was also predicted. The level of initial static shear stress ratio  $\alpha$  ( $= \tau_{sta}/\sigma'_{y0}$ ) is defined as driving initial static shear stress,  $\tau_{sta}$ , to initial vertical effective stress,  $\sigma'_{y0}$ .  $\alpha = 0.1$  and  $\alpha = 0.05$  are used to compare the effect of stress reversal patterns in the tests. The effect of

shear stress reversal can be examined by comparing response for different values of  $\tau_{cyc}$ . UBC simple shear test data used in evaluating stress reversal patterns is summarized in Table 4.5.

**Table 4.5** Summary of selected constant volume DSS tests on loose Fraser River sand with initial static shear stress (test data from Sriskandakumar, 2004).

Test Type	$\sigma'_{y0}$ (kPa)	$D_{rc}$ (%)	$\alpha$	Stress Reversal	CSR	$N_{Liq}$ (test)	$N_{Liq}$ (predicted)
Cyclic with initial static shear stress	100	40	0.1	No reversal	0.065	15.5	19
			0.1	Intermediate	0.1	0.5	2.5
			0.05	Reversal	0.1	2.5	4.5

Left sides of Figures 4.16 to 4.18 show the results with  $\sigma'_{y0} = 100$  kPa for no reversal ( $\alpha = 0.1$  &  $CSR = 0.065$ ), intermediate reversal ( $\alpha = 0.1$  &  $CSR = 0.1$ ) and reversal patterns ( $\alpha = 0.05$  &  $CSR = 0.1$ ), respectively. It may be seen from tests with initial static shear stress that once a sample starts to dilate, it follows up and down close to the phase transformation line. When no shear stress reversal occurred, much stiffer behaviour is observed. However, the accumulated strains become larger and larger, irrespective of stress reversal patterns. In simple shear tests strains larger than 10% may not be reliable. It is important to capture this behaviour in modeling liquefaction response of soils beneath slopes.

The test specimen was first sheared to the targeted initial static shear stress under drained condition, and then a constant volume condition was imposed by fixing the top boundary. Other conditions including input parameters are the same as calibrations without initial static shear stress. The predicted stress-strain and stress paths for  $K = 0.5$  (i.e.,  $\sigma'_{y0} = 100$  kPa,  $\sigma'_{x0} = 50$  kPa) and three CSRs are shown on right sides of Figures 4.16 to 4.18. The predictions generally

have given rise to a reasonable representation for three stress reversal patterns, including accumulating pattern of shear strain.

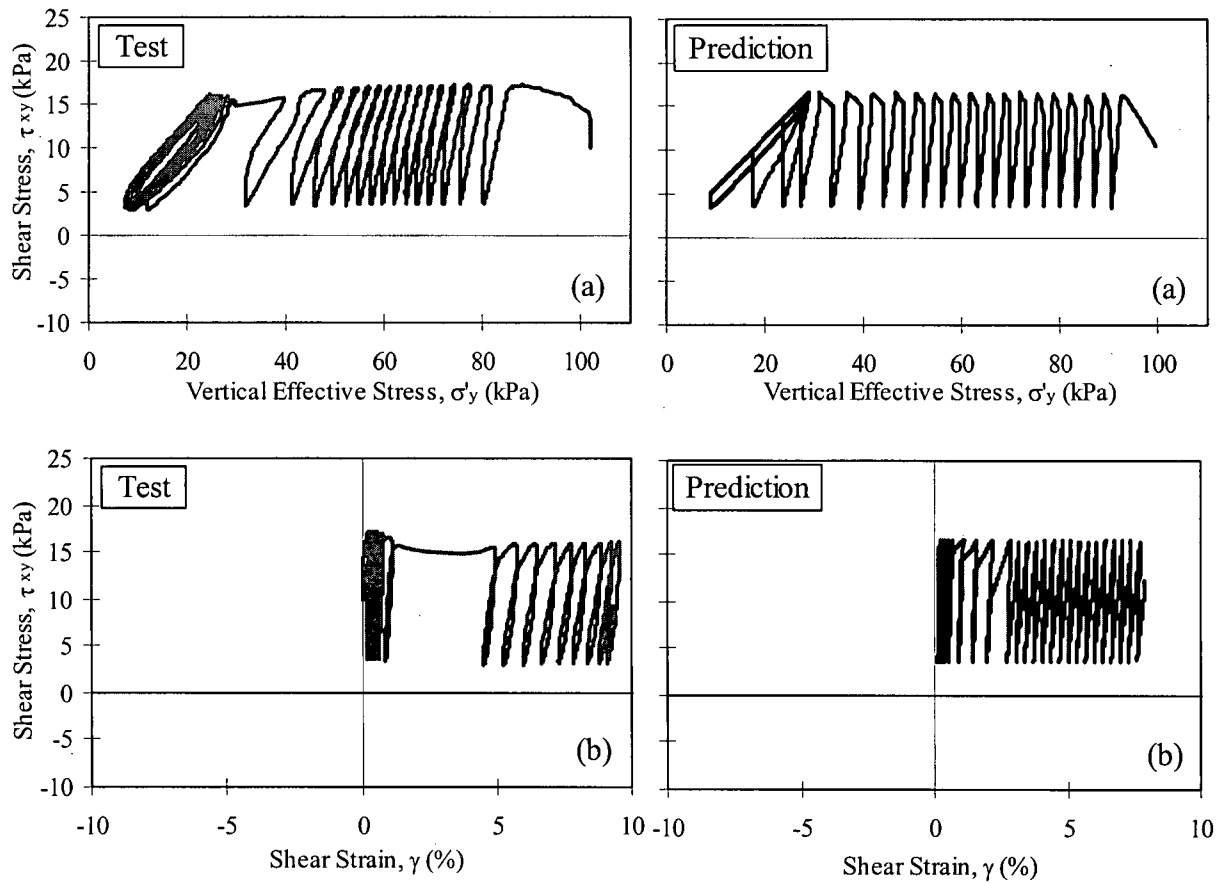


**Figure 4.16** Measured (left side) and predicted (right side) cyclic constant volume test on loose Fraser River sand with initial static shear stress ( $\alpha = 0.1$ ) under  $CSR = 0.065$ : (a) stress path, and (b) stress-strain curve (test data from Sriskandakumar, 2004).

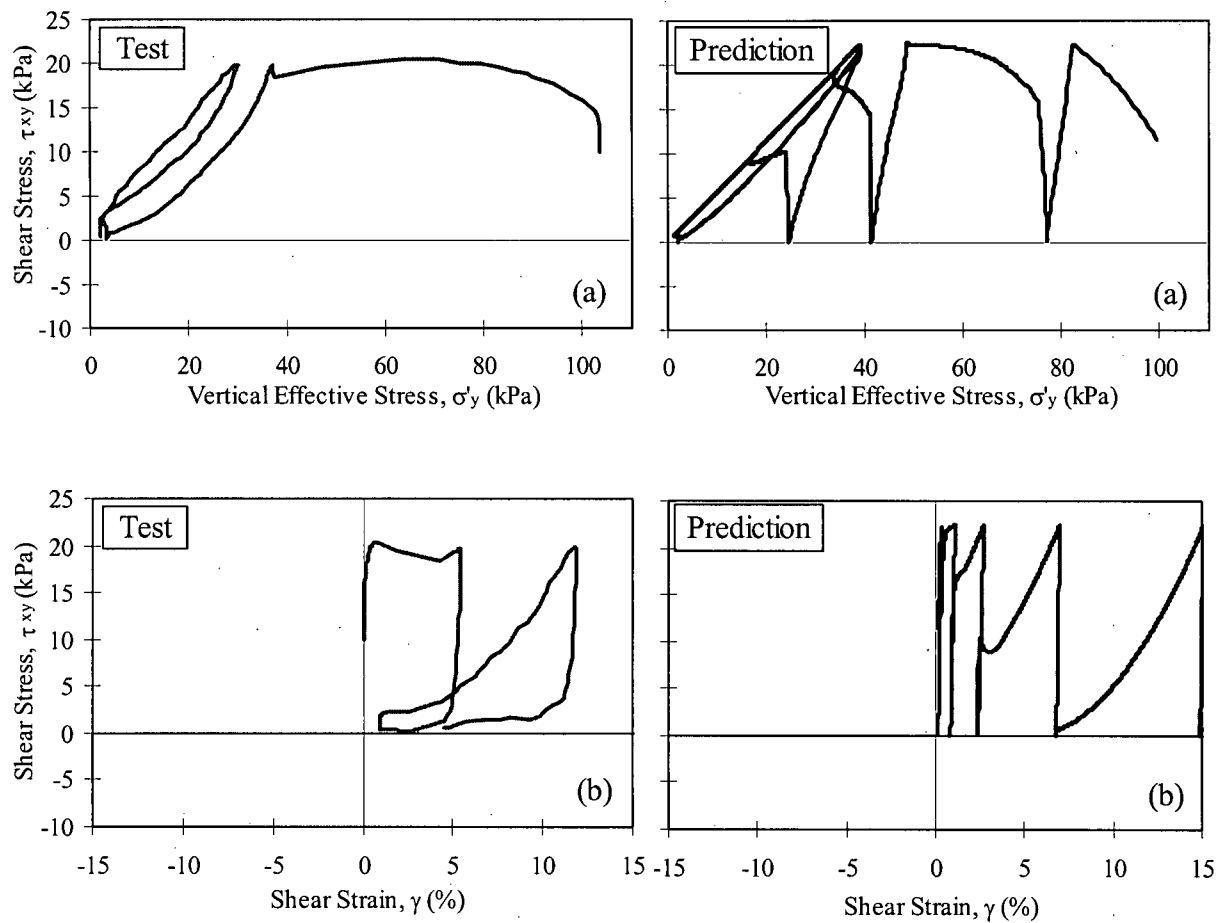


**Figure 4.17** Measured (left side) and predicted (right side) cyclic constant volume test on loose Fraser River sand with initial static shear stress ( $\alpha = 0.1$ ) under  $CSR = 0.1$ : (a) stress path, and (b) stress-strain curve (test data from Sriskandakumar, 2004).

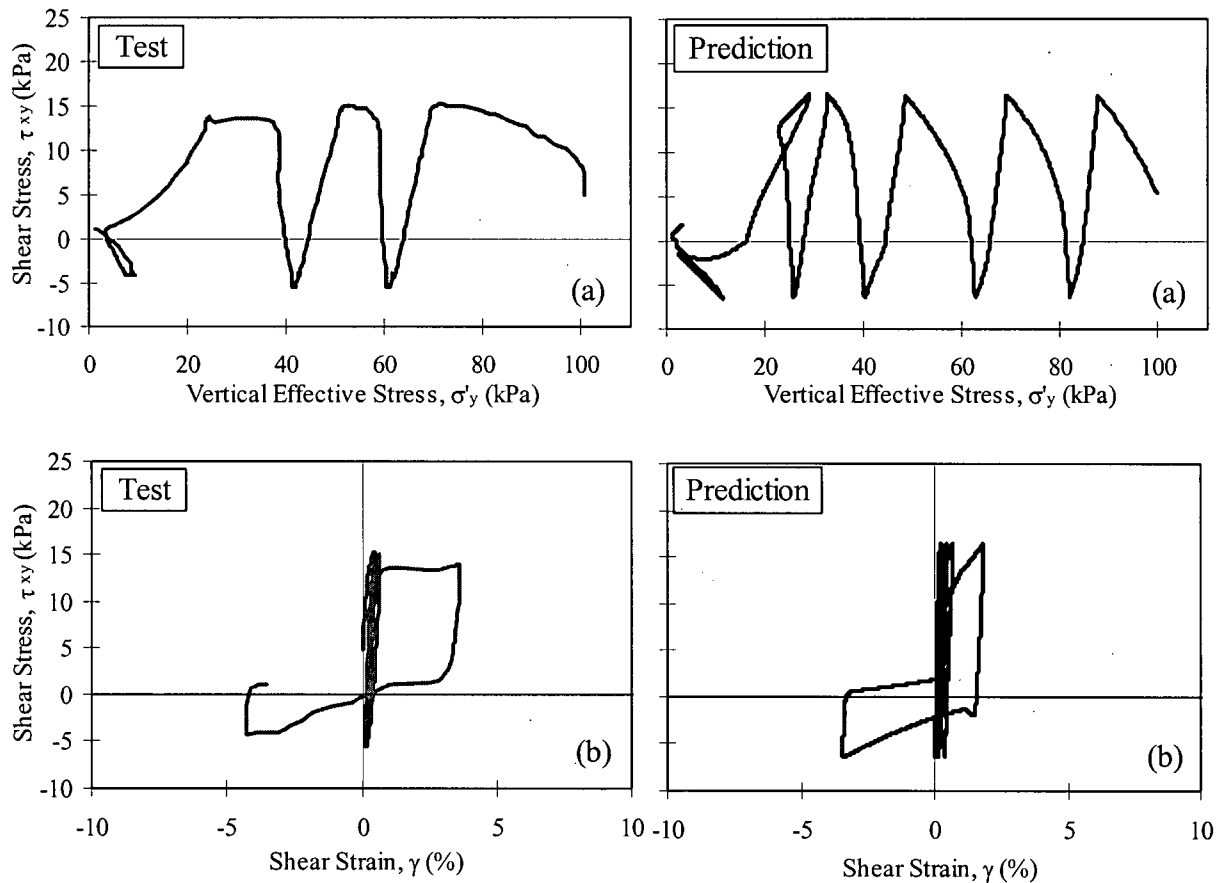


**Figure 4.18** Measured (left side) and predicted (right side) cyclic constant volume test on loose Fraser River sand with initial static shear stress ( $\alpha = 0.05$ ) under  $CSR = 0.15$ : (a) stress path, and (b) stress-strain curve (test data from Sriskandakumar, 2004).

The CSR versus number of cycles to liquefaction obtained from the numerical model is compared with laboratory data for the cases with and without initial static shear stress in Figure 4.19. For the test without stress reversal as shown in Figure 4.16,  $R_u$  never reaches zero state but results in significant accumulation of shear strain. This level of strain could result in damage or failure of some soil structures. With an initial static shear stress, the liquefaction cannot be solely defined by  $R_u$  because  $R_u$  is much less than 90%, or before reaching  $R_u = 90\%$  it causes larger displacements. Therefore, the occurrence of liquefaction was usually defined as  $\gamma > 3.75\%$ .

Without initial static shear stress ( $\alpha = 0$ ), loose Fraser River sand at  $\sigma'_{y0} = 100$  kPa delivers much higher cyclic resistance as compared to that with  $\alpha = 0.1$ . This is consistent with Harder and Boulanger (1997) but conflicts with Vaid et al.'s (2001) test results. The conflict may arise from different tests; Harder and Boulanger (1997) used data from direct simple shear and torsional simple shear tests, but Vaid et al. (2001) used data from triaxial tests. The UBCSAND2 model predicts a higher resistance at high CSR, but is in reasonable agreement at  $\text{CSR} = 0.1$  or slightly less for both  $\alpha = 0.0$  and  $\alpha = 0.1$  cases. The prediction of liquefaction resistance using the UBCSAND model is in good agreement with the laboratory data when the number of cycles to liquefaction is in the range of 5 to 10, but it overpredicts the CRR at 1 cycle.

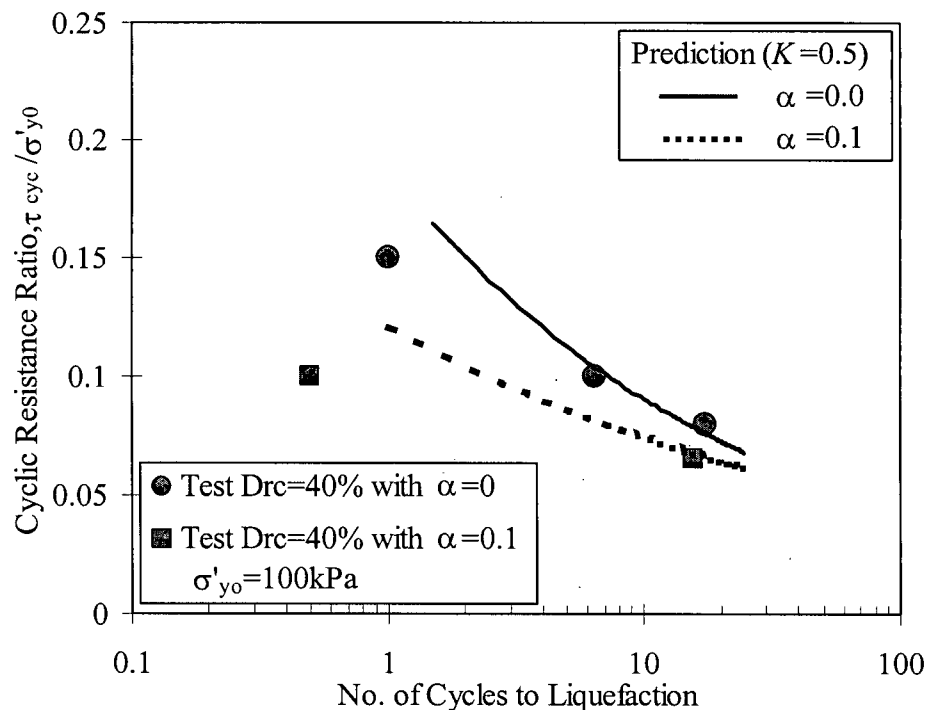


**Figure 4.19** Predicted liquefaction resistance under  $K = 0.5$  and test result with and without initial static shear stress in terms of  $\tau_{cyc} / \sigma'_{y0}$  (test data from Sriskandakumar, 2004).

### 4.3 Comparison between UBCSAND and UBCSAND2 for Simple Shear

The performance of the new model UBCSAND2 is compared with the old model UBCSAND in Figures 4.20 to 4.22. The assumption of  $K = 0.5$  and input parameters used in the prediction with UBCSAND2 were also used in the prediction undertaken employing UBCSAND.

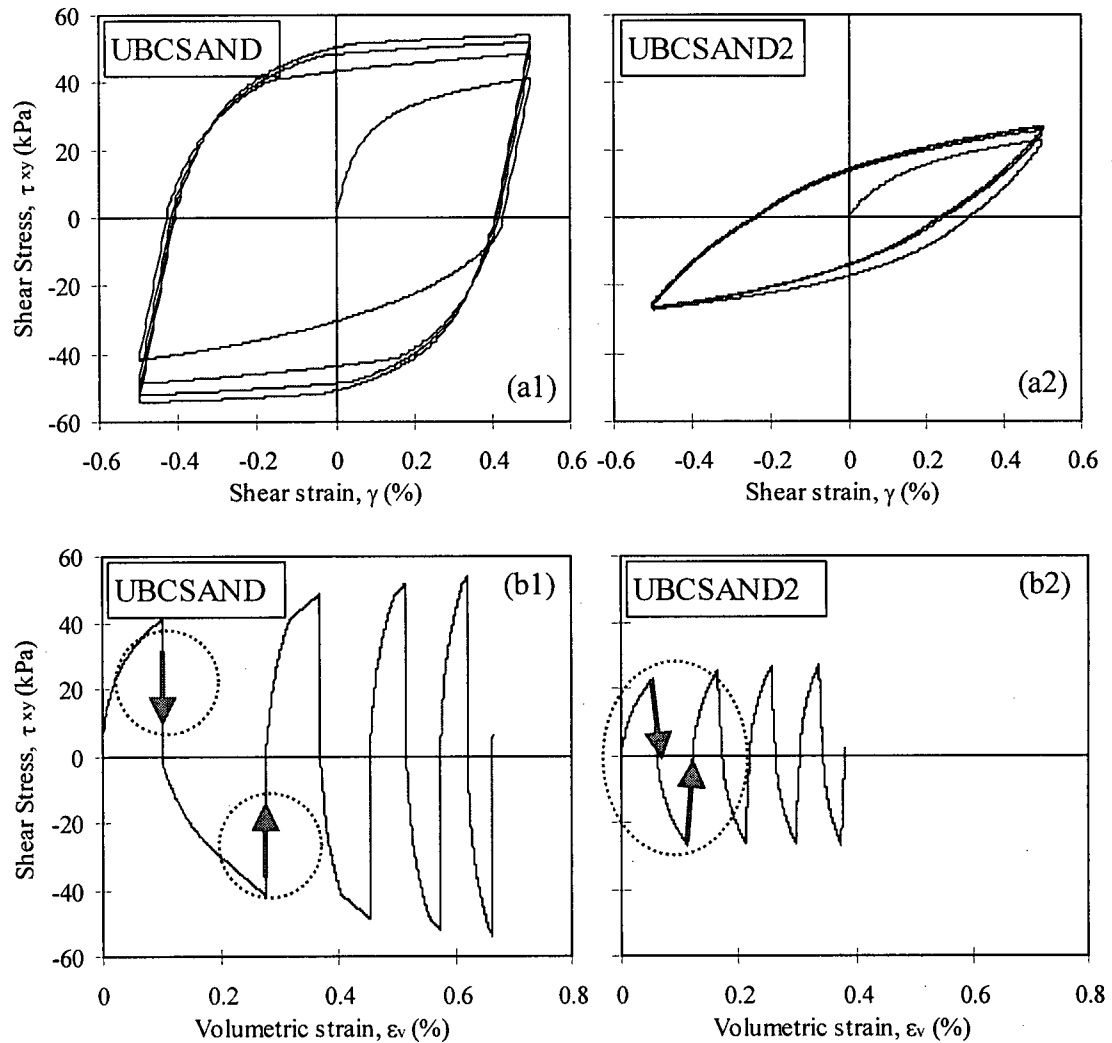


**Figure 4.20** Comparison of UBCSAND (left) and UBCSAND2 (right) using cyclic drained test on loose Fraser River sand with  $\gamma_{cyc} = 0.5\%$ : (a) shear stress vs. shear strain, and (b) shear stress vs. volumetric strain.

Figure 4.20 presents the drained DSS test response obtained using UBCSAND and UBCSAND2 (the same computations shown in Figure 4.5). As may be noted, UBCSAND computes a much stiffer stress-strain curve and a larger hysteric damping than UBCSAND2. It also becomes clear that UBCSAND is not able to compute plastic deformation (e.g., plastic volume change) during the unloading phase, as indicated by straight-downward arrows in Figures 4.20(b1).

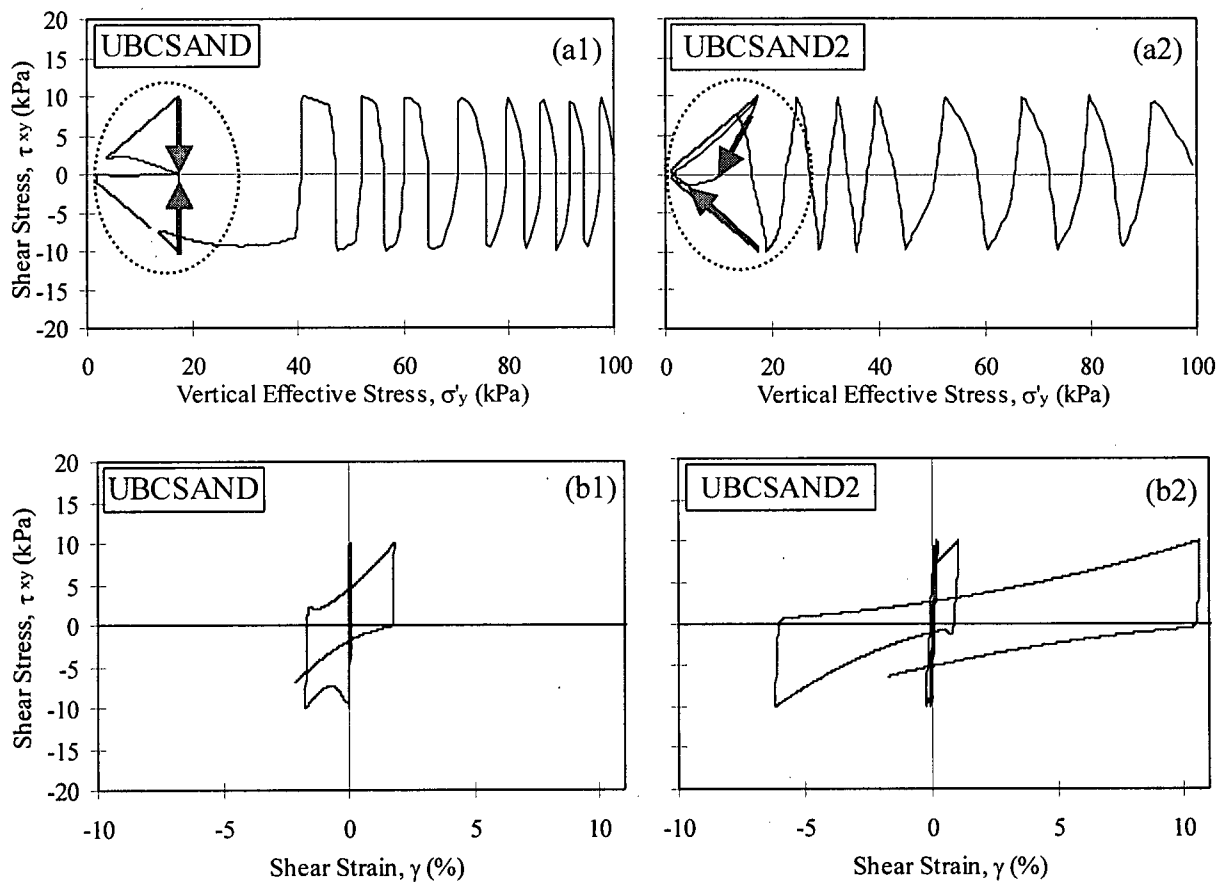


**Figure 4.21** Comparison of UBCSAND (left) and UBCSAND2 (right) using cyclic constant volume test on loose Fraser River sand under CSR = 0.1: (a) stress path, and (b) shear stress vs. shear strain.

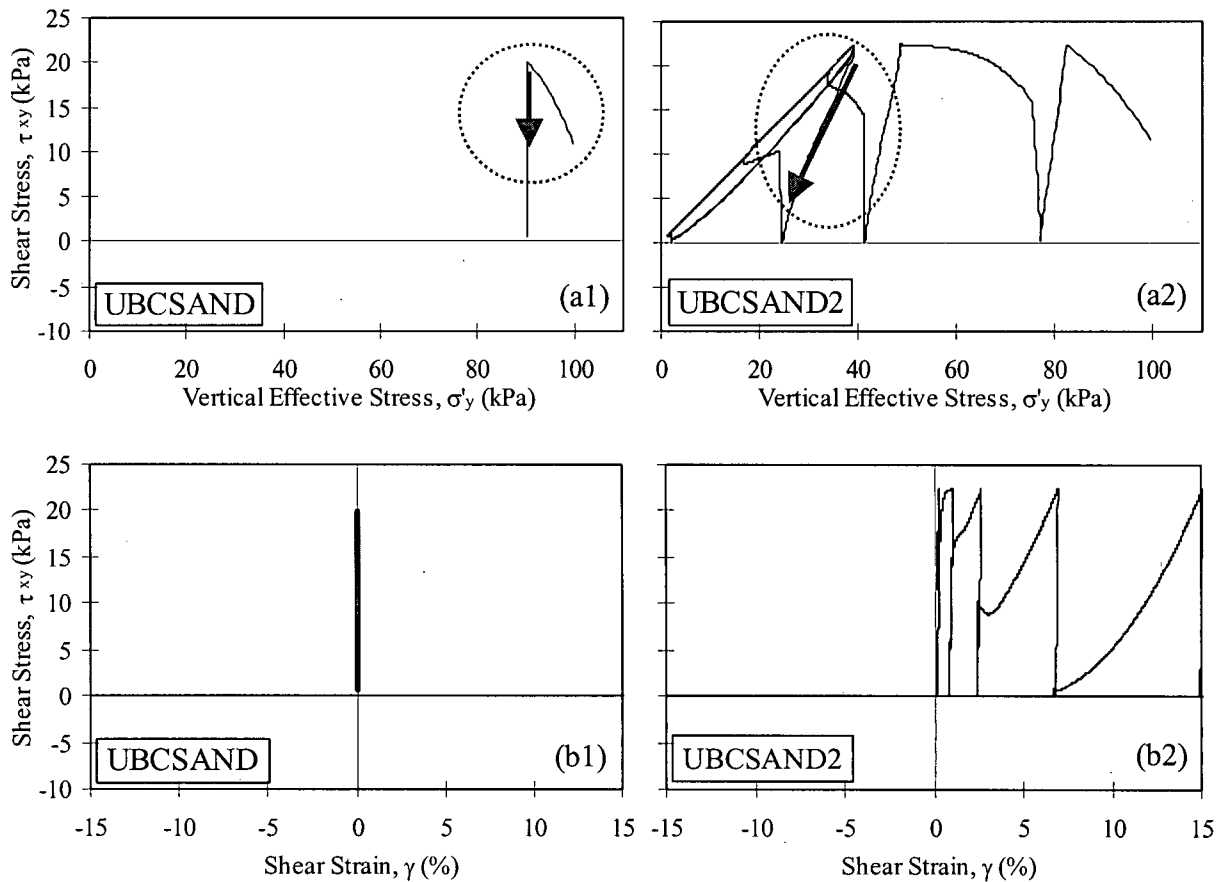


**Figure 4.22** Comparison of UBCSAND (left) and UBCSAND2 (right) using cyclic constant volume test on loose Fraser River sand with initial static shear stress ( $\alpha = 0.1$ ) under CSR = 0.1: (a) stress path, and (b) shear stress vs. shear strain.

The constant volume DSS tests with and without initial static shear stress, which were predicted earlier by UBCSAND2 and presented in Figures 4.12 and 4.17, are compared with those predicted using UBCSAND in Figures 4.21 and 4.22. Since UBCSAND cannot compute plastic deformation, no pore pressure rise is predicted from this model during the unloading phase, as indicated in Figures 4.21(a1) and 4.22(a1). As such, UBCSAND cannot simulate a test with initial static shear stress as illustrated in Figure 4.22(a1) and 4.22(b1). On the other hand, it is noted that UBCSAND2 computes plastic deformation (i.e., pore pressure rise) during the unloading phase as indicated by arrows inside circle in Figures 4.21(a2) and 4.22(a2), which is

consistent with data from DSS tests (Sriskandakumar, 2004). The ability to predict plastic unloading effects and the ability to account for rotation of principal stresses were the two major goals in developing UBCSAND2.

#### 4.4 General Calibration

The second part of the calibration process is referred to as “general calibration” because the model was applied to capture the general behavioral aspects of sand under given loading conditions. The general calibration comprises a part of the “Laboratory calibration” in Figure 4.1. As such, the calibration is still carried out using a single element of unit dimensions, and it addresses two subjects: volume change, and liquefaction triggering based on NCEER chart (Youd & Idriss, 1997). The details of this calibration are summarized in Table 4.6.

**Table 4.6** General calibration procedure of UBCSAND2.

Subject	Details	References
Volume change	Volumetric strain ( $\gamma_{cyc} = 0.1\%$ ) vs. Number of cycles	Martin et al. (1975)
	Volumetric strain ratio vs. Number of cycles	Tokimatsu & Seed (1987)
	Volumetric strain at 15 cycles vs. Shear strain	Tokimatsu & Seed (1987)(test data from Silver & Seed, 1971)
Liquefaction triggering	CSR, $(N_1)_{60}$ (or $D_r$ )	NCEER (Youd & Idriss, 1997)

#### 4.4.1 Volume Change during Cyclic Loading

The accumulated volume change during cyclic loading was captured as the initial part of this calibration. The hardening function of stress-dilatancy equation (see Eq.[3-33] in Section 3.4.4) was used to simulate the observed decreasing volumetric strain increments from cycle to cycle.

Martin et al. (1975) carried out constant amplitude cyclic simple shear tests using crystal silica sand with different levels of shear strain (e.g., 0.1%, 0.2%, and 0.3%). The increments of volumetric strain from these tests were decreasing from cycle to cycle, regardless of shear strain levels. Initial conditions are  $D_{rc} = 45\%$  and  $\sigma'_{y0} = 200$  kPa. Results from one ( $\gamma_{cyc} = 0.1\%$ ) of the tests was modeled by assuming  $K = 0.5$  (i.e.,  $\sigma'_{y0} = 200$  kPa,  $\sigma'_{x0} = 100$  kPa) to illustrate the performance of the cyclic volumetric hardening function. Input properties are listed in Table 4.7. The test results and calibration are compared in Figure 4.23. As may be noted, the volumetric hardening characteristic is well captured by UBCSAND2.

**Table 4.7** Input parameters for  $D_r = 45\%$ .

Parameter	Symbol	Value
Elastic shear modulus number	$k_G^e$	622
Bulk modulus factor	$\alpha_B$	0.7
Plastic shear modulus number	$k_G^p$	192
Friction angle at constant volume	$\phi_{cv}$	33°
Peak friction angle	$\phi_f$	35.3°
Failure ratio	$R_f$	0.92
Cyclic hardening shape parameter	$C_h$	1.6

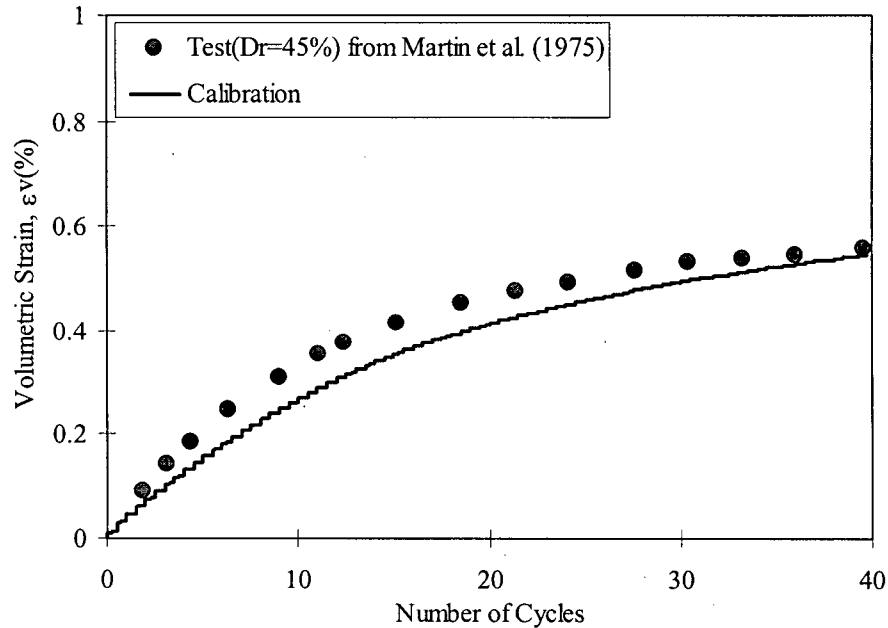


**Figure 4.23** Volumetric strains from constant amplitude ( $\gamma_{cyc} = 0.1\%$ ) cyclic simple shear and calibration (test data from Marin et al., 1975).

Silver and Seed (1971) investigated the volume change of a uniform crystal silica sand at various densities and relatively small shear strain levels (i.e., about 0.01% to 0.5%) under cyclic simple shear loading. Based on test data from Silver and Seed (1971), Tokimatsu and Seed (1987) have presented accumulated volumetric strains after 15 cycles for a range of cyclic shear strains and relative densities. Then data for loose sand ( $D_r = 45\%$ ) are shown in Figure 4.24. Calibrations were made with UBCSAND2 for a relative density of 45% at three cyclic shear strains:  $\gamma = 0.01\%$ , 0.1%, and 1%. The input parameters used in the calibration are listed in Table 4.7. The calibrated volumetric strains at the end of 15 cycles for loose sand plotted in Figure 4.24 shows that they are in a good agreement with test data for  $D_r = 45\%$ .

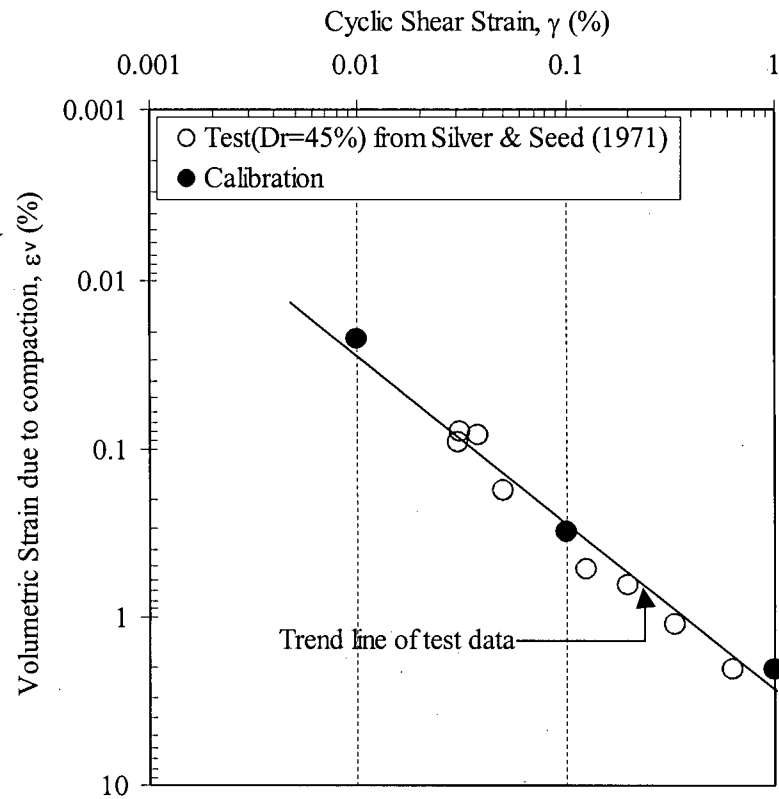


**Figure 4.24** Relationship between a volumetric strain and a shear strain for a uniform crystal silica sand (test data from Silver & Seed, 1971) and its UBCSAND2 calibration.

Tokimatsu and Seed (1987) also derived a correlation between relative density and volume change during cyclic loading of sand (Figure 4.25). The volumetric strain ratio,  $(\epsilon_v)_N/(\epsilon_v)_{15}$ , is defined as the ratio of the accumulated volumetric strain at the end of  $N$  cycles to 15 uniform cycles. A model calibration was made for a relative density of 45%, and the outcome is also presented in Figure 4.25 for comparison. Input parameters are listed in Table 4.7. The calibrated shape is found to be located between the ranges proposed by Tokimatsu and Seed (1987).

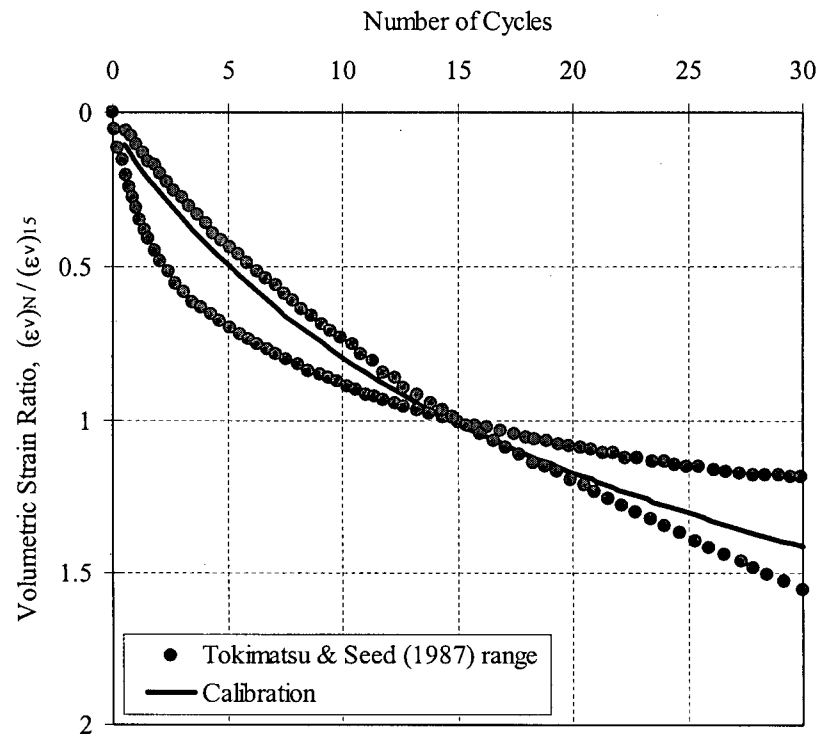


**Figure 4.25** Relationship between volumetric strain ratio and number of cycles for a uniform crystal silica sand (Tokimatsu & Seed, 1987).

#### 4.4.2 Calibration of Field Performance

UBCSAND2 was also used to calibrate liquefaction triggering response with respect to the NCEER chart (Youd & Idriss, 1997). The CSR to cause liquefaction in 15 cycles for four different densities represented by  $(N_1)_{60}$  is calibrated assuming  $K = 0.5$  (i.e.,  $\sigma'_{y0} = 100$  kPa,  $\sigma'_{x0} = 50$  kPa). Field penetration resistance has been correlated with relative density using an approximate conversion proposed by Skempton (1986):

$$\frac{(N_1)_{60}}{D_r^2} = \text{constant} \quad [4-6]$$

The constant in Eq. [4-6] ranges between 35 and 55 (Skempton, 1986). For the present study, the constant 38 was obtained for Fraser River sand by comparing field and laboratory data. The

input parameters used in the calibration of NCEER chart are listed in Table 4.8. The values of input parameters in Table 4.8 except  $\phi_{cv}$ ,  $R_f$  and  $C_h$  were basically obtained from corresponding relative density, regardless of sand types. As may be noted, the value of  $C_h$  was increased to match the number of cycles to liquefaction as density increases.

NCEER chart (Youd & Idriss, 1997) based on field experience can be well captured by the model based on  $K = 0.5$  as shown in Figure 4.26. In the modeling of laboratory tests, the cyclic stress ratio to cause a shear strain of 3.75% in 15 cycles was used as the Cyclic Resistance Ratio (CRR). The computed CRR values are also tabulated in Table 4.9. Very good agreement between the computed and field-based values of CRR can be noted suggesting the capability of the UBCSAND2 model to capture the liquefaction triggering response of sand.

**Table 4.8** Input parameters for NCEER chart calibration.

Parameter	Symbol	$(N_1)_{60}$			
		6	10	15	20
Relative density	$D_r$	40%	52%	63%	73%
Elastic shear modulus number	$k_G^e$	591	701	802	883
Bulk modulus factor	$\alpha_B$	0.7	0.7	0.7	0.7
Plastic shear modulus number	$k_G^p$	164	310	642	1159
Friction angle at constant volume	$\phi_{cv}$	33°	33°	33°	33°
Peak friction angle	$\phi_f$	34.8°	36°	37.5°	39°
Failure ratio	$R_f$	0.92	0.92	0.92	0.92
Cyclic hardening shape parameter	$C_h$	1.6	1.9	2.5	3.8

**Table 4.9** UBCSAND2 calibration at 15 cycles.

	$(N_1)_{60}$			
	6	10	15	20
Relative density, $D_r$	40%	52%	63%	73%
CRR	0.08	0.11	0.16	0.21

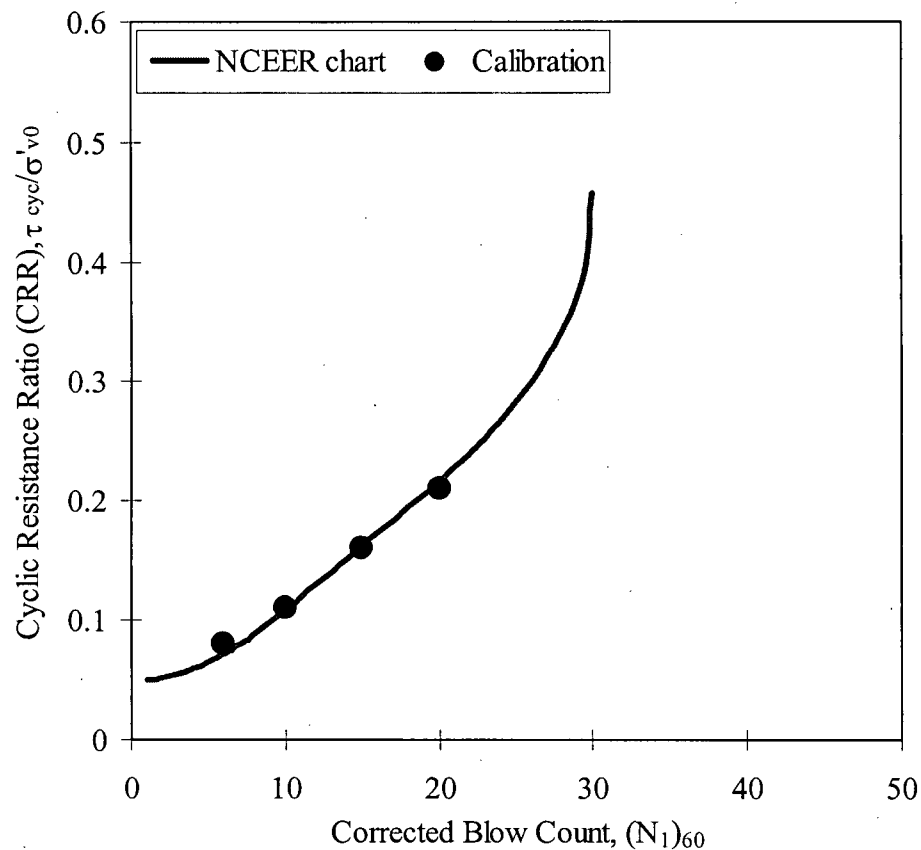


**Figure 4.26** Comparison of calibrated (UBCSAND2) and field-observed liquefaction resistance (NCEER chart from Youd & Idriss, 1997).

#### 4.5 Summary

The systematic calibration of UBCSAND2 was presented. The first stage, called “specific calibration”, was to calibrate the model with monotonic and cyclic drained behaviour of loose Fraser River sand in terms of stress-strain curve and volume change. Then, using the same soil parameters constant volume response was predicted. The model also has the ability to capture the constant volume tests with initial static shear stress. It was also shown how UBCSAND2 would model the element cyclic response of Fraser River sand in comparison to the predictions

from the old version of the model (UBCSAND), UBCSAND2 having due to the following two improvements:

- Accounting for the effect of principal stress rotation by addition of a second plane.
- Capable of plastic volumetric strains during unloading.

The second stage, called “general calibration”, was used to capture the general behaviour of loose sands under cyclic loading condition (e.g., volumetric strain response during drained cyclic loading, and liquefaction triggering based on NCEER chart).

Since the proposed model has been calibrated based on laboratory tests, it was further validated by capturing earthquake-induced deformations observed from centrifuge tests in the next chapter.

---

## Chapter 5

# Validation of UBCSAND2 using C-CORE Centrifuge Tests

Byrne and co-workers have undertaken a research project at UBC titled *Earthquake induced damage mitigation from soil liquefaction* (hereafter referred to as “UBC Liquefaction Research Project”). In the UBC Liquefaction Research Project, data from a series of dynamic centrifuge model tests conducted at C-CORE, St. John’s, NL, Canada (hereafter referred to as “C-CORE centrifuge tests”) are used to validate the state-of-the-art numerical procedures for predicting earthquake induced soil liquefaction response. As a part of this work, the UBCSAND2 model, developed herein and calibrated with laboratory element tests, was further verified by comparing to the test results from the C-CORE centrifuge. The validation of UBCSAND2 was achieved by comparing predicted and measured pore pressure, acceleration and displacement of the C-CORE centrifuge tests. The old constitutive model UBCSAND was also employed to capture several centrifuge tests on level ground during the early stage of this study, and some parts in this chapter will refer to earlier work by the author (Park & Byrne, 2004a; Byrne et al., 2004a).

## 5.1 Modeling of Sloping Ground

As discussed previously, failure due to earthquake loading is caused not only by reaching a state of zero effective stress but also by large residual deformations that can occur under non-zero effective stress states. As noted from the centrifuge tests conducted at the Engineer Research and Development Center (ERDC) and Rensselaer Polytechnic Institute (RPI) (Byrne et al., 2004a), 100% pore pressure rise and liquefaction occurred under level ground conditions, but residual shear displacements were small as there was no driving static shear stress. On the other hand, the C-CORE centrifuge tests with sloping ground sites indicate that 100% pore pressure rise may not occur, but displacements can be large due to driving static shear stress and non-reversing cyclic shear stress (C-CORE, 2005). Three patterns of cyclic loading that can occur under initial static shear stress conditions are explained in Figure 5.1 (Hyodo et al., 1991). The patterns depend on, whether the cyclic shear stress,  $\tau_{cyc}$ , is larger, equal to, or smaller than the initial static shear stress,  $\tau_{sta}$ . UBCSAND2 was used to capture these different stress reversal patterns as observed in UBC simple shear tests in Chapter 4.

UBCSAND had been applied to a dynamic centrifuge test on sloping ground tested by Taboada et al. (2002). The predicted excess pore pressures, accelerations and displacements were compared with the measurements (Park & Byrne, 2004b). The shear stress reversal patterns depend on static and cyclic shear stress levels, and are shown to play a key role in evaluating liquefaction response in sloping ground sites. When no stress reversals occur, the sand behaves in a stiffer manner that curtails the accumulated downslope displacements.

The effective stress approach, including the concept of shear stress reversal, can explain the different types of failure patterns observed in the vicinity of a slope. In this chapter, UBCSAND2, that was previously calibrated with cyclic DSS tests with and without initial static

shear stress, will be further verified by capturing C-CORE centrifuge tests representing a finite steep slope.

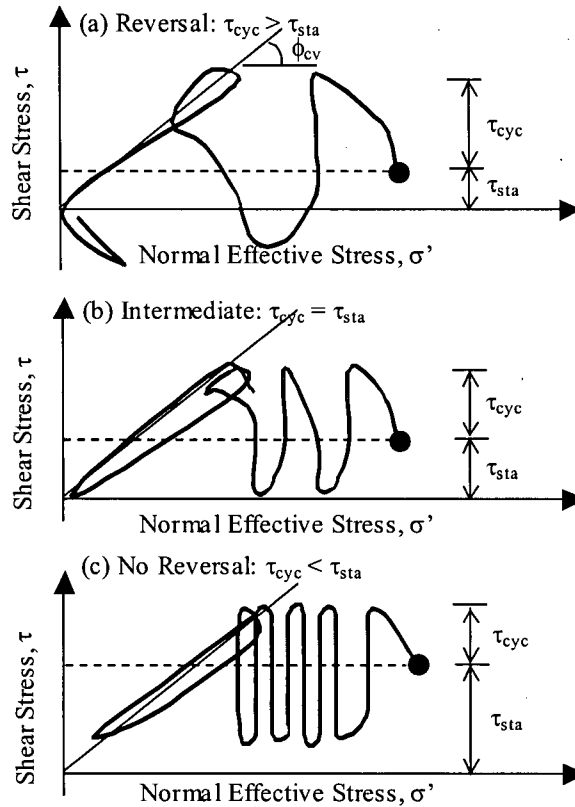


Figure 5.1 Patterns of shear stress reversal (after Hyodo et al., 1991).

## 5.2 C-CORE Centrifuge Tests for UBC Liquefaction Research Project

A series of dynamic centrifuge tests named CT1 to CT8 (C-CORE centrifuge tests) has been recently completed at C-CORE for the cooperative research project between the University of British Columbia, C-CORE, Memorial University of Newfoundland and industrial partners. The proposed centrifuge tests are summarized in Table 5.1. A475 and A2475 events indicate different applied earthquake records represented by a 10% and a 2% probability of occurrence in

a 50-year period within the Fraser River delta. All the results from these tests are available on the web site (<http://www.civil.ubc.ca/liquefaction>). The first 4 tests (CT1 to CT4) and the last 4 tests (CT5 to CT8) have different geometries. The first 4 tests have a slope with a level toe area on the right side and no impermeable (silt) layer. The last 4 tests have a slope without a level right side. The Class 'A' prediction (Lambe, 1973) of all 8 centrifuge tests using an old constitutive model UBCSAND had been carried out by Byrne and co-workers at UBC. Mehrabadi and Popescu (2004) at the Memorial University of Newfoundland had also conducted Class 'A' predictions of these tests using the DYNAFLOW™ (Prevost, 1998) program. The predictions are available on the project web site (<http://www.civil.ubc.ca/liquefaction>). Additional analyses have been conducted using the new constitutive model UBCSAND2. The test CT2 from Category I and the test CT6 from Category II are selected for the UBCSAND2 validation, since no remedial measures or impermeable layer are used.

**Table 5.1** Proposed centrifuge models at C-CORE.

Category	Test Number	Test Configuration	Earthquake event
I	CT1	Loose sand layer, No ground improvement	A475 followed by A2475
	CT2	Loose sand layer, No ground improvement	A2475
	CT3	Loose sand layer with dense dyke	A2475
	CT4	Loose sand layer with drainage dyke	A2475
II	CT5	Loose sand layer with barrier layer and 3 drainage dykes	2×A2475
	CT6	Loose sand layer	2×A2475
	CT7	Loose sand layer with barrier layer	2×A2475
	CT8	Loose sand layer with barrier layer and 3 drainage dykes	2×A2475

Analyses were carried out and all the results are presented in prototype scale. The measurements of centrifuge tests in Category I were separated into 3 characteristic zones: (i) Zone 1: Free field, (ii) Zone 2: Near-crest zone, and (iii) Zone 3: Near-slope zone as shown in Figure 5.2(a). Measured excess pore water (fluid) pressures, accelerations, and displacements at instrument locations are compared with predictions. The measurements of centrifuge tests in Category II were separated into 2 characteristic zones: (i) Zone 1: Deep zone and (ii) Zone 2: Near-slope shallow zone as shown in Figure 5.2(b).

The key information needed for numerical modeling of C-CORE centrifuge tests are given in the following sections. They include centrifuge model geometry, soil conditions, instrumentation, and earthquake input motions. More detailed information regarding the centrifuge tests can be obtained from several reports from C-CORE to UBC (C-CORE, 2004, 2005), which are also available from the web site (<http://www.civil.ubc.ca/liquefaction>).

### 5.2.1 Soil and Boundary Conditions

The cross section used in the centrifuge models is shown in Figure 5.2 and is comprised of a steep 2:1 slope in loose Fraser River sand ( $D_r = 40\%$ ). Two slightly different geometries were used for the two categories of centrifuge tests. The first geometry used in the tests CT1 through CT4 has a flat toe area on the right side as illustrated in Figure 5.2(a). The second geometry used in the tests CT5 through CT8 has no toe area on the right side as illustrated in Figure 5.2(b). The units of dimensions shown in Figure 5.2 are metres, in prototype scale. The applied centrifugal acceleration is 70 g. The tests CT1 through CT4 have dense Fraser River sand ( $D_r = 80\%$ ) in the lower region but the tests CT5 through CT8 have no dense layer in the bottom. As a remedial measure, densification and drainage dykes were compared in models CT3 and CT4.

CT5 to the CT8 were designed to study a flow slide phenomenon due to an impermeable layer (Kokusho, 1999, 2000, 2003).

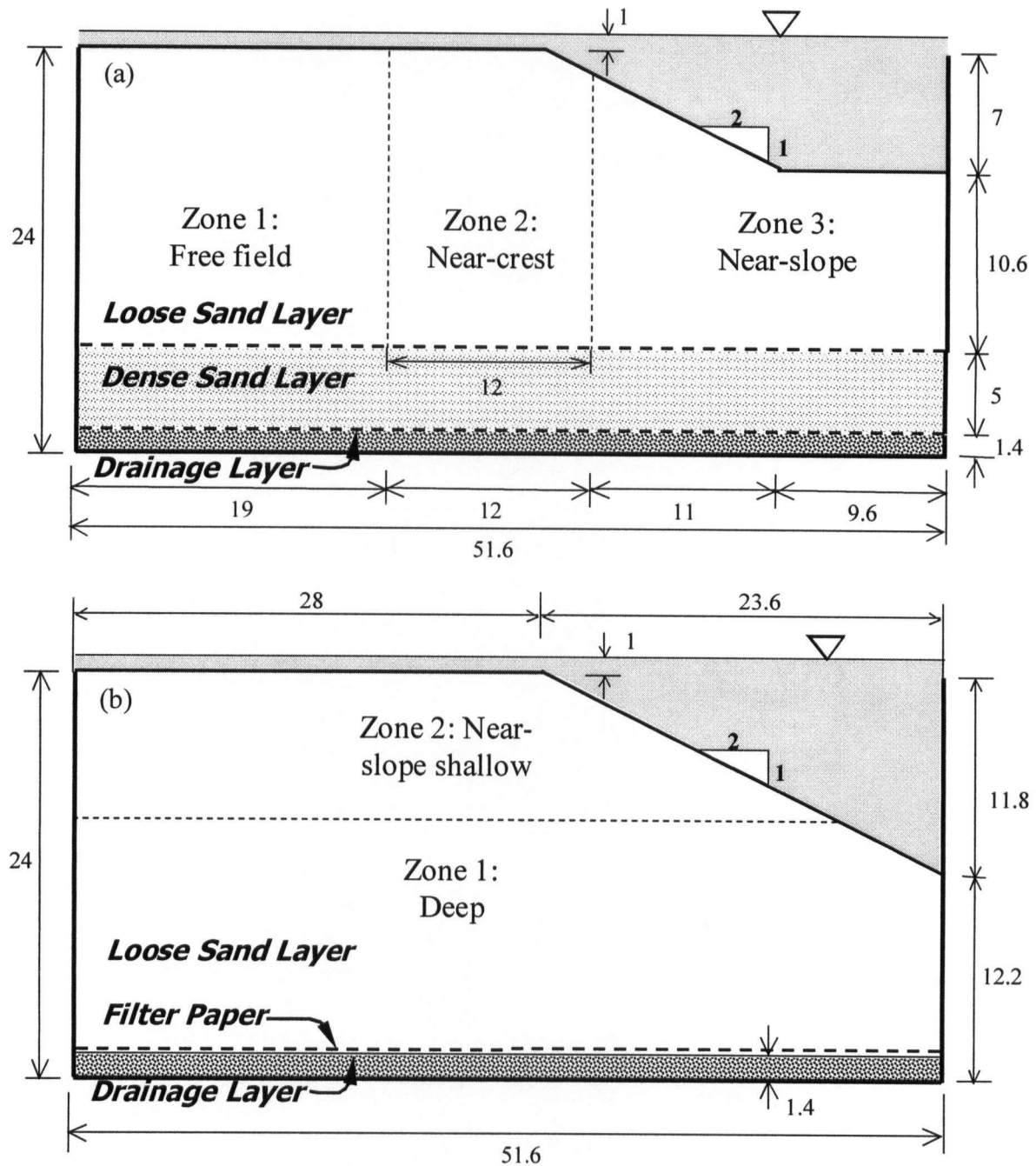


**Figure 5.2** Centrifuge model configurations: (a) Category I used for CT1 to CT4, and (b) Category II used for CT5 to CT8 (unit: m in prototype).

**(i) Boundary conditions**

- Bottom boundary is rough, and it is subject to horizontal earthquake motion.
- Left and right boundaries are fixed to base and rough.
- Earthquake time history is applied to the centrifuge box with the downslope direction designated as positive.

**(ii) Soil conditions**

Fraser River sand was used for laboratory element testing and centrifuge testing. Its basic properties are described in Section 4.2. The hydraulic conductivity for two different densities is shown in Table 5.2. A coarse sand with a  $D_{50}$  of 2.6 mm was used for drainage purposes, and its particle distribution curve is compared with one of Fraser River sand in Figure 5.3.

**Table 5.2** Soil conditions.

Layer	Sand type	Condition	Hydraulic conductivity (m/sec)
Loose Layer	Fraser River sand	Dr = 40%	4.3 E-4
Dense Layer	Fraser River sand	Dr = 80%	3.1 E-4
Drainage Layer	Coarse sand	Dense	4.0 E-2 <sup>(i)</sup>
Dense Dyke	Fraser River sand	Dr = 80%	3.1 E-4
Drain Dyke	Coarse sand	Loose	4.0 E-2 <sup>(i)</sup>

Note: (i) Approximately 100 times Fraser River sand ( $\sim 4.0 \text{ E-2}$ ) based on Hazen's equation (Lambe & Whitman, 1986b).

**5.2.2 Instrumentation Layout**

Three different transducer types: Pore Pressure transducer (PP), Accelerometer (ACC) and Linear Variable Differential Transformer (LVDT), were used in the centrifuge testing. More



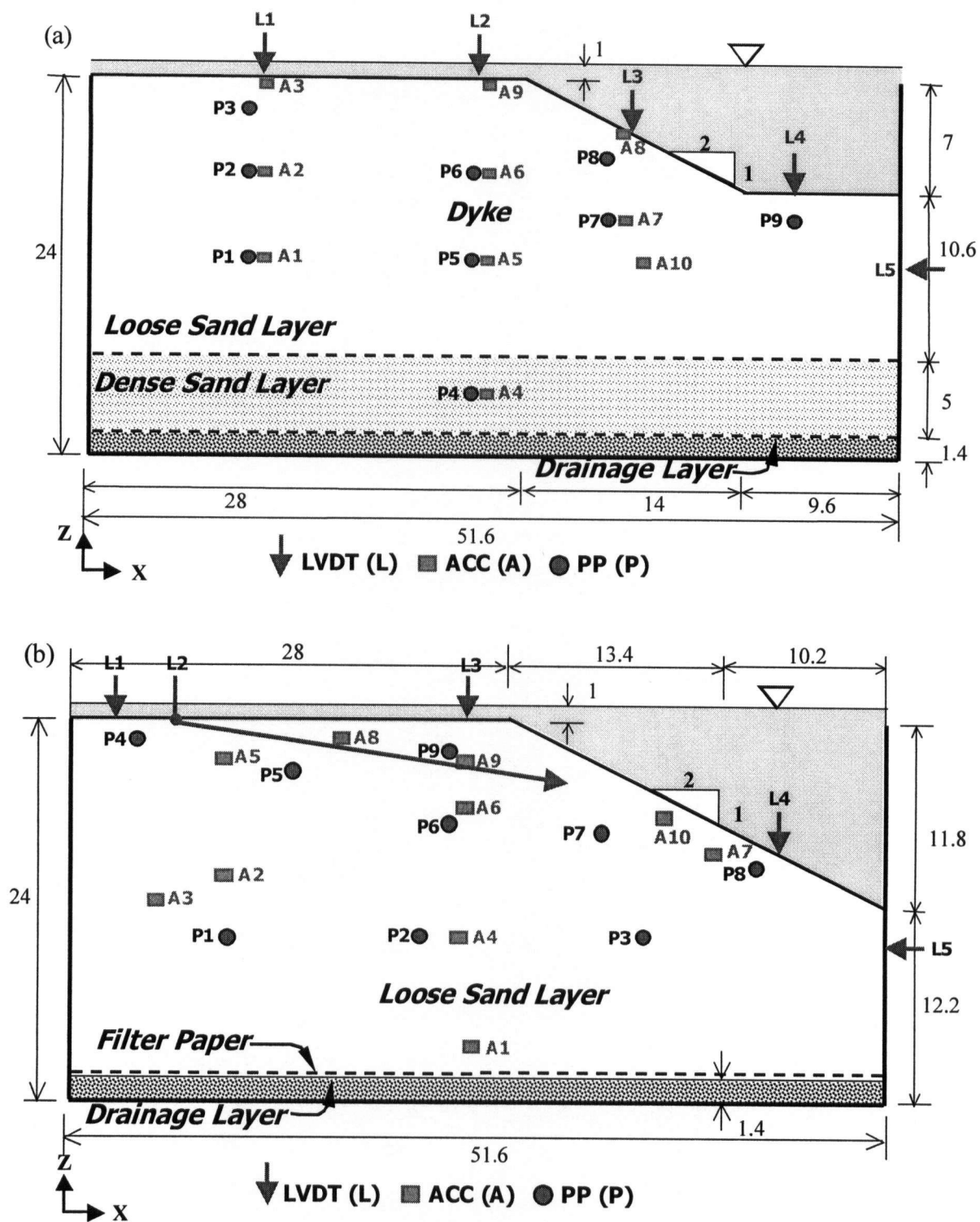


Figure 5.4 General instrumentations: (a) CT2 in Category I, and (b) CT6 in Category II (unit: m in prototype).

**Table 5.3(a)** Transducers' coordinates of CT2 in Category I (unit: m in prototype).

Transducer	$x$	$z$	$y$	Transducer	$x$	$z$	$y$
A1	11.0	12.5	-3.0	P1	10.0	12.5	-3.0
A2	11.0	18.0	3.0	P2	10.0	18.0	3.0
A3	11.0	23.5	0.0	P3	10.0	22.0	-3.0
A4	25.5	3.9	0.0	P4	24.5	3.9	0.0
A5	25.5	12.5	3.0	P5	24.5	12.5	0.0
A6	25.5	18.0	-3.0	P6	24.5	18.0	-3.0
A7	34.0	15.0	0.0	P7	33.0	15.0	-3.0
A8	34.0	20.5	3.0	P8	33.0	19.0	0.0
A9	25.5	23.5	0.0	P9	45.0	15.0	0.0
A10	36.0	12.5	-3.0	-	-	-	-
				L1	11.0	24.0	0.0
				L2	25.0	24.0	0.0
				L3	35.0	20.5	0.0
				L4	45.0	17.0	0.0
				L5	51.6	12.0	0.0

**Table 5.3(b)** Transducers' coordinates of CT6 in Category II (unit: m in prototype).

Transducer	$x$	$z$	Transducer	$x$	$z$
A1	25.7	3.7	P1	10.0	10.5
A2	9.8	14.2	P2	22.5	10.5
A3	5.6	12.6	P3	36.8	10.5
A4	25.0	10.5	P4	4.4	22.8
A5	9.8	21.7	P5	14.2	20.8
A6	25.1	18.5	P6	24.0	17.5
A7	40.8	15.6	P7	33.8	17.0
A8	17.2	23.1	P8	43.6	14.9
A9	25.1	21.5	P9	24.0	22.1
A10	32.6	19.9	L1	3.0	24.0
			L2	30.8	20.0
			L3	25.0	24.0
			L4	45.0	15.5
			L5	51.6	10.2

### 5.2.3 Earthquake Input Motions

Two earthquake input motions called A475 and A2475 were selected for the centrifuge tests (Seid-Karbasi, 2003). These will be applied in the positive direction (downslope). The proposed

two input motions are first filtered to remove high frequencies, and then baseline corrected to give zero residual displacement at the end of shaking (Seid-Karbasi, 2003). Figures 5.5(a) and 5.5(b) are A475 target motion and A2475 target motion, respectively. The actual input motion in centrifuge tests is subject to centrifuge shaker performance, and may be different from the proposed motion. The 2 times A2475 called “2×A2475” motion was applied to the tests CT5 through CT8.

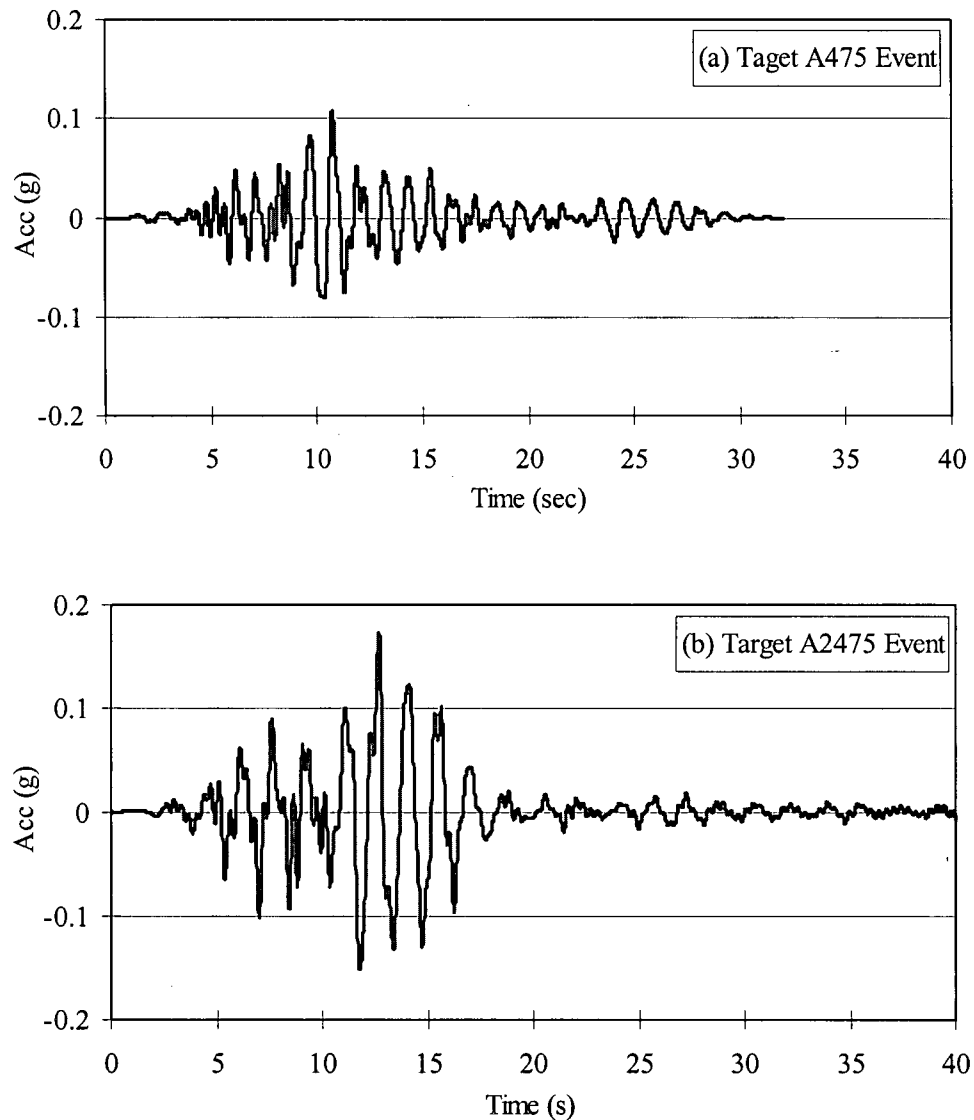


**Figure 5.5** Target earthquake input motions: (a) A475 event with 10%/50yr, and (b) A2475 event with 2%/50yr.

#### 5.2.4 Dynamic Centrifuge Testing

The dynamic centrifuge test has been used for verifying the numerical procedures for soil liquefaction since the VELAC project (Arulanandan & Scott, 1993), because it can create relatively realistic full-scale (or field) stress states and minimize much of the variability and uncertainty that is inherent in field conditions. More recently, Elgamal et al. (2002), Yang et al. (2004b), Muraleetharan et al. (2004), and Byrne et al. (2004a) have also used dynamic centrifuge tests to validate their effective stress models.

In the centrifuge test, a small model is subjected to a high acceleration field during the test. This has the effect of increasing its stresses by the ratio of the induced acceleration divided by the acceleration of gravity. This ratio is 70 for the C-CORE centrifuge tests. The centrifuge model under the increased acceleration field can also be thought of as representing a prototype that is 70 times larger than the actual model. Results from the centrifuge test can be presented at either the model or prototype scale.

While in flight, a motion simulating an earthquake time history is applied to the base of the model. For dynamic similitude at the model scale, the earthquake time scale must be decreased by a factor of 70, and the earthquake acceleration increased by the same factor. The hydraulic conductivity  $k$  will also increase by this same factor due to the increased unit weight of the fluid.  $k$  should be decreased for hydraulic similitude, although it is not necessary to model a specific  $k$ . It is common to use a fluid in the test that is 30 or 60 times more viscous than water to prevent rapid rates of dissipation that might unduly curtail liquefaction effects. In the C-CORE centrifuge test, a fluid 35 times more viscous than water was used.

The container for the centrifuge model was rigid and this was simulated in the FLAC model by applying the input motion to the vertical sides as well as the base. UBCSAND2 was

used to model two centrifuge tests, CT2 and CT6, as illustrated in Figure 5.4(a) and 5.4(b), respectively. These tests have no remediation measures and no silt layer. Their prediction will be compared with the measured response.

### **5.3 Centrifuge Testing Considerations and Inputs**

Prior to examining the centrifuge data and the results of the analyses, the effect of stress densification, pore fluid stiffness, and permeability will be addressed. These factors were considered in modeling of RPI and ERDC centrifuge tests on level ground using the UBCSAND model by Byrne et al. (2004a).

#### **5.3.1 Stress-induced Densification**

Park et al. (2004) computed excess pore pressures (EPP) with and without consideration of stress-induced densification, and compared with EPP measured from a RPI centrifuge test as shown in Figure 5.6. UBCSAND was used for numerical predictions, and details regarding the numerical model can be found in Byrne et al. (2004a). It is noted that UBCSAND has successfully predicted measured EPP by considering stress-induced densification as shown in Figure 5.6 (right side). In this regard, it is found that stress-induced densification on centrifuge tests can lead to erroneous conclusions if not taken into consideration when evaluating physical model test results as shown in Figure 5.6 (left side). This section briefly explains the concept and equation of stress-induced densification for modeling C-CORE centrifuge tests.

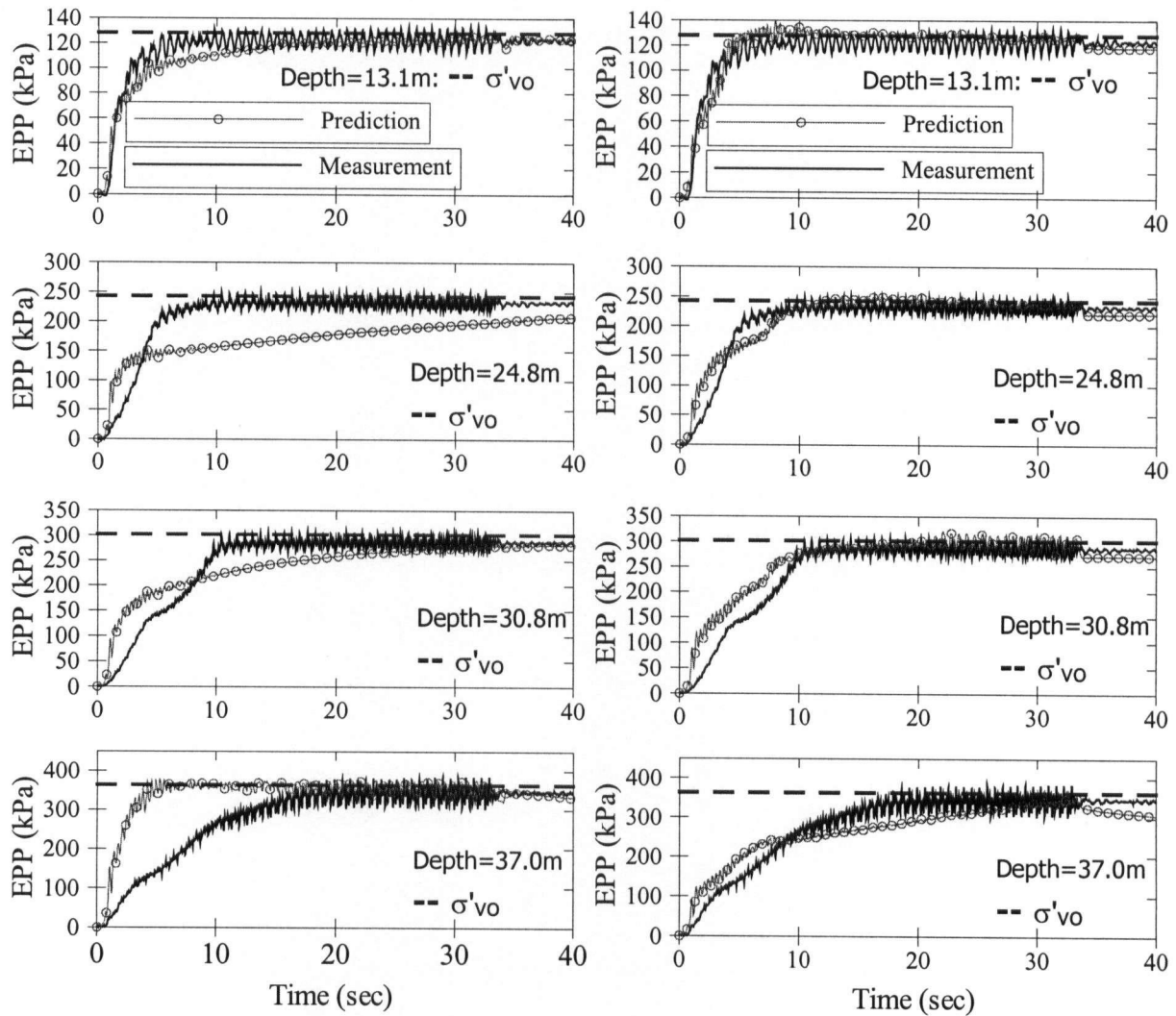


**Figure 5.6** Measured excess pore pressures (EPP) of RPI centrifuge test and predicted EPP with (right side) and without (left side) stress densification after Park et al. (2004) (measurements from Gonzalez et al., 2002).

The sand in the centrifuge model is first placed in the test box under gravity (1  $g$  acceleration field) at a specific void ratio or density. At this stage, the stresses in the model are very low and the densities are as-placed. Upon spin-up to 70  $g$ , the stresses increase 70 fold with high stresses at the base of the specimen and low stresses at the surface. In turn, these stresses induce compaction in the model causing significant increase in density at the base and little change at the surface. This increase in density can curtail liquefaction in the high stress region

near the base of the model and can be responsible for unexpected liquefaction response if it is not properly accounted in numerical modeling. For example, consider a uniform sand layer with the water table at the surface subjected to base motion causing little or no amplification. Current analysis procedures would predict liquefaction to occur first at the base and perhaps base isolate the upper layers. However, under these conditions in the centrifuge when the initial sand density is uniform, liquefaction always occurs at the surface first (Gonzalez et al., 2002; Park et al., 2004). This unexpected result is likely caused by stress-induced densification in the centrifuge.

The amount of stress densification depends on the compressibility of the soil and can be estimated from one-dimensional compression tests. The results of such compression tests on Fraser River sand (Park, 2002) are shown in Figure 5.7. It may be seen that the increase in relative density,  $D_r$ , is approximately proportional to the square root of vertical effective stress. It also depends on the placement density, with higher placement densities having less subsequent stress densification (Park & Byrne, 2004a). Park and Byrne (2004a) examined compression data on a number of sands, and found that all examined sands seem to behave in a similar manner as expressed by:

$$D_r = D_{r0} + \alpha_D \cdot \sqrt{\left(\frac{\sigma'_v}{P_a}\right)} \quad [5-1]$$

where  $\alpha_D = \left[ \frac{(1 + e_{\max})}{e_{\max} - e_{\min}} - D_{r0} \right] \cdot \frac{2 \cdot (1.5 - D_{r0})}{C}$ ,  $D_{r0}$  is initial relative density at 0 kPa,  $C$  is a sand stiffness number,  $P_a$  is atmospheric pressure and  $\sigma'_v$  is the vertical effective stress in kPa. The parameter  $\alpha_D$  in Eq. [5-1] depends on the placement relative density, and it becomes small for dense sands. The stiffness number  $C$  is a material constant not influenced by initial density and has a value of 270 for Fraser River sand. The derivation of Eq. [5-1] is presented in Appendix B.

The stiffness number for Fraser River sand is in the middle of the range of numbers noted for the examined sands (see Table B.1 in Appendix B), and thus it is considered moderately sensitive to stress densification effects. It is of interest to note that Marcuson and Bieganousky (1977) did consider stress densification effects in their large-scale chamber tests when evaluating stress and density effects on penetration resistance.

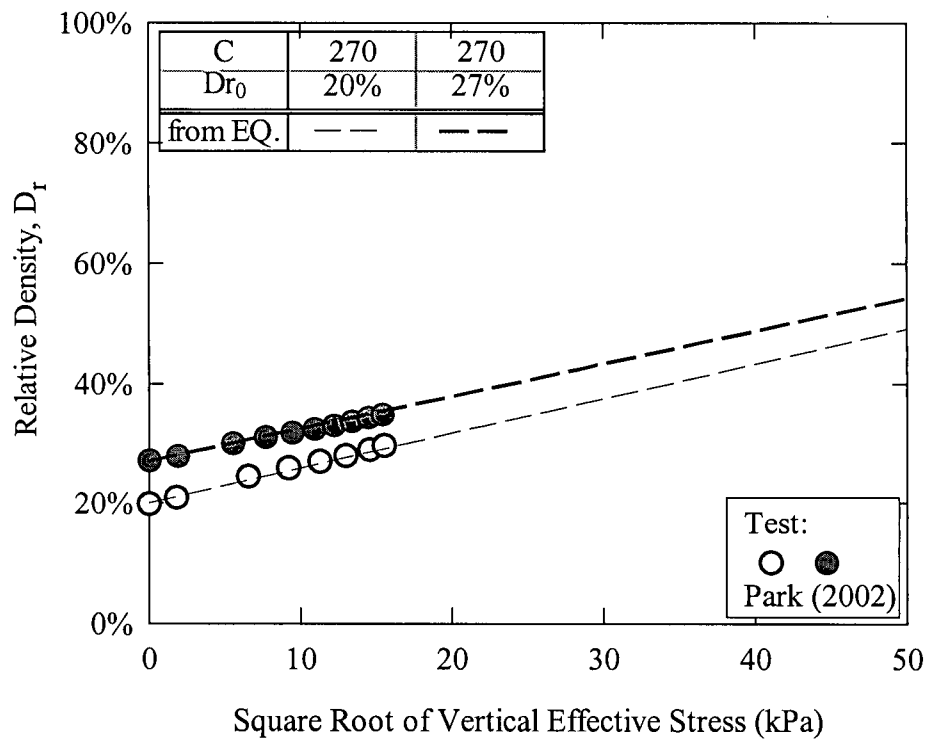


**Figure 5.7** Relative density change predicted and measured for Fraser River sand.

The effect arising from stress densification discussed above was applied during numerical modeling of loose Fraser River sand with respect to the C-CORE centrifuge tests. The loose sand layer in the C-CORE centrifuge tests was initially placed at  $D_r = 32\%$  at zero stress, and compacted and densified to  $D_r = 35\%$  due to handling (C-CORE, 2004, 2005). Assuming the relative density of the loose layer at zero stress  $D_{r0} = 35\%$ , the relative density increases from

35% to 40% at 100 kPa based on Eq. [5-1] having  $\alpha_D = 0.0503$  for  $D_{r0} = 35\%$  and Fraser River sand. The effect of stress densification on relative density  $D_r$  of the in-flight model was estimated from Eq. [5-1] and shown in Figure 5.8. This relationship indicates that  $D_r$  has increased from 35% to about 43% under vertical effective stress of 250 kPa that occurs near the base of loose sand layer.

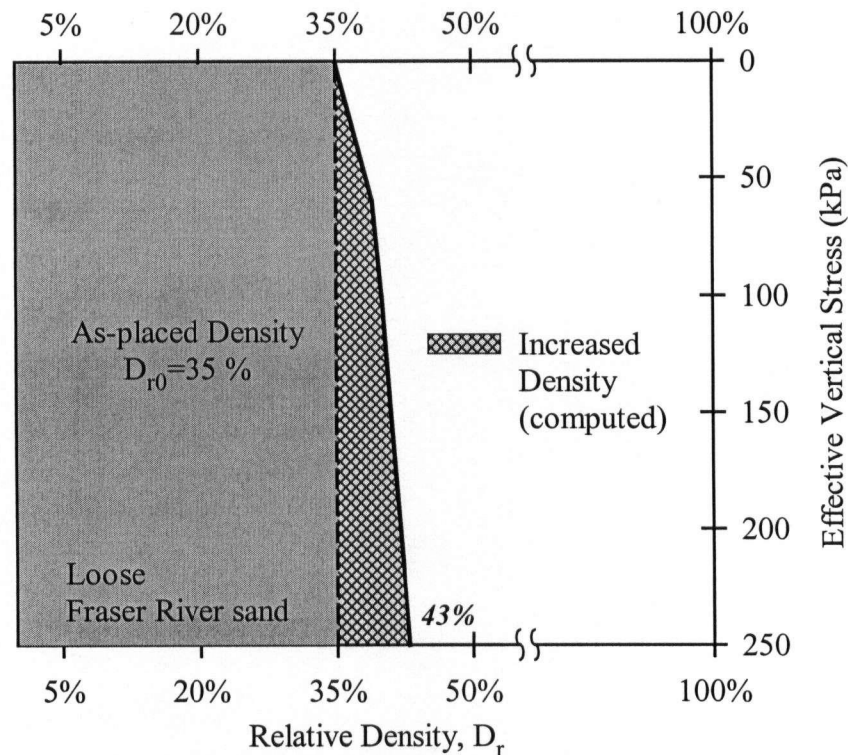


**Figure 5.8** As-placed density and increased density of C-CORE centrifuge model.

### 5.3.2 Effect of Saturation

The effect of saturation on undrained laboratory testing is well known. Poor saturation (less than 100%) gives unusually high liquefaction resistance (Xia & Hu, 1991; Ishihara et al., 2001). Even 99.3% saturated samples result in overestimation of liquefaction resistance compared to

fully saturated samples (Ishihara et al., 2001). The physics of pore pressure generation and the influence of saturation are discussed in this subsection.

The pore pressures of concern for liquefaction are those generated by plastic volumetric strains. For undrained conditions the resulting change in pore pressure,  $du$ , was derived in Appendix C as follows

$$du = \frac{B}{1 + \frac{B}{B_f/n}} \cdot d\varepsilon_v^p = B_{skem} \cdot B \cdot d\varepsilon_v^p \quad [5-2]$$

where  $B_{skem}$  is the Skempton's  $B$  value commonly used to assess the saturation of samples in the laboratory. It is clear that the ratio of the skeleton stiffness to pore fluid stiffness,  $B/B_f$ , is a major factor in pore pressure response.

The bulk modulus of the fluid,  $B_f$ , is a key parameter and can be derived from the gas laws in physics. From Boyle's law, and assuming the same pressure in both water and air,  $B_f$  is a function of  $p$ , the current absolute pressure of the fluid, and  $S_{ro}$ , the saturation at zero gauge pressure ( $p = 100$  kPa), as given by

$$B_f \cong \frac{p^2}{(1 - S_{ro}) \cdot P_a} < 2 \times 10^6 \text{ kPa} \quad [5-3]$$

$S_{ro}$  approximates the initial saturation in a centrifuge model prior to spin-up. If the pores are completely filled with water then  $B_f = 2 \times 10^6$  kPa, the bulk stiffness of water. If  $B = 6 \times 10^4$  kPa and  $n = 1/3$ , then  $B_{skem} = 0.99$  and  $du = 0.99 \cdot B \cdot d\varepsilon_v^p$ . But if the degree of saturation were reduced to  $S_{ro} = 0.98$ , then  $B_f$  drops to 5000 kPa at  $p = 100$  kPa, with  $B_{skem} = 0.2$  and  $du = 0.2 \cdot B \cdot d\varepsilon_v^p$ .

Poor saturation at low pore pressure will lead to a reduced pore pressure response to load. This is particularly so if the skeleton stiffness is high. This may occur in a centrifuge model near the water table when it is at depth or when a surface load is applied. For a water table at the surface and no surface load,  $B_{skem}$  may still be high as the skeleton stiffness will be low.

If the water pressure  $p$  in the soil increases, as it would during spin-up, then water will flow into the voids, compress the air, and increase  $B_f$ . This increase in fluid stiffness with pressure is included in Eq. [5-3]. The fluid stiffness,  $B_f$ , for a range of initial saturation and pressure conditions is shown in Figure 5.9. It may be seen that initial degrees of saturation in excess of 99.9% are required to obtain  $B_f > 5 \times 10^5$  kPa for pore pressures less than 100 kPa gauge. Such values of  $B_f$  will generally produce a liquefaction response similar to a fully saturated condition. Initial saturation is seen to be very important and can have a very large effect on pore pressure rise and liquefaction response that varies with depth in the model.

As described above, the degree of saturation plays a key role because it affects the rate of pore pressure generation. Initial saturations of 98.0% and 99.5% at 1/70 g scale were compared in the Class 'A' prediction made by Park and Byrne (2004d). The saturation and the bulk modulus of water ( $B_f$ ) will increase upon centrifuge spinup due to pore water pressure increase.

Researchers at C-CORE carried out compression wave (P-wave) tests to check the degree of saturation (C-CORE, 2004). From their P-wave tests, the initial saturation of the first 4 tests might be much lower than the 98% or 99.5% used in the Class 'A' predictions (Park & Byrne, 2004d). In this regard, the saturation between 97% and 98% will be considered in the numerical predictions of CT2 and CT6. During later tests, researchers at C-CORE pressurized the model

under more than 100 kPa for several days to achieve nearly saturated models before swinging up the centrifuge (C-CORE, 2005).

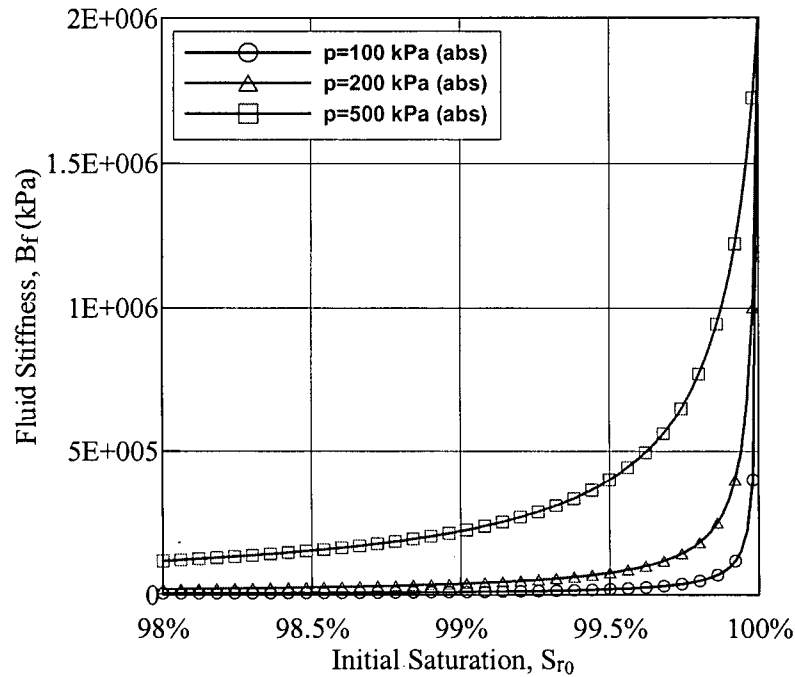


Figure 5.9 Variation of fluid stiffness on different initial saturations.

### 5.3.3 Permeability and Viscous Fluid

The hydraulic conductivity,  $k$ , used in the analyses is based on constant head permeability tests carried out by Sriskandakumar (2003) at UBC. The results are shown in Figure 5.10 where  $k$  varies between  $4.4 \times 10^{-4}$  m/sec at low relative density to  $3.2 \times 10^{-4}$  m/sec at high relative density. The hydraulic conductivity ( $k$ ) for water as a pore fluid under a 1 g field is shown in Table 5.2. For centrifuge tests in an acceleration field “ $N$ ” times greater than gravity, the effective  $k$  will be  $N$  times greater. If the viscosity of the fluid is  $M$  times greater than water as it may be for the centrifuge tests, then  $k$  would reduce by a factor  $M$ . Thus:

$$k^* = k \frac{N}{M} \quad [5-4]$$

where  $k^*$  is the effective hydraulic conductivity in the centrifuge and  $k$  is the hydraulic conductivity of the soil in a 1 g environment using water as a pore fluid. For this program,  $N = 70$  and  $M = 35$ , then  $k^* = 2 \cdot k$ . The hydraulic conductivity for loose and dense Fraser River sand, and the drainage layer is shown in Table 5.2. These values were used for the CT2 and CT6 predictions.

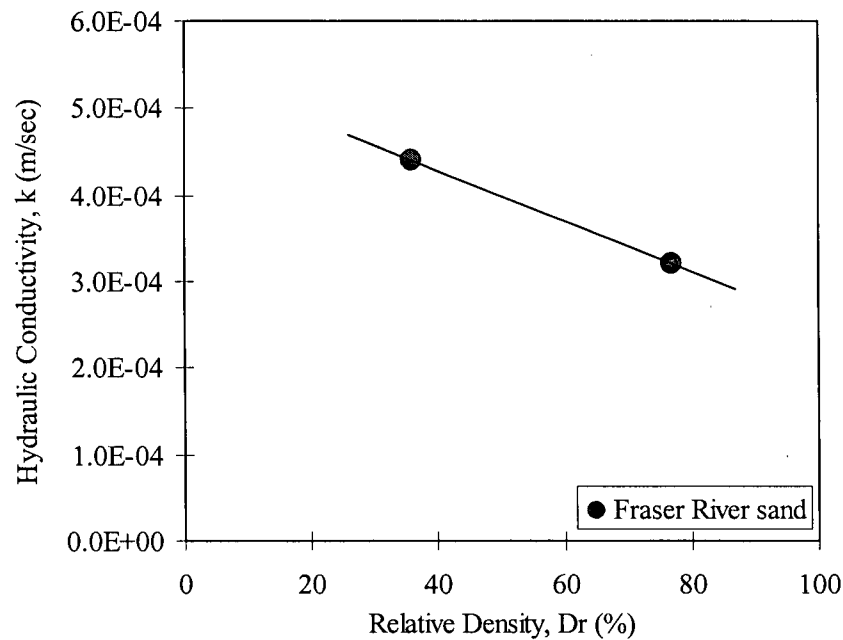


**Figure 5.10** Measured hydraulic conductivity  $k$  of Fraser River sand using water as a pore fluid (after Sriskandakumar, 2003).

Permeability used in numerical analysis will influence pore pressure dissipation more than it influences pore pressure generation. Taylor (1948) proposed an equation reflecting the influence of the permeant and the soil characteristics on permeability. A similar permeability as water at 1g can be obtained by using more viscous fluid in dynamic centrifuge tests. It is known that more viscous fluid than water used in centrifuge tests influences only dynamic flow and not

mechanical behaviour (Zeng et al., 1998). The importance of permeability in dynamic centrifuge tests was emphasized by several researchers (Okamura et al., 2001).

### 5.3.4 Input Parameters

The key elastic and plastic parameters used in UBCSAND2 can be expressed in terms of relative density,  $D_r$ . The model was made to match the observed response over the range of relative density. The predicted and observed liquefaction resistances of loose Fraser River sand were compared in Chapter 4. They are shown in Figure 5.11 and seen to be in close agreement.

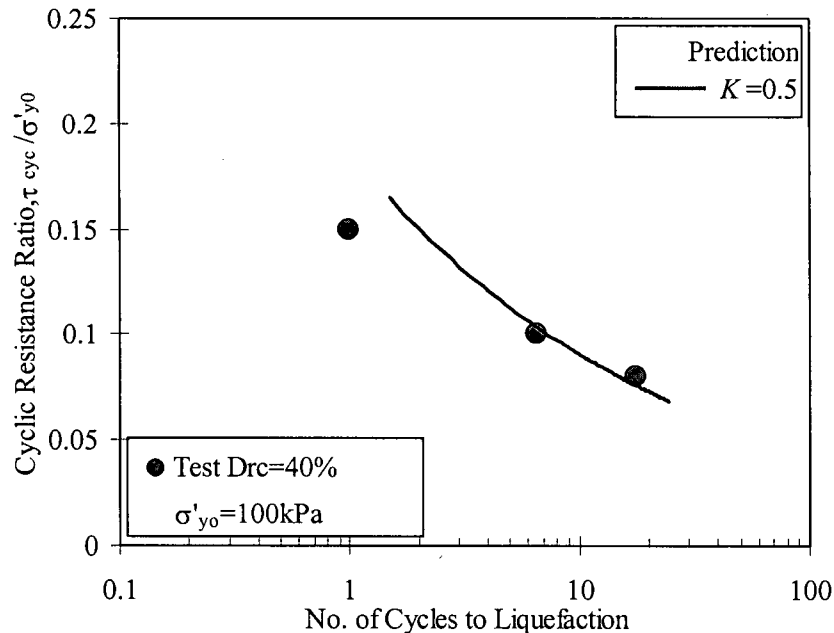


**Figure 5.11** Liquefaction resistance of loose Fraser River sand and UBCSAND2 prediction (test data from Sriskandakumar, 2004).

The elastic and plastic input parameters used in this centrifuge modeling are presented. Material zones are basically separated into loose ( $D_r = 40\%$ ) and dense ( $D_r = 80\%$ ) Fraser River sand. Bottom drainage layer is modeled as dense Fraser River sand ( $D_r = 80\%$ ) with high

permeability ( $4 \times 10^{-2}$  m/sec). Input parameters for two different density conditions are listed in Table 5.4. Input parameters for  $D_r = 80\%$  were estimated from correlations based on a relative density and calibrations of constant volume DSS tests on Fraser River sand at  $D_r = 80\%$  (Sriskandakumar, 2004).

**Table 5.4** Input parameters for C-CORE centrifuge tests, CT2 and CT6.

Parameter	Symbol	Values	
		Loose sand	Dense sand <sup>(i)</sup>
Relative density	$D_r$	40%	80%
Elastic shear modulus number	$k_G^e$	591	938
Bulk modulus factor	$\alpha_B$	0.7	0.7
Plastic shear modulus number	$k_G^p$	164	1721
Friction angle at constant volume	$\phi_{cv}$	33°	33°
Peak friction angle	$\phi_f$	34.8°	40.3°
Failure ratio	$R_f$	0.92	0.92
Cyclic hardening shape parameter	$C_h$	1.6	4.2

Note: (i) The detailed stress-strain curve and stress path of Fraser River sand at  $D_r = 80\%$  were not captured by the UBCSAND2. Instead, UBCSAND2 captured the number of cycles to liquefaction.

### 5.3.5 Criteria for Comparison between Measurement and Prediction

There are some uncertainties and difficulties encountered in modeling the C-CORE centrifuge tests. These include (a) the degree of initial saturation, (b) the exact locations of transducers during shaking, (c) permeability due to temperature change, and (d) density profiles after spin-up. The proposed constitutive model is an approximation in modeling complex skeleton behaviour during cyclic loading, and its prediction is sensitive to saturation, permeability, and relative density. In consideration of the above, the comparison between the measured and

predicted 'prototype' dynamic quantities (e.g., excess pore pressures, accelerations, displacements) for the C-CORE centrifuge tests is mainly based on the items listed in Table 5.5. The agreement is based on a mix of quantitative values and is expressed in qualitative terms as very good, reasonable, poor.

**Table 5.5** Evaluation items for the comparison between the measured and predicted C-CORE centrifuge tests.

Dynamic quantity	Evaluation items	
	During shaking	After shaking
Excess pore pressure	Peak value, rise time pattern	Pattern of dissipation rate
Acceleration	Amplitude, reduction, maximum and minimum values	N/A
Displacement	N/A	Magnitude of maximum displacement, deformation pattern

#### 5.4 Prediction of CT2 and its Comparison

The model is initially built with a lower relative density of 32% for the loose sand and 78% for the dense sand and densification occurs due to handling and spin-up (C-CORE, 2004). It is assumed for the loose sand that  $D_r$  would increase from 32% to 35% due to handling and that the increase from 35% to 40% is in accordance with Eq. [5-1]. This is considered in CT2 numerical modeling.

The CT2 is a base model of Category I with no ground improvement (densification or drainage). Only one motion, called A2475, has been applied to the model base and sides. The FLAC numerical analyses have been carried out in prototype (1 g) scale. The detailed simulation procedure by FLAC is presented in Appendix D. The target A2475 motion in Figure

5.12(a) was reasonably replicated by the Earthquake Simulator (EQS) of C-CORE centrifuge as shown in Figure 5.12(b). The actual input motion is slightly greater than the proposed one (in terms of a peak acceleration), so the actual input motion is more appropriate for the direct comparison with measurements. In the CT2 comparison with measurements the actual input motion was baseline corrected, and then applied to the model.

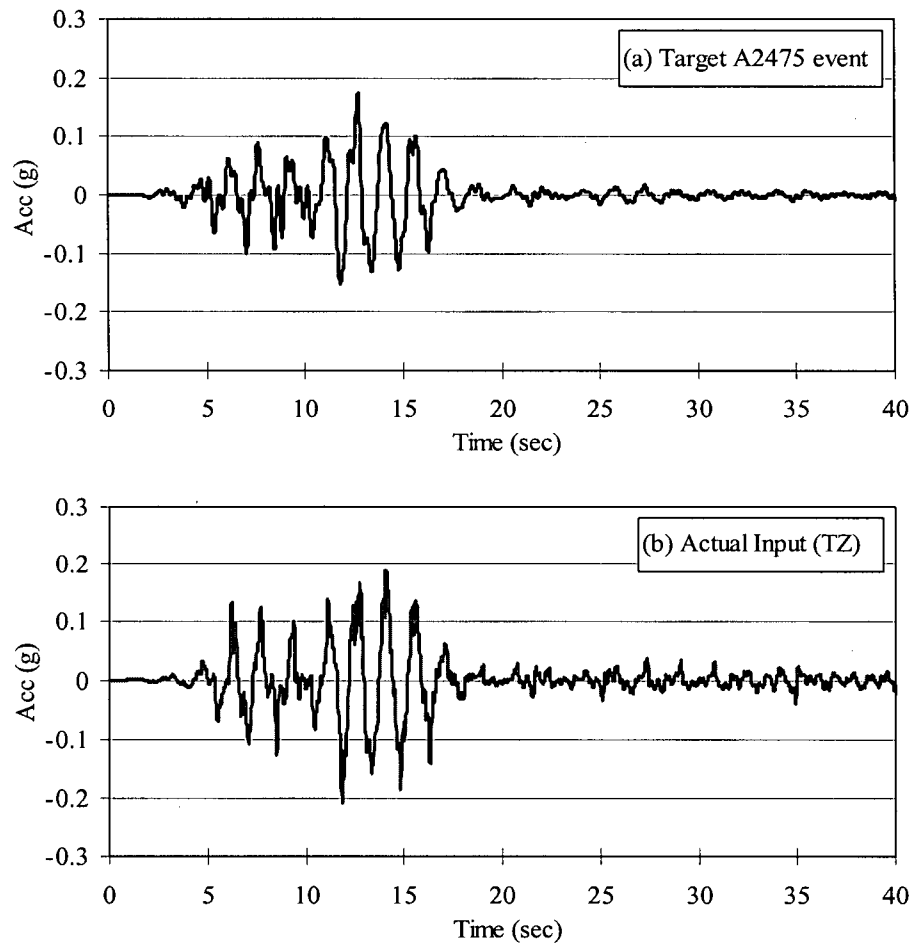


**Figure 5.12** Comparison of target A2475 motion and actual input motions applied into CT2: (a) target A2475 motion, and (b) actual A2475 input.

The comparison between test results and prediction is presented. The results are presented for three characteristic zones: (i) Zone 1: Free field, (ii) Zone 2: Near-crest zone, and (iii) Zone

3: Near-slope zone. All predictions at instrument locations are presented for one initial saturation  $S_{r0} = 97\%$  in right sides. The displacement vectors and distorted meshes are also compared.

#### 5.4.1 Measured and Predicted Excess Pore Pressures of CT2

Figures 5.13 to 5.15 compare the measured and predicted excess pore pressures at (i) Zone 1: Free field, (ii) Zone 2: Near-crest zone, and (iii) Zone 3: Near-slope zone, respectively. Figures on the left side show the centrifuge test results and figures on the right side show numerical predictions. The dotted line in each figure indicates the initial vertical effective stress ( $\sigma'_{y0}$ ) determined from the planned coordinates. This line may not be directly applicable to measured excess pore pressures (e.g., PP3 in Figure 5.13(a)) since actual locations of some transducers in the CT2 are not exactly the same as planned locations (C-CORE, 2004).

The predicted and observed excess pore pressures in the free field are shown in Figures 5.13. As expected,  $R_u$  (= excess pore pressure/ $\sigma'_{y0}$ , pore pressure ratio) of 100% at shallow depth (PP2 and PP3) is seen as similar trends observed in the level ground liquefaction centrifuge tests (Gonzalez et al., 2002). The excess pore pressure rise time for both measurement and prediction are very similar. The predicted excess pore pressure dissipation at depth (PP1) is somewhat slower than the measurement.

Generally, large pore pressure oscillations are observed except those measured in Free field area and one in dense layer (PP4). The large dilation spikes measured from PP5 in the Near-crest zone during main shaking are due to the rocking motion around the slope (C-CORE, 2004), and they are not captured by UBCSAND2. Some negative excess pore pressure spikes occur around the slope that coincide in time with the upslope acceleration spikes. As shown in

Figure 5.15, excess pore pressures measured from near slope showed most significant spikes due to dilation or rocking. UBCSAND2 predicted those pore pressure spikes due to dilation. The transducer PP4 is the only one in the dense layer, and gave less amount of excess pore pressure generation. Excess pore pressures are reasonably captured in terms of the peak values and patterns of excess pore pressure rise and dissipation by UBCSAND2.

**(i) Zone 1: Free field**

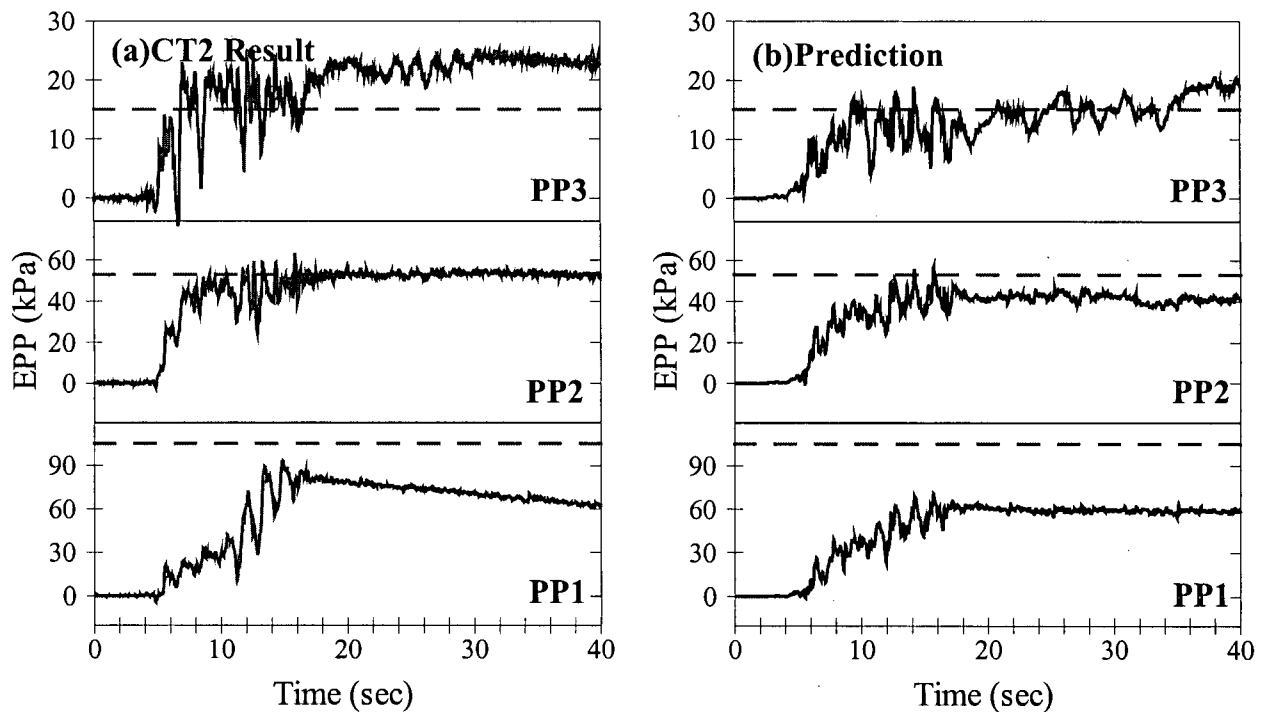


**Figure 5.13** Comparison of Excess Pore Pressures (EPP): (a) measured, and (b) predicted EPP at free field of CT2 (test data from C-CORE, 2004).

## (ii) Zone 2: Near-crest zone

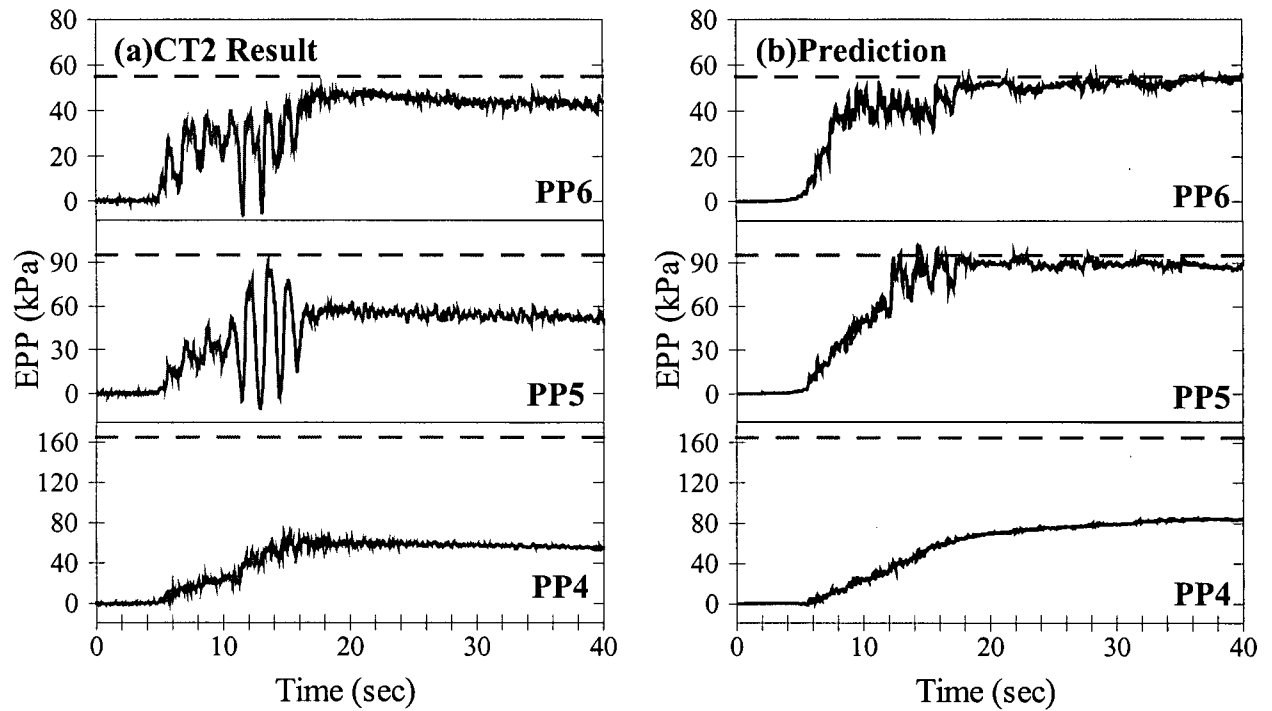


**Figure 5.14** Comparison of Excess Pore Pressures (EPP): (a) measured, and (b) predicted EPP at Near-crest zone of CT2 (test data from C-CORE, 2004).

## (iii) Zone 3: Near-slope zone

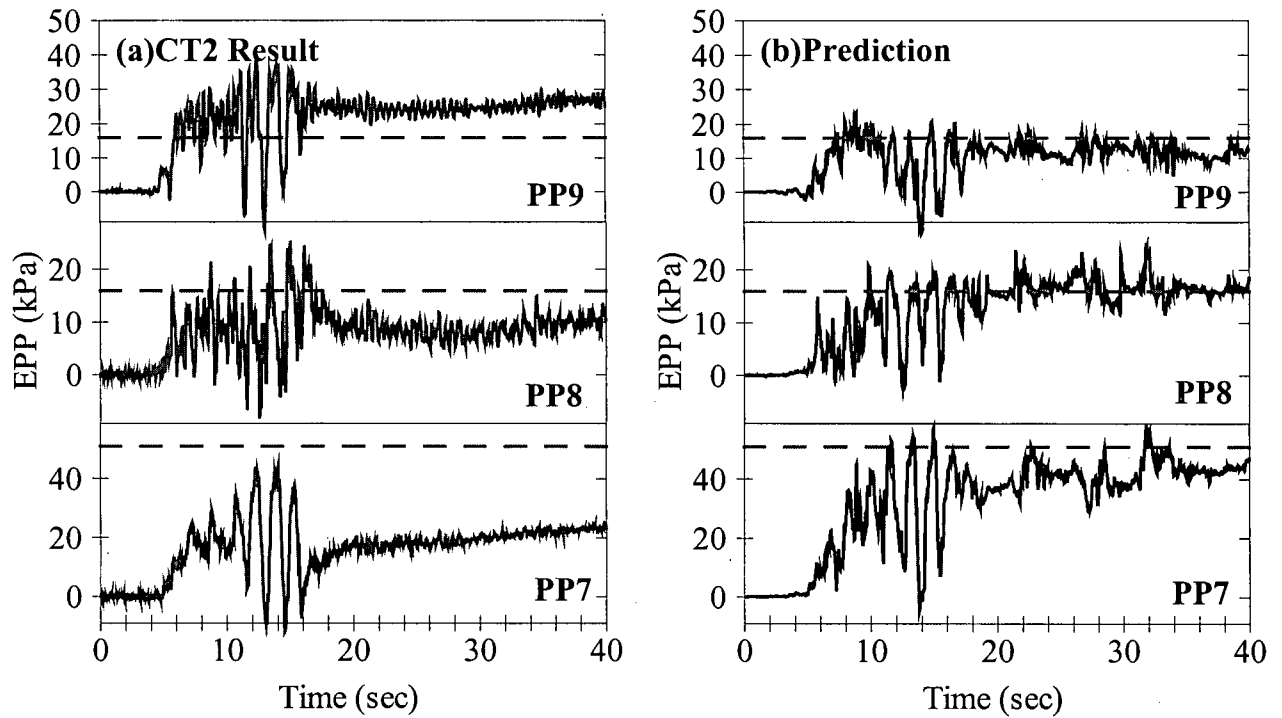
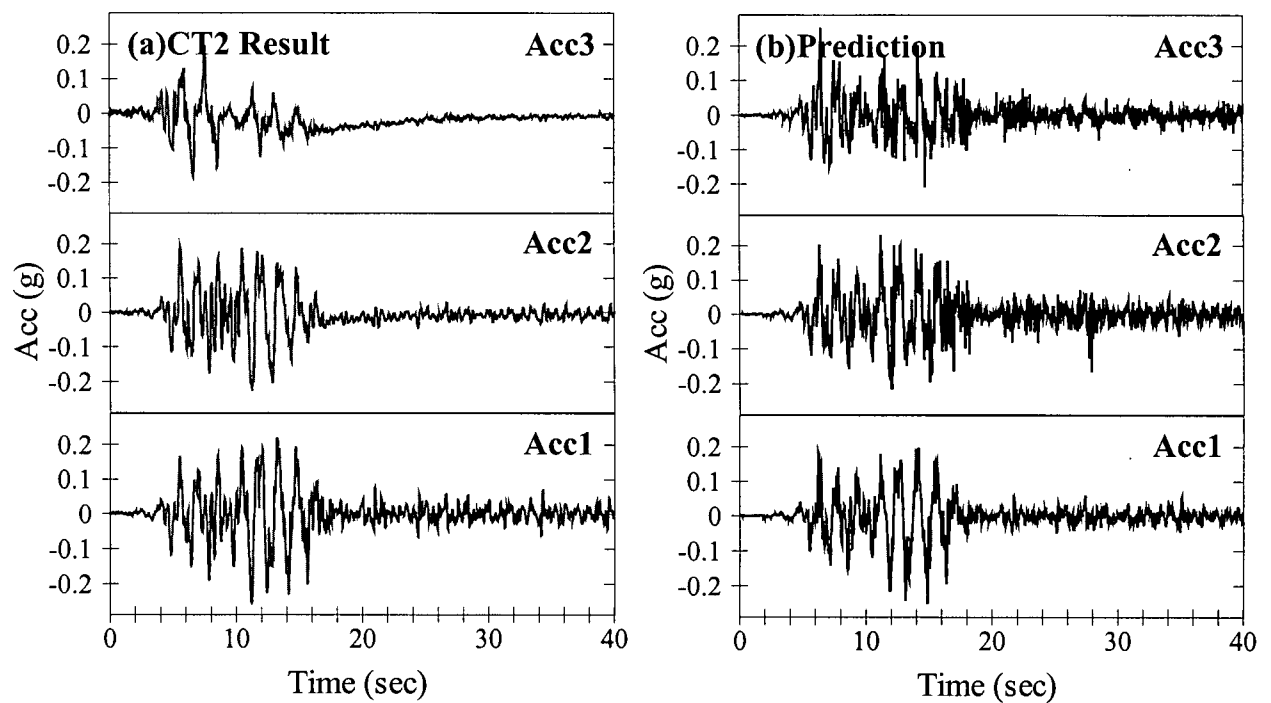


Figure 5.15 Comparison of Excess Pore Pressures (EPP): (a) measured, and (b) predicted EPP at Near-slope zone of CT2 (test data from C-CORE, 2004).

### 5.4.2 Measured and Predicted Accelerations of CT2

Figures 5.16 to 5.18 compare the measured and predicted accelerations at (i) Zone 1: Free field, (ii) Zone 2: Near-crest zone, and (iii) Zone 3: Near-slope zone, respectively. Left side figures show the centrifuge test results and right side figures show numerical predictions.

#### (i) Zone 1: Free field



**Figure 5.16** Comparison of Accelerations (ACC): (a) measured, and (b) predicted ACC at free field of CT2 (test data from C-CORE, 2004).

## (ii) Zone 2: Near-crest zone

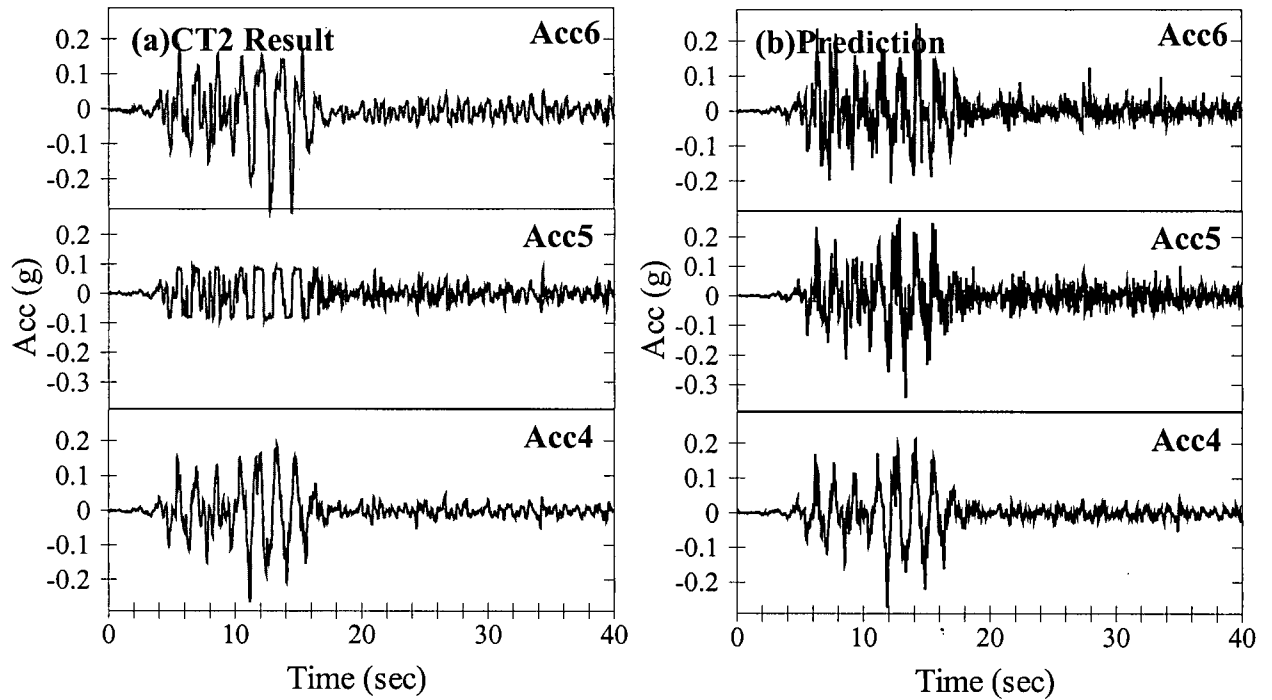


**Figure 5.17** Comparison of Accelerations (ACC): (a) measured, and (b) predicted ACC at Near-crest zone of CT2 (test data from C-CORE, 2004).

## (iii) Zone 3: Near-slope zone

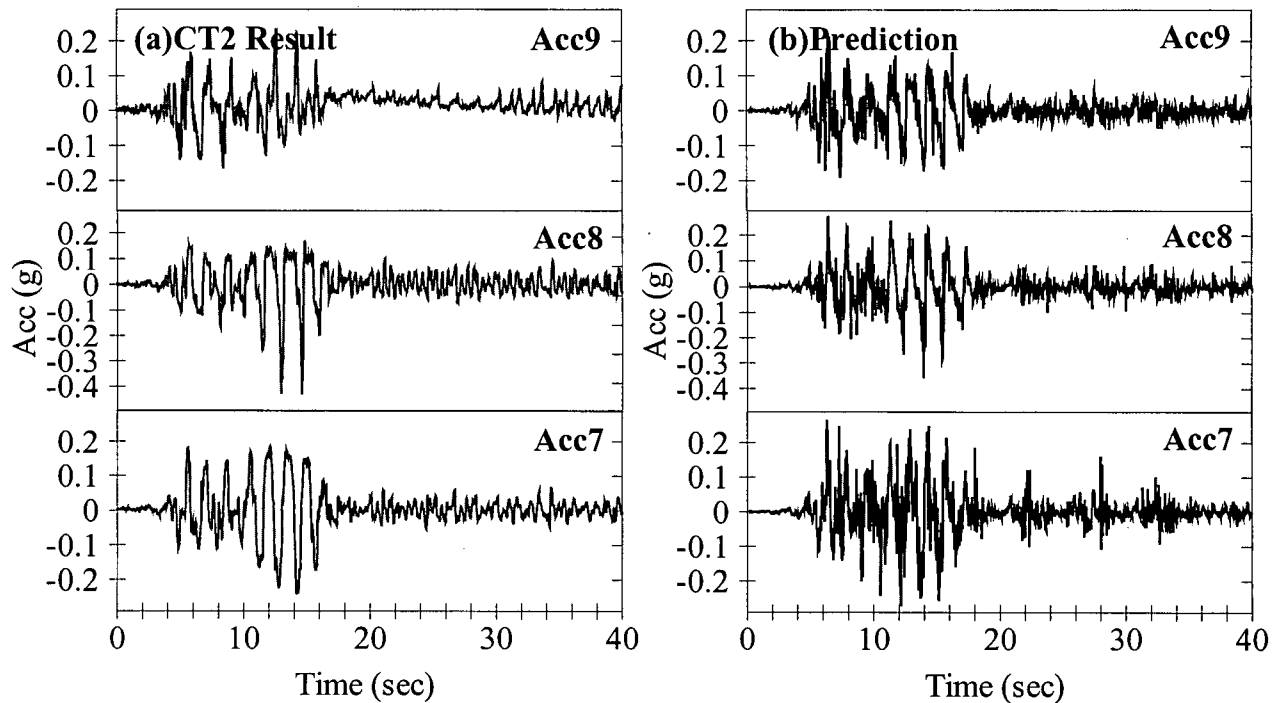


**Figure 5.18** Comparison of Accelerations (ACC): (a) measured, and (b) predicted ACC at Near-slope zone of CT2 (test data from C-CORE, 2004).

As expected, reduced accelerations are noted in the free field area. This is due to the “base isolation” effect caused by soil liquefaction and has been observed by others (Gonzalez et al., 2002). The ACC3 gradually tapered off due to liquefaction-induced base isolation. The ACC3 is located near the surface in the free field area. This indicates that liquefaction occurred top first and then propagated downward. This observation is consistent with most dynamic centrifuge tests (Gonzalez et al., 2002). UBCSAND2 showed a bit of a reduction in ACC3 but it is not clear enough. Measured ACC5 in Figure 5.17 was intentionally cut off to pick up a small P-

wave signal (C-CORE, 2004). UBCSAND2 generally gives an overall agreement with measured accelerations.

The measured pore pressures and accelerations near the slope are shown in Figures 5.15 and 5.18. It may be seen in those figures that there is little or no reduction in the accelerations. Instead, large upslope acceleration spikes (negative sign) are observed in ACC8 at 0.5 m below the slope. UBCSAND2 captured those negative spikes observed from ACC8. ACC7 at the 6 m below the crest did not show such large spikes. Predicted maximum and minimum accelerations are generally in agreement with measurements including acceleration reduction near the ground surface due to base isolation.

### 5.4.3 Measured and Predicted Displacements of CT2

Figure 5.19 compares the measured and predicted displacements from each LVDT. Left side figures show the centrifuge test results and right side figures show numerical predictions.

UBCSAND2 overpredicted the measured settlements. For example, predicted LVDT 1 (L1) in the free field is about twice that of the measurement. However, LVDT measured from dynamic centrifuge tests may not represent actual displacements during shaking. Model configurations of CT2 before and after tests are compared in Figure 5.20(a). Predicted deformation is also given in Figures 5.20(b). Figure 5.20(a) is from C-CORE Report (R-04-027-145, C-CORE, 2004). From this figure it can be seen that larger settlement due to liquefaction occurred in free field area but toe area indicates no soil heaving or movement. The measured deformation after test is quite different to other centrifuge tests, which showed heave near the toe area (Taboada et al., 2002). This discrepancy may arise from boundary effect due to different model configurations used in different tests. Measured displacement did not show any

deformation near the toe but the prediction showed large upward movement. The predicted maximum displacement is about 4 m as shown in Figure 5.20(b). This is not consistent with measurement as shown in Figure 5.20(a).

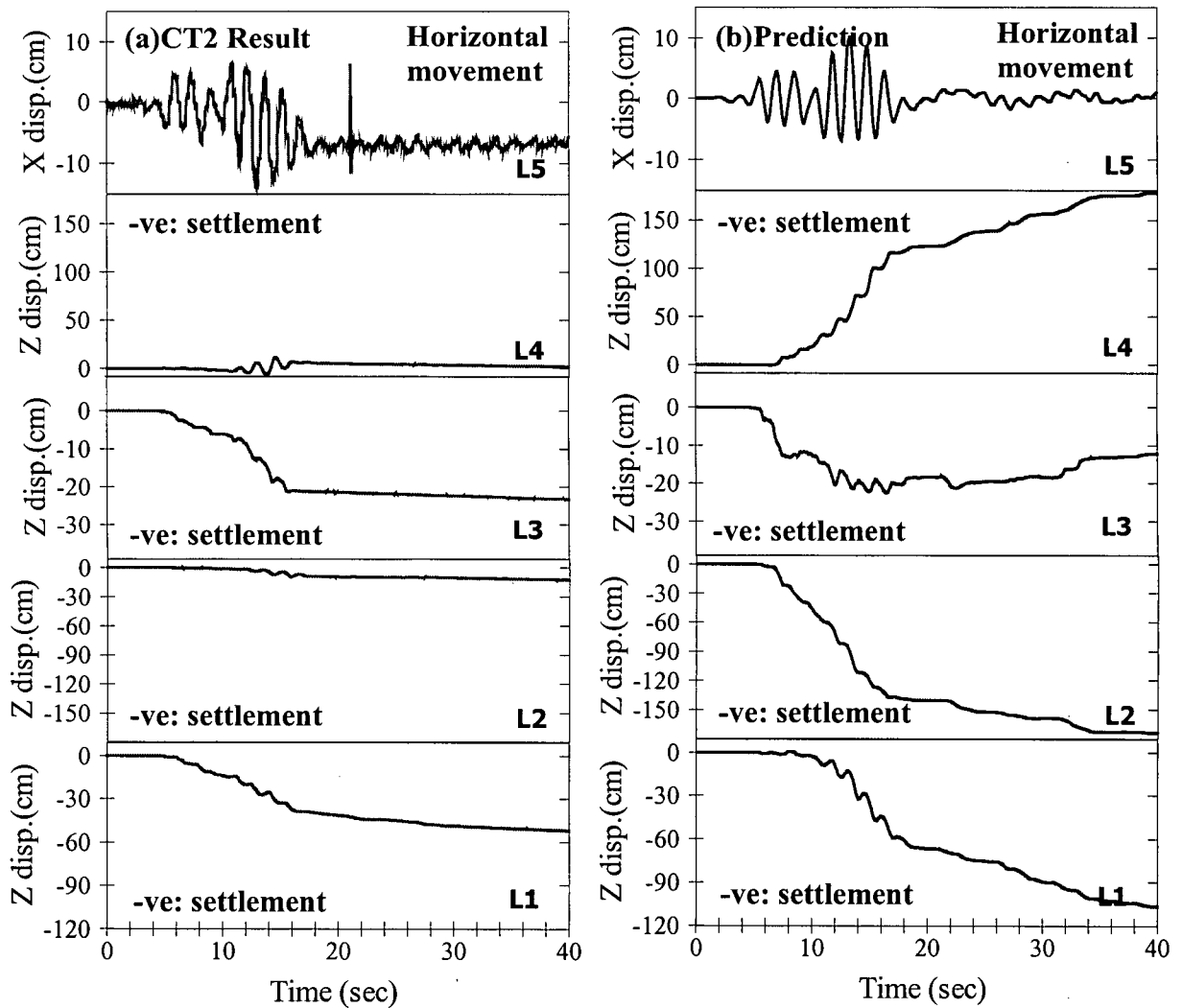


**Figure 5.19** Comparison of Displacements (Disp): (a) measured, and (b) predicted Disp of CT2 (test data from C-CORE, 2004).

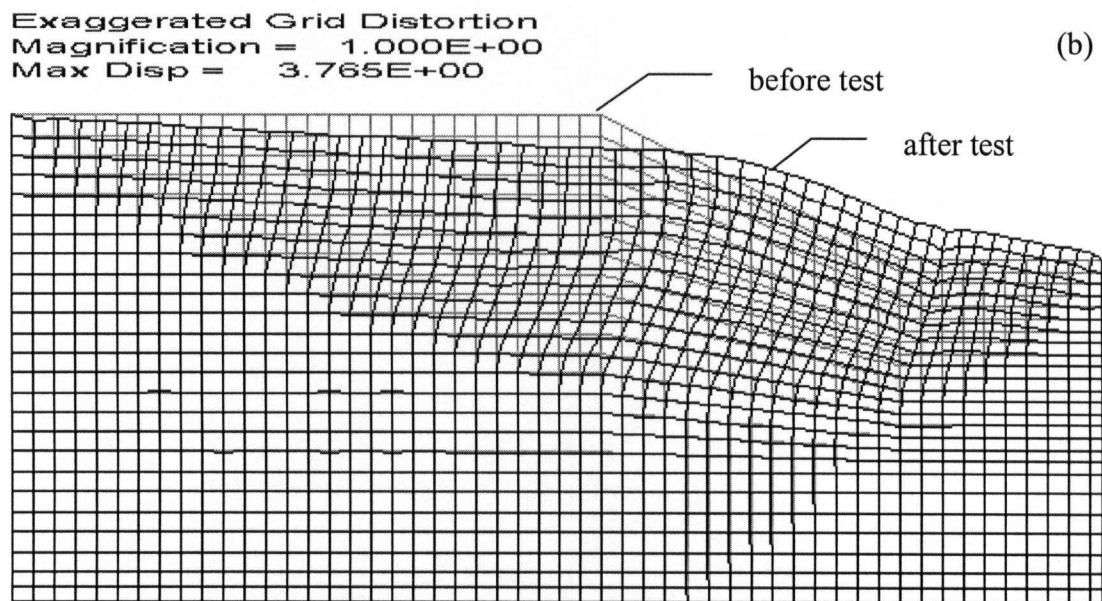
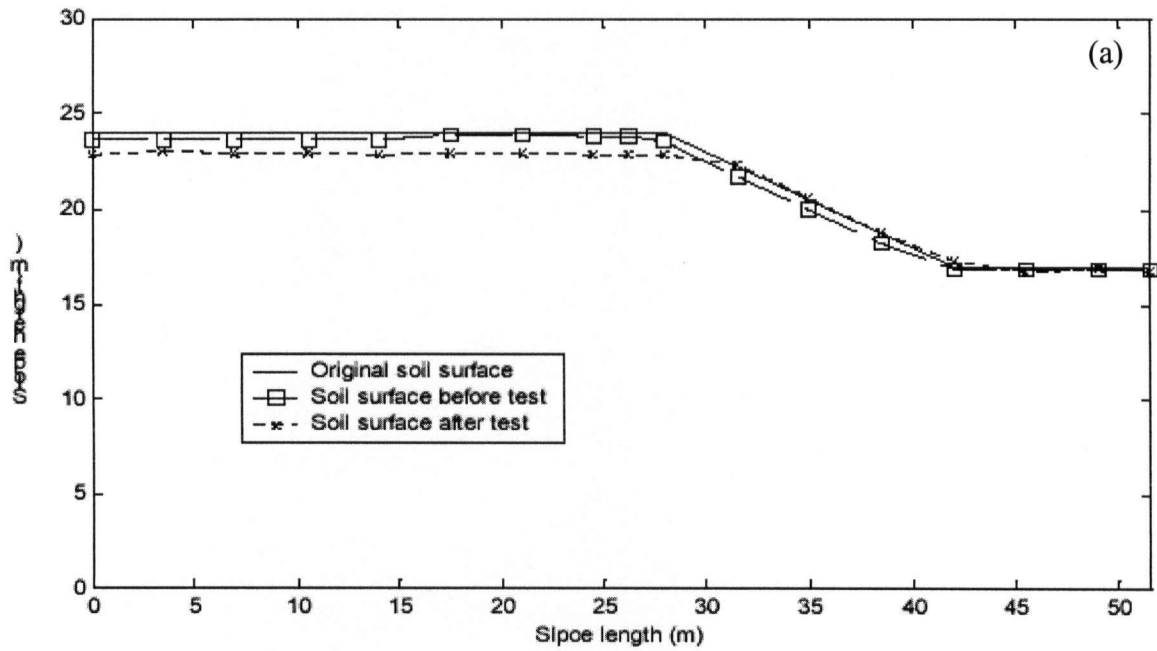


**Figure 5.20** CT2 Deformations before and after tests: (a) Measured deformation (after C-CORE, 2004), and (b) predicted deformation.

#### 5.4.4 Summary of CT2 Comparison

The CT2 is a base model of Category I with A2475 input motion. As expected,  $R_u$  of 100% and reduced accelerations are seen as similar trends observed in the level ground liquefaction centrifuge tests.

The measured accelerations and pore pressures near the slope showed there is little or no reduction in the accelerations. Instead, large upslope acceleration spikes occur. Large negative excess pore pressure spikes occur that coincide in time with the upslope acceleration spikes. The slope is steep and the upslope acceleration of the base tends to induce failure of the slope and relative downslope movement. The soil dilates as it shears in the downslope direction, producing negative pore pressures which stiffen the shear modulus. Enough strength is mobilized through this dilation to arrest the downslope movement and gives rise to the acceleration spike (Taboada et al., 2002).

UBCSAND2 provides a reasonable prediction of the peak values and patterns of accelerations and pore pressure response for the free field. Also, a reasonable agreement is observed for locations near the slope including dilation spikes (accelerations and excess pore pressures). However, it may be seen that both the magnitude and pattern of displacements are quite different. Some of these differences are partially due to UBCSAND2 overpredicting the displacements or centrifuge model configuration causing boundary effect. This requires further calibration of UBCSAND2 and investigation of CT2 results.

In summary,

- (a) UBCSAND2 provides reasonable agreement with this centrifuge test, although further study is needed for displacements near the toe area,

- (b) a decrease in accelerations after liquefaction was observed in the free field back from the slope face,
- (c) relatively large upslope acceleration spikes occurred near the slope,
- (d) a decrease in pore pressure due to dilation corresponded with these upslope acceleration spikes, and
- (e) the dilative spikes prevented very large displacements from occurring.
- (f) UBCSAND2 predicted heave near the toe area that is not observed in this test.

### 5.5 Prediction of CT6 and its Comparison

The CT6 is a base model of Category II. It has no silt layer and no ground improvement. Only one motion, 2 times A2475 called “2×A2475”, has been applied to the base. The proposed input motion of A2475 in Figure 5.5(b) was doubled by the Earthquake Simulator (EQS) of C-CORE centrifuge. FLAC numerical analyses have been carried out in prototype (1g) scale. The detailed simulation procedure by FLAC is presented in Appendix D. The peak and pattern of target 2×A2475 motion in Figure 5.21(a) was reasonably replicated by the Earthquake Simulator (EQS) of C-CORE centrifuge as shown in Figure 5.21(b). In CT6 comparison with measurements the actual input motion was baseline corrected, and then applied to the model.

The comparison between test results and prediction is presented. The results are separated into two characteristic zones: (i) Zone 1: Deep zone, and (ii) Zone 2: Near-slope shallow zone. All predictions at instrument locations are presented in the right sides. At present study, the prediction of CT6 will be made by assuming  $S_{r0} = 98\%$ . The saturation effect on C-CORE centrifuge tests should be investigated in a future study due to its importance in the modeling of

dynamic centrifuge tests (Byrne et al., 2004a). The displacement vectors and distorted meshes are also compared.

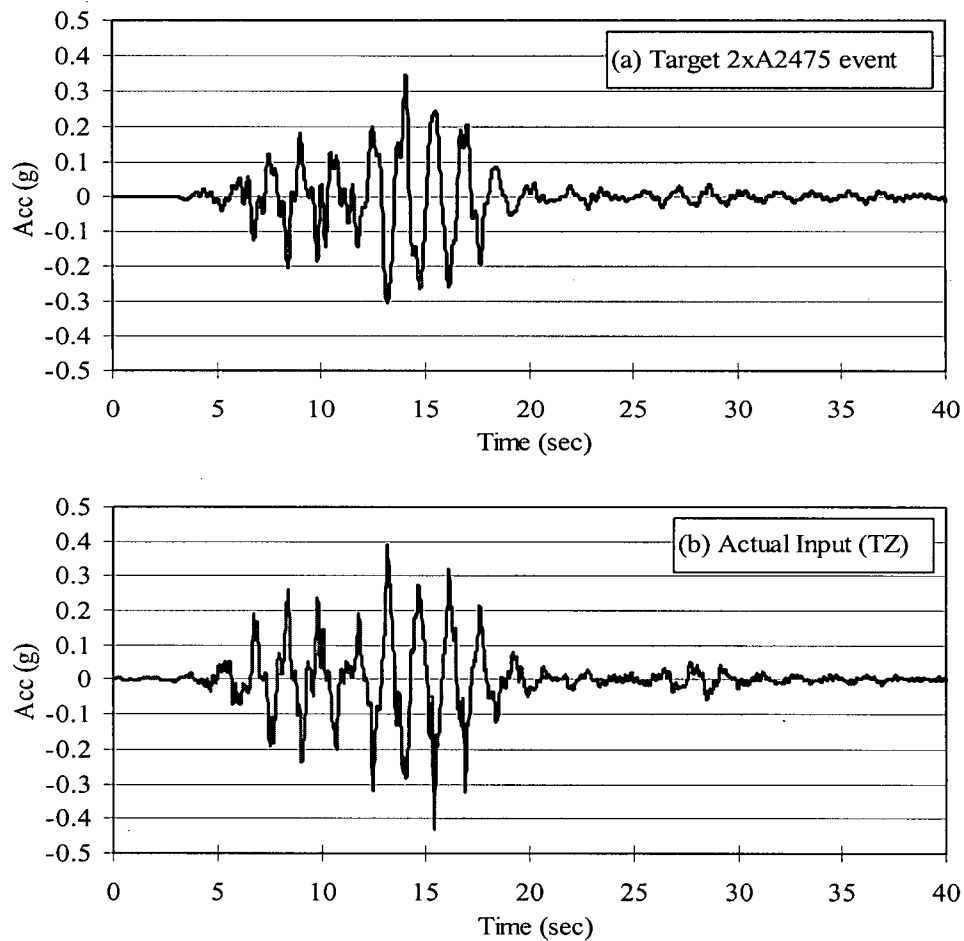


**Figure 5.21** Comparison of target 2×A2475 motion and actual input motions applied into CT6: (a) target 2×A2475 motion, and (b) actual 2×A2475 input.

### 5.5.1 Measured and Predicted Excess Pore Pressures of CT6

Figures 5.22 and 5.23 compare the measured and predicted excess pore pressures at (i) Zone 1: Deep zone, and (ii) Zone 2: Near-slope shallow zone, respectively. Left side figures show the centrifuge test results and right side figures show numerical predictions.

#### (i) Zone 1: Deep zone

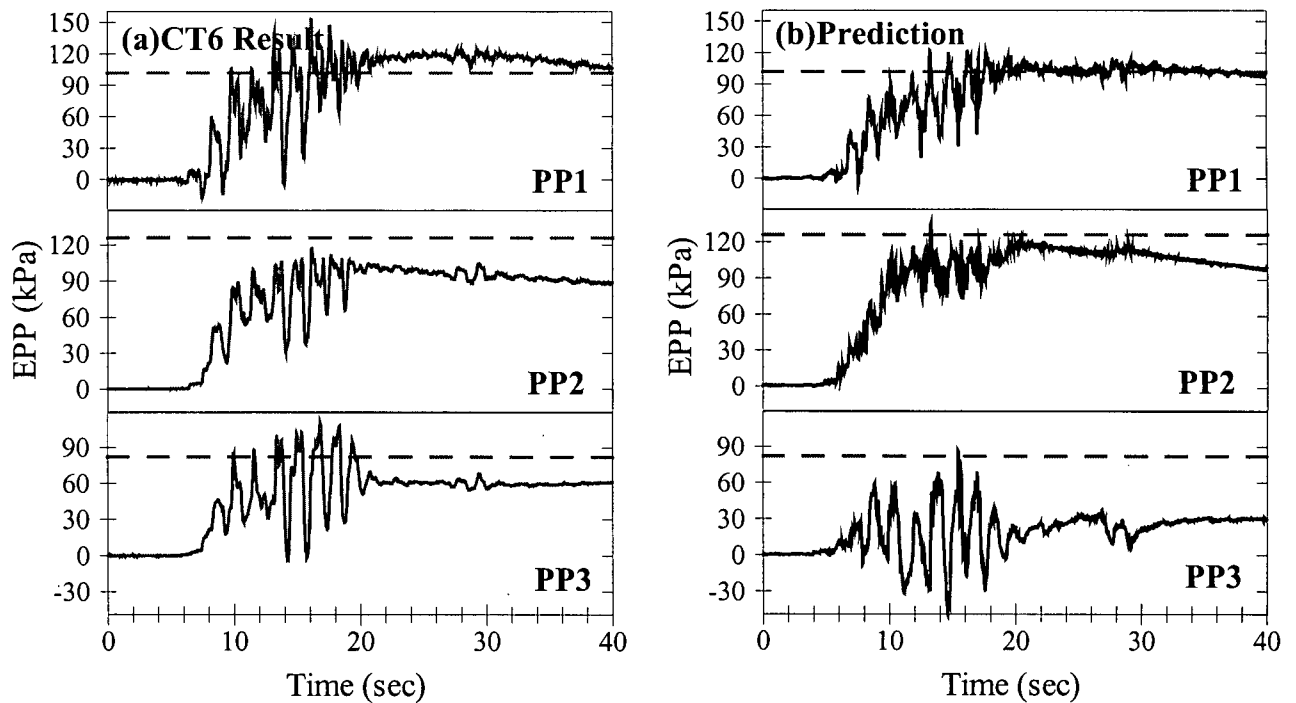


**Figure 5.22** Comparison of Excess Pore Pressures (EPP): (a) measured, and (b) predicted EPP at deep zone of CT6 (test data from C-CORE, 2005).

## (ii) Zone 2: Near-slope shallow zone

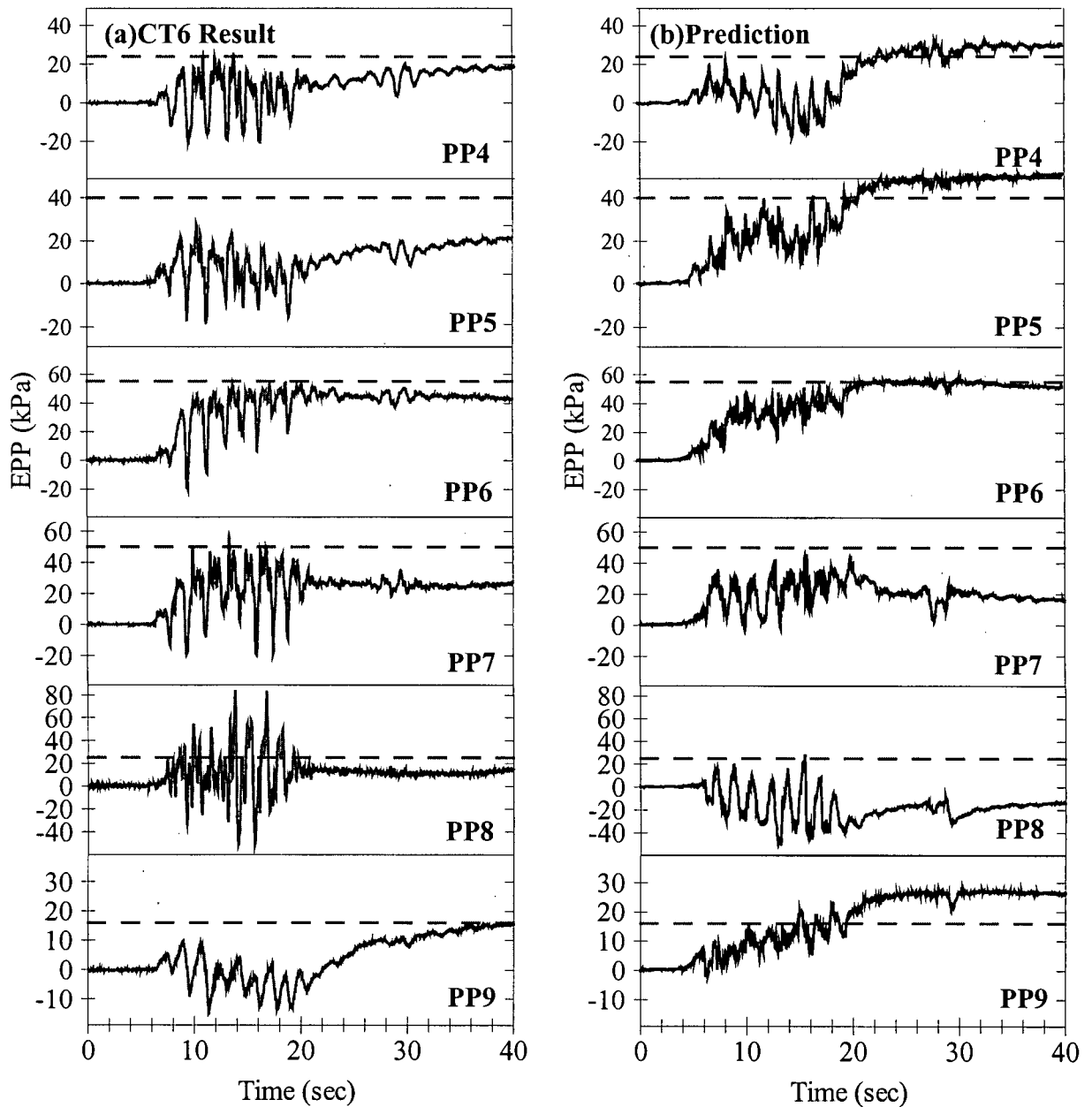


**Figure 5.23** Comparison of Excess Pore Pressures (EPP): (a) measured, and (b) predicted EPP at near-slope shallow zone of CT6 (test data from C-CORE, 2005).

The predicted and observed pore pressures in the deep zone are shown in Figures 5.22. As expected, most of the bottom loose Fraser River sand layer liquefied. Measured PP1 and PP2

seem to be less influenced by the slope but PP3 underneath the slope shows pore pressure spikes due to dilation effect. UBCSAND2 generally well predicted those measured peak values and patterns of excess pore pressure rise and dissipation in the deep area.

Generally, large pore pressure oscillations are observed in the near slope shallow area as shown in Figure 5.23. Here, measured excess pore pressures showed most significant spikes due to dilation or rocking. PP8 and PP9 in the shallow slope area showed some negative excess pore pressures. The pore pressure spikes, including negative excess pore pressures in the PP8 and PP9, were captured by UBCSAND2

Predicted excess pore pressures near the surface, PP4, PP5 and PP9 showed continuous increase of excess pore pressure after strong shaking, which might be due to upward flow after shaking. During shaking the location of PP8 was raised, and predicted PP8 after shaking is stabilized to lower value than one based on initial position. The initial vertical effective stress lines (i.e., dashed horizontal lines in Figure 5.23(b)) may not be directly applicable to predicted excess pore pressures after main shaking due to large deformation (e.g., PP4, PP5 and PP9).

### 5.5.2 Measured and Predicted Accelerations of CT6

Figures 5.24 and 5.25 compare the measured and predicted accelerations at (i) Zone 1: Deep zone, and (ii) Zone 2: Near-slope shallow zone, respectively. Left side figures show the centrifuge test results and right side figures show numerical predictions.

The measured accelerations at deep area and along the slope are shown in Figures 5.24 and 5.25. It may be seen in those figures that there is little or no reduction in the accelerations. Instead, large upslope acceleration spikes are observed near the shallow slope. Predicted

maximum and minimum accelerations during main shaking are generally in agreement with measurements.

**(i) Zone 1: Deep zone**

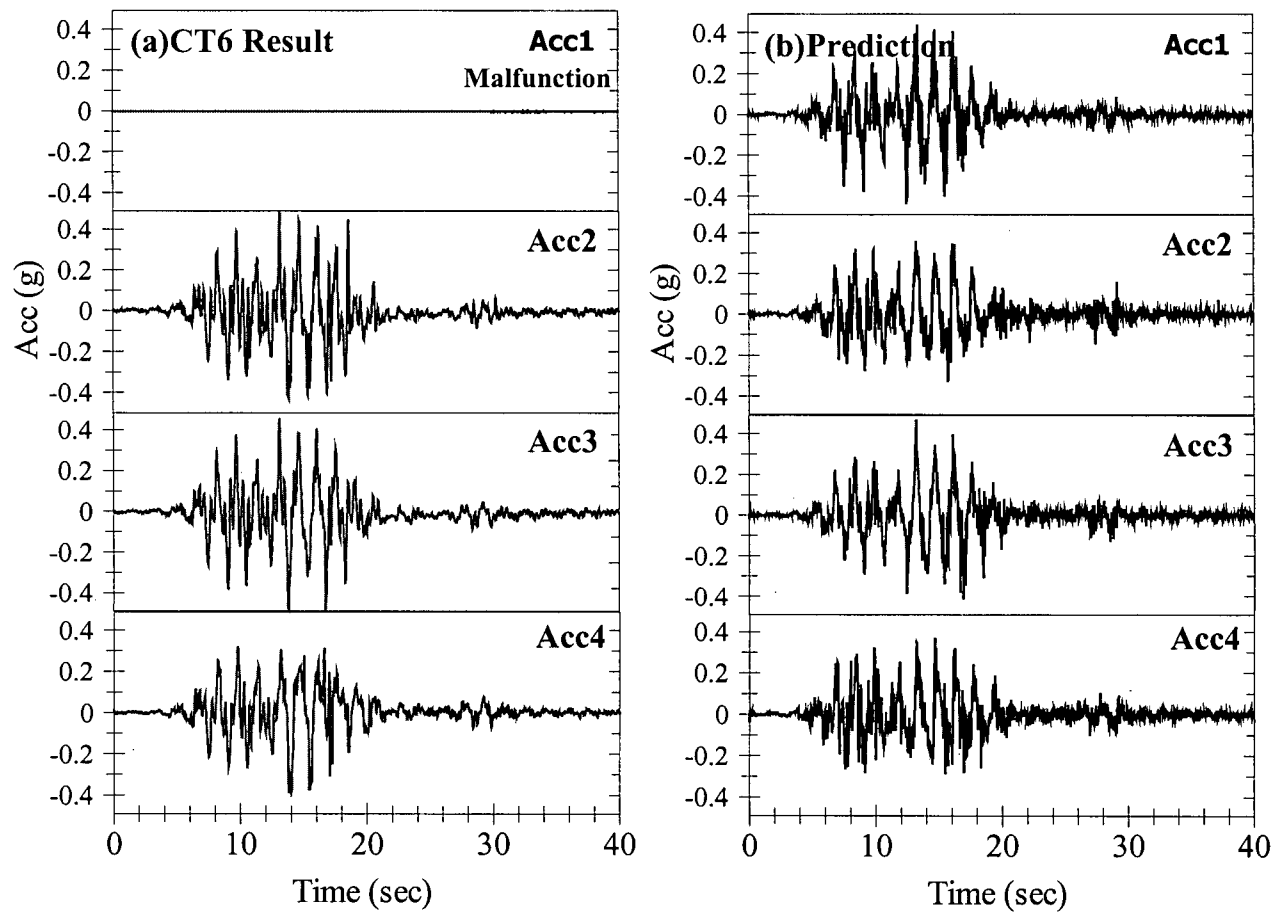


**Figure 5.24** Comparison of Accelerations (ACC): (a) measured, and (b) predicted ACC at deep zone of CT6 (test data from C-CORE, 2005).

## (ii) Zone 2: Near-slope shallow zone

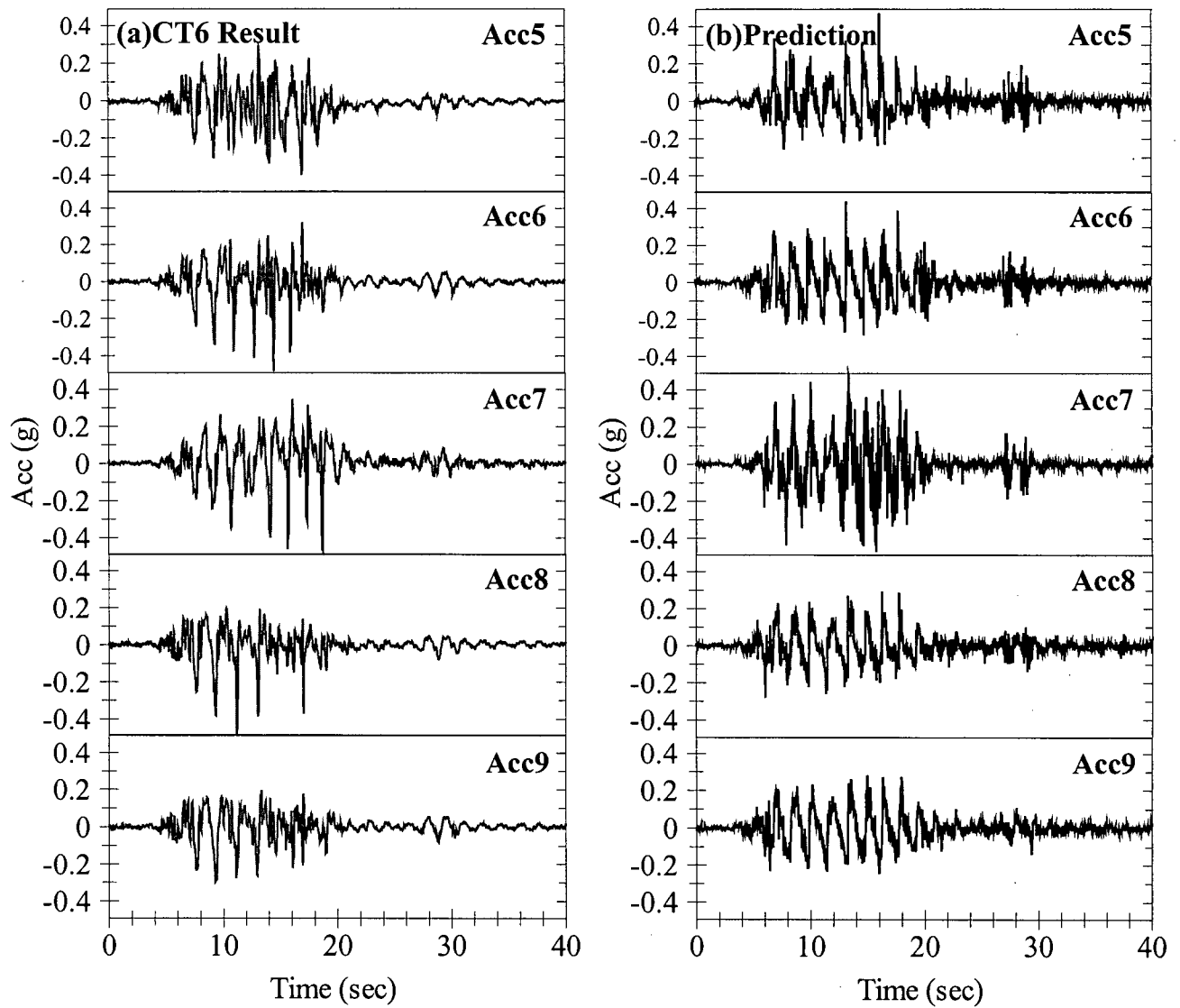
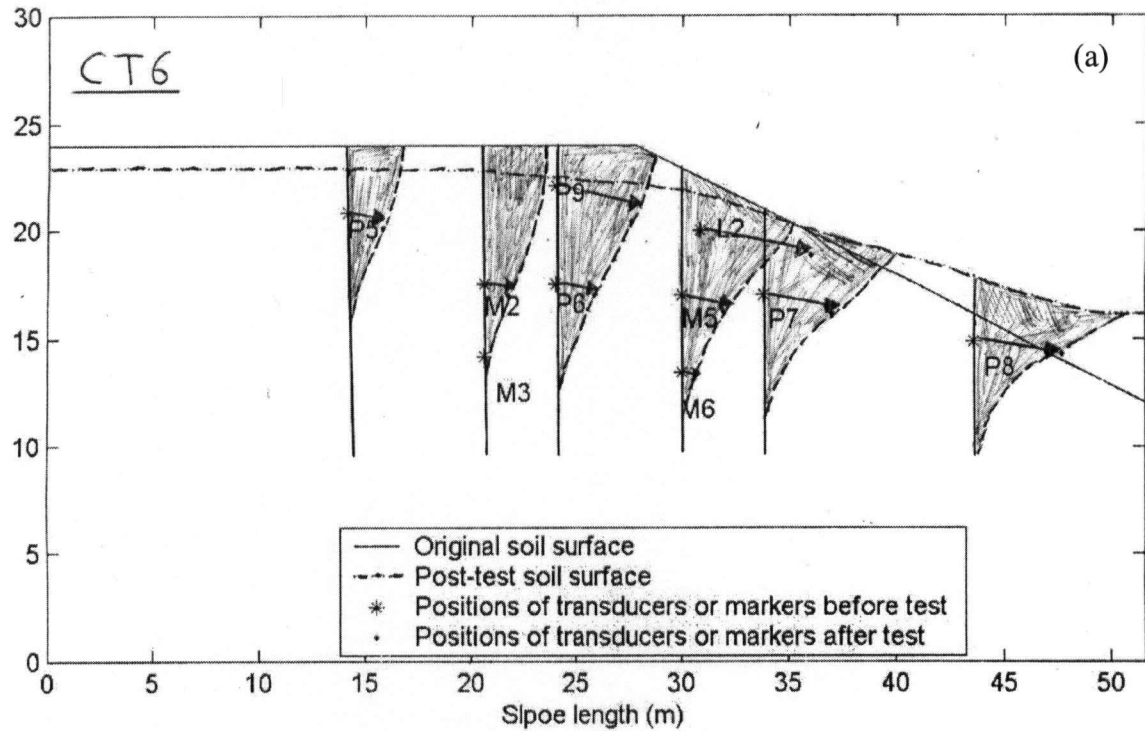


**Figure 5.25** Comparison of Accelerations (ACC): (a) measured, and (b) predicted ACC at near-slope shallow zone of CT6 (test data from C-CORE, 2005).

### 5.5.3 Measured and Predicted Displacements of CT6

From previous observations on several C-CORE centrifuge tests, it is found that displacements from the LVDTs are not very reliable (C-CORE, 2005). Some LVDTs (i.e., L1 & L4 in Figure 5.4(b)) sank due to liquefaction, over capacity or malfunction (C-CORE, 2005). Markers or embedded transducers were used to trace the displacement (C-CORE, 2005). In CT6 those markers or transducers are used to compare the displacements. Ground surfaces before and after tests are also used to compare displacements. Model configurations of CT6 before and after tests are compared in Figure 5.26(a). Predicted deformation is also given in Figures 5.26(b). Figure 5.26(a) is from C-CORE Report (R-04-094-145, C-CORE, 2005). From this figure it is found that larger settlement due to liquefaction occurred in the free field area, and about 5 m of soil accumulated near the toe area. It may be caused by slumping of sand near the crest during strong shaking. The deformed configuration is generally in agreement with measurement. The maximum displacement traced from markers is about 5 m, which is close to the predicted maximum displacement. To reveal the origin of accumulated soil near toe area, more investigation is required for measured displacement.



Exaggerated Grid Distortion  
 Magnification = 1.000E+00  
 Max Disp = 4.998E+00

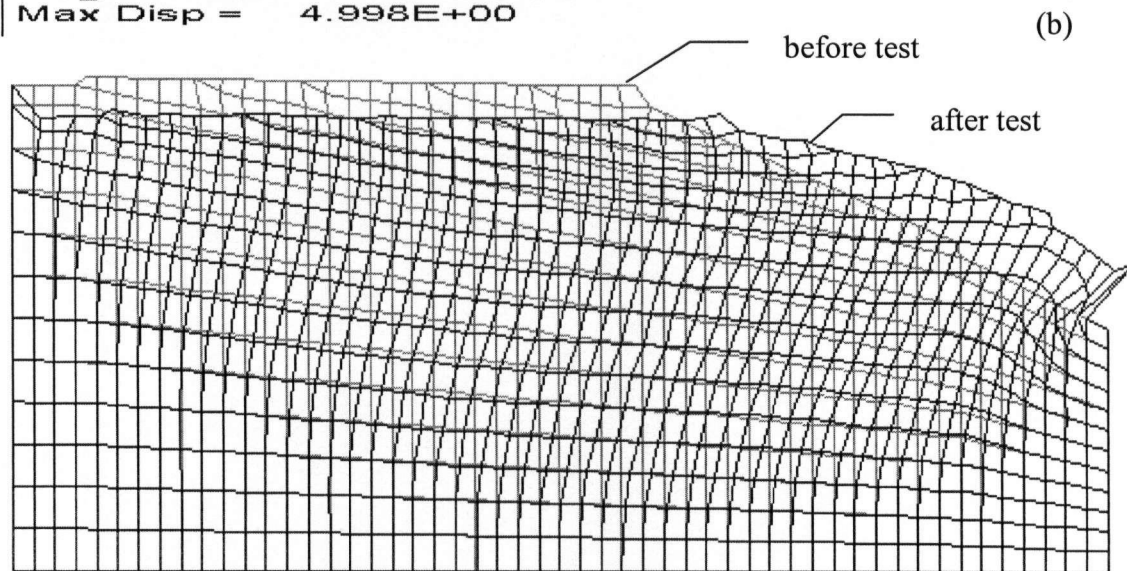


**Figure 5.26** CT6 Deformations before and after tests: (a) Measured deformation (modified from C-CORE, 2005), and (b) predicted deformation.

#### 5.5.4 Summary of CT6 Comparison

The CT6 is a base model of Category II with 2×A2475 input motion. UBCSAND2 provides a reasonable agreement of the accelerations and pore pressure response. Even though measured and predicted maximum displacements and patterns are similar, predicted displacements extend to greater depth. This requires more investigation of the result of CT6. The CT6 results are not fully evaluated at this moment.

#### 5.6 Comparison between UBCSAND and UBCSAND2 for Centrifuge Test

In this chapter a proposed model UBCSAND2 predicted CT2 and CT6 results after the experiment. Only CT2 results are introduced to compare the performance of UBCSAND2 with UBCSAND. An old model UBCSAND was used to make a Class 'A' prediction of C-CORE centrifuge tests by the author. More information about Class 'A' predictions made with UBCSAND is referred to UBC Liquefaction research project web site (<http://www.civil.ubc.ca/liquefaction>). After the test another prediction was made with UBCSAND using actual input motion because target and actual input motions were slightly different. The UBCSAND2 prediction was made using the same set of calibrated constitutive model parameters and without any adjustments. Both UBCSAND and UBCSAND2 predictions can be considered Class 'B' predictions (Lambe, 1973).

The CT2 predictions made by UBCSAND and UBCSAND2 presented in section 5.4 are compared with measurements. Both predictions used a baseline-corrected actual input motion applied to CT2 and an initial saturation of 97%. Figure 5.27 shows the measured and predicted maximum excess pore pressure during strong shaking (between 5 and 20 seconds in Figure

5.12); circles are measured CT2 results, squares are UBCSAND2 prediction, and crosses are UBCSAND prediction. Generally, UBCSAND2 shows a better agreement with measured peak excess pore pressures during strong shaking as shown in Figure 5.27.

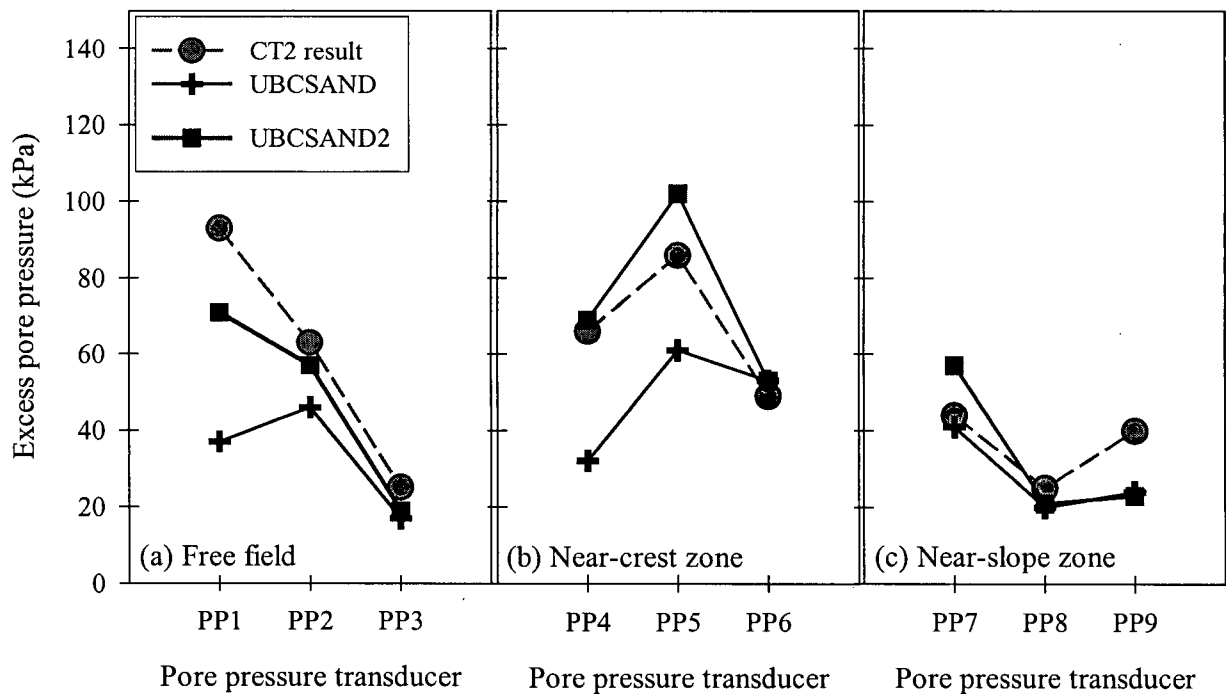


**Figure 5.27** Comparison of CT2 excess pore pressures predicted by UBCSAND and UBCSAND2 and measurement.

Figure 5.28 shows the measured and predicted maximum and minimum accelerations during strong shaking (between 5 and 20 seconds in Figure 5.12). Upper and lower figures are maximum and minimum accelerations, respectively. Both predictions made for the free field area and the Near-crest zone are similar but UBCSAND2 prediction near the slope is much better than UBCSAND. UBCSAND2 seems to better capture upslope (negative) dilation spikes as indicated from Figure 5.28(c). Predicted accelerations near the slope by UBCSAND2 were shown in Figure 5.18.

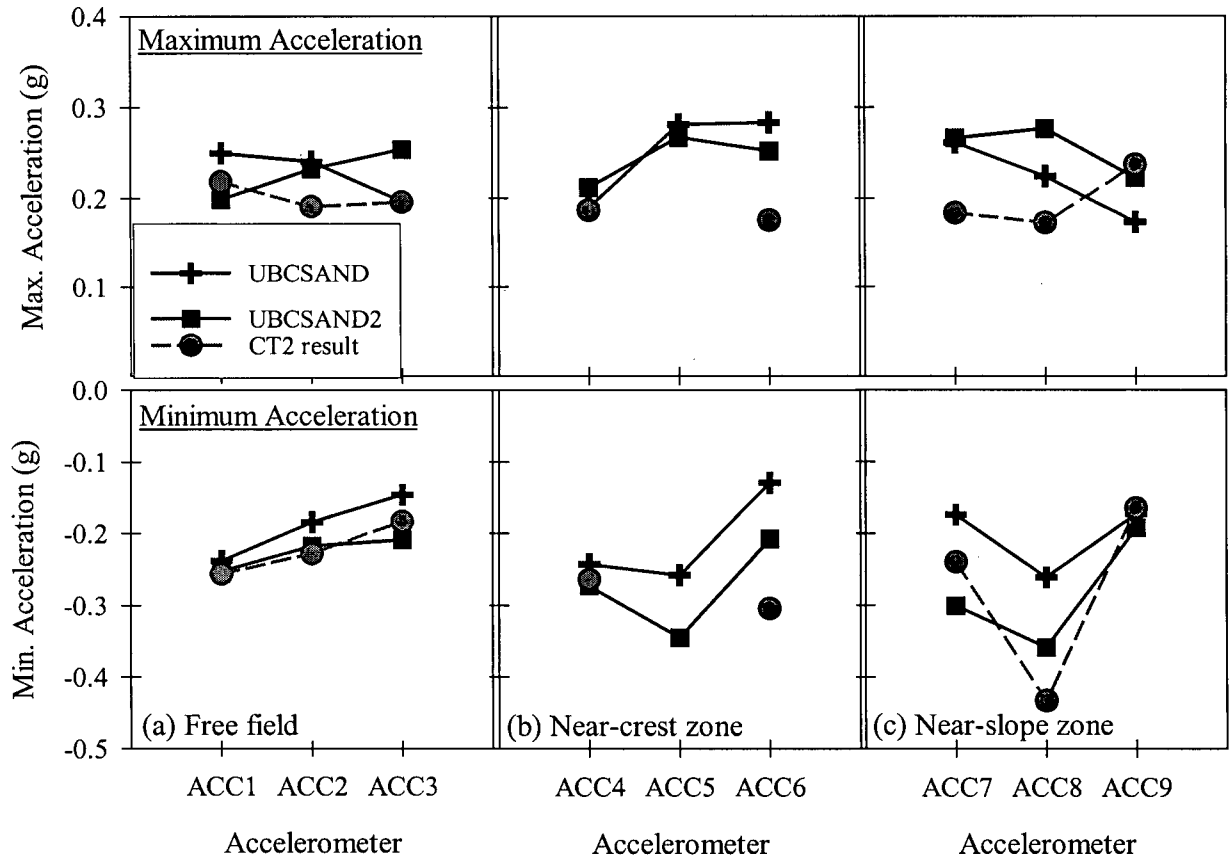


**Figure 5.28** Comparison of CT2 accelerations predicted by UBCSAND and UBCSAND2 and measurement (ACC5 was malfunction, C-CORE, 2004).

## 5.7 Summary of C-CORE Centrifuge Tests Prediction

The C-CORE centrifuge tests representing a steep slope condition in homogeneous loose Fraser River sand were examined and numerically modeled. Both CT2 and CT6 are quite similar in terms of soil conditions and geometry, but they give quite different pattern of deformation in tests. However, the predicted deformations of CT2 and CT6 show a consistent pattern, which has arc shape failure pattern and toe heaving.

---

Most measured excess pore pressures showed some amount of oscillation or some negative spikes rather than gradual increase even in free field condition. It is the increase in effective stress associated with these negative pore pressure spikes that curtails the displacements and makes the slope more stable than might be expected under cyclic loading. The results showed that some upslope acceleration spikes occurred near the face of the slope after liquefaction. These acceleration spikes corresponded with large negative excess pore pressure spikes associated with dilation but they are not so noticeable. The overall pattern of predicted response (e.g., excess pore pressure rise and dissipation, maximum and minimum accelerations) is in reasonable agreement with the measurements, although both the acceleration and pore pressure spikes are under predicted by the UBCSAND2 analysis.

# Chapter 6

## Summary and Conclusions

This thesis presents a new constitutive model that was developed to predict liquefaction-induced displacements. The model accounts for the effects of principal stress rotation and plastic unloading. Since the mechanical behaviour is captured considering the stress state on two specific planes, it is termed a Two Mobilized-plane model. This chapter summarizes the research contributions along with recommendations on research work for further advancement of the modeling technique. It also addresses the limitations of the proposed model.

### 6.1 Summary and Findings

Liquefaction-induced displacements have caused severe damage to structures and facilities during past earthquakes. Therefore, a reliable prediction of liquefaction and resulting displacements is required for the design and retrofit of structures located in areas of potentially liquefiable soils. The objective of this study was to develop and validate a constitutive model for soil liquefaction problems that can be practically applied to actual design problems. In particular it takes into account plastic loading as well as principal stress rotation effects. The number of input parameters is limited to seven to make it suitable for practical design problems.

Principal stress rotation causes plastic volume change under drained conditions and pore pressure increase under undrained conditions. It is particularly important under seismic loading conditions, and needs to be accounted for in numerical modeling. In addition, laboratory tests indicate that volumetric strains during unloading are not elastic and need to be accounted for in numerical models.

A new constitutive modeling concept called a Two Mobilized-plane framework was developed to account for both rotation of principal stress and plastic unloading, and allows a better prediction of static and earthquake-induced deformations. The constitutive model was based on experimental results on simple shear tests where a gradual rotation of principal stresses occurs. The characteristics of the proposed model are summarized as follows:

- The plastic behaviour can be accounted for using the stress conditions observed on two mobilized planes: a plane of maximum shear stress, which swings, and a horizontal plane which is spatially fixed. With the use of the horizontal plane, the model can take into account the principal stress rotation effect and plastic unloading.
- The plastic strain increments mobilized on the horizontal plane are gradually phased-out during principal stress rotation, and deactivated when the horizontal plane becomes the maximum shear stress plane. The phasing-out pattern of the contribution from the horizontal plane is considered in the proposed model.
- This model requires only seven parameters and most parameters can be estimated from relative density or normalized standard penetration test values.

Classical plasticity models based on the plane of maximum shear alone are particularly sensitive to  $K$  conditions, whereas the proposed model gives a similar skeleton behaviour for soils at the same density and mean stress, regardless of  $K$  conditions, as observed in laboratory tests. The

constitutive model was incorporated into the dynamic coupled stress-flow finite difference program FLAC. By implementing the proposed constitutive model into a commercial numerical method, this effective stress approach can be equally accessed by both practitioners and academics.

The proposed constitutive model was calibrated using data from drained tests, and using the same set of parameters the undrained response was then predicted and verified by comparing with data from constant volume (equivalent to undrained condition) tests at the same density and initial stress condition.

The calibration procedure of the model was separated into “specific calibration” and “general calibration”. Specific calibration captured the detailed stress-strain curve and stress path for loose Fraser River sand, and consisted of monotonic, cyclic drained and constant volume (equivalent to undrained condition) DSS tests. It was shown that the computed monotonic undrained response with incompressible fluid (e.g.,  $B_f \geq 1 \times 10^6$  kPa) was the same as the computed response for a constant volume test. Constant volume (equivalent to undrained condition) tests with initial static shear stress were also captured to simulate more general stress condition in the field. General calibration captured the pattern or general behavioral aspects of sand during cyclic loading. In an overall sense, the proposed model is able to capture the element behaviour of sand under monotonic and cyclic DSS loading conditions while considering the effect of principal stress rotation and plastic unloading. The model was also able to capture liquefaction triggering response with respect to the NCEER chart (Youd & Idriss, 1997).

As a validation, the new model was used in the prediction of boundary value problems modeled in a centrifuge. In C-CORE centrifuge tests, relatively large upslope acceleration

spikes occurred near the slope, and the dilative spikes prevented very large displacements from occurring in a slope with a level toe area (e.g., CT2). The proposed model provided reasonable agreement with C-CORE centrifuge tests, although further study was needed for displacements near the toe area. The key findings from modeling of dynamic centrifuge tests were as follows:

- A stress densification equation was developed to estimate the density increase due to applied stress changes. The equation was used to predict the amount of density increase due to applied stress in centrifuge. It was found that stress-induced densification impacted the pattern of liquefaction on dynamic centrifuge tests and can lead to erroneous conclusions if not taken into account when modeling dynamic centrifuge tests.
- Effect of pore fluid stiffness: initial saturation is very important because it controls the bulk modulus of pore fluid that directly influenced the generation of excess pore pressure.

## 6.2 Limitations of UBCSAND2

Although laboratory tests (e.g., DSS tests) are preferred to obtain input parameters, most parameters required in the UBCSAND2 can be estimated from a given relative density using empirical correlations, regardless of sand types. Limitations of the proposed model include:

- The proposed model is aimed at soil liquefaction problems that involve a reduction in mean effective stress and consider only shear-induced plastic behaviour. It does not consider plastic hardening associated with increased mean effective stress. The model does not have a cap and does not consider isotropic compaction.

- The current version of the proposed model does not consider the effect of stress level on the peak friction angle and the effect of the intermediate principal stress.
- It does not consider the state-dependent dilatancy as well as possible strain-softening behaviour of granular materials.

### 6.3 Further Research

The peak friction angle decreases with stress level as reported in test data (Meyerhof, 1950; Ladd et al., 1977; Bolton, 1986). In this regard, the variation of the peak friction angle depending on stress level could be implemented within the framework of the proposed constitutive model. The further calibration/validation work of the proposed model is suggested below.

#### *(i) Calibration of pure rotational tests*

A rotation of principal stress axis itself causes either volume decrease or pore pressure increase for loose sand. The proposed model has been calibrated based on simple shear tests, in which principal stresses rotate but cannot isolate the effect of principal stress rotation. Therefore, it is desirable to calibrate the model using pure rotation tests (e.g., hollow cylinder torsional tests).

#### *(ii) Calibration of lateral stress*

The proposed model computed the variation of lateral stress on simple shear during cyclic loading. However, very few measurements are currently available to validate the model performance. Therefore, the measurement of lateral stress variation under simple shear loading is recommended to validate or calibrate the computed lateral stress. The measurement of lateral

stress in simple shear during cyclic loading may encourage researchers to use simple shear tests for constitutive model calibration.

***(iii) Calibration of large strain cyclic drained tests***

Cyclic drained simple shear test data at large shear strain (e.g.,  $\gamma_{cyc} > 1\%$ ) are very rare and even limited to a few cycles due to long experiment time. More test data with many cycles are necessary to capture the hardening behaviour associated with volumetric strain, or to develop a dilatancy relation for cyclic loading.

***(iv) Validation of centrifuge tests***

Dynamic centrifuge tests have been used for validating the numerical procedures for soil liquefaction because they can minimize many uncertainties existing in the field. More investigations using centrifuge tests are required to confirm initial saturation conditions and measured displacements for soil liquefaction analyses. The correlation between P-wave velocity and Skempton's B value can be used to evaluate indirectly the degree of saturation in centrifuge models. In this regard, P-wave tests are recommended in centrifuge models. In order to trace the accurate deformation after centrifuge tests, colored sand layers or other embedded objects can be installed into the centrifuge model.

---

## References

1. Anandarajah, A. (1990). HOPDYNE - A finite element computer program for the analysis of static, dynamic and earthquake soil and soil-structure systems, The John Hopkins University, Baltimore, Maryland.
2. Arthur, J.R.F., Chua, K.S., Dunstan, T., & Rodriguez, del C.J.I. (1980). Principal stress rotation: a missing parameter. *Journal of the Geotechnical Engineering Division*, 106(GT4), 419-433.
3. Arthur, J.R.F., Chua, K.S., & Dunstan, T. (1977). Induced anisotropy in a sand. *Geotechnique*, 27(1), 13-30.
4. Arulanandan, K. (1996). Summary of VELACS Extension Project. Technical report prepared for the National Science Foundation, Department of Civil Engineering, University of California, Davis, California.
5. Arulanandan, K. & Scott, R.F. (1993). Verification of numerical procedures for the analysis of soil liquefaction problems. In *Proceedings of the International Conference on the Verification of Numerical Procedures for the Analysis of Soil Liquefaction Problems*, Vols. 1 and 2, Balkema, Rotterdam, the Netherlands.
6. Arulmoli, K., Muraleetharan, K.K., Hosain, M.M., & Fruth, L.S. (1992). VELACS laboratory testing program, soil data report. The Earth Technology Corporation, Irvine, California, Report to the National Science Foundation, Washington D.C., March.
7. Aydingun, O. & Adalier, K. (2003). Numerical analysis of seismically induced liquefaction in earth embankment foundations. Part I. Benchmark model, *Canadian Geotechnical Journal*, 40, 753-765.
8. Azizian, A. & Popescu, R. (2001). Backanalysis of the 1929 Ground Bank submarine slope failure. *2001 An Earth Odyssey*, pp 808-815.
9. Bardet, J.P. (1985). Application of bounding surface plasticity to cyclic sand behavior. In *Proceedings of the Second International Conference on Soil Dynamics and Earthquake Engineering*, pp2-3:2-16.
10. Bardet, J.P. (1986). Bounding surface plasticity model for sands. *Journal of Engineering Mechanics*, Vol. 112, No.11, pp 1198-1217.
11. Bardet, J.P. (1995). Scaled Memory model for cyclic behavior of soils. *Journal of Geotechnical Engineering*, Vol. 121(11), pp 766-775.

12. Batdorf, S.B. & Budiansky, B. (1949). A mathematical theory of plasticity based on the concept of slip. National Advisory Committee for Aeronautics, TN 1871.
13. Beaty, M. (2001). A synthesized approach for estimating liquefaction-induced displacements of geotechnical structures. Ph.D. Thesis, Department of Civil Engineering, University of British Columbia, Canada.
14. Beaty, M. & Byrne, P.M. (1998). An effective stress model for predicting liquefaction behaviour of sand. *Geotechnical Earthquake Engineering and Soil Dynamics III*. Edited by P. Dakoulas, M. Yegian, & R Holtz (eds.), ASCE, Geotechnical Special Publication 75 (1), pp. 766-777.
15. Been, K. & Jefferies, M.G. (1985). A state parameter for sands. *Geotechnique* 35, No.2, pp 99-112
16. Been, K., Jefferies, M.G., & Hachey, J. (1991). The critical state of sands. *Geotechnique*, Vol. 41, No. 3, pp 365-381.
17. Been, K. & Jefferies, M.G. (2004). Stress-dilatancy in very loose sand. *Canadian Geotechnical Journal*, 41, 972-989.
18. Been, K., Jefferies, M.G., Hachey, J.E., & Rothenburg, L. (1993). Numerical prediction for Model No 2. In *Proceedings of the International Conference on the Verification of Numerical Procedures for the Analysis of Soil Liquefaction Problems*, Balkema, Rotterdam, the Netherlands, Vol. 1, pp. 331-341.
19. Bjerrum, L. & Landva, A. (1966). Direct simple-shear tests on a Norwegian quick clay. *Geotechnique*, 16(1), 1-20.
20. Budhu, M. (1984). Nonuniformities imposed by simple shear apparatus. *Canadian Geotechnical Journal*, Vol. 20, pp 125-137
21. Byrne, P.M. (1991). A cyclic shear-volume coupling and pore pressure model for sand. In *Proceedings of the Second International Conference on Recent Advances in Geotechnical Earthquake Engineering and Soil Dynamics*, Vol. 1, pp. 47-55.
22. Byrne, P.M. (2001). The proposal of "Earthquake induced damage mitigation from soil liquefaction". Department of Civil Engineering, University of British Columbia, Canada.
23. Byrne, P.M., Cheung, H., & Yan, L. (1987). Soil parameters for deformation analysis of sand masses. *Canadian Geotechnical Journal*, 24(3), 366-376.
24. Byrne, P.M., Park, S.-S., Beaty, M., Sharp, M., Gonzalez, L., & Abdoun, T. (2004a). Numerical modeling of liquefaction and comparison with centrifuge tests. *Canadian Geotechnical Journal*, 41(2): 193-211.
25. Byrne, P.M., Park, S.-S., Beaty, M., Sharp, M., Gonzalez, L., & Abdoun, T. (2004b). Numerical modeling of dynamic centrifuge tests. In *Proceedings of the Thirteenth World*

- Conference on Earthquake Engineering, 1-6 August 2004, Vancouver, BC, Canada, Paper No. 3387.
26. Byrne, P.M., Roy, D., Campanella, R.G., & Hughes, J. (1995). Predicting liquefaction response of granular soils from pressuremeter tests. ASCE National Convention, San Diego, Oct. 23-27, ASCE, Geotechnical Special Publication 56, pp. 122-135.
  27. Calladine, C.R. (1971). A Microstructural view of the mechanical properties of saturated clay. *Geotechnique*, 21(4), 391-415.
  28. Casagrande, A. (1936). The shearing resistance of soils and its relation to the stability of earth dams. In Proceedings of the Soils and Foundation Conference of the U.S. Engineer Department.
  29. Casagrande, A. (1976). *Liquefaction and cyclic deformation of sands: A critical review*. Harvard Soil Mechanics No. 88.
  30. C-CORE (2004). Earthquake induced damage mitigation from soil liquefaction. Data report- centrifuge tests CT2. Contract report prepared for the University of British Columbia, C-CORE Report R-04-027-145, July 2004.
  31. C-CORE (2005). Earthquake induced damage mitigation from soil liquefaction. Data report- Centrifuge tests CT6. Contract report prepared for the University of British Columbia, C-CORE Report R-04-094-145, February 2005.
  32. Chan, A.H.C. (1993). User manual for DIANA-SWANDYNE II. School of Civil Engineering, University of Birmingham, Birmingham, U.K.
  33. Chern, J.C. (1985). Undrained response of saturated sands with emphasis on liquefaction and cyclic mobility. Ph.D Thesis, The University of British Columbia, Vancouver, Canada.
  34. Chung, E.K.F. (1985). Effects of stress path and pre strain history on the undrained monotonic and cyclic loading behaviour of saturated sand. M.A.Sc.Thesis, Department of Civil Engineering, University of British Columbia, Canada.
  35. Cole, E.R.L. (1967). The behaviour of soils in the simple shear apparatus. Ph.D. Thesis, University of Cambridge.
  36. Cornforth, D.H. (1974). One-dimensional consolidation curves of a medium sand. *Geotechnique*, 24(4), 678-683.
  37. Cudny, M. & Vermeer, P.A. (2004). On the modelling of anisotropy and destructuration of soft clays within the multi-laminate framework. *Computers and Geomechanics*, 31 (1), 1-22.
  38. Dafalias, Y.F. (1994). Overview of constitutive models using in VELACS. In Proceedings of the International Conference on the Verification of Numerical Procedures for the Analysis of Soil Liquefaction Problems, Balkema, Rotterdam, the Netherlands, Vol. 2, pp. 1293-1303.

39. Dafalias, Y.F. & Popov, E.P. (1975). A model for nonlinearly hardening materials for complex loading. *Acta Mech*, 21(3), 173-192.
40. Dafalias, Y.F. & Popov, E.P. (1976). Plastic internal variables formalism of cyclic plasticity. *Journal of Applied Mechanics*, 98(4), 645-651.
41. De Alba, P., Chan, C.K., & Seed, H.B. (1976). Sand liquefaction in large-scale simple shear tests. *Journal of the Geotechnical Engineering Division*, 102 (GT9), 909-927.
42. Drucker, D.C., Gibson, R.E., & Henkel, D.J. (1957). Soil mechanics and work-hardening theories of plasticity. *ASCE Transactions*, pp 338-346.
43. Duncan, J.M. & Chang, C.Y. (1970). Nonlinear analysis of stress and strain in soils. *Journal of the Soil Mechanics and Foundations Division*, 96(SM5), 1629-1653.
44. Dyvik, R., Berre, T., Lacasse, S., & Raddim, B. (1987). Comparison of truly undrained and constant volume direct simple shear tests. *Geotechnique*, 33(1), 3-10.
45. Elgamal, A., Yang, Z., & Parra, E. (2002). Computational modeling of cyclic mobility and post-liquefaction site response. *Soil Dynamics and Earthquake Engineering*, 22(4), 259-271.
46. Finn, W.D.L. (1985). Aspects of constant volume cyclic simple shear. *Advances in the Art of Testing Soils under Cyclic conditions*, ASCE, pp 74-98.
47. Finn, W.D.L. (1998). Seismic safety of embankment dams: developments in research and practice 1988-1998. In *Proceedings of the 1998 Specialty Conference on Geotechnical Earthquake Engineering and Soil Dynamics III*, Seattle. Edited by P. Dakoulas, M. Yegina, and B. Holtz. *Geotechnical Special Publication 75*, pp. 813-853.
48. Finn, W.D.L., Sasaki, Y., Wu, G., & Thavaraj, T. (1999). Stability of flood protection dikes with potentially liquefiable foundations: analysis and screening criterion. In *Proceedings of the Thirteenth Annual Vancouver Geotechnical Society Symposium*, May, Vancouver, B.C., pp. 47-54.
49. Finn, W.D.L. & Vaid, Y.P. (1977). Liquefaction potential from drained constant volume cyclic simple shear tests. In *Proceedings of the Sixth World Conference on Earthquake Engineering*, Vol. 3, pp 2157-2162.
50. Finn, W.D.L., Vaid, Y.P., & Bhatia, S.K. (1978). Constant volume cyclic simple shear testing. In *Proceedings of the Second International Conference on Microzonation for safer construction- research and application*, Vol. 2, pp 839-851.
51. Finn, W.D.L., Yogendrakumar, M., Yoshida, N., & Yoshida, H. (1986). TARA-3: A program to compute the seismic response of 2-D embankments and soil-structure interaction systems to seismic loadings. Department of Civil Engineering, University of British Columbia, Vancouver, Canada.

52. Gajo, A. & Wood, D.M. (1999). A kinematic hardening constitutive model for sands: the multiaxial formulation. *International Journal for Numerical and Analytical Methods in Geomechanics*, Vol. 23, pp 925-965
53. Gonzalez, L, Abdoun, T., & Sharp, M.K. (2002). Modeling of seismically induced liquefaction under high confining stress. *International Journal of Physical Modelling in Geotechnics*, 2(3), 1-15.
54. Gudehus, G. (1996). A comprehensive constitutive equation for granular materials. *Soils and Foundations*, 36(1), 1-12.
55. Hansen, B. (1958). Line ruptures regarded as narrow rupture zones; basic equation based on kinematic consideration. *Proceedings of Brussels Conference on Earth Pressure Problems*, Vol. 1, pp. 39-48.
56. Harder, L.F. Jr. & Boulanger, R. (1997). Application of  $K_\alpha$  and  $K_\sigma$  correction factors. In *Proceedings of the NCEER Workshop on Liquefaction Resistance of Soils*, Technical Report NCEER-97-0022, National Center for Earthquake Engineering Research, State University of New York at Buffalo, N.Y. Edited by T.L. Youd and I.M. Idriss, pp. 167-190.
57. Hardin, B.O. (1978). The nature of stress-strain behavior for soils. In *Proceedings of the ASCE Geotechnical Engineering Division Specialty Conference on Earthquake Engineering and Soil Dynamics*, Vol. 1, pp. 3-90.
58. Hardin, B.O. (1987). 1-D strain in normally consolidated cohesionless soils. *Journal of Geotechnical Engineering*, 113(12), 1449-1467.
59. Hausler, E.A. & Sitar, N. (2001). Performance of soil improvement techniques in earthquakes. In *Proceedings of the Fourth International Conference on Recent Advances in Geotechnical Earthquake Engineering and Soil Dynamics*. Paper No. 10.15.
60. Hight, D.W., Gens, A. & Symes, M.J.P.R. (1983). The development of a new hollow cylinder apparatus for investigating the effects of principal stress rotation in soils. *Geotechnique*, 33(4), 355-384.
61. Hill, R. (1950). *The mathematical theory of plasticity*. Oxford University Press, New York.
62. Hyodo, M., Murata, H., Yasufuku, N., & Fujii, T. (1991). Undrained cyclic shear strength and residual shear strain of saturated sand by cyclic triaxial tests. *Soils and Foundations*, 31(3), 60-76.
63. Iai, S., Matsunaga, Y., & Kameoka, T. (1992). Analysis of undrained cyclic behavior of sand under anisotropic consolidation. *Soils and Foundations*, 32(2), 16-20.
64. Idriss, I.M. & Sun, J.I. (1992). *User's Manual for SHAKE91*. Berkeley: University of California, Davis, Department of Civil & Environmental Engineering, California Center for Geotechnical Modeling.

65. Ishihara, K. (1996). *Soil behaviour in earthquake Geotechnics*. Clarendon Press, Oxford.
66. Ishihara, K. & Li, S.-L. (1972). Liquefaction of saturated sand in triaxial torsion shear test. *Soils and Foundations*, 12(2), 19-39.
67. Ishihara, K. & Towhata, I. (1983). Sand response to cyclic rotation of principal stress direction as induced by wave loads. *Soils and Foundations*, 23(4), 11-26.
68. Ishihara, K., Tsuchiya, H., Huang, Y., & Kamada, K. (2001). Recent studies on liquefaction resistance of sand- Effect of saturation. In *Proceedings of the Fourth International Conference on Recent Advances in Geotechnical Earthquake Engineering and Soil Dynamics*, San Diego, California, March 26-31, 2001.
69. Itasca (2000). *FLAC*, version 4.0. Itasca Consulting Group Inc., Minneapolis.
70. Iwan, W.D. (1967). On a class of models for the yielding behavior of continuous and composite systems. *Journal of Applied Mechanics*, Transactions of the ASME, 612-617.
71. Janbu, N. (1963). Soil compressibility as determined by oedometer and triaxial tests. In *Proceedings of the Third European Conference on Soil Mechanics and Foundation Engineering*, Vol. 1, pp. 19-25.
72. Jefferies, M.G. (1993). Nor-Sand: a simple critical state model for sand. *Geotechnique*, 43(1), 91-103.
73. Jefferies, M. (1997). Plastic work and isotropic softening in unloading. *Geotechnique*, 47(5), 1037-1042.
74. Kabilamany, K. & Ishihara, K. (1991). Cyclic behaviour of sand by the multiple shear mechanism model. *Soil Dynamics and Earthquake Engineering*, 10(2), 74-83.
75. Kokusho, T. (1999). Water film in liquefied sand and its effect on lateral spread. *Journal of Geotechnical and Geoenvironmental Engineering*, 125(10), 817-826.
76. Kokusho, T. (2000). Mechanism for water film generation and lateral flow in liquefied sand layer. *Soils and Foundations*, 40(5), 99-111.
77. Kokusho, T. (2003). Current state of research on flow failure considering void redistribution in liquefied deposits. *Soil Dynamics and Earthquake Engineering*, 23, 585-603.
78. Kolymbas, D. (2000). The misery of constitutive modelling. *Constitutive modelling of granular materials*. Edited by Dimitrios Kolymbas, pp. 11-24.
79. Kondner, R.L. (1963). Hyperbolic stress-strain response: cohesive soils. *Journal of Soil Mechanics and Foundation Division*, ASCE, 89(SM1), 115-143.
80. Krieg, R.D. (1975). A practical two surface plasticity theory. *Journal of Applied Mechanics*, September, pp 641-646

81. Kulhawy, F.H. & Mayne, P.W. (1990). Manual on Estimating Soil Properties for Foundation Design. EPRI EL-6800, Final Report. Electric Power Research Institute, 3412 Hillview Avenue, Palo Alto, CA, USA, 94304.
82. Lade, P.V. (2005). Overview of constitutive models for soils. *Calibration of constitutive models*, Geotechnical Special Publication, No. 139, ASCE.
83. Lade, P.V. & Duncan, J. M. (1975). Elastoplastic stress-strain theory for cohesionless soil. *Journal of the Geotechnical Engineering*, 101(GT 10), 1037-1053.
84. Lambe, T.W. (1973). Predictions in soil engineering. *Geotechnique*, 23(2), 149-202.
85. Lambe, T.W. & Whitman, R.V. (1986a). *Soil Mechanics*, SI Version. John Wiley & Sons, New York. p. 100.
86. Lambe, T.W. & Whitman, R.V. (1986b). *Soil Mechanics*, SI Version. John Wiley & Sons, New York, p. 290.
87. Lee, C.-J. (1991). Deformation of sand under cyclic simple shear loading. In *Proceedings of the Second International Conference on Recent Advances in Geotechnical Earthquake Engineering and Soil Dynamics*, March 11-15, St. Louis, Missouri, Vol. 1, pp. 33-36.
88. Lee, K.-H. & Pande, G.N. (2004). Development of a two-surface model in the Multilaminate framework. In *Proceedings of the Ninth International Symposium on Numerical Models in Geomechanics (NUMOG IX)*, Ottawa, Ontario, Canada, pp. 139-144.
89. Lee, K.L. & Seed, H.B. (1967). Drained strength characteristics of sands. *Journal of the Soil Mechanics and Foundations Division*, 93(SM6), 117-141.
90. Leroueil, S. & Hight, D.W. (2003). Behaviour and properties of natural soils and soft rocks. *Characterisation and Engineering Properties of Natural Soils*, Edited by Tan, T. S., Phoon, K. K., Hight, D. W. and Leroueil, S., Vol. 1, pp 29-254.
91. Li, X.S. (2002). A sand model with state-dependent dilatancy. *Geotechnique*, 50(4), 173-186.
92. Li, X.S. & Dafalias, Y.F. (2000). Dilatancy for cohesionless soils. *Geotechnique*, 50(4), 449-460.
93. Li, X. S., Dafalias, Y. F., & Wang, Z.L. (1999). State-dependent dilatancy in critical-state constitutive modelling of sand. *Canadian Geotechnical Journal*, Vol. 36, pp 599-611
94. Lucks, A.S., Christian, J.T., Brandow, G.E., & Hoeg, K. (1972). Stress conditions in NGI simple shear test. *Journal of Soil Mechanics and Foundation Engineering*, 98(SM1), 155-160.
95. Lysmer, J., Udaka, T., Tsai, C.-F., & Seed, H.B. (1975). FLUSH A Computer Program for Approximate 3-D Analysis of Soil-Structure Interaction Problems. Report No. EERC 75-30, Earthquake Engineering Research Center, University of California, Berkeley.

96. Madabhushi, S.P.G. & Zeng, X. (1998). Behaviour of gravity quay walls subjected to earthquake loading. Part II: Numerical Modelling. *Journal of Geotechnical and Geoenvironmental Engineering*, 124(5), 418-428.
97. Manzari, M.T. & Dafalias, Y. F. (1997). A critical state two-surface plasticity model for sands. *Geotechnique*, 47(2), 255-272.
98. Marcuson, W.F. & Bieganousky, W.A. (1977). SPT and relative density in coarse sands. *Journal of the Geotechnical Engineering Division*, 103(GT11), 1295-1309.
99. Martin, G.R., Finn, W.D.L., & Seed, H.B. (1975). Fundamentals of liquefaction under cyclic loading. *Journal of the Geotechnical Engineering Division*, 101(GT5), 423-438.
100. Matsuoka, H. (1974). Stress-strain relationships of sands based on the mobilized plane. *Soils and Foundations*, 14(2), 47-61.
101. Matsuoka, H. (1976). On the significance of the "Spatial Mobilized Plane". *Soils and Foundations*, 16(1), 91-128.
102. Matsuoka, H. & Sakakibara, K. (1987). A constitutive model for sands and clays evaluating principal stress rotation. *Soils and Foundations*, 27(4), 73-88.
103. Matsuoka, H., Suzuki, Y., & Sakakibara, K. (1988). A constitutive model of soils for evaluating principal stress rotation. *Numerical Methods in Geomechanics*, pp 343-348.
104. Mehrabadi, A.J. & Popescu, R. (2004). 'Class A' prediction of centrifuge tests at C-CORE, Earthquake Induced Damage Mitigation from Soil Liquefaction (<http://www.civil.ubc.ca/liquefaction/>).
105. Ming, H.Y. & Li, X.S. (2001). "SUMDES2D, a two dimensional fully-coupled geotechnical earthquake engineering program". Report to the Department of Civil Engineering, the Hong Kong University of Science and Technology, Hong Kong.
106. Miura, K. (1985). Study on the deformation behaviour of anisotropic sand under principal stress axes rotation. Ph. D Thesis, Hokkaido University, Japan.
107. Molenkamp, F. (1981). Elasto-plastic double hardening model MONOT. LGM Report, CO-218595, Delft Geotechnics.
108. Molenkamp, F. (1982). Kinematic model for alternating loading ALTERNAT. LGM Report, CO-218598, Delft Geotechnics.
109. Mroz, Z. (1967). On the description of anisotropic work hardening. *Journal of the Mechanics and Physics of Solids*, 15, 163-175.
110. Muraleetharan, K.K (1990). Dynamic behavior of earth dams. Ph.D. Thesis, University of California, Davis.

111. Muraleetharan, K.K. & Arulanandan, K. (1991). Dynamic behavior of earth dams containing stratified soils, Centrifuge 91, Edited by Hon Yim Ko et al., Balkema Press, Rotterdam.
112. Muraleetharan, K.K. Deshpandeet, S., & Adalier, K. (2004). Dynamic deformations in sand embankments: centrifuge modeling and blind, fully coupled analyses. *Canadian Geotechnical Journal*, 41, 48-69.
113. Muraleetharan, K.K., Mish, K.D., Yogachandran, C., & Arulanandan, K. (1988). DYSAC2 (version 1.0): dynamic soil analysis code for 2-dimensional problems. Computer Code, Department of Civil Engineering, University of California, Davis, California, USA.
114. Muraleetharan, K.K., Mish, K.D., Yogachandran, C., & Arulanandan, K. (1997). User's manual for DYSAC2 (version 7.0): dynamic soil analysis code for 2-dimensional problems. Technical Report, School of Civil Engineering and Environmental Science, University of Oklahoma, Norman, Okla.
115. Murayama, S. (1964). A theoretical consideration on a behaviour of sand. In *Proceedings of the International Conference on Rheology and Soil Mechanics*, pp 146-159.
116. Naesgaard, E, Byrne, P.M., Seid-Karbasi, M., & Park, S.S. (2005). Class 'A' prediction of centrifuge test CT6 at C-CORE. *Earthquake Induced Damage Mitigation from Soil Liquefaction* (<http://www.civil.ubc.ca/liquefaction/>).
117. Negussey, D., Wijewickreme, D., & Vaid, Y.P. (1988). Constant volume friction angle of granular materials. *Canadian Geotechnical Journal*, 25(1), 50-55.
118. Newmark, N.M. (1965). Effects of earthquakes on dams and embankments. *Geotechnique*, 15(2), 139-160.
119. Nova, R. (1982). A constitutive model for soil under monotonic and cyclic loading. *Soil mechanics-Transient and Cyclic Loads* edited by Pande, G.N. and Zienkiewicz, O.C., pp. 343-373.
120. NRC. (1985). *Liquefaction of soils during earthquakes*. National Research Council Report CETS-EE-001, National Academic Press, Washington, D.C.
121. Okamura, M., Abdoun, T.H., Dobry, R., Sharp, M. K., & Taboada, V.M. (2001). Effects of sand permeability and weak aftershocks on earthquake-induced lateral spreading. *Soils and Foundations*, 41(6), 63-77.
122. Pande, G.N. & Pietruszczak, S. (1982). Reflecting surface model for soils. In *Proceedings of the International Symposium on Numerical Models in Geomechanics*, pp 50-64.
123. Pande, G.N. & Sharma, K.G. (1983). Multi-laminate model of clays-a numerical evaluation of the influence of rotation of the principal stress axes. *International Journal for Numerical and Analytical Methods in Geomechanics*, 7, 397-418.

124. Pande, G.N. & Yamada, M. (1994). The Multilaminar framework of models for rock and soil masses. In Proceedings of the First International Workshop on Applications of Computational Mechanics in Geotechnical Engineering, Rio de Janeiro, pp 105-123.
125. Park, S.-S. (2000). Bearing behavior of crushable volcanic sands. M.Eng. Thesis, Tokyo Institute of Technology, Tokyo, Japan.
126. Park, S.-S. (2002). One-dimensional compression tests for Fraser River sand. Internal Report, Department of Civil Engineering, University of British Columbia, Canada.
127. Park, S.-S. & Byrne, P.M. (2004a). Stress densification and its evaluation. Canadian Geotechnical Journal, 41(1), 181-186.
128. Park, S.-S. & Byrne, P.M. (2004b). Numerical modeling of soil liquefaction at slope site. In Proceedings of the International Conference on Cyclic behaviour of soils and liquefaction phenomena, 31 March-02 April 2004, Bochum, Germany, pp. 571-580.
129. Park, S.-S. & Byrne, P.M. (2004c). Practical constitutive model for soil liquefaction. In Proceedings of the Ninth International Symposium on Numerical Models in Geomechanics (NUMOG IX), 25-27 August 2004, Ottawa, Ontario, Canada, pp. 181-186.
130. Park, S.-S. & Byrne, P.M. (2004d). Class 'A' prediction of centrifuge tests at C-CORE, Earthquake Induced Damage Mitigation from Soil Liquefaction (<http://www.civil.ubc.ca/liquefaction/>).
131. Park, S.-S. & Byrne, P.M. (2005). Multi-plane model for soil liquefaction. In Proceedings of the GeoFrontiers 2005, 24-26 January 2005, Austin, Texas, USA.
132. Park, S.-S., Byrne, P.M., & Wijewickreme, D. (2005). A swinging plane model for soil liquefaction analysis. In Proceedings of the Sixteenth International Conference on Soil Mechanics and Foundation Engineering, September 2005, Osaka, Japan.
133. Park, S.-S., Sharp, M.K., & Byrne, P.M. (2004). The influence of stress densification and centrifuge model preparation method for soil liquefaction. In Proceedings of the Fifty Seventh Canadian Geotechnical Conference, 24-27 October 2004, Quebec City, Quebec, Canada.
134. Pastor, M., Zienkiewicz, O.C., & Leung, K.H. (1985). Simple model for transient soil loading in earthquake analysis - II. Non-associative models for sands. International Journal of Numerical and Analytical Methods in Geomechanics, 9: 477-498.
135. Pastor, M., Zienkiewicz, O.C., & Chan, H.C. (1990). Generalized plasticity and the modelling of soil behaviour. International Journal for Numerical and Analytical Methods in Geomechanics. 14, 151-190.
136. Peacock, W.H. & Seed, H.B. (1968). Sand liquefaction under cyclic loading simple shear conditions. Journal of the Soil Mechanics and Foundations Division, 94(SM3), 689-708.

137. Pestana, J.M., Biscontin, G., Nadim, F., & Andersen, K. (2000). Modeling cyclic behavior of lightly overconsolidated clays in simple shear, *Soil Dynamics and Earthquake Engineering*, 19, 501-519.
138. Pestana, J.M. & Whittle, A.J. (1995). Compression model for cohesionless soils. *Geotechnique*, 45(4), 611-631.
139. Pestana, J.M., Whittle, A.J., Salvati, L.A. (2002). Evaluation of a constitutive model for clays and sands: Part I - sand behaviour. *International Journal for Numerical and Analytical Methods in Geomechanics*, 26, 1097-1121.
140. Poorooshasb, H.B., Holubec, I., & Sherbourne, A.N. (1966). Yielding and flow of sand in triaxial compression Part I. *Canadian Geotechnical Journal*, 3(4), 179-190.
141. Popescu, R. & Prevost, J.H. (1995). Comparison between VELACS numerical Class 'A' predictions and centrifuge experimental soil test results. *Soil Dynamics and Earthquake Engineering*, 14, 79-92.
142. Poulos, S.J. (1981). The steady state of deformation. *Journal of the Geotechnical Engineering Division*, 107(GT5), 553-563.
143. Prager, W. (1956). A new method of analyzing stresses and strains in work-hardening plastic solids. *Journal of Applied Mechanics*, ASME, vol. 23, pp 493-496
144. Prevost, J.H. (1977). Mathematical modelling of monotonic and cyclic undrained clay behaviour. *International Journal for Numerical and Analytical Methods in Geomechanics*, 1, 195-216.
145. Prevost, J.H. (1985). A simple plasticity theory for frictional cohesionless soils. *Soil Dynamics and Earthquake Engineering*, 4(1), 9-17.
146. Prevost, J.H. (1998). DYNAFLOW user's manual. Technical Report. Department of Civil Engineering and Operations Research, Princeton University, Princeton, N.J.
147. Puebla, H. (1999). A constitutive model for sand and the analysis of the CANLEX embankments. Ph.D. Thesis, Department of Civil Engineering, University of British Columbia, Canada.
148. Puebla, H., Byrne, P.M., & Phillips, R. (1997). Analysis of CANLEX liquefaction embankments: prototype and centrifuge models. *Canadian Geotechnical Journal*, 34(5), 641-657.
149. Roscoe, K. H. (1953). An apparatus for the application of simple shear to soil samples. In *Proceedings of the Third International conference on SMFE*, Vol. 1, pp 186-191.
150. Roscoe, K.H. (1970). The Tenth Rankin Lecture: The influence of strains in soil mechanics. *Geotechnique*, 20, 129-170.

151. Roscoe, K. H. & Burland, J.B. (1968). On the generalized behaviour of 'wet' clay. *Engineering plasticity*, Heyman, J. and Leckie, F.A. (Eds), Cambridge University Press, Cambridge, pp. 535-609.
152. Roscoe, K.H., Schofield, A.N., & Thurairajah, A. (1963). Yielding of clays in states wetter than critical. *Geotechnique*, 13(3), 211-240.
153. Roscoe, K.H., Schofield, A.N., & Wroth, C.P. (1958). On the yielding of soils. *Geotechnique*, 8(1), 22-52.
154. Rowe, P.W. (1962). The stress-dilatancy relation for static equilibrium of an assembly of particles in contact. In *Proceedings of the Royal Society of London, Mathematical and Physical Sciences, Series A 269*, 500-557.
155. Rowe, P.W. (1972). Theoretical meaning and observed values of deformation parameters for soil. In *Stress-strain behaviour of soils, Proceedings of the Roscoe Memorial Symposium*, pp. 143-194.
156. Sayao, A.S.F. (1989). Behaviour of sand under general stress paths in the hollow cylinder torsional device. Ph.D. Thesis, Department of Civil Engineering, University of British Columbia, Canada.
157. Schofield, A.N. & Wroth, C.P. (1968). *Critical state soil mechanics*. McGraw-Hill, Maidenhead, UK.
158. Seed, H.B. & Idriss, I.M. (1967). Analysis of soil liquefaction: Niigata earthquake. *Journal of the Soil Mechanics and Foundations Division*, 93(SM3), 84-108.
159. Seed, H.B. & Idriss, I.M. (1970). Soil moduli and damping factors for dynamic response analyses. Report No. EERC 70-10, EERC, UCB, Dec. 1970, 40pp.
160. Seed, H.B. & Idriss, I.M. (1971). Simplified procedure for evaluating soil liquefaction potential. *Journal of the Soil Mechanics and Foundations division*, 97(SM9), 1249-1273.
161. Seed, H.B., Tokimatsu, K., Harder, L.F., & Chung, R.M. (1985). The influence of SPT procedures in soil liquefaction resistance evaluations. *Journal of Geotechnical Engineering*, 111(12), 1425-1445.
162. Seed, H.B., Wong, R.T., Idriss, I.M., & Tokimatsu, K. (1986). Moduli and damping factors for dynamic analyses of cohesionless soils. *Journal of Geotechnical Engineering*, 112(11), 1016-1032.
163. Seid-Karbasi, M. (2003). Review of input motion time histories suggested for dynamic testing in C-CORE centrifuge facilities, Report No. 2003/01, Department of Civil Engineering, University of British Columbia, Canada.
164. Silver, M.L. & Seed, H.B. (1971). Volume changes in sands during cyclic loading. *Journal of the Soil Mechanics and Foundations Division*, 97(SM9), 1171-1182.

165. Sivathayalan, S. (2000). Fabric, initial state and stress path effects on liquefaction susceptibility of sands. Ph.D. Thesis, Department of Civil Engineering, University of British Columbia, Canada.
166. Skempton, A.W. (1986). Standard penetration test procedures and the effects in sands of overburden pressure, relative density, particle size, ageing and overconsolidation. *Geotechnique* 36(3), 425-447.
167. Sriskandakumar, S. (2003). Fraser River sand index tests, Earthquake Induced Damage Mitigation from Soil Liquefaction (<http://www.civil.ubc.ca/liquefaction/>).
168. Sriskandakumar, S. (2004). Cyclic loading response of Fraser River sand for validation of numerical models simulating centrifuge tests. M.A.Sc. Thesis, Department of Civil Engineering, University of British Columbia, Canada.
169. Sture, S., Budiman, J.s., Ontuna, A.K., & Ko, H.-Y. (1987). Directional shear cell experiments on a dry cohesionless soil. *Geotechnical Testing Journal*, 10(2), 71-79.
170. Symes, M.J., Gens, A., & Hight, D.W. (1988). Drained principal stress rotation in saturated sand. *Geotechnique*, 38(1), 59-81.
171. Symes, M.J., Hight, D.W., & Gens, A. (1982). Investigating anisotropy and the effects of principal stress rotation and of the intermediate principal stress using a hollow cylinder. *Deformation and Failure of Granular Materials, International Union of Theoretical and Applied Mechanics Symposium, Balkema*, pp 441-449.
172. Taboada, V.M., Martinez-Ramirez, G., & Abdoun, T. (2002). Centrifuge modeling of seismic behavior of a slope in liquefiable soil. *Soil Dynamic and Earthquake Engineering*, 22, 1043-1049.
173. Taylor, D.W. (1948). *Fundamentals of Soil Mechanics*. John Wiley & Sons, Inc.
174. Thomas, J. (1992). Static, cyclic and post liquefaction undrained behaviour of Fraser River sand. M.A.Sc. Thesis, Department of Civil Engineering, University of British Columbia, Canada.
175. Tokimatsu, K. & Seed, H.B. (1987). Evaluation of settlements in sands due to earthquake shaking. *Journal of Geotechnical Engineering*, 113(8), 861-878.
176. Vaid, Y.P., Byrne, P.M., & Hughes, J.M.O. (1981). Dilation angle and liquefaction potential. In *Proceedings of the International Conference on Recent Advances in Geotechnical Engineering and Soil Dynamics, St. Louis, MO., April 26-May 3, 1981, Vol. 1*, pp 161-165.
177. Vaid, Y.P., Chern, J.C. & Tumi, H. (1985). Confining pressure, grain angularity, and liquefaction. *Journal of Geotechnical Engineering*, 111(10), 1229-1235.

178. Vaid, Y. P., Sayao, A., Hou, E. & Negussey, D. (1990). Generalized stress-path-dependent soil behaviour with a new hollow cylinder torsional apparatus. *Canadian Geotechnical Journal*, 27, 601-616.
179. Vaid, Y.P., Stedman, J.D., & Sivathayalan, S. (2001). Confining stress and static shear effects in cyclic liquefaction. *Canadian Geotechnical Journal*, 38, 580-591.
180. Vermeer, P.A. (1978). A double hardening model for sand. *Geotechnique* 28, No. 4, pp 413-433
181. Vermeer, P.A. (1984). Non-associated plasticity for soils, concrete and rock. *HERON*, Vol. 29, No. 3, pp 1-64.
182. Vermeer, P.A. (1998). Non-Associated plasticity for soils, concrete and rock. NATO advanced study institute on Physics of Dry Granular Media, pp 163-196
183. Vesic, A.S. & Clough, G.W. (1968). Behaviour of granular materials under high stresses. *Journal of the Soil Mechanics and Foundations Division*, 94(SM3), 661-688.
184. Wan, R.G. & Guo, P.J. (1998). A simple constitutive model for granular soils: Modified stress-dilatancy approach. *Computers and Geotechnics*, 22(2), 109-133.
185. Wang, Z.-L. & Makdisi, F.I. (1999). Implementing a bounding surface hypoplasticity model for sand into the FLAC program. *FLAC and Numerical Modeling in Geomechanics*, pp 483-490
186. Wijewickreme, D., Sriskandakumar, S., & Byrne, P.M. (2005). Cyclic loading response of loose air-pluviated Fraser River sand for validation of numerical models simulating centrifuge tests. *Canadian Geotechnical Journal*, 42(2), 550-561.
187. Wijewickreme, D. & Vaid, Y.P. (1991). Stress non-uniformities in hollow cylinder torsional specimens. *Geotechnical Testing Journal*, 14(4), 349-362.
188. Wijewickreme, D. & Vaid, Y.P. (1993). Behaviour of loose sand under simultaneous increase in stress ratio and principal stress rotation. *Canadian Geotechnical Journal*, 30(6), 953-964.
189. Wijewickreme, D. & Vaid, Y.P. (2005). A descriptive framework for the drained response of sands under simultaneous increase in stress ratio and rotation of principal stresses. Submitted to *Soils and Foundations*.
190. Wood, D.M., Drescher, A. & Budhu, M. (1979). On the determination of stress state in the simple shear apparatus. *Geotechnical Testing Journal*, 2(4), 211-221.
191. Woodward, P.K. & Molenkamp, F. (1999). Application of an advanced multi-surface kinematic constitutive soil model. *International Journal for Numerical and Analytical Methods in Geomechanics*, 23, 1995-2043.

192. Wroth, C.P. (1958). Soil behaviour during shear-existence of critical voids ratios. *Engineering*, 186, 403-413.
193. Wroth, C.P. & Bassett, R.H. (1965). A stress-strain relationship for the shearing behaviour of a sand. *Geotechnique*, 15(1), 32-56.
194. Wu, G. (2001). Earthquake-induced deformation analyses of the upper San Fernando Dam under the 1971 San Fernando Earthquake. *Canadian Geotechnical Journal*, 37, 1-15.
195. Xia, H. & Hu, T. (1991). Effects of saturation and back pressure on sand liquefaction. *Journal of Geotechnical Engineering*, 117(9), 1347-1362.
196. Yang, D, Naesgaard, E., Byrne, P.M., Adalier, K., & Abdoun, T. (2004a). Numerical model verification and calibration of George Massey Tunnel using centrifuge models. *Canadian Geotechnical Journal*, 41(5), 921-942.
197. Yang, Z, Elgamal, Al, Adalier, K., & Sharp, M. (2004b). Earth dams on liquefiable foundation: numerical prediction of centrifuge experiments. *Journal of Engineering Mechanics*, 130(10), 1168-1176.
198. Yang, J. & Li, X.S. (2004). State-dependent strength of sands from the perspective of unified modeling, *Journal of Geotechnical and Geoenvironmental Engineering*, 130(2), 186-198.
199. Yogachandran, C. (1991). Numerical and centrifuge modeling of seismically induced flow failure. Ph.D. Thesis, University of California, Davis.
200. Youd, T.L. (1977). Packing changes and liquefaction susceptibility. *Journal of the Geotechnical Engineering Division*, 103(GT8), 918-922.
201. Youd, T.L. & Craven, T.N. (1975). Lateral stress in sands during cyclic loading. *Journal of the Geotechnical Engineering Division*, 101(GT2), 217-221.
202. Youd, T.L. & Idriss, I.M. (Editors). (1997). *Proceedings of the NCEER Workshop on Evaluation of Liquefaction Resistance of Soils*, National Center for Earthquake Engineering Research, State University of New York at Buffalo.
203. Youd, T.L., Idriss, I.M., Andrus, R.D., Arango, I., Castro, G., Christian, J.T., Dobry, R., Finn, W.D.L., Harder Jr., L.F., Hynes, M.E., Ishihara, K., Koester, J.P., Liao, S., Marcuson III, W.F., Martin, G.R., Mitchell, J.K., Moriwaki, Y., Power, M.S., Robertson, P.K., Seed, R.B., & Stokoe, K.H. (2001). *Liquefaction Resistance of Soils: Summary Report from the 1996 NCEER and 1998 NCEER/NSF Workshops on Evaluation of Liquefaction Resistance of Soils*. *Journal of Geotechnical and Geoenvironmental Engineering*, 127(10), 817-833.
204. Zeng, X., Wu, J., & Young, B.A. (1998). Influence of viscous fluids on properties of sand. *Geotechnical Testing Journal*, 21(1), 45-51.

- 
205. Zienkiewicz, O.C., Chan, A.H.C., Pastor, M., Paul, D.K., & Shiomi, T. (1990). Static and dynamic behavior of soils: a rational approach to quantitative solutions, Part I: fully saturated problems. In Proceedings of the Royal Society of London, Mathematical and Physical Sciences, Series A, 429, 285-309.
  206. Zienkiewicz, O.C., Chan, A.H.C., Pastor, M., Schrefler, B.A., & Shiomi, T. (1999). *Computational Geomechanics*. John Wiley and Sons Press, Chichester, U.K.
  207. Zienkiewicz, O.C. & Mroz, Z. (1984). Generalized plasticity formulation and applications to geomechanics. *Mechanics of Engineering Materials*, pp 655-679
  208. Zienkiewicz, O.C. & Pande, G.N. (1977). Time-dependent multilaminate model of rocks—a numerical study of deformation and failure of rock masses. *International Journal for Numerical and Analytical Methods in Geomechanics*, 1, 219-247.

## Appendix A

### Derivation of Plastic Deformation on the Horizontal Plane

The yield function acting on the horizontal plane,  $f_2$ , can be expressed by

$$[A-1] \quad f_2 = t_2 - s' \cdot \sin \phi_{m2}$$

where  $t_2 = \tau_{xy}$  (the shear stress acting on the horizontal plane);  $s' = (\sigma'_x + \sigma'_y) / 2$ ; and  $\phi_{m2}$  = the friction angle mobilized on the horizontal plane. Differentiating Eq. [A-1] gives an incremental form of shear yield function.

$$[A-2] \quad df_2 = dt_2 - 0.5(d\sigma'_x + d\sigma'_y) \cdot \sin \phi_{m2} - 0.5(\sigma'_x + \sigma'_y) \cdot \cos \phi_{m2} \cdot d\phi_{m2}$$

$$[A-3a] \quad df_2 = dt_2 - 0.5(d\sigma'_x + d\sigma'_y) \cdot \sin \phi_{m2} - 0.5(\sigma'_x + \sigma'_y) d\eta_2$$

Since  $0.5(\sigma'_x + \sigma'_y) d\eta_2 = G^{p2} \cdot d\gamma^{p2}$ , then

$$[A-3b] \quad df_2 = dt_2 - 0.5(d\sigma'_x + d\sigma'_y) \cdot \sin \phi_{m2} - G^{p2} \cdot d\gamma^{p2}$$

$$[A-3c] \quad df_2 = dt_2 - 0.5(d\sigma'_x + d\sigma'_y) \cdot \sin \phi_{m2} - G^{p2} \cdot \lambda_2$$

Incremental form of shear yield function on horizontal plane can be obtained.

$$[A-4] \quad df_2 = dt_2 - 0.5(d\sigma'_x + d\sigma'_y) \cdot \sin \phi_{m2} - G^{p2} \cdot \lambda_2$$

In Eq. [A-4] the general stress increments  $d\sigma'_x$ ,  $d\sigma'_y$ ,  $d\tau_{xy}$  are necessary and can be obtained as follows:

$$[A-5a] \quad \{d\sigma'\} = [D]^e \{d\varepsilon\} - [D]^e \{d\varepsilon\}^p = \{d\sigma'\}^* - [D]^e \{d\varepsilon\}^p$$

$$[A-5b] \quad \begin{Bmatrix} d\sigma'_x \\ d\sigma'_y \\ d\tau_{xy} \end{Bmatrix} = \begin{Bmatrix} d\sigma_x^* \\ d\sigma_y^* \\ d\tau_{xy}^* \end{Bmatrix} - \begin{bmatrix} \alpha_1 & \alpha_2 & 0 \\ \alpha_2 & \alpha_1 & 0 \\ 0 & 0 & 2G \end{bmatrix} \begin{Bmatrix} -0.5D_{t2} \\ -0.5D_{t2} \\ 1 \end{Bmatrix} \lambda_2$$

$$\text{where, } \alpha_1 = B + (4/3)G \text{ and} \\ \alpha_2 = B - (2/3)G$$

$$[A-6a] \quad d\sigma'_x = d\sigma_x^* + (\alpha_1 + \alpha_2)0.5D_{t2} \cdot \lambda_2$$

$$[A-6b] \quad d\sigma'_y = d\sigma_y^* + (\alpha_1 + \alpha_2)0.5D_{t2} \cdot \lambda_2$$

$$[A-6c] \quad d\tau_{xy} = d\tau_{xy}^* - 2G \cdot \lambda_2$$

Substitute Eqs. [A-6] into Eq. [A-4] and then  $df_2 = 0$ .

$$[A-7] \quad df_2 = d\tau_{xy}^* - 2G \cdot \lambda_2 - 0.5 \sin \phi_{m2} \cdot (d\sigma_x^* + d\sigma_y^* + (\alpha_1 + \alpha_2)D_{t2} \cdot \lambda_2) - G^{p2} \cdot \lambda_2 = 0$$

Manipulate Eq. [A-7] and then:

$$[A-8] \quad d\tau_{xy}^* - 0.5 \sin \phi_{m2} (d\sigma_x^* + d\sigma_y^*) = 2G\lambda_2 + 0.5(\alpha_1 + \alpha_2) \sin \phi_{m2} \cdot D_{t2} \cdot \lambda_2 + G^{p2} \cdot \lambda_2$$

$$d\tau_{xy}^* - 0.5 \sin \phi_{m2} \cdot (d\sigma_x^* + d\sigma_y^*) = (2G + 0.5(\alpha_1 + \alpha_2) \cdot \sin \phi_{m2} \cdot D_{t2} + G^{p2}) \lambda_2$$

Finally, we can get the  $\lambda_2$ .

$$[A-9] \quad \lambda_2 = \frac{d\tau_{xy}^* - 0.5 \sin \phi_{m2} \cdot (d\sigma_x^* + d\sigma_y^*)}{(2G + 0.5(\alpha_1 + \alpha_2) \cdot \sin \phi_{m2} \cdot D_{t2} + G^{p2})}$$

If  $\lambda_2^s$  is known, we can get the new stress increments,  $d\sigma_x, d\sigma_y, d\tau_{xy}$ .

$$[A-10] \quad \begin{Bmatrix} d\sigma'_x \\ d\sigma'_y \\ d\tau_{xy} \end{Bmatrix} = \begin{Bmatrix} d\sigma_x^* \\ d\sigma_y^* \\ d\tau_{xy}^* \end{Bmatrix} + \begin{bmatrix} \alpha_1 & \alpha_2 & 0 \\ \alpha_2 & \alpha_1 & 0 \\ 0 & 0 & 2G \end{bmatrix} \begin{Bmatrix} 0.5D_{t2} \\ 0.5D_{t2} \\ -1 \end{Bmatrix} \lambda_2$$

Then, add the stress increments to old principal stresses to get new stresses.

$$\begin{aligned} & (\sigma'_x)_{\text{new}} = (\sigma'_x)_{\text{old}} + d\sigma'_x \\ \text{[A-11]} \quad & (\sigma'_y)_{\text{new}} = (\sigma'_y)_{\text{old}} + d\sigma'_y \text{ where } (\sigma_i)_{\text{old}} \text{ comes from previous step.} \\ & (\tau_{xy})_{\text{new}} = (\tau_{xy})_{\text{old}} + d\tau_{xy} \end{aligned}$$

## Appendix B

### Derivation of Stress Densification Equation

Relative density change can be calculated in terms of the volumetric strain as follows:

$$[B-1] \quad D_r - D_{r0} = \frac{e_0 - e}{e_{\max} - e_{\min}} = \frac{(1 + e_0) \cdot \varepsilon_v}{e_{\max} - e_{\min}} = \left[ \frac{(1 + e_{\max})}{e_{\max} - e_{\min}} - D_{r0} \right] \cdot \varepsilon_v$$

For the one-dimensional case the volumetric strain  $\varepsilon_v$  is equal to the axial strain  $\varepsilon_a$ , hence

$$[B-2] \quad D_r - D_{r0} = \left[ \frac{(1 + e_{\max})}{e_{\max} - e_{\min}} - D_{r0} \right] \cdot \varepsilon_a$$

The axial strain  $\varepsilon_a$  from one-dimensional condition derived by Janbu (1963) is described below.

The axial strain increment  $d\varepsilon_a$  can be expressed by the constrained modulus  $M$ .

$$[B-3] \quad d\varepsilon_a = \frac{d\sigma'_v}{M}$$

where the constrained modulus  $M$  is given by  $M = k_M \cdot P_a \cdot \left( \frac{\sigma'_v}{P_a} \right)^{1-m}$ ,  $\sigma'_v$  is the vertical effective stress and  $k_M$  is a dimensionless one-dimensional stiffness that depends on  $D_r$ .

The vertical strain  $\varepsilon_a$  corresponding to a vertical stress increase from  $\sigma'_{v0}$  to  $\sigma'_v = \sigma'_{v0} + \Delta\sigma'_v$  is obtained by integration of  $d\varepsilon_a$  as follows:

$$[B-4] \quad \varepsilon_a = \frac{1}{k_M \cdot m} \cdot \left[ \left( \frac{\sigma'_v}{P_a} \right)^m - \left( \frac{\sigma'_{v0}}{P_a} \right)^m \right]$$

In the case of zero initial vertical stress,  $\sigma'_{v0} = 0$ , [B-4] becomes

$$[B-5] \quad \varepsilon_a = \frac{1}{k_M \cdot m} \cdot \left( \frac{\sigma'_v}{P_a} \right)^m$$

Substituting [B-5] into [B-2] yields

$$[B-6] \quad D_r - D_{r0} = \left[ \frac{(1 + e_{\max})}{e_{\max} - e_{\min}} - D_{r0} \right] \cdot \frac{1}{k_M \cdot m} \cdot \left( \frac{\sigma'_v}{P_a} \right)^m$$

The stress densification response of eight sands shown in Figures B.1-B.8 indicates that the exponent  $m = 0.5$  gives good agreement with the data. This is in agreement with others (Janbu, 1963; Cornforth, 1974; Hardin, 1987) for first time loading at stresses below the grain crushing level, so [B-6] becomes

$$[B-7] \quad D_r - D_{r0} = \left[ \frac{(1 + e_{\max})}{e_{\max} - e_{\min}} - D_{r0} \right] \cdot \frac{2}{k_M} \cdot \sqrt{\frac{\sigma'_v}{P_a}}$$

Pestana and Whittle (1995) defined  $k_M = C \cdot f(n)$  where  $C$  is a constant and  $f(n)$  is a function of porosity.

If  $k_M$  is defined as  $k_M = C \cdot f(D_{r0})$ , then  $f(D_{r0}) = \frac{1}{1.5 - D_{r0}}$  was found to give a good fit

to the data. Hence  $k_M = \frac{C}{1.5 - D_{r0}}$ , where  $C$  is a material stiffness property independent of void ratio.

Substituting  $k_M = \frac{C}{1.5 - D_{r0}}$  into [B-7] yields

$$[B-8] \quad D_r = D_{r0} + \alpha \cdot \sqrt{\frac{\sigma'_v}{P_a}}$$

$$\text{where, } \alpha = \left[ \frac{(1 + e_{\max})}{e_{\max} - e_{\min}} - D_{r0} \right] \cdot \frac{2 \cdot (1.5 - D_{r0})}{C}$$

The C values found to fit the data for the eight sands are listed in Table B.1.

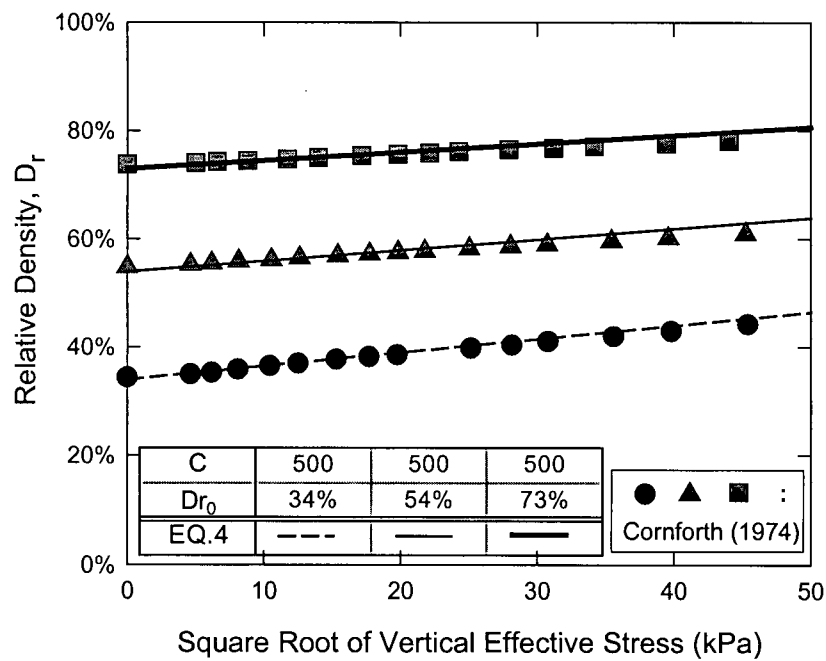


Figure B.1 Relative density change predicted and measured for Brasted sand.

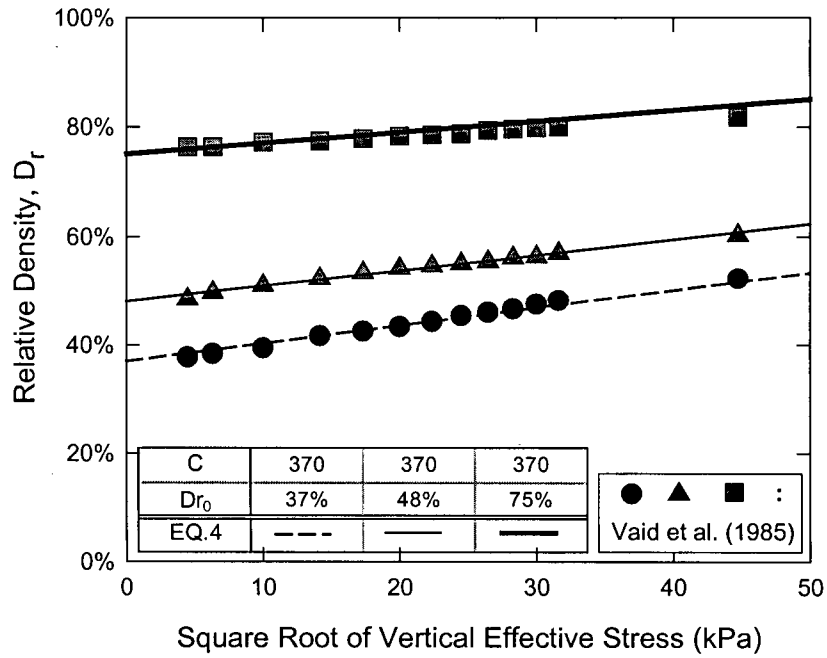


Figure B.2 Relative density change predicted and measured for Ottawa sand.

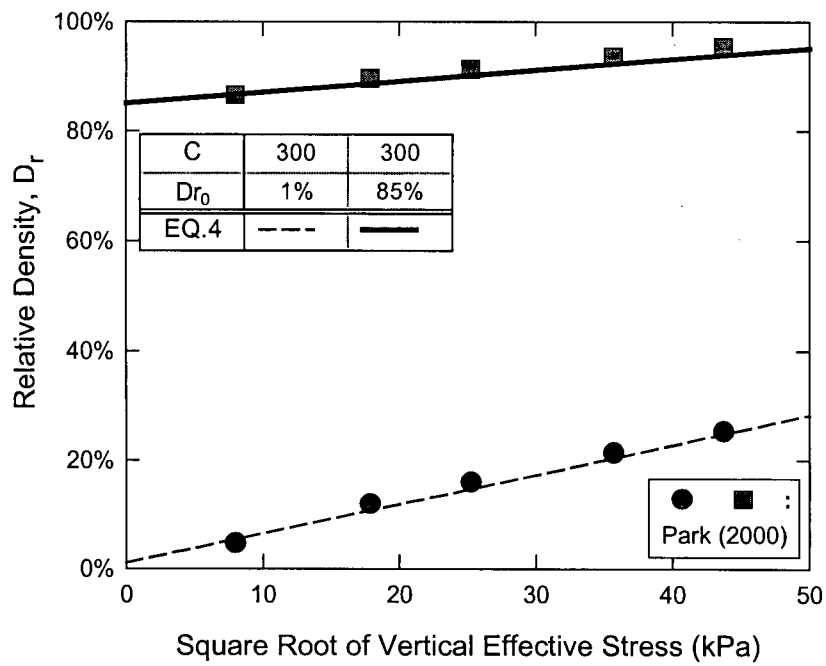


Figure B.3 Relative density change predicted and measured for Toyoura sand.

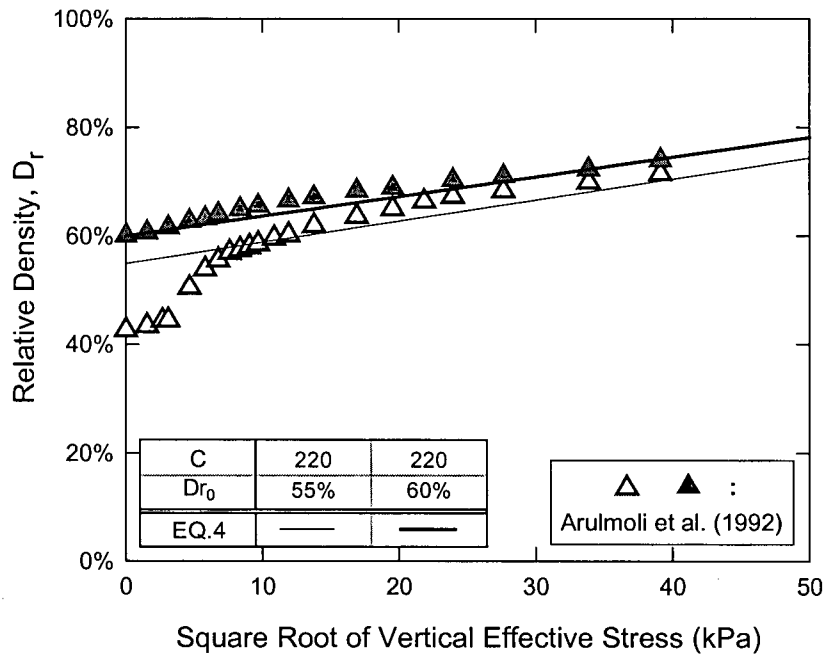


Figure B.4 Relative density change predicted and measured for Nevada sand.

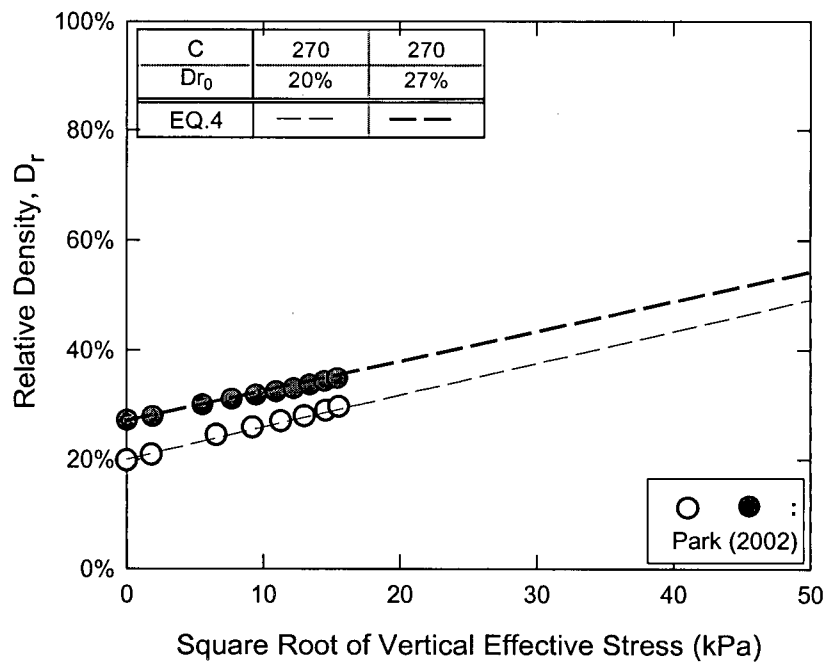


Figure B.5 Relative density change predicted and measured for Fraser River sand.

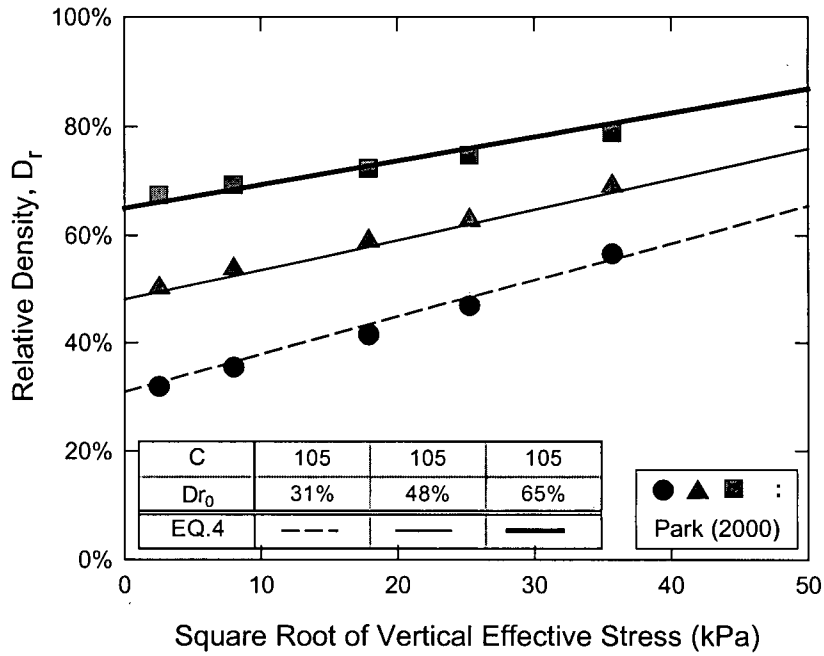


Figure B.6 Relative density change predicted and measured for Volcanic sand.

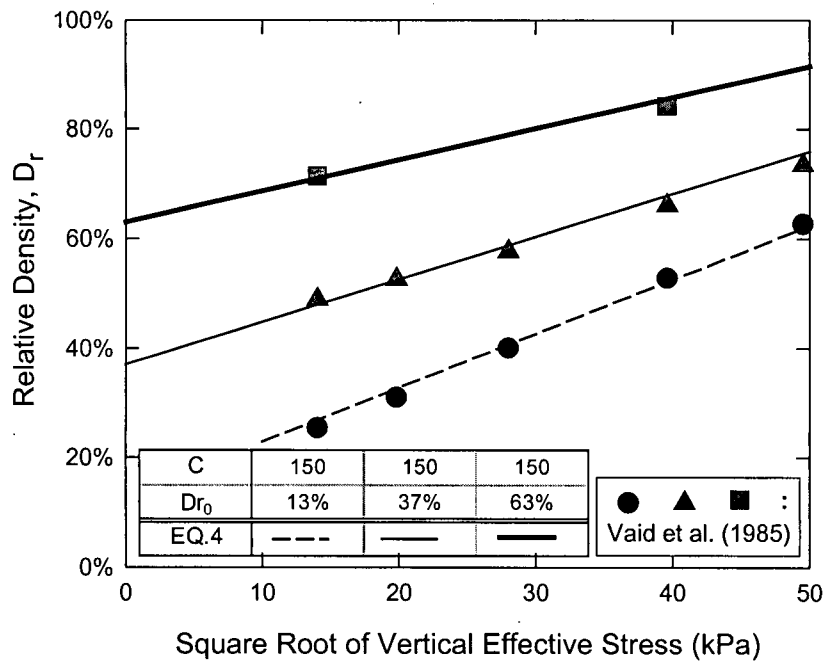
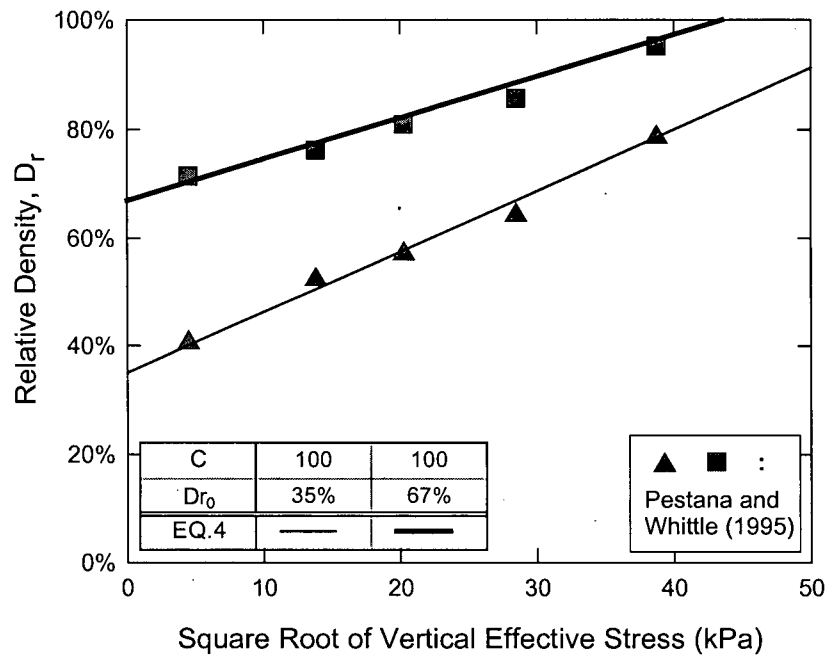


Figure B.7 Relative density change predicted and measured for Mine Tailing sand.



**Figure B.8** Relative density change predicted and measured for Quiou sand.

**Table B.1** Estimation of relative density change due to stress increase.

Sands	C	Stress level (kPa)		
		0	500	1000
Brasted Sand (BS)	500	50%	55%	57%
Ottawa Sand (OS)	370	50%	56%	59%
Toyoura Sand (TS)	300	50%	57%	61%
Nevada Sand (NS)	220	50%	59%	63%
Fraser River Sand (FRS)	270	50%	60%	63%
Volcanic Sand (VS)	105	50%	62%	67%
Mine Tailing Sand (MTS)	150	50%	65%	71%
Quiou Sand (QS)	100	50%	71%	80%

## Appendix C

### Pore Pressure Change under Undrained Condition

The response of sand is controlled by the skeleton behaviour. The skeleton behaviour of the proposed model has been fully presented in Chapter 3. This appendix explains how excess porewater pressures for undrained conditions are related to plastic volumetric strains for the special case of simple shear. A fluid in the pores of the sand acts as a volumetric constraint on the skeleton if drainage is curtailed. Simply, undrained response is captured by imposing this volumetric constraint. The pore pressures of concern are those generated by plastic volumetric strain. Pore pressures may also be generated by transient changes in total stress, but this is accounted for in test procedure. A vertical stress increment  $d\sigma$  is applied to two elements as shown in Figure C.1. An applied load increment will induce a total volumetric strain increment,  $d\varepsilon_v$ , that is the sum of the elastic and plastic increments,  $d\varepsilon_v^e$  and  $d\varepsilon_v^p$ .

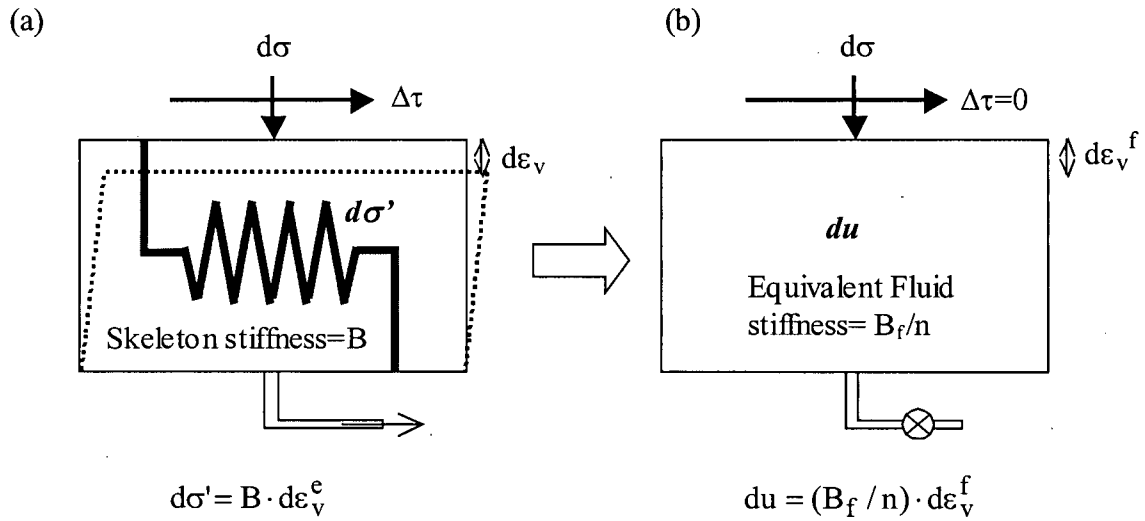


**Figure C.1** Soil element and equivalent fluid models under simple shear.

For undrained conditions, the  $d\epsilon_v$  is equal to the equivalent fluid volumetric strain increment  $d\epsilon_v^f$ . The resulting change in pore pressure,  $du$ , is therefore

$$[C-1] \quad du = \left( \frac{B_f}{n} \right) \cdot d\epsilon_v$$

where  $(B_f/n)$  is the equivalent fluid stiffness;  $B_f$  is the bulk stiffness of the pore fluid; and  $n$  is the porosity of the soil. The corresponding change in effective mean stress,  $d\sigma'$ , due to an increment of volumetric strain is

$$[C-2] \quad d\sigma' = B \cdot d\epsilon_v^e$$

The increment of total mean stress,  $d\sigma$ , is equal to the increments of effective mean stress and pore pressure. If, for simplicity we assume  $d\sigma = 0$ , then  $du = -d\sigma'$ . Substituting from Eqs. [C-1] and [C-2] gives

$$[C-3] \quad du = -B \cdot d\epsilon_v^e = -B \cdot (d\epsilon_v - d\epsilon_v^p) = -B \cdot \left( \frac{du}{B_f/n} - d\epsilon_v^p \right)$$

Rearranging Eq. [C-3] to  $du$  gives  $du \left( 1 + \frac{B}{B_f/n} \right) = B \cdot d\varepsilon_v^p$  and then,

$$[C-4] \quad du = \frac{B}{1 + \frac{B}{B_f/n}} \cdot d\varepsilon_v^p = B_{skem} \cdot B \cdot d\varepsilon_v^p$$

where  $B_{skem}$  is the Skempton value commonly used to assess the saturation of samples in the laboratory. It is clear that the ratio of the skeleton stiffness to pore fluid stiffness,  $B/B_f$ , is a major factor in pore pressure response.

## Appendix D

### FLAC Simulation and Boundary Conditions of C-CORE Centrifuge Tests

#### D.1 FLAC Simulation Procedures of Centrifuge Test (Naesgaard et al., 2005)

The model was set up and run as follows:

- (a) The grid is built with fixed left, right and bottom boundaries.
- (b) Fluid flow is set to off, gravity to 1/70 g, model to Mohr Coulomb. The fluid pressures are initialized as being hydrostatic with a level one meter above final top of model as illustrated in Figure 5.2(a). Pressures are applied to the top model boundary to emulate the fluid.
- (c) Shear modulus is set as a function of effective stress (used Shear modulus,  $G = G_{\max}/3$  and Bulk modulus,  $B = 2 \times G$ ).
- (d) The model was then "Spun-up" to 1 g in seven steps. During each step the soil moduli are updated as a function of effective stress, and the applied pressures and pore pressures along the top boundary are adjusted.
- (e) Set flow on, fluid modulus to 5 kPa, permeability and bring to equilibrium.
- (f) Set dynamic on with local damping of 0.6 and bring to equilibrium.
- (g) Damping is changed to Raleigh. A damping ratio of 2% centered at 3 Hz is used.  
Equilibrium is re-established.
- (h) The constitutive model is changed to UBCSAND2 with properties corresponding to each relative density with allowance for stress densification during the centrifuge spin-up.

- 
- (i) Fluid modulus depends on the degree of saturation and is calculated based on assumed initial saturation, current pore pressure and  $B_f = 2e6$  kPa. The model is brought to equilibrium.
  - (j) Displacements, velocities, and applied top boundary pressures are reset and  $x$  and  $y$  velocities of zero are applied to the bottom, left, and right boundaries. This is then stepped for 10 sec of dynamic time so all is at equilibrium.
  - (k) Initial pore pressure, initial effective stress, initial pore pressure ratio, and  $x$  and  $y$  displacements are set.
  - (l) Histories and dynamic time are reset and the earthquake  $x$ -velocity time history is applied to the bottom, left, and right boundaries. Zero  $y$ -velocity is also applied at the same time.
  - (m) Solve for the duration of the earthquake with the applied pressures and pore pressures on the upper surface being adjusted every 0.1 sec.

## D.2 FLAC Boundary conditions

Fixed Gridpoints  
 B Both directions  
 P Pore-pressure  
 S Saturation

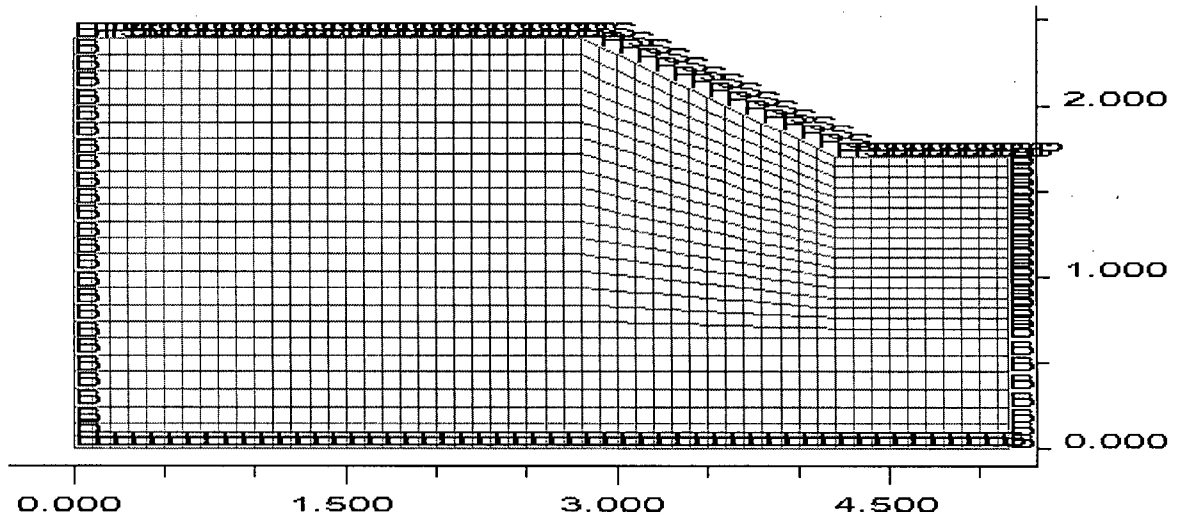


Figure D.1 Meshes and boundary conditions used in FLAC analysis of CT2 (axis scale: x10 m).

Fixed Gridpoints  
 B Both directions  
 P Pore-pressure  
 S Saturation

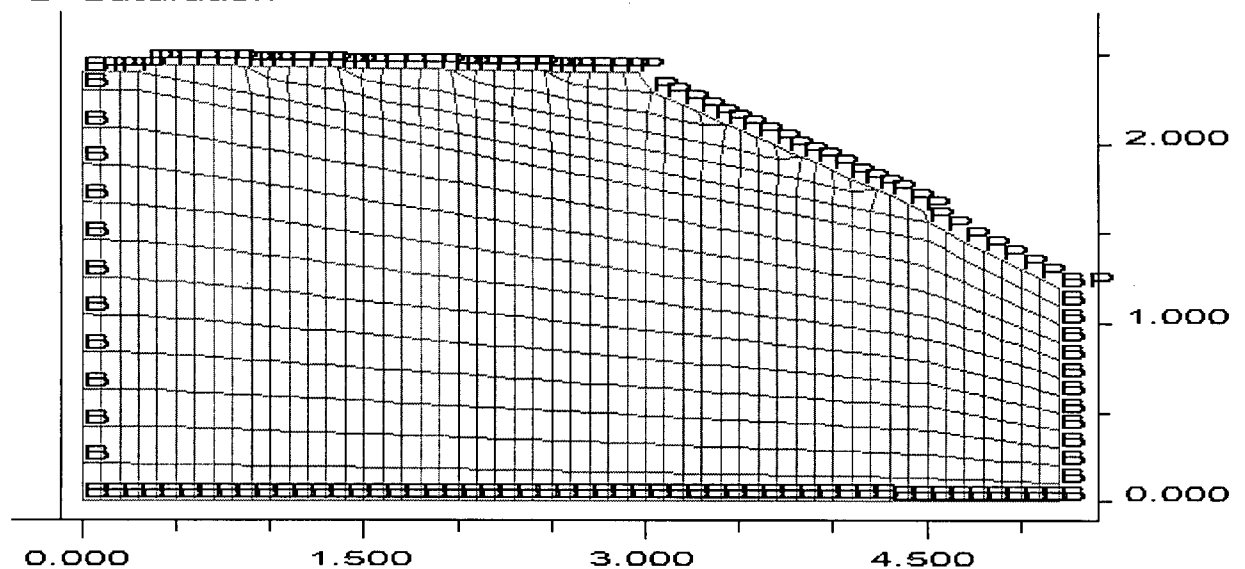


Figure D.2 Meshes and boundary conditions used in FLAC analysis of CT6 (axis scale: x10 m).